

SPRINGER SERIES ON CHEMICAL
SENSORS AND BIOSENSORS

08

Series Editor G. Urban

Volume Editors M. Zourob · A. Lakhtakia

Optical Guided-wave Chemical and Biosensors II

 Springer

8

**Springer Series on Chemical
Sensors and Biosensors**

Methods and Applications

Series Editor: G. Urban

For further volumes:

<http://www.springer.com/series/5346>

Springer Series on Chemical Sensors and Biosensors

Series Editor: G. Urban

Recently Published and Forthcoming Volumes

Optical Guided-wave Chemical and Biosensors II

Volume Editors: M. Zourob, A. Lakhtakia
Vol. 8, 2010

Optical Guided-wave Chemical and Biosensors I

Volume Editors: M. Zourob, A. Lakhtakia
Vol. 7, 2010

Hydrogel Sensors and Actuators

Volume Editors: Gerlach G., Arndt K. -F.
Vol. 6, 2009

Piezoelectric Sensors

Volume Editors: Steinem C., Janshoff A.
Vol. 5, 2006

Surface Plasmon Resonance Based Sensors

Volume Editor: Homola J.
Vol. 4, 2006

Frontiers in Chemical Sensors

Novel Principles and Techniques

Volume Editors: Orellana G., Moreno-Bondi M. C.
Vol. 3, 2005

Ultrathin Electrochemical Chemo- and Biosensors

Technology and Performance
Volume Editor: Mirsky V. M.
Vol. 2, 2004

Optical Sensors

Industrial, Environmental
and Diagnostic Applications

Volume Editors:
Narayanaswamy R., Wolfbeis O. S.
Vol. 1, 2003

Optical Guided-wave Chemical and Biosensors II

Volume Editors: Mohammed Zourob • Akhlesh Lakhtakia

With contributions by

I. Abdulhalim · H. S. Dhadwal · T. Eftimov · M. El-Sherif · X. Fan
Y. Fang · Y. Matsuura · A. Menikh · B. L. Miller · H. Schmidt
M. Skorobogatiy · J. D. Suter · H. Zhu

 Springer

Chemical sensors and biosensors are becoming more and more indispensable tools in life science, medicine, chemistry and biotechnology. The series covers exciting sensor-related aspects of chemistry, biochemistry, thin film and interface techniques, physics, including opto-electronics, measurement sciences and signal processing. The single volumes of the series focus on selected topics and will be edited by selected volume editors. The Springer Series on Chemical Sensors and Biosensors aims to publish state-of-the-art articles that can serve as invaluable tools for both practitioners and researchers active in this highly interdisciplinary field. The carefully edited collection of papers in each volume will give continuous inspiration for new research and will point to existing new trends and brand new applications.

ISSN 1612-7617

ISBN 978-3-642-02826-7

e-ISBN 978-3-642-02827-4

DOI 10.1007/978-3-642-02827-4

Springer Heidelberg Dordrecht London New York

Library of Congress Control Number: 2009933989

© Springer-Verlag Berlin Heidelberg 2010

This work is subject to copyright. All rights are reserved, whether the whole or part of the material is concerned, specifically the rights of translation, reprinting, reuse of illustrations, recitation, broadcasting, reproduction on microfilm or in any other way, and storage in data banks. Duplication of this publication or parts thereof is permitted only under the provisions of the German Copyright Law of September 9, 1965, in its current version, and permission for use must always be obtained from Springer. Violations are liable to prosecution under the German Copyright Law.

The use of general descriptive names, registered names, trademarks, etc. in this publication does not imply, even in the absence of a specific statement, that such names are exempt from the relevant protective laws and regulations and therefore free for general use.

Cover design: WMXDesign GmbH, Heidelberg, Germany

Printed on acid-free paper

Springer is part of Springer Science+Business Media (www.springer.com)

Series Editor

Prof. Dr. Gerald Urban

IMTEK - Laboratory for Sensors
Institute for Microsystems Engineering
Albert-Ludwigs-University
Georges-Köhler-Allee 103
79110 Freiburg
Germany
urban@imtek.de

Volume Editors

Dr. Mohammed Zourob

GDG ENVIRONNEMENT LTÉE
430, rue Saint-Laurent
Trois-Rivières (Quebec)
G8T 6H3 Canada
mohammed.zourob@gdg.ca

INRS Énergie, Matériaux et Télécommunications
1650, boul. Lionel-Boulet
Varenes, Québec,
J3X 1S2 Canada
zourob@emt.inrs.ca

Prof. Dr. Akhlesh Lakhtakia

Pennsylvania State University
Dept. Engineering Science & Mechanics
University Park PA 16802
USA
axl4@psu.edu

Springer Series on Chemical Sensors and Biosensors Also Available Electronically

For all customers who have a standing order to Springer Series on Chemical Sensors and Biosensors, we offer the electronic version via SpringerLink free of charge. Please contact your librarian who can receive a password or free access to the full articles by registering at:

springerlink.com

If you do not have a subscription, you can still view the tables of contents of the volumes and the abstract of each article on SpringerLink. Just click on “Online version available” on the series homepage (www.springer.com/series/5346).

Preface

Optical sensing techniques based on the modification of the refractive index because of either the incursion of a chemical species (analyte) or interactions between two different types of chemical species, one of which is the analyte and the other is the ligand, have had a long history that goes back to beginning of the nineteenth century if not earlier. More recently, fluorescence resulting from an appropriate labeling/modification of the ligand–analyte interaction has been used for optical sensing. Applications of these techniques are commonplace in industry to ascertain the density of a manufactured material in solution; in biomedical labs to detect the presence of a toxin or biological analytes in a fluid; and so on.

Two recent developments have further spurred research on the sensing of chemicals and analytes of biological importance. First, in the aftermath of the horrific events that occurred on September 11, 2001, a major nightmare of homeland-security planners and providers is the deliberate introduction of toxins and pathogens – which include pesticides (e.g., atrazine and 2,4-dichlorophenol) and bacteria (such as *Vibrio cholerae* and *Salmonella paratyphi*) – in a nation’s water resources and urban water-distribution systems. Rapidly acting toxins and pathogens may be released in ponds, lakes, and rivers by enemy troops in war-zones to disable the soldiers fighting them. The same strategy may also be employed by guerrilla fighters sneaking behind the forward positions of regular armed forces. Thus, multianalyte sensing systems with remote monitoring capabilities, high sensitivity, and low incidence of false results are urgently needed to quickly assess both internal and external threats implemented by saboteurs.

Second, our air and water are increasingly more polluted from relentless industrialization in many rapidly developing countries and the conversion of farming from a family-based enterprise to agribusiness throughout the world. Water pollution is already a serious global problem, as the contents of wastewaters have become very complex. Chemical mutagens and carcinogens derived from industrial waste, pesticides, and urban sewage are known to cause metabolic damage in living organisms. For example, endocrine-disrupting compounds are able to either mimic or counter antagonize the effects of hormones such as estrogens and androgens. When present in the environment, endocrine-disrupting compounds engender

reproductive abnormalities in humans, wild animals, and laboratory animals. Incidences of cancer among humans and domestic animals can also be ascribed to these compounds. Clearly then, endocrine-disrupting compounds can be used by terrorists to debilitate dense population centers as well as damage ecosystem features necessary to grow and harvest food.

Although many sensing modalities exist and are being currently investigated, optical sensors are very attractive for a variety of reasons. Most importantly, optical sensing schemes are very sensitive, so much so that single molecules could eventually be sensed optically. Next, many light signals can be sent over the same optical beam because light signals at different frequencies do not interfere with one another. Several optical techniques generate an optical signal only when the target analyte is present, which is an attractive feature. The intrinsic amplification in some optical techniques, such as fluorescence, is also very desirable. Finally, optical signals do not require a material medium to travel in.

A variety of optical-sensing mechanisms exist, including luminescence, fluorescence, phosphorescence, absorbance, elastic scattering, Raman scattering, surface-plasmon resonance, guided-wave resonance, interference, and reflection/transmission microscopy. The need to measure multiple parameters has been fulfilled by bundling several sensors together for multiplexing.

A host of surface phenomena are being employed for optical sensing. Local-field effects that are orders of magnitude larger than comparable bulk effects can be obtained at surfaces with high-aspect-ratio features, thereby enabling measurements with much higher sensitivity. Local surface-plasmon resonance, surface-enhanced Raman scattering, and surface-enhanced fluorescence exemplify such phenomena. Smaller particles have larger surface-to-volume ratios and can access more of the analyte than bulk materials can. Some surface-sensitive techniques can detect reactions occurring only at the surface and consequently can be designed to be insensitive to the bulk medium, thereby making such techniques less susceptible to interference from extraneous signals.

The book entitled *Optical Guided-wave Chemical and Biosensors* is devoted to optical sensing techniques employing the phenomenon of guided wave propagation. The structure guiding the wave can be a planar waveguide, a circular waveguide, or an optical fiber. Even the interface of two dissimilar materials can guide the propagation of an optical wave. The characteristic length scale of a guided wave is provided by its angular frequency and its phase speed in the direction of propagation. The phase speed at a specific angular frequency can vary if the constitutive properties of any part of the waveguide are disturbed, either by the presence of an analyte by itself or because of the binding of ligand molecules with the analyte molecules. After calibration, this disturbance can be used to sense the presence and the concentration of the target analyte.

Published in the Springer Series on Chemical Sensors and Biosensors, the book comprises 19 chapters written by 27 researchers actively working in North America, Europe, and Asia. The authors were requested to adopt a pedagogical tone in order to accommodate the needs of novice researchers such as graduate students and postdoctoral scholars as well as of established researchers seeking new

avenues. This has resulted in duplication of some material we have chosen to retain, because we know that many a reader will pick only a specific chapter to read at a certain time.

We have divided the book into two volumes comprising six parts. Volume I has two parts and Volume II has four parts. Volume I covers the planar-waveguide and plasmonic platforms. Volume II covers waveguide sensors with periodic structures, optical-fiber sensors, hollow-waveguide and microresonator sensors, and finally terahertz biosensing.

Volume II: The incorporation of periodic structures to exploit the Bragg phenomenon for sensing is the theme of Part I. Planar waveguides with periodic stratification either normal or parallel to the direction of propagation of light can be used for sensing. Those made of nano-structured silicon are presented in the first chapter by Miller (University of Rochester, USA). This concept can be fruitfully used for sensing multiple analytes captured by microarrays of ligands, as discussed in the second chapter by Fang (Corning, USA). The use of hollow waveguides with analyte-filled cores and periodically stratified cladding for optical sensing is discussed in the chapter by Skorobogatiy (Ecole Polytechnique de Montréal, Canada). Abdulhalim (Ben Gurion University of the Negev) provides in the fourth chapter a succinct review of resonant nanostructures for optical sensing. These structures include grating-based resonant structures, metallic nanoparticles, and nanoapertures. A comparative analysis of the refractive-index sensitivity of various techniques is the hallmark of this chapter.

Part II is focused on optical-fiber sensors. Initially, El-Sherif (Photonics Laboratories, USA) provides an overview of chemical sensors and biosensors employing optical fibers as sensing elements. Sensing mechanisms, sensor design and development, and characterization of sensors are presented with examples. Key examples of sensing applications of fiber gratings are surveyed by Eftimov (Plovdiv University, Bulgaria), with emphasis on sensing solutes, gases, proteins, and other biomolecules. Matsuura (Tohoku University, Japan) shows in the next chapter that the spectrum of the reflection from a biological surface positioned at the end of a metal-clad hollow fiber provides a remote-sensing modality.

Part III is focused on hollow waveguides and microresonators. The insertion of a solution containing the target analyte inside the hollow core of a waveguide can be expected to enhance the interaction of light and the analyte, as discussed by Schmidt (University of California, Santa Cruz, USA). Dhadwal (Stony Brook University, USA) extensively discusses the capabilities of such waveguides for sensing DNA. One way to enhance the interaction of light with the analyte in a waveguide is to make the waveguide end at its beginning. The light then recirculates in the ring resonator thus formed, thereby enhancing the sensitivity. Zhu, Suter, and Fan (University of Michigan, USA) describe these sensors in the last chapter of Part III.

Part IV contains only one chapter. Menikh (Siemens Medical Solutions Diagnostics, USA) reviews the tremendous expansion of terahertz technology for medical sensing applications as diverse as tumor recognition and the detection of dental cavities, and molecular recognition by sensing ligand-analyte interactions.

Menikh focuses not only on current capabilities and progress in THz biosensing technologies, but also on their limitations.

We are confident that research on optical sensors for chemicals and biochemicals will lead to label-free, multianalyte, highly reliable, highly sensitive, miniature, and expensive sensors. Waveguide sensors will be among the commonly used ones. We shall be delighted if this two-volume book facilitates the emergence of optical sensors with highly desirable attributes.

University Park and Montreal
October 2009

Akhlesh Lakhtakia and Mohammed Zourob

Contents of Volume II

Part I Waveguide Sensors with Periodic Structures

Nano-structured Silicon Optical Sensors 3
Benjamin L. Miller

Resonant Waveguide Grating Biosensor for Microarrays 27
Ye Fang

**Resonant Biochemical Sensors Based on Photonic Bandgap
Waveguides and Fibers** 43
Maksim Skorobogatiy

**Nanophotonic and Subwavelength Structures for Sensing
and Biosensing** 73
I. Abdulhalim

Part II Optical-Fiber Sensors

Fiber-Optic Chemical and Biosensors 109
Mahmoud El-Sherif

Applications of Fiber Gratings in Chemical and Biochemical Sensing 151
Tinko Eftimov

Hollow-Optical Fiber Probes for Biomedical Spectroscopy 177
Yuji Matsuura

Part III Hollow-Waveguide and Micro-Resonator Sensors

Liquid-Core Waveguide Sensors	195
Holger Schmidt	
Capillary Waveguide Biosensor Platform	221
Harbans S. Dhadwal	
Label-Free Optical Ring Resonator Bio/Chemical Sensors	259
Hongying Zhu, Jonathan D. Suter and Xudong Fan	

Part IV Terahertz Biosensing

Terahertz-Biosensing Technology: Progress, Limitations, and Future Outlook	283
Abdellah Menikh	
Index	297
Erratum to page 147	303

Contents of Volume I

Part I Planar-Waveguide Sensors

Total-Internal-Reflection Platforms for Chemical and Biological Sensing Applications

Kim E. Sapsford

High-Refractive-Index Waveguide Platforms for Chemical and Biosensing

Katrin Schmitt and Christian Hoffmann

Planar-Waveguide Interferometers for Chemical Sensing

Daniel P. Campbell

Broadband Spectroelectrochemical Interrogation of Molecular Thin Films by Single-Mode Electro-Active Integrated Optical Waveguides

Sergio B. Mendes, S. Scott Saavedra and Neal R. Armstrong

Part II Plasmonic-Waveguide Sensors

Surface Plasmon Resonance: New Biointerface Designs and High-Throughput Affinity Screening

Matthew J. Linman and Quan Jason Cheng

Nanohole Arrays in Metal Films as Integrated Chemical Sensors and Biosensors

Alexandre G. Brolo, Reuven Gordon and David Sinton

**Nanostructure-Based Localized Surface Plasmon Resonance
Biosensors**

Donghyun Kim

**Gold Nanoparticles on Waveguides For and Toward Sensing
Application**

Silvia Mittler

Part I
Waveguide Sensors with
Periodic Structures

Nano-structured Silicon Optical Sensors

Benjamin L. Miller

Abstract Porous silicon, a material produced by a simple electrochemical etch process on n- or p-type silicon, has generated considerable interest for its photo-physical properties ever since its discovery in the late 1950s. The last decade, in particular, has seen a tremendous amount of research in the use of porous silicon for the construction of label-free optical biosensors. This chapter gives an overview of the broad range of three-dimensional matrix structures that can be made in porous silicon, and their uses in biosensing. As many of these photonic structures are “one-dimensional photonic bandgap” devices, I also discuss the next dimension in sensing with silicon–two-dimensional photonic bandgap structures.

Keywords Porous silicon · Microcavities · Photonic bandgap · Rugate filter · Enzymes

Contents

1	Introduction	4
2	Origins and Definitions	5
3	Types of PSi Sensors	6
4	Porous Silicon Sensing with Single-Layer Interferometers	6
5	Rugate Filters	7
6	Multilayer Devices: Bragg Reflector	7
7	Multilayer Devices: Thue–Morse Sequence	7
8	Porous Silicon Microcavities in Meso- and Macroporous Silicon: Further Confinement of Light	8
9	Double-Layer, Self-Referenced PSi Sensors	12
10	Special Applications: Monitoring Peptide Synthesis	13
11	Characterizing Porous Silicon Via Enzymatic Reactions	14
12	Characterizing Enzymatic Reactions with Porous Silicon	15

B.L. Miller

Department of Dermatology, University of Rochester, Rochester, NY, USA

e-mail: benjamin_miller@urmc.rochester.edu

13	Detection of Small-Molecule Analytes	15
14	Monitoring Diffusion <i>out</i> of a Sensor for Drug Delivery	17
15	Alternative Sensor Configurations: Waveguides	17
16	Towards <i>In Vivo</i> Applications: Enhancing the Stability of PSi Via Surface Derivatization	18
17	Sensor Infiltration and Sensor Efficiency	18
18	Exploiting the Filtration Capacity of PSi Sensors: Detection in Whole Blood	20
19	Beyond the 1D PBG: Towards 2D PBG Sensors	20
20	Concluding Remarks	23
	References	23

Abbreviations

AIR	Arrayed imaging reflectometry
BSA	Bovine serum albumin
(EO) ₆	Hexaethylene glycol
FFT	Fast fourier transform
GlnBP	Glutamine binding protein
GST	Glutathione- <i>S</i> -transferase
OSPA	Orthogonal subspace signal processing algorithm
PBG	Photonic band gap
PMMA	Polymethyl methacrylate
PSi	Porous silicon
RIFS	Reflective interferometric spectroscopy
RIFTS	Reflective interferometric fourier transform spectroscopy
TNBS	Trinitrobenzene sulfonic acid
TNT	Trinitrotoluene
TWTCP	Tetra tryptophan <i>ter</i> cyclopentane

1 Introduction

While labeled biodetection methods continue to serve as the workhorse techniques for medical diagnostics and basic research, it is widely recognized that “label-free” methods have significant potential advantages in terms of cost (fewer consumable reagents and simplified operator requirements) and accuracy (fewer operational steps can translate to a decreased potential for error). Therefore, the search for materials with optical or electrical properties that change on binding of an analyte has attracted a large number of research groups. One raw material that has proven to be exceptionally versatile for the construction of sensors is silicon, which is inexpensive and widely available. Silicon’s status as the central building block for the microelectronics industry means that an immense amount of worldwide

effort has gone into the development of methods for manipulating silicon into a stunning range of configurations. Many of these have optical properties that are useful in the context of sensing. Silicon is also advantageous as a substrate material for biosensor development because it is readily derivatized (i.e., numerous chemistries are available for attaching probe molecules, such as antibodies or nucleic acids) and biocompatible.

This chapter focuses on the use of silicon for the construction of three-dimensional (matrix) photonic materials for sensing. As such, we will neglect planar-silicon sensors, such as AIR [37] and RIFS [31]. The bulk of our discussion will center on PSi, a network structure produced by an electrochemical etching process. We will also confine our discussion primarily to the preparation of biosensors, defined as devices designed to detect biological macromolecules characteristic of the presence of a particular organism. A significant amount of work has also been done on the use of silicon as a substrate for gas sensing. Other nanoporous materials have also found utility as sensing substrates. For example, the Rothberg group has demonstrated DNA detection in porous alumina sensors [49].

Evidence of the popularity of PSi as a sensor material can be found in the large amount of literature devoted to it (a recent SciFinder Scholar search generated 743 hits for “PSi sensor”). PSi sensors have been the subject of numerous reviews, both by the Rochester group of collaborators [38, 39] and others [54]. Therefore, this chapter primarily focuses on recent examples, with a few selected earlier cases to provide context. The community of researchers examining applications of PSi in biosensing is large and diverse, and thus, we have attempted to select a series of examples that provide an overview of the potential configurations of this material. The sections that follow are by no means complete, and we apologize to any authors whose work we have inadvertently neglected. I focus the discussion on optical sensors, although some examples of electrical sensing based on PSi platforms have been published [1].

2 Origins and Definitions

PSi was initially studied in the late 1950s by Uhlir [61] and Turner [60]. Its use as a sensor material was driven in large part by excitement surrounding the observation by Canham that mesoporous silicon exhibits room-temperature visible photoluminescence [4]. As I discuss in many of the examples that follow, however, photoluminescence is not the only property that can be monitored in PSi sensors; in fact, most applications have centered on the observation of changes in the reflectivity spectrum produced by PSi photonic structures. The electrochemical etch process that yields PSi can be tuned based on changes in the etchant solution and based on the substrate (wafer) material itself to yield a broad range of pore sizes and pore morphologies. By convention, silicon with pores <10 nm is termed “nanoporous”; material in the 10–100 nm range is “mesoporous,” and >100 nm is described as “macroporous” silicon. Mesoporous Si tends to have a complex, highly branched

structure, while macropores are typically smooth and straight. The majority of research on PSi sensors has centered on mesoporous material, although sensing with macroporous Si has also been described.

3 Types of PSi Sensors

Because the porosity of PSi can be changed by altering the etching current, changing this current as a function of time allows the production of complex structures within the PSi matrix. In the context of biosensing, this has led to the production and testing of several structures (Fig. 1). Illumination of single-layer PSi produces a reflection spectrum incorporating Fabry–Pérot type interference fringes (a “Fabry–Pérot interferometer”). If the current is modulated in a sinusoidal fashion with respect to time, one can produce a rugate filter (Fig. 1b). Alternatively, stepwise changes in current can produce materials with a high refractive index contrast between well-defined layers of differing porosity, yielding a Bragg mirror (Fig. 1c), a Thue–Morse mirror (Fig. 1d), or a microcavity (Fig. 1e). All these structures can be viewed as one-dimensional photonic bandgap devices. Two-layer (self-referenced) and waveguide structures have also been examined, and will be discussed later. Very recent work has also shown that two-dimensional photonic bandgap structures can be produced in silicon, and have the potential to yield sensors with ultra-high (i.e., single-particle) sensitivity.

4 Porous Silicon Sensing with Single-Layer Interferometers

Some of the earliest demonstrations of PSi-based biosensing were provided by Sailor, Ghadiri, and coworkers, who showed that shifts in the Fabry–Pérot fringes produced by illumination of single-layer mesoporous silicon could be used to detect DNA hybridization and antigen–antibody binding [34]. While some of these initial results were complicated by baseline drift due to ambient reaction of the sensor surface, the authors found in subsequent efforts that ozonolysis prior to other chemical derivatization steps was an effective method of stabilizing optical performance [25]. Such surface passivation methods have proven to be essential, and other strategies including thermal oxidation in oxygen ambient or attachment of hydrocarbon groups via hydrosilylation have also found favor [57]. The efforts

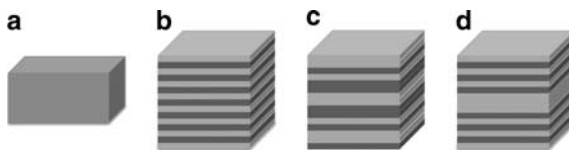


Fig. 1 Types of PSi sensors. (a) single-layer; (b) Bragg filter; (c) Thue–Morse filter; (d) Microcavity

described in [25], also provide the first demonstration of sensing in macroporous (up to 1,200 nm diameter) silicon, using a similar optical detection strategy to that described in their 1997 work. Subsequent efforts by Sailor and colleagues showed that incorporation of BSA as an intervening layer between the PSi surface and the covalently attached capture molecule was able to further stabilize the optical properties of the sensor [12].

5 Rugate Filters

The production of a rugate filter in PSi by sinusoidal variation in the current as a function of time during wafer etching was described by Beger et al. [2]. Such devices, essentially the first in a series of one-dimensional photonic crystal [26, 36] configurations we will discuss, provide a single sharp feature in the optical reflectivity spectrum. Sailor and colleagues showed that PSi rugate filters can be released from the support wafer, broken into fragments, and retain their optical properties, thus allowing solution-phase sensing with “smart dust” [35, 55]. Several other applications of PSi rugate filters are described later in this chapter.

6 Multilayer Devices: Bragg Reflector

If the current density is suddenly changed during the etching process (rather than smoothly varied as in the production of rugate filters), one generates a sharply defined change in the porosity, which in turn translates to a sharp refractive-index contrast. Carrying out this change repetitively – that is, producing a structure with layers of alternating high and low index contrast – produces a Bragg reflector. The Bragg reflector is characterized by a sharp “stop band” in its optical spectrum, the position of which varies as a function of materials infilling the pores of the device. The potential advantages of such a structure for sensing were initially explored by Canham in the context of chemical vapor detection [56], but, as I discuss in subsequent examples, this device configuration has found favor in biosensing as well.

7 Multilayer Devices: Thue–Morse Sequence

Moretti et al. modeled an alternative multilayer structure to the Bragg stack, based on the Thue–Morse sequence [40]. Like the Bragg mirror, this device also consists of alternating high- and low-porosity layers. However, rather than being evenly spaced (periodic), a Thue–Morse multilayer structure is generated by beginning

with a layer of a particular porosity (i.e., “Low,” or “L”), and replacing “L” in the next position by “LH” (and, conversely, “H” by “HL”). Thus, sequences grow as: L, LH, LHHL, LHHLLHH, . . .

Subsequent experiments [41] comparing performance of the Thue–Morse reflector to the Bragg stack in the context of methanol exposure suggest a higher sensitivity (in terms of refractive index unit or alternatively wavelength shift) for the Thue–Morse structure. The authors attribute this in large part to a lower number of low porosity/high porosity interfaces, thereby simplifying infiltration of analyte into the pores. Whether this translates to higher performance in the context of biosensing remains to be seen.

8 Porous Silicon Microcavities in Meso- and Macroporous Silicon: Further Confinement of Light

If a Bragg mirror is interrupted by a thick central layer of PSi (a “defect”), one can produce a microcavity resonator [9]. Such a device has a defect line in the center of the stopband of its optical reflectivity spectrum and exhibits enhanced photoluminescence relative to Bragg structures or single-layer devices. Both the defect feature and photoluminescence lines can be quite narrow (described as a function of the “quality factor” Q of the microcavity), potentially allowing visualization of very small shifts in the reflectance or photoluminescence spectra. In 2000, Chan et al. demonstrated a PSi microcavity sensor for DNA [9]. Application of complementary DNA to a mesoporous Si microcavity derivatized with a DNA probe caused a shift in the photoluminescence spectrum presumed to result from DNA hybridization. In a control experiment, application of a “scrambled” DNA sequence (which would not be expected to bind to the immobilized probe) caused no analogous photoluminescence shift. Similarly, full-length bacteriophage *lambda* virus DNA could be detected in this manner (Fig. 2), providing the first example of a PSi sensor for viruses.

A recent demonstration of a related virus sensor has been provided by the Rossi group, who used antibody-functionalized single-layer PSi sensors for the detection of bacteriophage MS2 virus [52]. Antibodies were immobilized by first functionalizing the Si–H terminated surface with acrylic acid via hydrosilylation, then coupling to amino groups on the antibody via carbodiimide chemistry. An alternative strategy employed photochemical activation of an aryldiazirine cross linker; this was found to be less efficient than the carbodiimide mediated method. Notably, the authors employed dye-labeled virus as the analyte; this allowed for independent validation of the sensor response with fluorescence measurements. These measurements indicated that the sensor had a limit of detection of 2×10^7 pfu/ml (plaque forming units, a measure of active virus, per ml) of virus and a dynamic range of 3 logs.

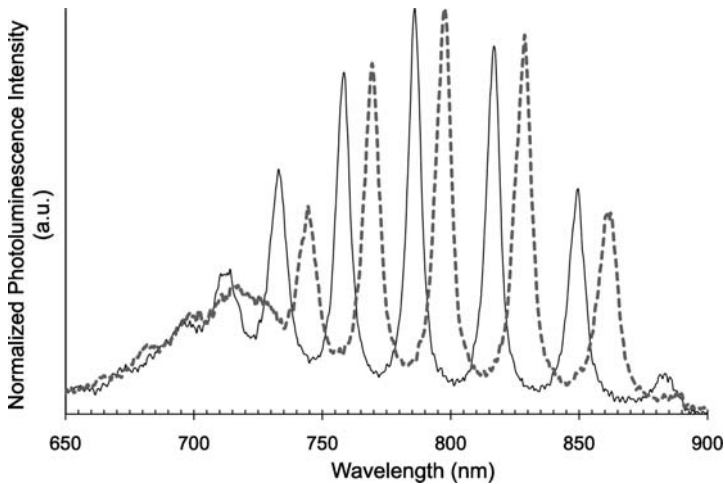


Fig. 2 PSi microcavity-based detection of bacteriophage *lambda* (adapted from [9]). The *solid line* represents the photoluminescence spectrum of the DNA-derivatized device, while the *dotted line* shows the photoluminescence spectrum of the sensor following exposure to the bacteriophage virus

Further development of the PSi microcavity resonator as a biosensor for pathogens was reported by the Rochester group in 2001 [10]. Using a PSi microcavity derivatized with TWTCP (Fig. 3a), a synthetic compound able to bind bacterial lipid A [24], the authors were able to produce a sensor that gave a signal (a photoluminescence shift) when exposed to Gram(-) bacteria, such as *E. coli* and *Salmonella* (Fig. 3b), but no shift was observed when exposed to Gram(+) bacteria, such as *Bacillus subtilis* or *Lactobacillus acidophilus* (Fig. 3c). This sensor therefore constitutes a digital analog of the Gram stain, a staple procedure of microbiology laboratories essentially unchanged since its discovery in the late 1800s [63].

The behavior of a PSi microcavity sensor operating in reflectivity mode was examined in a particularly interesting context by DeLouise et al. [13, 14]). After releasing a mesoporous microcavity from the underlying wafer, it was transferred to a commercial hydrogel bandage material by contact lamination (Fig. 4). This rough treatment of the delicate microcavity structure did not prevent it from continuing to operate as a sensor; exposure of the PSi/hydrogel matrix to increasing concentrations of sucrose in water produced a concentration-dependent shift in the reflectivity spectrum. Importantly, treatment of the hydrogel-embedded sensor with water following each successive sucrose treatment caused the spectrum to return to its initial state. Perhaps the most impressive (and surprising) observation, however, was that the hydrogel-embedded sensor could be subjected to successive cycles of hydration and drying *over the course of more than a year* without substantial loss in optical performance (DeLouise, personal communication). These results are

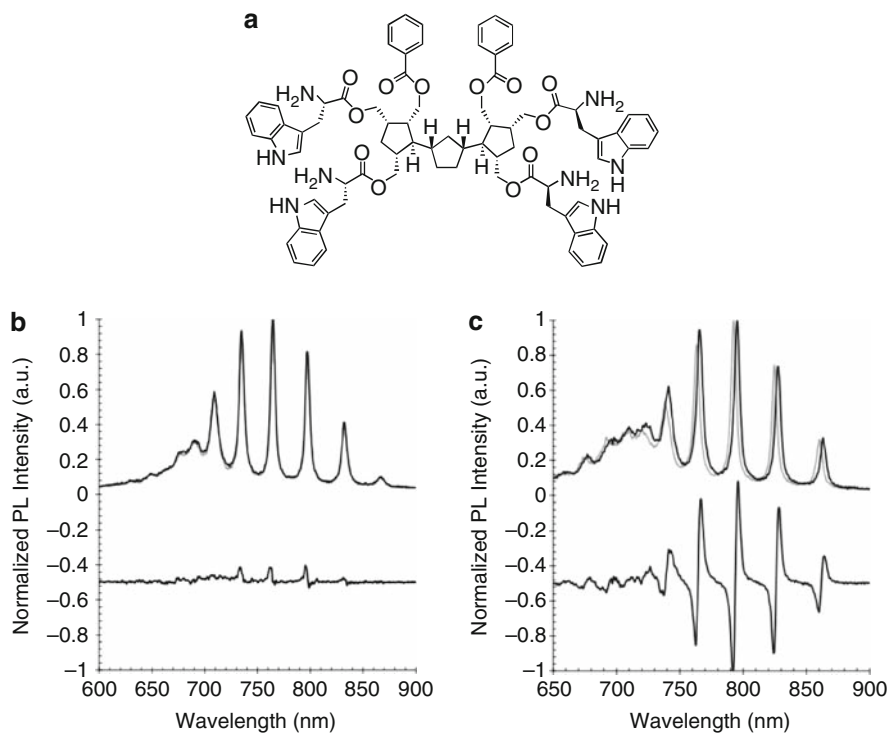


Fig. 3 Digital Gram Stain: Functionalization of a porous silicon microcavity with a synthetic receptor (a) for bacterial lipid A yields a device that responds in the presence of Gram(-) bacteria (b), but gives no response to Gram(+) bacteria (c). Upper traces represent photoluminescence spectra pre (*gray*) and post (*black*) exposure to the respective bacteria, while lower traces are difference spectra

strongly encouraging with regard to the possibility of producing *smart bandages*, or materials that can provide ongoing feedback as a wound heals.

The sensitivity of a PSi microcavity biosensor decreases as the pore size increases, primarily due to changes in the sensing surface to void volume ratio [14, 46]. Sensitivity must be balanced in many cases against ease of infiltration, and for many analytes (particularly large proteins), infiltration into mesoporous silicon is impossible because of the small size of the pores and because the most common methods of etching mesoporous silicon produce pores that are both crooked and highly branched. The barrier function of PSi has been exploited by a number of groups in specific sensing applications; conversely, the fabrication and performance of macroporous silicon microcavities, able to accommodate infiltration of relatively large analytes, has been studied by Ouyang et al. [43–45]. Building on the observation that the doping level of n-type silicon could be used as a guide to the size of pores that would be etched in a standard electrochemical process (Fig. 5), the authors first prepared microcavities with pores ranging from 20 to 120 nm diameter.

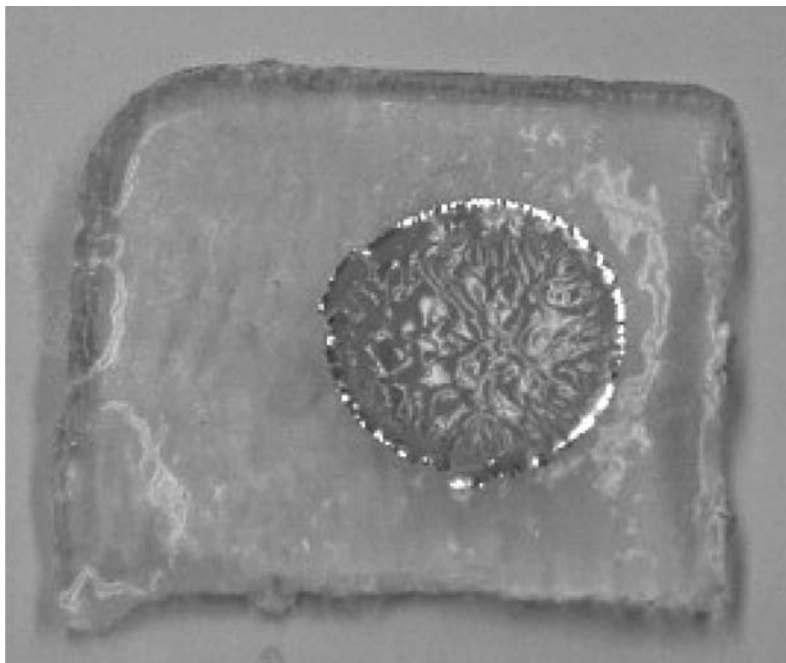


Fig. 4 Hydrogel-embedded porous silicon microcavity

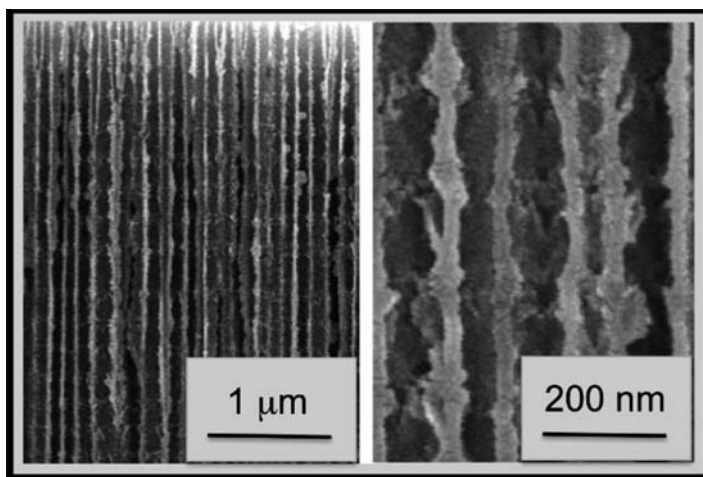


Fig. 5 Macroporous silicon microcavities at two different magnifications (adapted from [43]). Multilayer structure is visible as regular variation in the thickness of the silicon “columns” supporting the structure

Initial demonstration of biosensing ability was provided by the streptavidin–biotin couple; subsequent work with a secreted receptor protein from enteropathogenic *E. coli* showed that detection of specific targets in bacterial lysate was possible.

9 Double-Layer, Self-Referenced PSi Sensors

Pacholski and Sailor have noted that the inability of large molecules to diffuse into PSi films can be used to advantage by effectively allowing the deeper portion of the film to serve as a “reference channel” for the upper portion of the film (the “detection channel”) [47]. In a simple test system, sucrose (a small molecule able to penetrate fully into the film) was readily differentiated from BSA (a protein able to engage in electrostatic interactions with the surface of the oxidized PSi film, but unable to penetrate into the pores). This differentiation was accomplished by comparing changes in the peak produced by the stopband of a rugate filter and changes in Fabry–Pérot fringes produced by the top and bottom surfaces of the film.

Building on this work, the Sailor group employed their PSi-based “reflective interferometric Fourier transform spectroscopy,” or RIFTS, to detect a specific antibody–antigen interaction [48]. In this study, a two-layer PSi structure was etched with a high porosity layer on top of a lower-porosity layer (Fig. 6). Material and etching parameters were chosen such that the pore diameter was less than 10 nm, or too small to allow infiltration of either the capture molecule (protein A in

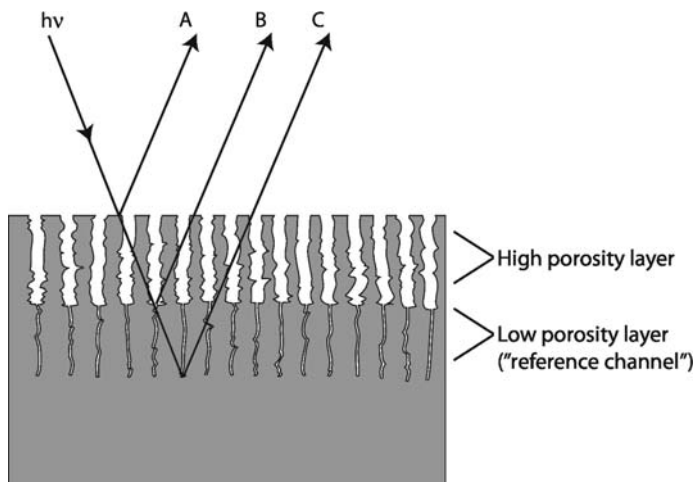


Fig. 6 Reflective interferometric Fourier-transform spectroscopy (RIFTS) sensor, Sailor group. Adapted from [48]. Reflections produced by particular layer interfaces are characterized by “A,” “B,” and “C”; only “A” and “B” are affected by analyte binding, while “C” is not

this case) or target analyte (IgG). After absorbing protein A on the surface of the sensor, IgG was readily detected on binding based on FFT analysis of the interference spectra produced by the device. Furthermore, monitoring the signal as a function of IgG concentration allowed accurate extraction of the protein A – IgG binding constant.

10 Special Applications: Monitoring Peptide Synthesis

A particularly novel application for PSi sensors has been reported by the DeLouise group, who employed mesoporous silicon microcavities as substrates for peptide synthesis [21]. Using “standard” solid-phase amino acid coupling methodology, the authors demonstrated that the PSi could serve as an effective synthesis scaffold. Notably, optical response of the sensor allowed for monitoring the degree of reaction completion, since attachment of each amino acid caused a red-shift up to a maximum value determined by the amino acid loading, and deprotection of individual amino acids after each coupling step caused a blue shift as material corresponding to the protecting group was removed. Figure 7 shows the optical response for silanization of the PSi chip, followed by attachment of a cleavable linker and protected arginine. The authors went on to synthesize a tripeptide (Arg–Asp–Gly), important in cell adhesion. In addition to monitoring synthesis by sensor optical response, the presence of selected intermediates in the synthesis of the peptide was verified by mass spectrometry.

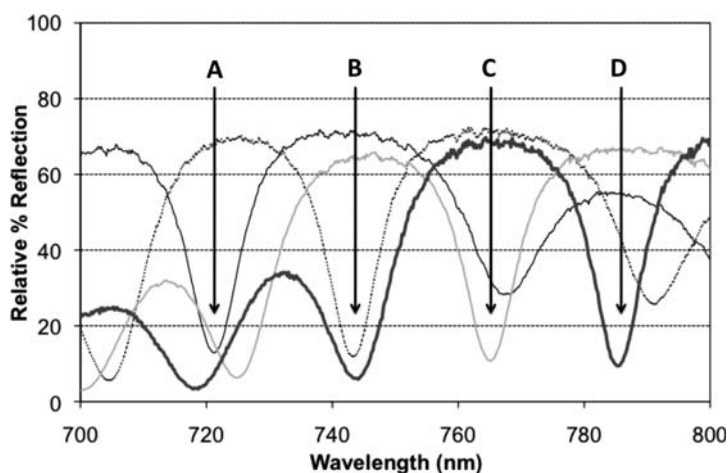


Fig. 7 Peptide synthesis on a PSi microcavity with on-chip optical monitoring (Adapted from [21]). Reflectivity minima indicate successive attachment of chemical species during synthesis: (a) bare porous silicon; (b) silane linker; (c) rink peptide linker; (d) arginine

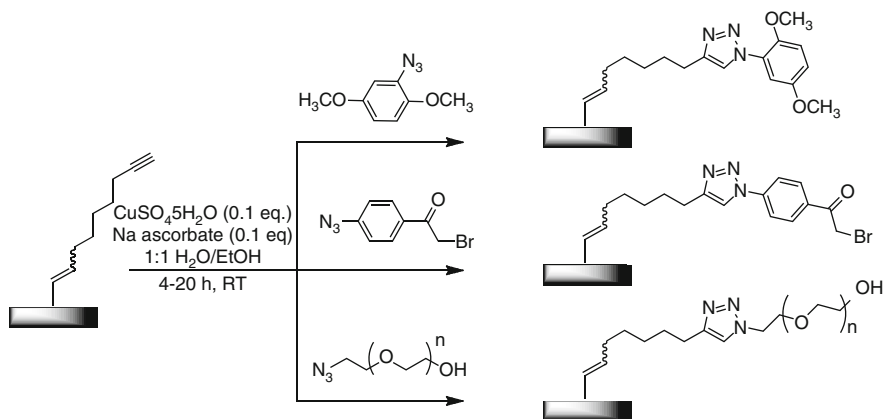


Fig. 8 Derivatization of PSi surfaces via “click” reactions (adapted from [11])

Gooding and colleagues also examined the suitability of PSi as a substrate for chemical synthesis, by employing rugate filters to monitor the progress of copper-catalyzed alkyne–azide cycloadditions, commonly called “click” reactions [11]. After employing thermal hydrosilylation to attach a bis-alkyne to hydride-terminated PSi, subsequent copper-catalyzed “click” chemistry allowed attachment of a number of different azide-functionalized moieties (Fig. 8). Immobilization was verified by observation of bands characteristic of specific organic functional groups in transmission mode Fourier-transform infrared (FTIR) spectra. As in the DeLouise work, red shifts in reflectivity spectra also served as a reporter for the progress of the reaction. While the authors focused their efforts on applying the “click” reaction for the attachment of groups with potential antifouling properties (i.e., polyethylene glycol derivatives capable of limiting nonspecific protein binding), the methodology also has promise for other applications. In particular, since one can, in principle, specifically label proteins, antibodies, or other capture molecules with azido functionality, and the “click” reaction occurs readily in water or buffered solution, one could use this strategy as an effective means of probe molecule attachment for biosensing.

11 Characterizing Porous Silicon Via Enzymatic Reactions

A potential concern with label-free sensors such as those we have been describing is that (paradoxically) the detection is an inferred process, that is, if one observes a shift in a spectrum, does that really correspond to the capture of a biomolecule, and if so, does the amount of the shift correspond with what one expects based on theory? DeLouise and Miller set out to test that question in the context of mesoporous silicon sensors in a series of papers focused on correlating the optical response to loading of the enzyme GST, a parameter that could be measured independently

based on colorimetric observation of enzyme activity. After initially verifying that GST could indeed be immobilized in a mesoporous matrix, and that the amount of immobilized enzyme correlated well with the thickness of the PSi layer [16, 17], efforts focused on evaluating the performance of the immobilized enzyme. Surprisingly, immobilization of GST in the PSi matrix only compromised its activity by a factor of 2- to 4-fold [15], suggesting that PSi might have general utility as a support for immobilized enzyme reactions, in addition to its uses in biosensing. Further studies demonstrated that the optical response of the sensor did indeed correlate strongly with the enzyme loading of the device and its activity, although, curiously, optical linearity extended well beyond the point at which enzyme loading was high enough to induce nonlinear behavior in the enzymatic reaction [13, 14].

12 Characterizing Enzymatic Reactions with Porous Silicon

In addition to serving as a support for immobilized enzymes, PSi sensors can be employed to capture and detect the products of enzymatic reactions. As labeled (colorimetric) substrates for enzymes can be expensive, this potentially opens up new and more convenient methods for monitoring enzyme activity and/or screening libraries of potential enzyme inhibitors. In 2006, the Sailor group [42] produced a Bragg reflector from p-type silicon, and then stabilized the film via electrochemical grafting of methyl groups [23]. The authors then coated zein, a general substrate for proteases, onto the PSi film. As the full-length protein is too large to infiltrate efficiently into the approximately 10 nm diameter pores of the device, the hypothesis was that proteolysis of the full-length protein would produce smaller fragments that would infiltrate into the sensor, thereby producing a shift in the reflectivity spectrum. Indeed, this is what was observed: quantitation of protease (pepsin) activity was readily accomplished based on the optical response.

Application of this concept to the detection of gelatinase activity was accomplished by Gao and coworkers in 2008 [22]. After first preparing a 20-layer rugate film via standard methods, the authors spin-coated a layer of gelatin on the chip. This was allowed to crosslink and dry, producing a sensor chip with a reflectivity peak at 521 nm (corresponding to a green color). Treatment of the chip with varying concentrations of matrix metalloproteinase-2 (MMP-2, a gelatinase implicated [8] in a broad range of cancers) caused digestion of the gelatin to varying degrees, readily visible both as shifts in the reflectance spectrum and to the naked eye.

13 Detection of Small-Molecule Analytes

Relatively little work has been done towards the *specific* (i.e., receptor-mediated) detection of small molecules with PSi sensors, although considerable effort has been exerted on *non-specific* small molecule detection (for example, bulk effects

caused by exposure to organic solvents or gases). The former is much more difficult, because small molecules are, by definition, small; their capture by a surface-immobilized antibody or other receptor causes only a slight perturbation in the environment of the sensor. Two strategies that can be employed to increase the amount of signal generated by specific binding of a small-molecule analyte are to employ a displacement assay (binding of the small molecule to a target causes displacement of a larger molecule), or to use a receptor molecule that undergoes a significant conformational change on target binding.

The latter strategy was reported in 2006 by De Stefano and colleagues, who took advantage of the strong (5 nM dissociation constant) affinity of GlnBP for glutamine to develop a PSi glutamine sensor [19]. First, GlnBP was nonspecifically adsorbed inside a Si-H terminated Fabry-Pérot interferometer. According to the authors, GlnBP has an unusually hydrophobic surface that allows for this “hydrophobic capture” to take place; analogous treatment of an oxidized (Si-OH terminated, hydrophilic) surface did not lead to any retention of GlnBP. Treatment of the sensor with a solution of glutamine caused a shift in the reflectivity spectrum, presumed to be the result of a conformational change in GlnBP induced by glutamine binding. Importantly, no reflectivity shift was observed following treatment with a solution of glucose.

The alternative strategy of using a small molecule to displace a larger molecule has been reported by Tinsley-Bown et al. [59]. Presented in the context of developing an alternative to Fourier transform-based analysis of the optical response of single-layer PSi sensors, the authors demonstrated that a technique termed “orthogonal subspace signal processing algorithm” (OSPA) was able to detect optical shifts characteristic of target binding even when FFT methods failed because of instability in the measurement (for example, due to changes in the physical properties of the PSi matrix itself, or thermal fluctuations in the illuminating light source or detection system). The displacement assay involved attaching TNBS, a TNT analog, to BSA. This TNBS-BSA conjugate was then immobilized on a single layer film of mesoporous Si (Fig. 9). Exposure of the chip to an anti-TNT antibody produced a device with a strongly shifted optical spectrum; subsequent displacement of the anti-TNT antibody by TNT in solution caused the sensor response to shift back to its precapture of anti-TNT state. Using this scheme, the authors reported a limit of detection of 1 $\mu\text{g/ml}$ TNT in solution.

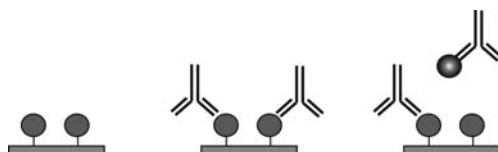


Fig. 9 Displacement assay for TNT, as developed by Tinsley-Bown and colleagues. Porous silicon bearing a TNT analog (*left*) is treated with TNT-binding antibody (*center*). Subsequent exposure to TNT in solution (*right*) causes displacement of the antibody, and a shift in the optical response

14 Monitoring Diffusion *out* of a Sensor for Drug Delivery

Diffusion of materials *out* of a P*Si* sensor was monitored by Koh and coworkers in a proof-of-concept device for monitored drug delivery applications [29]. Poly-methyl methacrylate (PMMA) containing 0.25 mg/ml caffeine was first cast onto a free-standing P*Si* thin film. Exposure of this composite material to a pH 7 buffer caused a time-dependent decrease in the intensity of reflection at a fixed wavelength, or alternatively a time-dependent blue shift of the peak, corresponding to diffusion of the small molecule out of the PMMA–P*Si* composite. These data correlated well with appearance of caffeine in the buffer solution, as measured by UV–Vis spectrophotometry.

15 Alternative Sensor Configurations: Waveguides

Although the vast majority of research on P*Si* sensors has centered on single measurement (static) systems based on reflectance or photoluminescence shifts, waveguide sensors have also been demonstrated. Theoretical analysis of such a structure designed by analogy to the Kretschmann surface plasmon resonance (SPR) sensor configuration (Fig. 10) suggested that it could have exceptional sensitivity [53]. Weiss and coworkers reduced this concept to practice [51], fabricating a device from mesoporous Si (20 nm pore diameter), with a 310 nm layer of 56% porosity on top of a 1,550 nm layer with 84% porosity (note that this is similar to the device configuration employed by Sailor and coworkers, although the measurement strategy is different). Immobilization of a DNA probe via standard aminosilane + glutaraldehyde chemistry provided a functional device. Pouring a solution of complementary DNA over the sensor produced a signal (visualized as a shift in reflectivity minimum), while noncomplementary DNA did not. The limit of detection was calculated to be 50 nM or 5 pg/mm²; although this is less sensitive than predicted by theory (an observation the authors ascribe to limited stability of the DNA immobilization chemistry, and other experimental issues that will likely yield to optimization), it nonetheless constitutes an interesting method for achieving flow-through sensors with P*Si*.

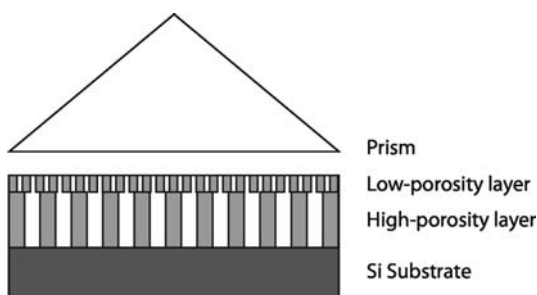


Fig. 10 P*Si* waveguide sensor, Weiss group

16 Towards *In Vivo* Applications: Enhancing the Stability of PSi Via Surface Derivatization

An important concern for any sensor system is its stability under a broad range of conditions, since the sensor may need to operate in a relatively harsh environment. An early selling point for PSi in bioapplications was its biocompatibility and ability to degrade *in situ*. Indeed, this has led to the exploration of PSi as a substrate for a number of *in vivo* scaffolding applications such as bone regeneration [58]. However, how might this impact the performance of the material as a sensor? Canham and colleagues studied this problem initially in 1995, noting that underivatized, highly porous (>70%) silicon degrades within a matter of hours of continuous exposure to simulated plasma [5, 6]. Revisiting this topic in 2000, Canham and colleagues demonstrated that passivation of an 80-layer PSi mirror either by treatment with trichlorododecylsilane or via hydrosilylation with 1-dodecyne provided a considerable increase in stability [7]. For example, the trichlorododecylsilane-treated mirror was found (as determined by SEM) to retain 72 layers of the mirror after 425 h of exposure to simulated plasma, and approximately 50 layers after 2,125 h (88.5 days!) exposure. Furthermore, heavily degraded mirrors still retained a clear stopband, although optical performance was somewhat degraded. The hydrosilylated (1-dodecyne treated) surface fared even better, with very little degradation observed even after 2,125 h in the simulated plasma.

Although these results are highly encouraging, the highly hydrophobic surface produced by dodecyne treatment is potentially problematic for sensor applications. Kilian et al. examined the performance, stability, and antifouling properties of PSi rugate filters derivatized with a hydrophilic passivation agent [28]. Polyethylene glycol (PEG) is a common material for the creation of biocompatible coatings [50] and has found favor in sensing applications because of its ability to inhibit nonspecific binding. Kilian et al.'s study coupled hexa-ethylene glycol ((EO)₆) amine to acid-terminated PSi. Initial demonstration of antifouling capabilities was provided by comparing the ability of a planar (EO)₆-Si chip to retain fluor-tagged BSA relative to undecylenic acid-terminated chips. As expected, (EO)₆ provided a roughly 10-fold improvement (i.e., approximately 10% as much BSA nonspecifically retained). Similar trends were observed for porous Si chips. Critically, (EO)₆ treated chips were found to produce a highly stable optical response even after having been exposed to blood plasma for 72 h at 37°C.

17 Sensor Infiltration and Sensor Efficiency

For any 3-dimensional sensor substrate, the question arises as to how efficiently and evenly material is able to penetrate into the sensor. This issue has been discussed by a number of authors in the context of examining sensor performance vs pore

diameter. For example, DeLouise and Miller demonstrated that a post-etch KOH treatment could be applied to mesoporous silicon microcavities to increase pore diameter by 15% [17]. This modest increase was sufficient to allow infiltration of analytes that otherwise were too large to penetrate into the sensor. For example, on treatment of an as-etched and KOH-treated sensor with a solution of GST, only the KOH-treated sensor showed a wavelength shift in the reflectivity spectrum consistent with GST infiltration.

De Stefano and D'Auria used confocal microscopy to explicitly analyze diffusion of a fluorophore-tagged protein into single- and multilayer films [18]. While the amount of labeled protein present in the single-layer chip appeared to be symmetrically distributed through the film in a Gaussian fashion after an overnight incubation, distribution in the multilayer (alternating porosity) film was much more strongly weighted towards the top surface. While this was only a single set of experiments, the results are nonetheless intriguing and suggest that further study is necessary to understand the impact of such uneven probe (and analyte) distribution on sensor performance. Of course, others have employed such filtration (or analyte-barring) properties as an integral part of the sensing scheme; the Sailor and Weiss examples described above are representative of this strategy. An ability to filter much larger materials (particulates and cells, for example) is another property of PSi that can be employed to advantage, as we discuss below.

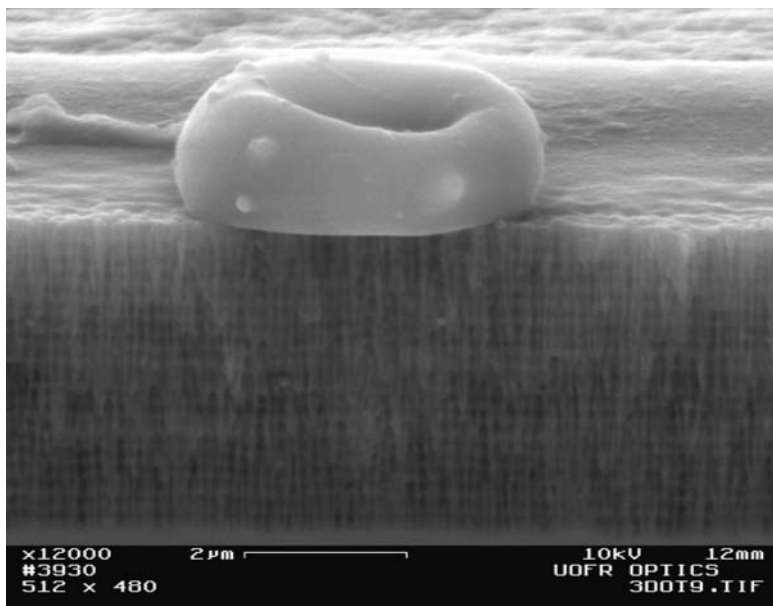


Fig. 11 SEM image of a red blood cell resting on a porous silicon microcavity (courtesy L. M. Bonanno and L. A. DeLouise)

18 Exploiting the Filtration Capacity of PSi Sensors: Detection in Whole Blood

As far as I am aware, the only published example detailing the performance of a PSi sensor in the context of detecting an analyte in serum or whole blood is that reported by Bonanno and DeLouise in 2007 [3]. PSi is ideally suited to the preparation of sensors for use in whole blood, since red blood cells (and other cells that might be present in whole blood) cannot penetrate into the pores. The authors elegantly demonstrated this in a series of SEM images; for example, see Fig. 11. Microcavities prepared from n-type silicon were oxidized and silanized along standard lines, then derivatized with an amine-reactive derivative of biotin. Treatment of the biotin-functionalized surface with streptavidin set the stage for capture of a biotinylated antibody; in this case, rabbit anti-IgG was used. Exposure of the sensor chips to whole rabbit blood, or rabbit serum, showed responses consistent with binding of rabbit IgG. Control experiments with human blood or sensors derivatized with anti-chicken IgG and treated with rabbit blood gave a minimal sensor response.

19 Beyond the 1D PBG: Towards 2D PBG Sensors

While 1D photonic bandgap structures have numerous attractive properties, as described above, they do not provide sufficient sensitivity for some applications in which “ultrasensitive” (single or near-single copy) detection is essential. Building on the hypothesis that increasing the dimensionality of the photonic crystal device would significantly enhance sensitivity, an emerging area of research centers on the use of silicon for the production of 2D photonic bandgap structures. Two-dimensional photonic crystals, consisting of a two-dimensional array of evenly spaced regions of high refractive index and low refractive index in a dielectric medium, are an attractive sensing platform because they provide exceptionally strong light confinement. Like 1D microcavity sensors, a point defect may be introduced into a 2D photonic crystal, allowing defect states to be pulled down from the air band (the “holes” in the structure) or up from the substrate band (the bulk silicon). The corresponding optical spectrum shows narrow transmission peaks inside the bandgap; the position of those peaks is determined by the refractive index of the holes. Thus, the presence of molecules on the walls of the holes can be detected by monitoring a small spectral shift, especially if high-Q microcavities, which have been reported both theoretically [20] and experimentally [62], are used. The potential for using two-dimensional PhC microcavities as chemical sensors was first realized in 1982 [27] and an ambient refractive index change of 0.002 has been detected. However, biomatter recognition depends on the surface chemistry, instead of filling up the holes uniformly.

In preliminary work by the Fauchet group [32], electron-beam lithography was used to fabricate a 2D PBG structure in silicon (Fig. 12), consisting of a hexagonal

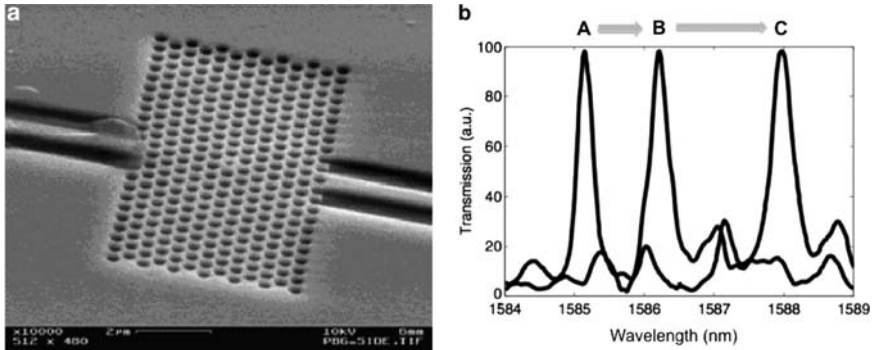
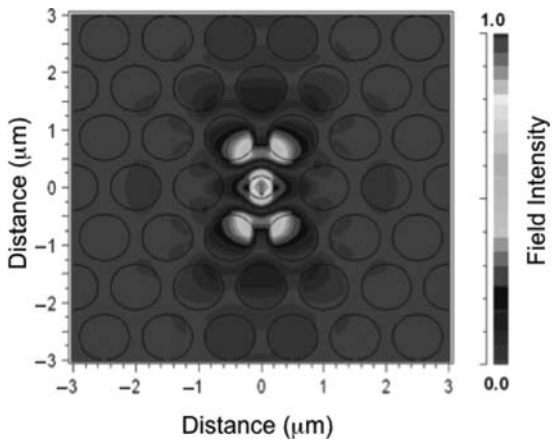


Fig. 12 (a) SEM image of a typical 2D PBG structure. Note the smaller “defect” hole at the center of the device, and waveguides to the left and right of the 2D PBG array. (b) Normalized transmission spectra of the PhC microcavity (A) after oxidation and silanization; (B) after treatment with glutaraldehyde, and (C) after infiltration and covalent capture of BSA. Adapted from [32]

Fig. 13 Calculated field confinement in a 2D PhC microcavity with a central defect point. *Lighter areas* indicate regions of greater field intensity



array of cylindrical air holes in a 400 nm-thick silicon (Si) slab separated from the Si substrate by 1 μm of SiO₂ to provide a good vertical confinement for the propagation modes. In order to couple light in and out of the 2D PBG, two tapered ridge waveguides (visible to the left and right of the 2D PBG microcavity shown in Fig. 12a) were created [26]. Initial sensing performance of the device was characterized by covalently capturing BSA on a layer of glutaraldehyde; this produced a 1.7 nm shift in the optical spectrum (Fig. 12b).

Calculations conducted on the 2D PBG structure suggested that the detection limit of the device was on the order of 2.5 fg of target, assuming a uniform coating on the surface of the pores, and a minimum detectable shift of 0.1 nm. Already impressive, this improves still further if target capture is confined to the defect hole

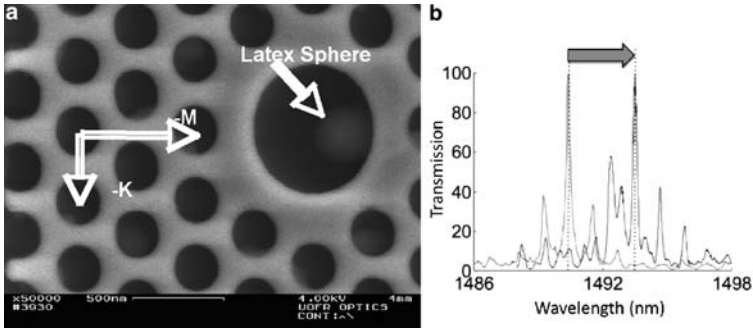


Fig. 14 Single particle detection with a 2DPBG device. The single latex sphere visible in the SEM in (a) causes a shift in the normalized reflection spectrum (b), as indicated by the *arrow*. The notations “K” and “M” in (a) indicated lattice axes. Adapted from [33]

Table 1 Typical sizes for human viral pathogens [30]

Virus	Size (nm)
HIV	120 (spherical)
Vaccinia, Variola	360 × 270 × 250 (“brick-shaped”)
Influenza	100 (spherical)
Rabies virus	50–95 × 130–389 (“bullet-shaped”)
Rhinovirus	22–30 (icosahedral)

at the center of the 2D PBG: as shown in Fig. 13, calculated electric field distribution for the device shows the greatest sensitivity at the defect, suggesting that single-particle detection could take place.

To test this hypothesis, Fauchet and Lee designed a microcavity with a larger central defect than the surrounding holes (685 nm vs. 240 nm) [33]. Such a device would allow a particle with a diameter larger than that of the surrounding holes to be trapped in the defect, while preventing it from penetrating into any other portion of the 2D photonic crystal. Indeed, treatment of the sensor with a solution of 370 nm-diameter latex spheres produced a red shift in the transmission spectrum; subsequent imaging of the chip by SEM confirmed that a single sphere had been captured in the defect (Fig. 14).

While considerable research remains to be done, this ability of the 2D PBG sensor to carry out size selection based on the configuration of the device suggest that it will be particularly well suited for detection of viruses (Table 1): the active (defect) portion of the device may be configured such that large (micron sized and greater) objects such as most bacteria and eukaryotic cells do not penetrate into the defect, while virus particles are “size matched” to the defect hole. Objects smaller than viruses (single proteins, single copies of nucleic acids) also penetrate the defect, but (even if nonspecifically bound) do not provide sufficient mass as to provide a shift as large as for capture of a virus-sized particle.

20 Concluding Remarks

Efforts in the development of specific biosensors based on photonic structures derived from silicon are entering their second decade. While published examples to date show considerable promise – and unique features of three-dimensional silicon structures that can be used advantageously – much work remains in order to turn these devices from laboratory curiosities to robust, sensitive, and general biosensors deployable in “real world” situations. As stated at the outset of this chapter, however, a significant advantage of these materials is their ubiquity in the microelectronics industry. This depth of industrial knowledge should smooth the transition of PSi and other silicon-based photonic structures into the marketplace.

References

1. Archer M, Christophersen M, Fauchet PM (2004) Macroporous silicon electrical sensor for DNA hybridization detection. *Biomed Microdevices* 6:203–211
2. Beger MG, Arens-Fischer R, Thoenissen M, Krueger M, Billat S, Lueth H, Hilbrich S, Theiss W, Grosse P (1997) Dielectric filters made of PS: advanced performance by oxidation and new layer structures. *Thin Solid Films* 297:237–240
3. Bonanno LM, DeLouise LA (2007) Whole blood optical biosensor. *Biosens Bioelectron* 23:444–448
4. Canham LT (1990) Silicon quantum wire array fabrication by electrochemical and chemical dissolution of wafers. *Appl Phys Lett* 57:1046–1048
5. Canham LT (1995) Bioactive silicon structure fabrication through nanoetching techniques. *Adv Mater* 7:1033–1037
6. Canham LT, Reeves CL, King DO, Branfield PJ, Crabb JG, Ward MCL (1996) Bioactive polycrystalline silicon. *Adv Mater* 8:850–852
7. Canham LT, Steward MP, Buriak JM, Reeves CL, Anderson M, Squire EK, Allcock P, Snow PA (2000) Derivatized porous silicon mirrors: implantable optical components with slow resorbability. *Phys Stat Sol A* 182:521–525
8. Chambers AF, Matrisian L (1997) Changing views of the role of matrix metalloproteinases in metastasis. *J Natl Cancer Inst* 89:1260–1270
9. Chan S, Fauchet PM, Li Y, Rothberg LJ, Miller BL (2000) Porous silicon microcavities for biosensing applications. *Physica Status Solidi A* 182:541–546
10. Chan S, Horner SR, Miller BL, Fauchet PM (2001) Identification of gram negative bacteria using nanoscale silicon microcavities. *J Am Chem Soc* 123:11797–11798
11. Ciampi S, Böcking T, Kilian KA, Harper JB, Gooding JJ (2008) Click chemistry in mesoporous materials: functionalization of porous silicon rugate filters. *Langmuir* 24:5888–5892
12. Dancil K-P S, Greiner DP, Sailor MJ (1999) A porous silicon optical biosensor: detection of reversible binding of IgG to a protein A-modified surface. *J Am Chem Soc* 121:7925–7930
13. DeLouise LA, Fauchet PM, Miller BL, Pentland AA (2005) Hydrogel-supported optical microcavity sensors. *Adv Mat* 17:2199–2203
14. DeLouise LA, Kou PM, Miller BL (2005) Cross-correlation of optical microcavity biosensor response with immobilized enzyme activity – insights into biosensor sensitivity. *Anal Chem* 77:3222–3230
15. DeLouise LA, Miller BL (2005) Enzyme immobilization in porous silicon: quantitative analysis of the kinetic parameters for Glutathione-S-Transferases. *Anal Chem* 77:1950–1956

16. DeLouise L, Miller BL (2004) Quantitative assessment of enzyme immobilization capacity in porous silicon. *Anal Chem* 76:6915–6920
17. DeLouise L, Miller BL (2004) Optimization of mesoporous silicon microcavities for proteomics sensing. *Mater Res Soc Symp Proc* 782:A5.3.1–A5.3.7
18. De Stefano L, D'Auria S (2007) Confocal imaging of protein distributions in porous silicon optical structures. *J Phys Condens Matter* 18:395009
19. De Stefano L, Rotiroli L, Rendina I, Moretti L, Scognamiglio V, Rossi M, D'Auria S (2006) Porous silicon-based optical microsensor for the detection of L-glutamine. *Biosens Bioelectron* 21:1664–1667
20. Emerich DF (2005) Nanomedicine—prospective therapeutic and diagnostic applications. *Expert Opin Biol Ther* 5:1–5
21. Furbert P, Lu C, Winograd N, DeLouise LA (2008) Label-free optical detection of peptide synthesis on a porous silicon scaffold/sensor. *Langmuir* 24:2908–2915
22. Gao L, Mbonu M, Cao L, Gao D (2008) Label-free colorimetric detection of gelatinases on nanoporous silicon photonic films. *Anal Chem* 80:1468–1473
23. Gurtner C, Wun AW, Sailor MJ (1999) Surface modification of porous silicon by electrochemical reduction of organo halides. *Angew Chem Int Ed* 38:1966–1967
24. Hubbard RD, Horner SR, Miller BL (2001) Highly substituted *ter*-Cyclopentanes as receptors for lipid A and simple carbohydrates in aqueous solution. *J Am Chem Soc* 123:5810–5811
25. Janshoff A, Dancil K-P S, Steinem C, Greiner DP, S-Y LV, Gurtner C, Motesharei K, Sailor MJ, Ghadiri MR (1998) Macroporous p-type silicon Fabry-Perot layers. Fabrication, characterization, and applications in biosensing. *J Am Chem Soc* 120:12108–12116
26. Joannopoulos JD, Meade RD, Winn JN (1995) *Photonic crystals: molding the flow of light*. Princeton University Press, Princeton
27. John S (1982) Strong localization of photons in certain disordered dielectric superlattices. *Phys Rev Lett* 58:2486
28. Kilian KA, Böcking T, Ilyas S, Gaus K, Jessup W, Gal M, Gooding JJ (2007) Forming antifouling organic multilayers on porous silicon rugate filters towards in vivo/ex vivo biophotonic devices. *Adv Funct Mater* 17:2884–2890
29. Koh Y, Jang S, Kim J, Kim S, Ko YC, Cho S, Sohn H (2008) DBR PSi/PMMA composite materials for smart patch application. *Colloids Surf A Physicochem Eng Asp* 313–314: 328–331
30. Koneman EW, Allen SD, Janda WM, Schreckenberger PC, Winn WC Jr (1997) *Color atlas and textbook of diagnostic microbiology*, 5th edn. Lippincott Williams & Wilkins, Philadelphia, pp 1186–1195
31. Kröger K, Bauer J, Fleckenstein B, Rademann J, Jung G, Gauglitz G (2002) Epitope-mapping of transglutaminase with parallel label-free optical detection. *Biosens Bioelectron* 17:937–944
32. Lee M, Fauchet PM (2007) Two-dimensional silicon photonic crystal based biosensing platform for protein detection. *Opt Express* 15:4530–4535
33. Lee MR, Fauchet PM (2007) Nanoscale microcavity sensor for single particle detection. *Opt Lett* 32:3284–3286
34. Lin VS-Y, Motesharei K, Dancil K-PS, Sailor MJ, Ghadiri MR (1997) A porous silicon-based optical interferometric biosensor. *Science* 278:840–843
35. Link JR, Sailor MJ (2003) Smart dust: self-assembling, self-orienting photonic crystals of porous Si. *Proc Natl Acad Sci USA* 100:10607–10610
36. Lopez C (2003) Materials aspects of photonic crystals. *Adv Mat* 15:1679
37. Mace CR, Striemer CC, Miller BL (2006) A theoretical and experimental analysis of arrayed imaging reflectometry as a sensitive proteomics technique. *Anal Chem* 78:5578–5583
38. Miller BL, Fauchet PM, Horner SR, Chan S (2004) Porous silicon microcavities for biosensing applications. In: Schwarz JA, Contescu CI, Putyera K (eds) *Encyclopedia of nanotechnology*. Marcel Dekker, Inc., New York, pp 343–350
39. Miller BL (2007) Porous silicon in biosensing applications. In: Knopf GK, Bassi AS (eds) *Smart biosensor technology*. CRC Press, Boca Raton, FL, pp 271–290

40. Moretti L, Rea I, Rotiroli L, Rendina I, Abbate G, Marino A, De Stefano L (2006) Photonic band gaps analysis of Thue-Morse multilayer's made of porous silicon. *Opt Express* 14: 6264–6272
41. Moretti L, Rea I, De Stefano L, Rendina I (2007) Periodic versus aperiodic: enhancing the sensitivity of porous silicon based optical sensors. *Appl Phys Lett* 90:191112
42. Orosco MM, Pacholski C, Miskelly GM, Sailor MJ (2006) Protein-coated porous-silicon photonic crystals for amplified optical detection of protease activity. *Adv Mat* 18:1393–1396
43. Ouyang H, Christophersen M, Viard R, Miller BL, Fauchet PM (2005) Macroporous silicon microcavities for macromolecule detection. *Adv Funct Mater* 15:1851–1859
44. Ouyang H, DeLouise LA, Miller BL, Fauchet PM (2007) Label-free quantitative detection of protein using macroporous silicon photonic bandgap biosensors. *Anal Chem* 79:1502–1506
45. Ouyang H, Lee M, Miller BL, Fauchet PM (2005) Silicon photonic bandgap biosensors. *Proc SPIE* 2018:93–103
46. Ouyang H, Striemer CC, Fauchet PM (2006) Quantitative analysis of the sensitivity of porous silicon optical biosensors. *Appl Phys Lett* 88:163108
47. Pacholski C, Sailor MJ (2007) Sensing with porous silicon double layers: a general approach for background suppression. *Phys Stat Sol C* 4:2088–2092
48. Pacholski C, Yu C, Miskelly GM, Godin D, Sailor MJ (2006) Reflective interferometric Fourier transform spectroscopy: a self-compensating label-free immunosensor using double-layers of porous SiO₂. *J Am Chem Soc* 128:4250–4252
49. Pan S, Rothberg LJ (2003) Interferometric sensing of biomolecular binding using nanoporous aluminum oxide templates. *Nano Lett* 3:811–814
50. Prime KL, Whitesides GM (1993) Adsorption of proteins onto surfaces containing end-attached oligo(ethylene oxide): a model system using self-assembled monolayers. *J Am Chem Soc* 115:10714–10721
51. Rong G, Najmaie A, Sipe JE, Weiss SM (2008) Nanoscale porous silicon waveguide for label-free DNA sensing. *Biosens Bioelectron* 23:1572–1576
52. Rossi AM, Wang L, Reipa V, Murphy TE (2007) Porous silicon biosensor for detection of viruses. *Biosens Bioelectron* 23:741–745
53. Saarinen JJ, Weiss SM, Fauchet PM, Sipe JE (2005) Optical sensor based on resonant porous silicon structures. *Opt Express* 13:3754–3764
54. Sailor MJ (2007) Color me sensitive: amplification and discrimination in photonic silicon nanostructures. *ACS Nano* 1:248–251
55. Schmedake TA, Cunin F, Link JR, Sailor MJ (2002) Standoff detection of chemicals using porous silicon “smart dust” particles. *Adv Mat* 14:1270–1272
56. Snow PA, Squire EK, Russell PSJ, Canham LT (1999) Vapor sensing using the optical properties of porous silicon Bragg mirrors. *J Appl Phys* 86:1781–1785
57. Stewart MP, Buriak JM (2000) Chemical and biological applications of porous silicon technology. *Adv Mat* 12:859–869
58. Sun W, Puzas JE, Sheu T-J, Fauchet PM (2007) Porous silicon as a cell interface for bone tissue engineering. *Phys Stat Sol A* 204:1429–1433
59. Tinsley-Bown A, Smith RG, Hayward S, Anderson MH, Koker L, Green A, Torrens R, Wilkinson A-S, Perkins EA, Squirrell DJ, Nicklin S, Hutchinson A, Simons AJ, Cox TI (2005) Immunoassays in a porous silicon interferometric biosensor combined with sensitive signal processing. *Phys Stat Sol A* 202:1347–1356
60. Turner TR (1958) Electropolishing silicon in hydrofluoric acid solutions. *J Electrochem Soc* 105:402–408
61. Uhlir A (1956) Electrolytic shaping of germanium and silicon. *Bell Syst Tech J* 35:333
62. Yablonovitch E (1987) Inhibited spontaneous emission in solid-state physics and electronics. *Phys Rev Lett* 58:2059
63. Young LS, Martin WJ, Meyer RD, Weinstein RJ, Anderson ET (1977) Gram-negative rod bacteremia: microbiologic, immunologic, and therapeutic considerations. *Ann Intern Med* 86:456–471

Resonant Waveguide Grating Biosensor for Microarrays

Ye Fang

Abstract A microarray consists of an indexed series of micron-sized spots of biological specimens for biomolecular interaction analysis. Microarray technologies present miniaturized and multiplexed approaches for sensitive and selective profiling of genes, proteins, and/or small molecules. Concurrent with the increasing applications of microarrays is the continuous efforts in developing novel detection systems for improving sensitivity and reliability in signal detection. This chapter describes the concept and applications of microarray technologies, and the principle of detection with an emphasis of resonant waveguide grating biosensor for microarray-based assays.

Keywords Microarray · DNA microarray · Carbohydrate microarray · Protein microarray · Antibody microarray · G protein-coupled receptor microarray · Cellular microarray · Optical biosensor · Resonant waveguide grating biosensor · Surface plasmon resonance · Dynamic mass redistribution

Contents

1	Introduction	28
2	Microarray Technologies	29
2.1	DNA Microarrays	30
2.2	Carbohydrate Microarrays	30
2.3	Protein Microarrays	31
2.4	Antibody Microarrays	31
2.5	Membrane Protein Microarrays	31
2.6	Cellular Microarrays	32
2.7	Microarray Fabrication	32
2.8	Microarray Assays and Detection	32

Y. Fang

Biochemical Technologies, Science and Technology Division, Corning Incorporated, Sullivan Park, Corning, NY 14831, USA
e-mail: fangy2@corning.com

3	Resonant Waveguide Grating Biosensor for Microarrays	33
3.1	RWG Biosensor	34
3.2	RWG Imager	34
3.3	Label-Dependent Detection	35
3.4	Label-Independent Detection	37
4	Concluding Remarks	39
	References	39

Abbreviations

DMR	Dynamic mass redistribution
DNA	Deoxyribonucleic acid
GPCR	G protein-coupled receptor
mRNA	Messenger RNA
RNA	Ribonucleic acid
RWG	Resonant waveguide grating
SPR	Surface plasmon resonance

1 Introduction

Microarrays are powerful analytical tools that enable simultaneous analysis of many biomolecular interactions in a single experiment. Microarrays typically consist of an indexed series of microscopic spots of biological probe elements. Compared to conventional assays using single targets, microarray-based assays are advantageous. Thousands of probe elements in a single array enable highly parallel and efficient analysis of many biomolecular interactions at once. The small footprints of microarrays allow the use of low sample volumes, which lead to the consumption of smaller amounts of both precious samples (e.g., clinical samples) and expensive molecules (e.g., antibodies or proteins). By using internal standard controls, microarray-based assays can be reproducible and sensitive, and enable quantitative measurements of analytes (e.g., small molecules, proteins, biomarkers, etc.) with high accuracy over a large concentration range. Furthermore, advances in detection methods have been and will continue accelerating the wide adoption of microarrays in many different fields of research and development. Optical biosensors enable both label-dependent and independent detections, and hold great promise in microarray applications, in particular, where real-time kinetic analysis of biomolecular interactions is important.

2 Microarray Technologies

There are two types of microarray platforms – standard and “liquid” microarrays. The standard microarrays are those on which assays are carried out on a shared substrate containing a spatially resolved and indexed series of biological elements. Conversely, the liquid microarrays utilize many particles or beads to carry out multiplexed assays, wherein each particle contains a biological element and is identified with a unique characteristic (e.g., code) [55].

A standard microarray possesses three distinct characteristics: (a) an indexed series of microscopic spots of probe elements, (b) a shared, typically two-dimensional, substrate, and (c) specific binding between the probe elements in the array and target molecules in a sample solution (Fig. 1). The probe biomolecules are often covalently immobilized onto the substrate, and remain in location throughout the assay. The assay identification is made by coordinate location. The amount of binding is proportional to the concentration of the target molecule and affinity of the probe–target interaction. Microarrays can be classified into many categories, depending on the classes of probe elements in the array. Figure 2 illustrates several classes of probe microarrays.

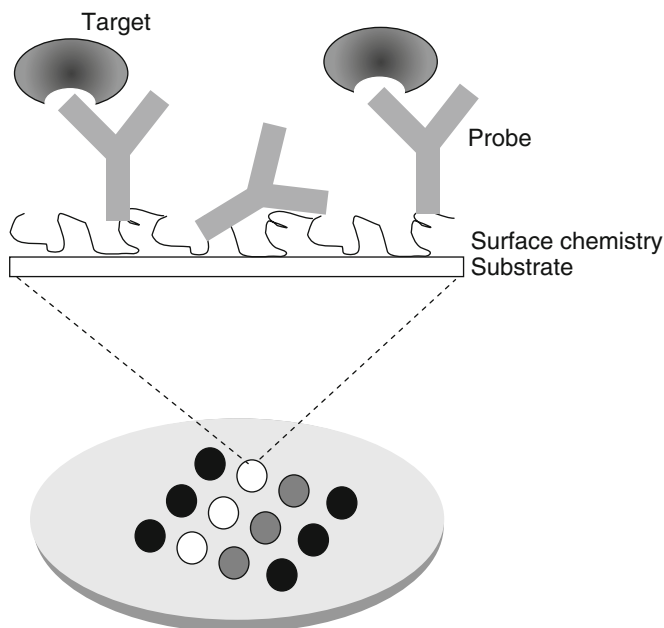


Fig. 1 A microarray of 3×4 probe elements. The probe elements are immobilized on to the surface of a shared substrate, and are used to “fish” out their corresponding interacting target molecules in a sample

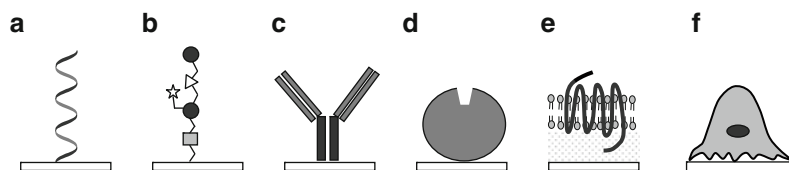


Fig. 2 Common types of microarrays: DNA microarray (a), carbohydrate microarray (b), antibody microarray (c), functional protein microarray (d), biomembrane and membrane protein microarray (e), and cellular microarray (f)

2.1 DNA Microarrays

DNA (deoxyribonucleic acid) contains the genetic instructions used in the development and functioning of all known living organisms and some viruses. RNA (ribonucleic acid) is transcribed from DNA by RNA polymerases and is generally further processed by other enzymes. RNA is central to the translation process from DNA to proteins. Advances in molecular biology in the past several decades have rendered the synthesis, isolation, labeling, amplification, and storage of nucleic acid a routine task. Thus, DNA microarrays were among the first ones to be developed [42, 49], and are now fairly well-established as analytical tools in basic research, drug discovery, and diagnostics [48]. In a gene expression profiling experiment, the microarrays are used to detect mRNAs (most commonly as complementary DNA after reverse transcription) [50], while in a comparative genomic hybridization, the microarrays are used to detect DNA [44]. DNA microarrays allow comparisons of gene expression at the genomic scale in all kinds of combinations of samples derived from normal and diseased tissues, treated and nontreated cells or tissues, different time courses of treated cells, and different stages of differentiation or development. The gene expression profiles are useful for understanding the molecular basis of phenotype, pathology, or treatment.

2.2 Carbohydrate Microarrays

Carbohydrates are often presented in the form of glycoproteins, glycolipids, glycosaminoglycans, or other glycoconjugates [35]. Carbohydrates are known to play important roles in numerous biological processes, including viral and bacterial infection, immune response, differentiation and development, and the progression of tumor cell metastasis. Carbohydrates are diverse in structure, as the current list of known *N*-linked and *O*-linked glycans found in mammalian proteins contains more than 2,000 structures [43]. Carbohydrate arrays [24] are commonly used for profiling glycan binding proteins (e.g., lectins, growth factors, cytokines, antibodies, and microbial toxins) and screening drug molecules modulating the glycan–protein interactions [3].

2.3 Protein Microarrays

Proteins, not mRNAs, are the true functional components of cells. Unlike DNA microarrays, on which interactions are based on Watson–Crick base pairing, biomolecular interactions on protein microarrays are determined by complex associations between the probe proteins and the target molecules. Individual protein–ligand pairs could differ greatly in their affinities. Furthermore, unlike DNA whose structure is relatively simple, proteins are extremely diverse in structure and functions, and often display many variables, such as posttranslational modifications. Protein microarrays are useful for determining numerous protein interactions including protein–protein [59], protein–DNA [26], and protein–small molecule interactions [30], or identifying the substrates of protein kinases [58].

2.4 Antibody Microarrays

The most common analytical microarray is the antibody microarray. Antibodies are immunoglobulin proteins found in blood or other bodily fluids of vertebrates, and are used by the immune system to identify and neutralize foreign objects, such as bacteria and viruses. Since changes in gene expression do not always correlate with protein abundance, antibody microarrays can offer complementary but crucial information about protein abundance independently of gene expression [2]. Antibody microarrays are commonly used to profile a complex mixture of proteins. However, unlike DNA microarrays wherein a single array can cover the entire genome, an antibody array made today can only contain a small portion of the proteome. Beside protein profiling, antibody microarrays are also useful for identifying biomarkers [38], characterizing the coordinated changes of members of signaling pathways [31, 32, 40], and measuring changes in modification or expression level of cancer related proteins [51].

2.5 Membrane Protein Microarrays

Molecules associated with the cell membrane – lipids, proteins, and small molecules – are not only the recognition sites for exogenous signals, but are also often directly involved in downstream signal transduction through dynamic interactions with intracellular proteins. Membrane proteins make up around one-third of the proteome of a cell [29]. Molecules in the cell membrane, including GPCRs (G protein-coupled receptors), ion channels, and receptor tyrosine kinases, are key targets for therapeutic intervention [8]. The functions of membrane proteins often require their direct association with lipid molecules, and depend on the biophysical characteristics (e.g., long-range fluidity) and structural integrity of the lipid membrane. Thus, unlike any other microarrays in which only probe molecules are

arrayed, membrane protein microarrays require the coimmobilization of membrane proteins and their associated membranes. Air-stable biomembrane microarrays, including GPCR microarrays [15] and glycolipid microarrays [16, 17], are useful for selectivity profiling of drug candidate molecules against multiple receptors [20, 21], and for identifying glycolipid binding proteins and pathogens [16, 17].

2.6 Cellular Microarrays

Array of cells at different states or cellular backgrounds enables molecularly delineating the characteristics of individual cells from complex cell systems. Living cells can be arrayed via two fundamentally different approaches. First, biological chips that contain spots of various materials (e.g., antibodies, proteins, or lipids) capable of interacting with specific cells are used to capture living cells on to specific spots to form a cellular microarray [5]. Besides their ability to capture cells, the materials in each spot can also be used to trigger a cellular response, leading to alteration in phenotype, or to enable on-site detection of a response from the cell, such as a specific secreted factor. Second, microarrays of genes (e.g., DNA vectors, or interference RNA) precomplexed with transfection reagents are used to alter the genetic backgrounds of a cell system overlaid the substrate surface, resulting in the formation of transfected cellular microarrays [60]. These microarrays are useful for studying signal transduction pathways and screening drug molecules [39], and for large-scale functional characterization of gene products in cellular environments [54].

2.7 Microarray Fabrication

Two fundamentally different ways can be used to fabricate biomicroarrays. The standard approach is to use a high-speed spotting robot to deposit biological materials onto a chemically modified substrate, leading to a deposited and spatially resolved microarray after affixation via covalent coupling or physical immobilization (e.g., electrostatic interactions) [28, 42]. The spotting robot can be contact pin printing devices [37] or noncontact inkjet printing devices or dispenser [7]. Alternatively, in situ synthesis of biological elements can also be used. Such approach is feasible for generating microarrays of oligonucleotides, peptides, or even functional proteins using cell-free synthesis of proteins [27].

2.8 Microarray Assays and Detection

Bioassays for microarrays exploit a similar protocol: labeled or unlabeled target molecules in a solution sample are brought to interact with the immobilized probe molecules (Fig. 3). Target molecules are commonly labeled with fluorescent tags.

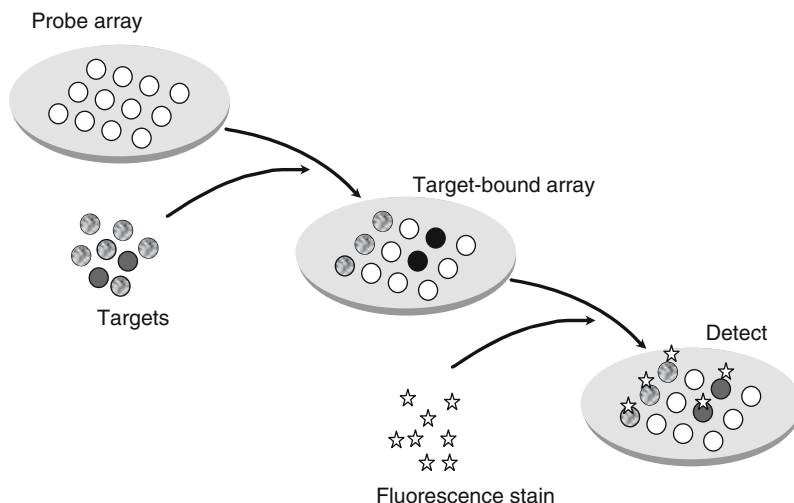


Fig. 3 Typical microarray-based assay. A microarray is incubated with a solution containing multiple target molecules. After removal of unbound molecules, the target-bound microarray is stained with fluorescence, followed by imaging and quantification

However, affinity, photochemical, or radioisotope tags can also be used. After removal of unbound molecules in solution, the microarrays are subject to detection to determine the binding of target molecules, or the target molecule-induced alteration of live cells in the microarrays. These interactions are usually detected and quantified by the fluorescence of fluorophore-labeled target molecules. Fluorescent detection is sensitive, can have high resolution, and is compatible with many fluorescence-based microarray scanners.

For comparative studies, two-color binding assays are often used, wherein two different sets of fluorescent-labeled target molecules from two separate populations are made, and interacted with a microarray. The relative level in a specific target (e.g., a protein, or mRNA transcripts for each gene) is measured by the fluorescent ratio [50].

3 Resonant Waveguide Grating Biosensor for Microarrays

Fluorescent or other labels can, in some cases, interfere with the molecular interactions or cell biology of target receptors, thus resulting in false information [6]. Labels, particularly for small molecules, can be difficult to be optimized, thus introducing additional complexity and assay development time to the process. Label-free detection methods not only overcome the problem of steric hindrance of a label, but also enable kinetic measures of biomolecular interactions [46].

Optical biosensors including SPR and RWG are the most popular label-free techniques for detecting biomolecular interactions [12].

3.1 RWG Biosensor

A RWG biosensor utilizes the resonant coupling of light into a waveguide by means of a diffraction grating. A polarized light, covering a range of incident wavelengths, is used to illuminate the waveguide; light at specific wavelengths is coupled into and propagate along the waveguide (Fig. 4). The resonant wavelength at which a maximum incoupling efficiency is achieved is a function of the local index of refraction at or near the sensor surface [52]. The binding of target molecules in a sample to the immobilized receptors increases the local index of refraction, leading to a shift in the resonant wavelength.

Unlike SPR, which employs a relatively large incident angle, RWG biosensors with appropriate designs allow lights at nominally normal incident angle for illumination. This, in turn, enables a RWG optical system for simultaneous signal detection from a biosensor having a large footprint, or a large array of biosensors, such as in a standard 384-well or 1,536-well microtiter plates [34].

3.2 RWG Imager

In a conventional RWG biosensor, the binding signals typically represent the averaged response of the binding at a defined area, as predetermined by the size of illumination light (e.g., 100 μm) as well as the distance of the propagation length

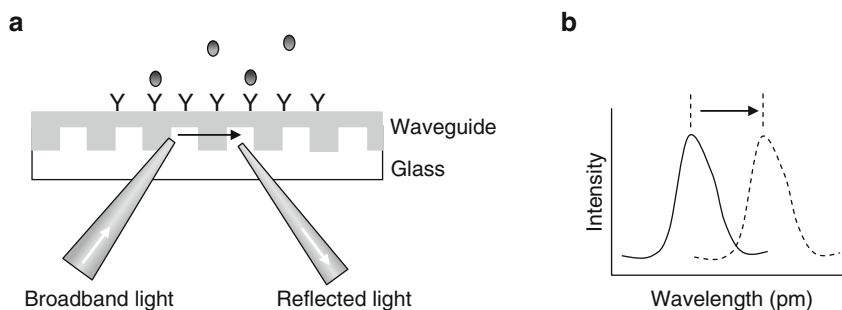


Fig. 4 The principle of RWG biosensor. (a) A typical configuration of a RWG for biochemical assays. The incident light coupled into the waveguide is achieved by the diffraction grating. The receptor (Y) is covalently coupled to the derivatized surface of a biosensor. (b) The intensity of reflected light as a function of wavelength. The shift in the resonant wavelength is a function of the binding of the target molecules to the immobilized receptors

of the coupled light traveling within the waveguide. The propagation length is typically in the range of several micrometers to hundreds of micrometers, depending on the sensor design and detection system.

To meet the needs for microarray-based assays, several optical imaging systems have been developed. SPR imager typically uses prism-coupled [57] or grating-coupled [56] SPR at a fixed angle of incidence, and records the reflectance from different locations on the sensor surface. Similarly, RWG imager can be achieved by scanning the whole biosensor using a broadband light source at a fixed angle. The binding is detected by measuring changes in the wavelength of light reflected from a subwavelength grating structure [33, 36]. In a recently developed angular RWG imaging system [18, 19], a light launch system is used to generate an array of light beams at a specific wavelength such that each illuminates a RWG sensor with an adjustable dimension (e.g., $\sim 200 \times 3,000 \mu\text{m}^2$), while a CCD camera-based receive system is used to record the resonant image of a biosensor array. The arrayed light beams are obtained through a beam splitter and diffractive optical lenses. This system allows up to 49 sensors in a microplate (in a 7×7 -well sensor array) to be simultaneously sampled every 3 s. Each sensor gives rise to a resonant band, which can be divided into multiple segments for data collection and analysis (Fig. 5). This system can be reconfigured for microarray-based applications.

3.3 *Label-Dependent Detection*

RWG biosensors enable sensitive detection of surface-bound fluorescence molecules without the need of removal of unbound fluorescent molecules in solution. This is achieved by evanescent wave-excited fluorescence, similar to total internal reflection fluorescence. Unlike epi-fluorescence, the evanescent wave whose strength decays exponentially with distance from the surface only excites the labels within the penetration depth of the field, thereby eliminating the interference of the bulk signal [10, 25]. This leads to a significant reduction of the background noise resulting from excitation of unbound molecules from the bulk, enabling simplified detection procedure in which washing steps are no longer necessary.

The evanescent wave enhanced fluorescence obtained with RWG biosensors is clearly advantageous compared to SPR. In classical SPR, the plasmonic enhancement is highly dependent on the distance of the fluorophore to the metal surface, because the metal surface can cause the quenching of fluorophores, which typically occurs within short distances (<several nanometers). In a RWG biosensor, the planar waveguide is made of a high index material, such as Nb_2O_5 , Ta_2O_5 , TiO_2 , or SiN_x , neither of which causes the quenching of fluorophores. In a commercially available Zeptosens device, the biosensor consists of a separate grating coupling section and a planar-waveguide detection region (Fig. 6). This design is optimized for evanescent wave-based fluorescence excitation. The fluorescence is excited by guided planar-waveguide mode, rather than the leaky waveguide mode. The waveguide grating coupler leaks a small amount of light, resulting in bulk fluorescence

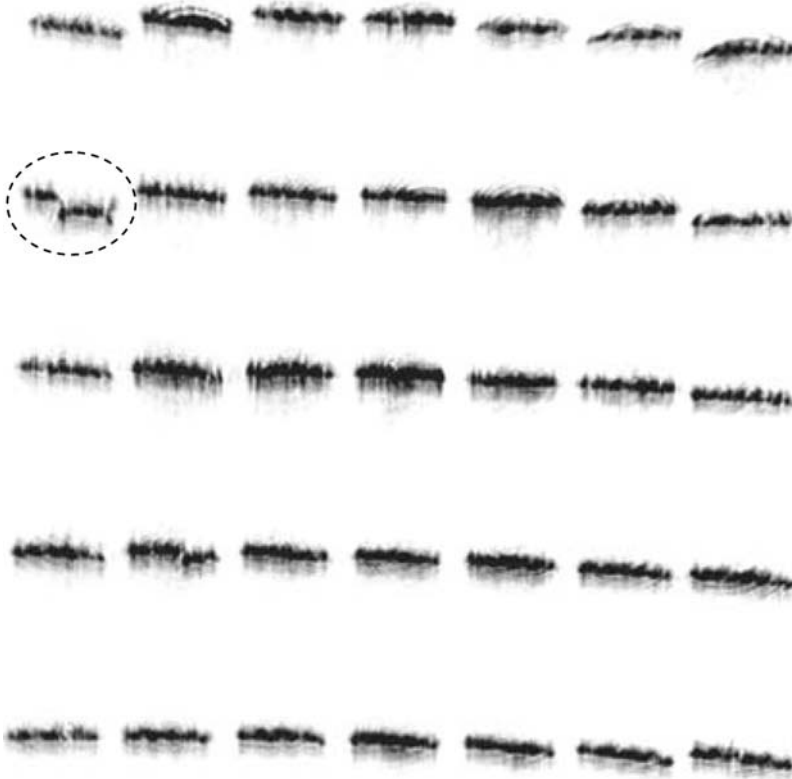


Fig. 5 An actual resonant band image of 5 rows of 7 sensors in a 96-well sensor microplate containing living cells obtained using the arrayed angular interrogation system. The *broken circle* indicated that the cell density was not even across this specific sensor, which was confirmed by light microscope imaging (Reproduced with permission from ref. [18])

excitation. Thus, by using this design, the bulk fluorescence is minimized in the planar-waveguide section. A drawback of this system is that its waveguide section cannot be used for label-free measurements.

The evanescent wave enhanced fluorescence using RWG biosensors has been realized for sensitive hybridization studies using DNA microarrays [4, 9], and for multiplexed and quantitative detection of low-abundant proteins using protein microarrays [41]. In a recent DNA microarray study [23], the RWG evanescent wave fluorescence detection was used for identifying bacteria frequently responsible for septicemia. Compared to regular DNA hybridization assays, which typically require overnight reaction, the DNA hybridization was completed in a short time (<6 h). Furthermore, because of its high sensitivity, this approach led to a limit of detection down to 0.02 molecules per μm^2 (~500 molecules per spot). Rapid and accurate detection, particularly using small amounts of samples

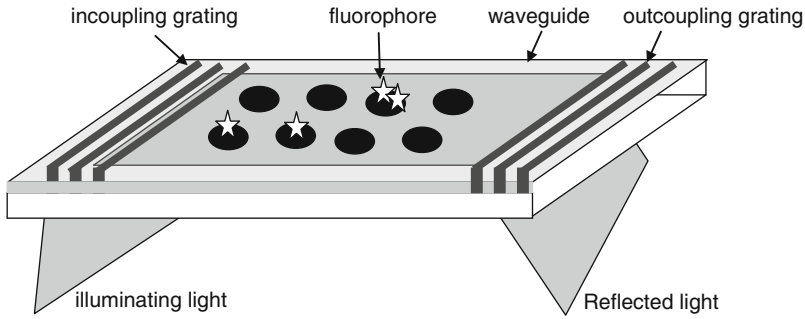


Fig. 6 Evanescent wave excited fluorescence imaging system using resonant waveguide grating biosensor. The waveguide thin film of Ta_2O_5 is deposited on glass. Two separate gratings are used for coupling light in and out of the waveguide, respectively. The coupled light propagates the waveguide detection region between the grating structures. Surface-bound fluorophores are excited by the evanescent wave resulting from the total internal reflection of the laser beam. Fluorescence is detected by a CCD camera placed below the waveguide

(e.g., microdissections, needle biopsies), are prerequisites for clinical diagnosis of these bacteria associated diseases.

3.4 Label-Independent Detection

The evanescent wave can be exploited for both surface-bound fluorescence excitation and index of refraction sensing. Minute changes of refractive index in the waveguide surface are translated into shifts in the resonant condition of the grating coupler. Current label-free microarray biosensing is dominated by imaging SPR and to a certain extent by imaging ellipsometry. Although less sensitive than fluorescence measurements, label-free detection does offer valuable means for biomolecular interaction analysis [1].

For imaging SPR, a CCD camera is used as the detector to monitor simultaneously the reflectivity change of the whole sensing area in a single experiment. The achievable array density is limited by the lateral resolution of imaging SPR, which is a function of decay length of the surface plasmons (typically micrometers) [47].

Large-scale RWG imagers for high-density biosensor microtiter plates (e.g., 384-well or 1,536-well) have been used to study both biomolecular interactions and ligand-induced DMR in living cells [20, 21]. The ability to examine living cells is increasingly important for both basic and applied biological researches. Although more complex and less specific than biomolecular interaction analysis, cell-based assays show superior ability to facilitate the measurements of mode of action, pathway activation, toxicity, and phenotypic responses of cells induced by drug compounds. RWG biosensors have been shown to be very effective for probing cell signaling in both high throughput and high information content fashions [12].

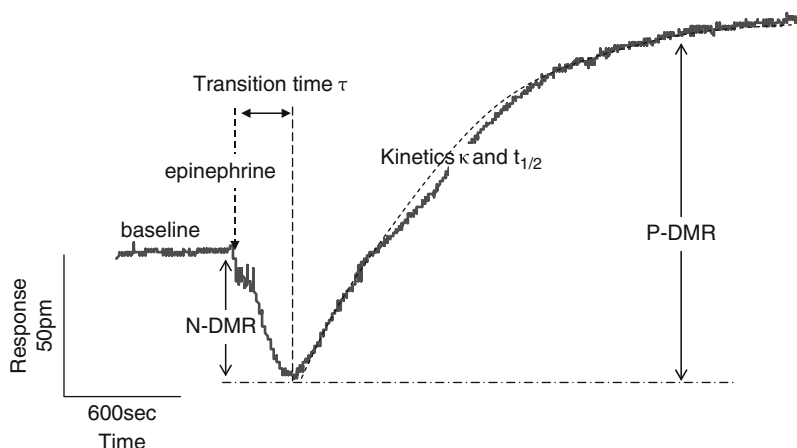


Fig. 7 RWG biosensor for monitoring ligand-induced dynamic mass redistribution signals in living cells. Epinephrine is a natural agonist for endogenous β_2 -adrenoceptors in human skin cancer cell line A431. 2 nM epinephrine was added into a well, the bottom of which contains a RWG biosensor covered by a highly confluent monolayer of A431 cells. Following a steady baseline, the cells responded to the epinephrine stimulation with an initial decrease in signal (*Negative-DMR* N-DMR) then a slow increase in signal (*Positive-DMR* P-DMR). The *discontinuous curved line* indicated the fitting of the P-DMR event with a nonlinear exponential regression to determine its kinetic parameters (Reproduced with permission from ref. [14])

High throughput and cell-based assays are the two most unmet needs of label-free biosensors. Figure 7 shows the optical signals of an endogenous G_s -coupled receptor β_2 -adrenoceptor in living cells. Optical biosensors can track in real time a ligand-induced DMR signal in native cells or cell systems, without the need of any labels or manipulations of cells [11]. The DMR signal represents an integrated and physiologically relevant cellular response, and is an approximately global representation of cell signaling and physiology of a compound acting on cells [13, 18, 19, 22]. The DMR signal is a real-time kinetic response of cells, and offers multiparameters for analysis of receptor signaling and ligand pharmacology (e.g., overall dynamics, phases, amplitude and kinetics of each phases, and the transition time from one phase to another, etc) [14].

High-resolution RWG imaging systems are also feasible. Spots or microspots of biological molecules on the biosensor surfaces were shown to be readily distinguished, using a photonic crystal biosensor – a variant RWG biosensor [36]. The optical grating acts as a wavelength filter for the reflected light such that upon molecular binding, the optical conditions change and the resonant light shifts towards higher wavelengths. After binding of a complex sample to an array, the spectra of the captured samples are laterally recorded and analyzed via a CCD camera.

An advantage of label-free biosensors for microarray assays is their ability to obtain kinetic information with a time resolution of seconds [45]. A recent demonstration of simultaneously monitoring 400 antibody–target binding reactions in

real-time revealed the great potential of label-free biosensors, including RWG biosensors for microarray-based detection [53].

4 Concluding Remarks

Large-scale analysis of biomolecular interactions becomes increasingly important in many areas of basic and applied biological research. Microarray technologies are excellent high-throughput methods and hold great potentials for human genomic and proteomic studies, and clinical diagnosis. New detection methodologies tailored to specific applications have been and will continue to play important roles in the development of microarrays. The outstanding issue of labeling complex proteomes can be resolved by adopting label-free biosensing methods. An ideal label-free microarray sensing technology is that it should not only be able to detect diverse types of molecules including small molecules, but also should enable the detection of low-abundant biomolecules and have a wide dynamic range. High sampling rate is also important for kinetic measurements. Although promising, current optical biosensor systems, such as imaging SPR and RWG, are still in infancy for microarray detection. New developments in instrumentation, biosensor fabrication, and assay methods will narrow the existing gap of optical biosensing systems for microarray applications, particularly for label-free assays using cellular microarrays.

References

1. Bally M, Halter M, Vörös J, Grandin HM (2006) Optical microarray biosensing techniques. *Surf Interface Anal* 38:1442–1458
2. Bertone P, Snyder M (2005) Advances in functional protein microarray technology. *FEBS J* 272:5400–5411
3. Bochner BS, Alvarez RA, Mehta P, Bovin NV, Blixt O, White JR, Schnaar RL (2005) Glycan array screening reveals a candidate ligand for Siglect-8. *J Biol Chem* 280:4307–4312
4. Budach W, Abel AP, Bruno AE, Neuschafer D (1999) Planar waveguides as high performance sensing platforms for fluorescence-based multiplexed oligonucleotide hybridization assays. *Anal Chem* 71:3347–3355
5. Chen DS, Davis MM (2006) Molecular and functional analysis using live cell microarrays. *Curr Opin Chem Biol* 10:28–34
6. Cooper MA (2006) Optical biosensors: where next and how soon. *Drug Discov Today* 11:1061–1067
7. Delehanty JB (2004) Printing functional protein microarrays using piezoelectric capillaries. *Methods Mol Biol* 264:135–143
8. Drews J (2000) Drug discovery: a historical perspective. *Science* 287:1960–1963
9. Duveneck GL, Pawlak M, Neuschafer D, Bar E, Budach W, Pieleus U, Ehrat M (1997) Novel bioaffinity sensors for trace analysis based on luminescence excitation by planar waveguides. *Sensors Actuators B Chem* 38:88–95

10. Duveneck GL, Bopp MA, Ehrat M, Balet LP, Haiml M, Keller U, Marowsky G, Soria S (2003) Two-photon fluorescence excitation of macroscopic areas on planar waveguides. *Biosens Bioelectron* 18:503–510
11. Fang Y (2006) Label-free cell-based assays with optical biosensors in drug discovery. *Assay Drug Dev Technol* 4:583–595
12. Fang Y (2007) Non-invasive optical biosensor for probing cell signaling. *Sensors* 7: 2316–2329
13. Fang Y, Ferrie AM (2007) Optical biosensor differentiates signaling of endogenous PAR₁ and PAR₂ in A431 cells. *BMC Cell Biol* 8:e24
14. Fang Y, Ferrie AM (2008) Label-free optical biosensor for ligand-directed functional selectivity acting on β_2 adrenoceptor in living cells. *FEBS Lett* 582:558–564
15. Fang Y, Frutos AG, Lahiri J (2002) Membrane protein microarrays. *J Am Chem Soc* 124:2394–2395
16. Fang Y, Frutos AG, Lahiri J (2003) Ganglioside microarrays for toxin detection. *Langmuir* 19:1500–1505
17. Fang Y, Lahiri J, Picard L (2003) G protein-coupled receptor microarrays for drug discovery. *Drug Discov Today* 8:755–761
18. Fang Y, Ferrie AM, Fontaine NH, Yuen PK (2005) Characteristics of dynamic mass redistribution of EGF receptor signaling in living cells measured with label free optical biosensors. *Anal Chem* 77:5720–5725
19. Fang Y, Li G, Peng J (2005) Optical biosensor provides insights for bradykinin B2 receptor signaling in A431 cells. *FEBS Lett* 579:6365–6374
20. Fang Y, Ferrie AM, Fontaine NH, Mauro J, Balakrishnan J (2006) Resonant waveguide grating biosensor for living cell sensing. *Biophys J* 91:1925–1940
21. Fang Y, Peng J, Ferrie AM, Burkhalter RS (2006) Air-stable G protein-coupled receptor microarrays and ligand binding characteristics. *Anal Chem* 78:149–155
22. Fang Y, Li G, Ferrie AM (2007) Non-invasive optical biosensor for assaying endogenous G protein-coupled receptors in adherent cells. *J Pharmacol Toxicol Methods* 55:314–322
23. Francois P, Charbonnier Y, Jacquet J, Utinger D, Bento M, Lew D, Kresbach GM, Ehrat M, Schlegel W, Schrenzel J (2006) Rapid bacterial identification using evanescent-waveguide oligonucleotide microarray classification. *J Microbiol Methods* 65:390–403
24. Fukui S, Feizi T, Galustian C, Lawson AM, Chai W (2002) Oligosaccharide microarrays for high-throughput detection and specificity assignments of carbohydrate-protein interactions. *Nat Biotechnol* 20:1011–1017
25. Grandin HM, Stadler B, Textor M, Voros J (2006) Waveguide excitation fluorescence microscopy: a new tool for sensing and imaging the biointerface. *Biosens Bioelectron* 21:1476–1482
26. Hall DA, Zhu H, Zhu X, Royce T, Gerstein M, Snyder M (2004) Regulation of gene expression by a metabolic enzyme. *Science* 306:482–484
27. He M, Wang MW (2007) Arraying proteins by cell-free synthesis. *Biomol Eng* 24:375–380
28. Hook AL, Thissen H, Voelcker NH (2006) Surface manipulation of biomolecules for cell microarray applications. *Trends Biotechnol* 24:471–477
29. Hopkins AL, Groom CR (2002) The druggable genome. *Nat Rev Drug Discov* 1:727–730
30. Huang J, Zhu H, Haggarty SJ, Spring DR, Hwang H, Jin F, Snyder M, Schreiber SL (2004) Finding new components of the target of rapamycin (TOR) signaling network through chemical genetics and proteome chips. *Proc Natl Acad Sci USA* 101:16594–16599
31. Ivanov SS, Chung AS, Yuan ZL, Guan YJ, Sachs KV, Reichner JS, Chin YE (2004) Antibodies immobilized as arrays to profile protein post-translational modifications in mammalian cells. *Mol Cell Proteomics* 3:788–795
32. Jones RB, Gordus A, Krall JA, MacBeath G (2006) A quantitative protein interaction network for the ErbB receptors using protein microarrays. *Nature* 439:168–174
33. Li PY, Lin B, Gerstenmaier J, Cunningham B (2004) A new method for label-free imaging of biomolecular interactions. *Sensors Actuators B Chem* 99:6–13

34. Li G, Ferrie AM, Fang Y (2006) Label-free profiling of endogenous G protein-coupled receptors using a cell-based high throughput screening technology. *J Assoc Lab Autom* 11:181–187
35. Liang PH, Wu CY, Greenberg WA, Wong CH (2008) Glycan arrays: biological and medical applications. *Curr Opin Chem Biol* 12:1–7
36. Lin B, Gerstenmeier J, Li P, Pien H, Pepper J, Cunningham BA (2002) Label-free optical technique for detecting small molecule interactions. *Biosens Bioelectron* 17:827–834
37. MacBeath G, Schreiber SL (2000) Printing proteins as microarrays for high throughput function determination. *Science* 289:1760–1763
38. Miller JC, Zhou H, Kwekel J, Cavallo R, Burke J, Butler EB, Teh BS, Haab BB (2003) Antibody microarray profiling of human prostate cancer sera: antibody screening and identification of potential biomarkers. *Proteomics* 3:56–63
39. Mishina YM, Wilson CJ, Bruett L, Smith JJ, Stoop-Myer C, Jong S, Amaral LP, Pedersen R, Lyman SK, Myer VE, Kreider BL, Thompson CM (2004) Multiplex GPCR assay in reverse transfection cell microarrays. *J Biomol Screen* 9:196–207
40. Nielsen UB, Cardone MH, Sinskey AJ, MacBeath G, Sorger PK (2003) Profiling receptor tyrosine kinase activation by using Ab microarrays. *Proc Natl Acad Sci USA* 100:9330–9335
41. Pawlak M, Schick E, Bopp MA, Schneider MJ, Oroszlan P, Ehrat M (2002) Zeptosens' protein microarrays: a novel high performance microarray platform for low abundance protein analysis. *Proteomics* 2:383–393
42. Pease AC, Solas D, Sullivan EJ, Cronin MT, Holmes CP, Fodor SP (1994) Light-generated oligonucleotide arrays for rapid DNA sequence analysis. *Proc Natl Acad Sci USA* 91:5022–5026
43. Pilobello KT, Mahal L (2007) Deciphering the glycode: the complexity and analytical challenge of glycomics. *Curr Opin Chem Biol* 11:300–305
44. Pollack JR, Perou CM, Alizadeh AA, Eisen MB, Pergamenschikov A, Williams CF, Jeffrey SS, Botstein D, Brown PO (1999) Genome-wide analysis of DNA copy-number changes using cDNA microarrays. *Nat Genet* 23:41–46
45. Ramachandran N, Larson DN, Stark PRH, Hainsworth E, LaBear J (2005) Emerging tools for real-time label-free detection of interactions on functional protein microarrays. *FASEB J* 27:5412–5425
46. Rich RL, Myszka DG (2007) Higher-throughput, label-free, real-time molecular interaction analysis. *Anal Biochem* 361:1–6
47. Rothenhausler B, Knoll W (1988) Surface-plasmon microscopy. *Nature* 332:615–617
48. Sassolas A, Leca-Bouvier BD, Blum J (2008) DNA biosensors and microarrays. *Chem Rev* 108:109–139
49. Schena M, Shalon D, Davis RW, Brown PO (1995) Quantitative monitoring of gene expression patterns with a complementary DNA microarray. *Science* 270:467–470
50. Shalon D, Smith SJ, Brown PO (1996) A DNA microarray system for analyzing complex DNA samples using two-color fluorescent probe hybridization. *Genome Res* 6:639–645
51. Sreekumar A, Nyati MK, Varambally S, Barrette TR, Ghosh D, Lawrence TS, Chinnaiyan AM (2001) Profiling of cancer cells using protein microarrays: discovery of novel radiation-regulated proteins. *Cancer Res* 61:7585–7593
52. Tiefenthaler K, Lukosz W (1989) Sensitivity of grating couplers as integrated-optical chemical sensors. *J Opt Soc Am B* 6:209–220
53. Usui-Aoki K, Shimada K, Nagano M, Kawai M, Koga H (2005) A novel approach to protein expression profiling using antibody microarrays combined with surface plasmon resonance technology. *Proteomics* 5:2396–2401
54. Wheeler DB, Carpenter AE, Sabatini DM (2005) Cell microarrays and RNA interference chip away at gene function. *Nat Genet* 37:S25–S30
55. Wilson R, Cossins AR, Spiller DG (2006) Encoded microcarriers for high-throughput multiplexed detection. *Angew Chem Int Ed* 45:6104–6117

56. Yeatman EM (1996) Resolution and sensitivity in surface plasmon microscopy and sensing. *Biosens Bioelectron* 11:635–649
57. Yuk JS, Jung SH, Jung JW, Hong DG, Han JA, Kim YM, Ha KS (2004) Analysis of protein interactions on protein arrays by a wavelength interrogation-based surface plasmon resonance biosensor. *Proteomics* 4:3468–3476
58. Zhu H, Klemic JF, Chang S, Bertone P, Casamayor A, Klemic KG, Smith D, Gerstein M, Reed MA, Snyder M (2000) Analysis of yeast protein kinases using protein chips. *Nat Genet* 26:283–289
59. Zhu H, Bilgin M, Bangham R, Hall D, Casamayor A, Bertone P, Lan N, Jansen R, Bidlingmaier S, Houfek T, Mitchell T, Miller P, Dean RA, Gerstein M, Snyder M (2001) Global analysis of protein activities using proteome chips. *Science* 293:2101–2105
60. Ziauddin J, Sabatini DM (2001) Microarrays of cells expressing defined cDNA. *Nature* 411:107–110

Resonant Biochemical Sensors Based on Photonic Bandgap Waveguides and Fibers

Maksim Skorobogatiy

Abstract I describe photonic bandgap (PBG) fiber-based resonant optical sensors of analyte's refractive index which have recently invoked strong interest due to the development of novel fiber types and of techniques for the activation of fiber microstructure with functional materials. Particularly, I consider two sensors types. One employs hollow-core photonic bandgap fibers where the core-guided mode is confined in the analyte's filled core through resonant effect in the surrounding periodic reflector. The other employs metallized photonic bandgap waveguides and fibers, where core-guided mode is phase-matched with a plasmon wave propagating at the fiber/analyte interface. In resonant sensors, one typically employs fibers with strongly nonuniform spectral transmission characteristics that are sensitive to changes in the real part of the analyte's refractive index. Moreover, if narrow absorption lines are present in the analyte transmission spectrum, due to Kramers–Kronig relation, this will also result in strong variation in the real part of the refractive index in the vicinity of an absorption line. Therefore, resonant sensors allow detection of minute changes both in the real part of the analyte's refractive index ($10^{-6} - 10^{-4}$ RIU) and in the imaginary part of the analyte's refractive index in the vicinity of absorption lines. Although the operational principle of almost all PBG fiber-based sensors relies on strong sensitivity of the PBG fiber losses to the value of the analyte's refractive index, particular transduction mechanisms for biodetection vary significantly. Finally, I detail various sensor implementations, modes of operation, as well as analysis of sensitivities for some of the common transduction mechanisms for biosensing applications.

Keywords Photonic bandgap fibers · Bragg fibers · Resonant optical sensors · Optical fiber sensors · Plasmonics · Plasmonic sensors

M. Skorobogatiy

Department of Engineering Physics, Ecole Polytechnique de Montréal, C.P. 6079, succ. Centre-ville, Montréal (Québec), Canada H3C 3A7

e-mail: yuji@ecei.tohoku.ac.jp

Contents

1	Introduction	45
2	Detection Strategies for Absorption-Based Sensors	47
3	Sensing Using Hollow-Core Photonic Bandgap Fibers	49
3.1	Nonresonant Sensing	50
3.2	Resonant Sensing	52
3.3	Effect of Fiber Bending on Sensor Performance	55
4	Plasmon-Assisted Sensing Using PCFs	56
4.1	SPR Sensors Using Planar Photonic Bandgap Waveguides	59
4.2	SPR Sensors Using Photonic Bandgap Bragg Fibers	62
4.3	SPR Sensors Using Photonic Bandgap Honeycomb Fibers	65
5	Concluding Remarks	69
	References	69

Abbreviations

FOS	Fiber-optic sensors
PBG	Photonic band gap
PCF	Photonic crystal fiber
PCR	Polymerize chain reaction
SPR	Surface plasmon resonance
TIR	Total internal reflection

Symbols

d	Layer thickness in a multilayer waveguide
dA	Area differential in the transverse cross section of a waveguide
E	Electric field vector
E_t	Transverse electric field vector
f	Overlap factor
H	Magnetic field vector
H_t	Transverse magnetic field vector
L	Waveguide length
n	Refractive index
P	Power of guided light
R_{core}	Fiber core diameter
R_{bend}	Fiber bending radius
S_a	Amplitude sensitivity
S_λ	Spectral sensitivity
\hat{z}	Vector along the waveguide direction
α	Waveguide loss coefficient per unit of length
ε	Relative permittivity
λ	Wavelength of light in vacuum
δ	Small parameter characterizing changes in the measurand

1 Introduction

Research and development into fiber-optic sensors (FOS) for biological and chemical sensing has made a lot of progress during the last 10 years. This is due to the appealing properties of FOS, such as immunity to electromagnetic interference, safety in explosive environments, and potential to provide continuous quantitative and qualitative real-time analysis. Chemically sensitive thin films deposited on selected areas of optical fibers can influence the propagation of light in such fibers, depending on the presence or absence of chemical molecules in the surrounding environment [38]. A wide range of optical sensors has been developed for selective biomolecule detection. Most of them have reliability issues as they employ very fragile antibodies as sensing elements. These sensors include high refractive index waveguides [30], SPR sensors [5], resonant mirrors [62], and classical fiber-optical sensors [11, 47]. Most optical sensors are based on evanescent wave sensing, where the perturbations in the refractive index close to the sensor surface are probed by the exponentially decaying optical wave. Such sensors have proven to be highly sensitive in detection of small targets such as proteins and viruses, but they experience difficulties in detecting larger targets such as bacteria (0.5–5 μm), since in that case much larger penetration of the evanescent field into analyte is required [66, 67].

PCFs and photonic bandgap (PBG) fibers (which are a subset of PCFs) promise a viable technology for the mass production of highly integrated and intelligent sensors in a single manufacturing step. In standard TIR fiber-based evanescent-wave sensors, the fiber polymer jacket is stripped and the fiber cladding is polished to the core in order to obtain an overlap between the optical field and analyte, with sensor sensitivity proportional to such an overlap. Compared to the conventional solid-core optical fibers, PCFs offer a number of unique advantages in sensing applications. A defining feature of a microstructured fiber is the presence of air holes running along its entire length. Fiber-optical properties are then determined by the size, shape, and relative position of the holes. Particularly, a remarkable ability of PCFs is to accommodate biological and chemical samples in gaseous or liquid forms inside of the air holes in the immediate vicinity of the fiber core [14, 15, 32]. The concept of combining optical detection with PCF devices is appealing as it achieves dual use of the PCF as light guiding and as a fluidic channel. The PCF's architecture makes it a very promising sensing platform for chemical and biological detection. First, PCFs naturally integrate optical detection with the microfluidics, allowing for continuous on-line monitoring of dangerous samples in real time without exposing the personnel to danger. In addition, the samples can be transferred in the enclosed PCF optofluidic system for further confirmation analysis, e.g., polymerase chain reactions (PCR), if needed. Such channels can be further functionalized with biorecognition layers that can bind and progressively accumulate target biomolecules, thus enhancing sensor sensitivity and specificity. Second, the PCF hole size is in sub-100 μm range, leading to very small fluid samples required for sensing. Third, PCF-based sensors can be

coiled into very long sensing cells (~ 10 m), thus dramatically increasing their sensitivity. The same is impossible to achieve with traditional TIR fiber sensors as side-polishing step limits sensor length to several centimeters. Fourth, the desired PCFs can be mass-produced using commercial fiber draw tower in a very cost-effective manner. Fifth, the PCFs can potentially be scaled up into a two-dimensional array with small dimensions, which is suitable for making portable point-of-care devices for simultaneous on-site detection of different kinds of analytes. Sixth, PCFs can be designed to guide light directly in their analyte-field hollow cores [44]. In such fibers, light-analyte coupling is considerably stronger than that in evanescent sensors.

In this chapter, I describe PBG fiber-based resonant optical sensors, which have recently invoked strong interest due to development of novel fiber types and of techniques for activation of the fiber microstructure with functional materials. In resonant sensors, one typically employs fibers with strongly non-uniform spectral transmission characteristics that are sensitive to changes in the real part of the analyte's refractive index. Moreover, if narrow absorption lines are present in the analyte's transmission spectrum, due to Kramers–Kronig relation, this will also result in strong variation in the real part of the refractive index in the vicinity of an absorption line. Therefore, resonant sensors allow detection of minute changes both in the real part of the analyte's refractive index and in the imaginary part of the analyte's refractive index in the vicinity of absorption lines. Although the operational principle of almost all PBG fiber-based sensors relies on strong sensitivity of the PBG fiber losses to the value of the analyte's refractive index, particular transduction mechanism for biodetection can vary. Thus, in one implementation, one can label the target biomolecules with highly absorbing particles of known absorption spectra, such as metal nanoparticles or quantum dots. The presence of such particles in the aqueous fiber core can then be quantified by detecting the appearance of the absorption lines in the fiber transmission spectrum, or through resonant changes in the fiber transmission losses induced by variations in the real part of the core refractive index. In another implementation, a functional layer that binds specific biomolecules can be deposited on the inside of the hollow fiber core. Biomolecule binding events to such a layer can then be detected through resonant changes in the fiber transmission losses induced by variations in the real part of the layer refractive index.

In this chapter, I discuss two types of resonant sensors. One type of sensor relies on changes in the optical confinement of a mode propagating inside of a resonant fiber structure due to changes in the real part of an analyte's refractive index. An example of such a resonant sensor is a photonic bandgap fiber featuring a hollow core filled with analyte. The geometry of such a fiber is chosen to provide strong optical confinement of the guided mode in the analyte's filled core for a particular value of an analyte's refractive index. When changing the real part of an analyte's refractive index, resonant condition for mode confinement will change, resulting in strong variation of the fiber transmission loss (see Fig. 1a, top left). Such sensors can also be used in a standard non-resonant mode for detection of changes in the imaginary part of the analyte's refractive index (analyte absorption) (see Fig. 1a bottom left). Even in non-resonant mode, sensitivity of the hollow-core PBG

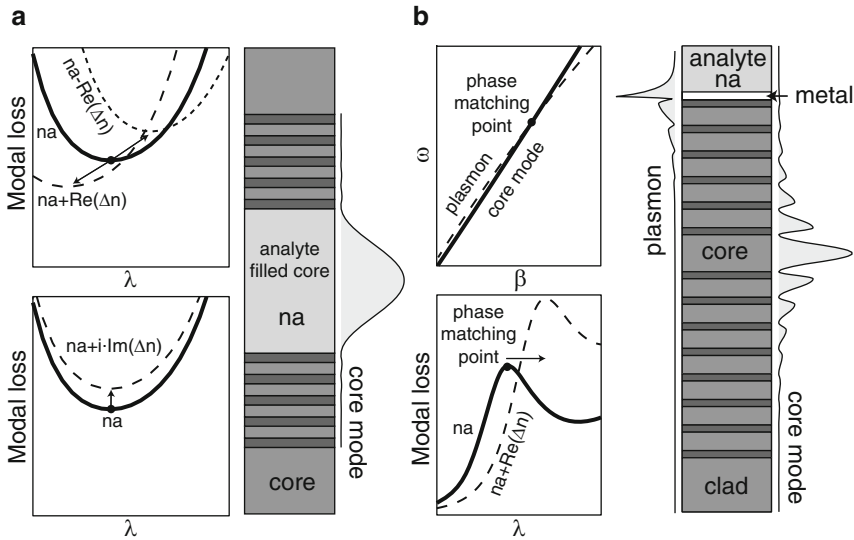


Fig. 1 Operational principles and schematics of two types of the resonant optical sensors. (a) Analyte-filled hollow photonic bandgap fiber-based sensor. Transmission loss through such a sensor is very sensitive to the values of both the real and imaginary parts of the analyte's refractive index. (b) Sensor operating near the phase-matching point of a convenient-to-excite core-guided mode and a second mode featuring large overlap with the analyte region. In the case of phase-matching with a plasmon mode, propagation loss of a core-guided mode is strongly dependent on the real part of the analyte's refractive index

fiber-based sensors is, generally, superior to that of traditional TIR fiber-based sensors due to greatly improved modal overlap with analyte. The second type sensor considered in this chapter is operated in the vicinity of a phase-matching wavelength between an easy to excite core-guided mode and some other mode that shows high sensitivity of its propagation properties to changes in the real part of the analyte's refractive index (Fig. 1b). For example, by activating fiber surface with a thin metal layer, at a specific resonant wavelength, one can induce strong optical loss of a core-guided mode due to coupling to an absorbing plasmon mode propagating at the metal/analyte interface. As plasmon mode is largely delocalized in the analyte region, wavelength of phase-matching between the two modes will be very sensitive to the value of the real part of analyte's refractive index.

2 Detection Strategies for Absorption-Based Sensors

I now describe amplitude-based and spectral-based detection strategies for sensors that exploit changes in their transmission losses in the presence of a target analyte.

In the amplitude-based detection methodology, one operates at a fixed wavelength λ and records changes in the amplitude of a signal, which are then reinterpreted in terms of changes in the analyte's refractive index. To characterize

sensitivity of a fiber-based sensor of length L , one employs an amplitude sensitivity function $S_a(\lambda, L)$, which is defined as a relative change in the intensity $P(\delta, \lambda, L)$ of a transmitted light for small changes in the measurand δ . Note that δ can be any parameter that influences transmission properties of a fiber sensor. This includes concentration of absorbing particles in the analyte, thickness of a biolayer that can change due to capture of specific biomolecules, as well as real or imaginary parts of the analyte's refractive index. Amplitude sensitivity is thus defined as:

$$S_a(\lambda, L) = \lim_{\delta \rightarrow 0} \frac{P(\delta, \lambda, L) - P(0, \lambda, L)}{\delta \cdot P(0, \lambda, L)} = \frac{\partial P(\delta, \lambda, L) / \partial \delta |_{\delta=0}}{P(0, \lambda, L)}. \quad (1)$$

Denoting by $\alpha(\delta, \lambda)$, the fiber propagation loss at a fixed value δ of a measurand, light intensity at the fiber output can be written as:

$$P(\delta, \lambda, L) = P_{\text{in}}(\lambda) \exp(-\alpha(\delta, \lambda)L), \quad (2)$$

where $P_{\text{in}}(\lambda)$ is the light intensity launched into a fiber. Substituting (2) into (1), the amplitude sensitivity function can be then expressed as:

$$S_a(\lambda, L) = -\partial \alpha(\delta, \lambda) / \partial \delta |_{\delta=0} \cdot L, \quad (3)$$

As follows from (3), sensor sensitivity is proportional to the sensor length L . In turn, as follows from (2), the maximal sensor length is limited by the absorption loss of a fiber. Defining $P_{\text{det}}(\lambda)$ to be the power detection limit at which changes in the light intensity can still be detected reliably, the maximal sensor length allowed by the power detection limit can be calculated from (2) as:

$$L = \frac{\log(P_{\text{in}}(\lambda) / P_{\text{det}}(\lambda))}{\alpha(0, \lambda)}. \quad (4)$$

Defining a new function $\eta_{\text{det}}(\lambda) = \log(P_{\text{in}}(\lambda) / P_{\text{det}}(\lambda))$, maximal sensitivity allowed by the power detection limit can be written using (3) as:

$$S_a(\lambda) = -\eta_{\text{det}}(\lambda) \frac{\partial \alpha(\delta, \lambda) / \partial \delta |_{\delta=0}}{\alpha(0, \lambda)}. \quad (5)$$

In all the simulations that follow, I assume that $\eta_{\text{det}}(\lambda) = 1$, which allows us to characterize an inherent sensitivity of a sensor system, while separating it from the issue of a power budget that might bring additional sensitivity enhancement. Finally, given sensor amplitude sensitivity, to estimate sensor resolution of a measurand δ , one can use expression (1). Assuming that the minimal detectable relative change in the signal amplitude is $(\Delta P / P)_{\text{min}}$ (which is typically on the order of 1% if no advanced electronics is used), then the minimum value of a measurand that can be detected by such a sensor is:

$$\delta_{\text{min}} = \frac{(\Delta P / P)_{\text{min}}}{S_a(\lambda)}. \quad (6)$$

Another popular sensing methodology is based on spectral interrogation. It uses detection of displacements of spectral singularities in the presence of a measurand with respect to their positions for a zero measurand. This sensing approach is particularly effective in the resonant sensor configurations that feature sharp transmission or absorption peaks in their spectra. Defining $\lambda_p(\delta)$ to be the position of a peak in a sensor transmission spectrum as a function of a measurand value δ , spectral sensitivity function can be defined as:

$$S_\lambda = \partial\lambda(\delta)/\partial\delta|_{\delta=0}. \quad (7)$$

Given sensor spectral sensitivity, to estimate sensor resolution of a measurand δ , one can use expression (7). Thus, assuming that the minimal detectable spectral shift in the peak position is $(\Delta\lambda_p)_{\min}$ (which is typically on the order of 0.1 nm in the visible spectral range if no advanced optical detection is used), then the minimum value of a measurand that can be detected by such a sensor is:

$$\delta_{\min} = \frac{(\Delta\lambda_p)_{\min}}{S_\lambda}. \quad (8)$$

3 Sensing Using Hollow-Core Photonic Bandgap Fibers

Recently, novel type of optical fibers, called hollow-core PBG fibers, has been introduced. In their cross section, PBG fibers can contain periodically arranged micron-sized air voids [31, 46, 53] (Fig. 2a), rings of holes separated by nanosupports [4, 61] (Fig. 2b), or a periodic sequence of micron-sized layers of different materials [45, 57] (Fig. 2c). PBG fibers are currently available in silica glass, polymer, and specialty soft glass implementations. The key functionality of such

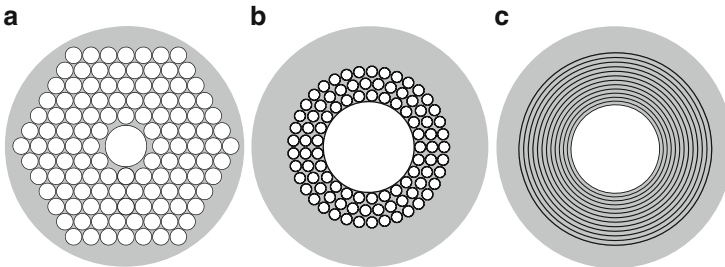


Fig. 2 Various types of hollow-core photonic bandgap fibers. (a) Photonic crystal fiber featuring small hollow core surrounded by a periodic array of large air holes. (b) Microstructured fiber featuring medium-sized hollow core surrounded by several rings of small air holes separated by nano-size bridges. (c) Bragg fiber featuring large hollow core surrounded by a periodic sequence of high and low refractive index layers

fibers is their ability to guide light directly in the hollow or liquid-filled cores with refractive index smaller than that of a surrounding cladding material. Unlike microstructured fibers, PBG fibers confine light in their hollow cores by photonic bandgap effect, rather than by TIR. Practically, bandgaps are defined as frequency regions of enhanced fiber transmission, and they are the result of destructive interference of the core-guided light inside of the fiber microstructured cladding. When launching spectrally broad light into a PBG fiber, only the spectral components guided by the fiber bandgaps will reach the fiber end, while all the spectral components not located within the bandgaps will be irradiated out near the fiber coupling end. Moreover, even in the absence of fiber material losses, core-guided modes always exhibit radiation loss. This is a direct consequence of guidance in a core with refractive index smaller than that of a cladding. As we will see in what follows, core mode radiation loss can be very sensitive to the value of the real part of the refractive index of the material filling the fiber core, which can be utilized for sensor applications. Finally, PBG fibers have a tendency to improve the beam quality of guided light, while being effectively single mode in the limit of long propagation distances. This is a consequence of the fact that radiation losses (and, generally, absorption losses too) of the core-guided modes of a PBG fiber are strongly differentiated with only a few low-order modes having small propagation losses. Thus, when exciting several modes at the fiber input end, only the modes having the lowest losses will survive till the fiber end. For historical reference, I mention that before the invention of the all-dielectric PBG fibers, guidance in the hollow-core fibers has been demonstrated in the context of metal coated capillaries [22, 49].

I now detail some of the advantages offered by the hollow-core PBG fibers for sensing applications. One has to distinguish two modes of operation of such sensors. First, is sensing of changes in the imaginary part of the analyte's refractive index (analyte absorption) by detecting the presence and strength of the narrow absorption bands in the fiber transmission spectrum. This is the simplest, non-resonant application of the hollow PBG fibers for optical sensing in which one only takes advantage of the large optical field overlap with analyte. In such sensors, signal strength due to analyte absorption, as well as sensor sensitivity are directly proportional to the sensor length. Recently, several experimental implementations of such absorption-based sensors have been demonstrated [7, 8, 28, 33, 54]. Second mode of operation of a PBG fiber-based sensor is sensing of changes in the real part of the analyte's refractive index by detection of shifts in the fiber bandgap position. As it will be explained in the following sections, such a sensor operates in the resonant regime with sensitivity that is largely independent of the sensor length.

3.1 *Nonresonant Sensing*

Classic perturbation theory considerations [55] predicts that changes in the effective refractive index of a guided mode Δn_{eff} are related to the changes in the

refractive index Δn_a of analyte infiltrating the fiber, through the overlap factor f defined as:

$$\Delta n_{\text{eff}} = \Delta n_a \cdot f = \text{Re}(\Delta n_a) \cdot f + i \cdot \text{Im}(\Delta n_a) \cdot f$$

$$f = \frac{\int_{\text{analyte}} dA |\mathbf{E}|^2}{\text{Re} \left(\hat{\mathbf{z}} \cdot \int_{\text{crosssection}} dA \mathbf{E}_t^* \times \mathbf{H}_t \right)}, \quad (9)$$

where \mathbf{E}_t , and \mathbf{H}_t are the transverse electromagnetic fields of a fiber mode, while \mathbf{E} is a complete electric field of a mode. Strictly speaking, expression (9) is only valid for the truly guided square integrable modes of the TIR fibers. In the case of hollow-core PBG fibers, the guided modes are, generally, non-square integrable leaky modes [16]. In this case, however, expression (9) can still be used but only approximatively. Particularly, to avoid divergence in the denominator of (9), one performs integration only over the finite fiber cross section limited by the interface between the multilayer reflector and a cladding. For the hollow-core PBG fibers, detailed simulations show that f is typically larger than 0.9. The value of an overlap increases rapidly when the fiber core size increases, reaching values higher than 0.99 for even the small core sizes $R_{\text{core}} \sim 5 - 10\lambda$ (compared to the wavelength of light). Such a high value of the overlap factor is explained by high confinement of the guided mode in the fiber core (see, for example, energy flux distribution of the core-guided mode in Fig. 1a right).

Expression (9) is fundamental for the analysis of non-resonant absorption-based sensors. Consider, for example, a microstructured or a hollow-core fiber filled with aqueous solution. One possible biosensor implementation utilizing such fibers can, for example, monitor presence and concentration of specific biomolecules labeled by highly absorbing nanoparticles. In such a sensor, biomolecules in the aqueous solution are purged through the fiber microstructure. Defining C to be the concentration (measurand; $\delta = C$ in (1)) of the absorbing particles mixed with analyte, and assuming that nanoparticle bulk absorption per unit of concentration is $\alpha_C(\lambda)$, while fiber loss in the absence of nanoparticles is $\alpha_f(\lambda)$, then total fiber loss in the presence of absorbing nanoparticles can be written using (9) as:

$$\alpha(C, \lambda) = \alpha_f(\lambda) + f C \alpha_C(\lambda). \quad (10)$$

In the derivation of (10), I used the fact that $\text{Im}(\Delta n_a) \sim C \alpha_C$, $\alpha(C, \lambda) \sim \text{Im}(n_{\text{eff}})$. By substituting (10) into (5), I now find expression for the maximal non-resonant sensor sensitivity to changes in the nanoparticle concentration:

$$S_a(\lambda) = -f \frac{\alpha_C(\lambda)}{\alpha_f(\lambda)}. \quad (11)$$

Note that as nanoparticle absorption $\alpha_C(\lambda)$ is completely independent from the fiber loss $\alpha_f(\lambda)$ in the absence of nanoparticles, sensitivity (11) of a non-resonant

sensor is, thus, directly proportional to the fiber length $L \sim 1/\alpha_f(\lambda)$. Consequently, to increase sensor sensitivity, one has to simply work with longer fibers featuring low propagation loss.

3.2 Resonant Sensing

Note that expression (9), when applied to PBG fibers, does not account for the spectral shift of the PBG fiber bandgap (see Fig. 1a top left) due to changes in the real part of the refractive index of an analyte. In fact, for the hollow-core PBG fibers in place of (9), one has to use the following modified expression:

$$\Delta n_{\text{eff}} = \text{Re}(\Delta n_a) \cdot f + i[\text{Im}(\Delta n_a) \cdot f + \text{Re}(\Delta n_a) \cdot f_{\text{rad}}]. \quad (12)$$

Here, f_{rad} is a radiation factor that describes changes in the confinement losses of a photonic bandgap-guided mode due to spectral shift of a fiber bandgap caused by changes in the real part of the refractive index of an analyte.

To understand the radiation loss contribution in (12), one has to recall the principles of design and operation of the hollow-core PBG fibers. Consider, as an example, the case of a hollow-core plastic Bragg fiber featuring a water-filled core (refractive index n_w) surrounded by a Bragg reflector (Fig. 3a) made of a periodic sequence of two optically different materials with refractive indices n_l, n_h , which are assumed to be purely real [44, 45, 50]. I now design Bragg reflector to feature the fundamental bandgap in the visible at $\lambda_0 = 0.5\mu\text{m}$. The reflector layer thicknesses d_l, d_h have to be chosen in a very specific way as to guarantee the destructive interference of guided light in the periodic fiber cladding, hence efficient modal confinement in the fiber hollow core. Particularly, by choosing the reflector layer thicknesses to satisfy the quarter wave condition:

$$d_{l,h} = \frac{\lambda_0}{4\sqrt{n_{l,h}^2 - \text{Re}(n_{\text{core}})^2}}. \quad (13)$$

One guarantees that the fundamental bandgap of a Bragg reflector is centered in the near vicinity of a design wavelength λ_0 [16].

I now consider particular implementation of a Bragg fiber having the core of radius $R_{\text{core}} = 25 \mu\text{m}$ surrounded by six reflector layers with $n_h = 1.6$, $n_l = 1.4$ and the layer thicknesses given by (13), where $n_{\text{core}} = 1.34$. In Fig. 2b in thick solid curve I present propagation loss of the fundamental Gaussian-like HE_{11} core mode of a Bragg fiber. In fact, HE_{11} mode plays a key role in the operation of a majority of the hollow-core-based sensors as it is the easiest mode to excite with an external Gaussian-like laser source. While total propagation loss is a sum of the modal radiation and absorption losses, this particular fiber is operating in the radiation

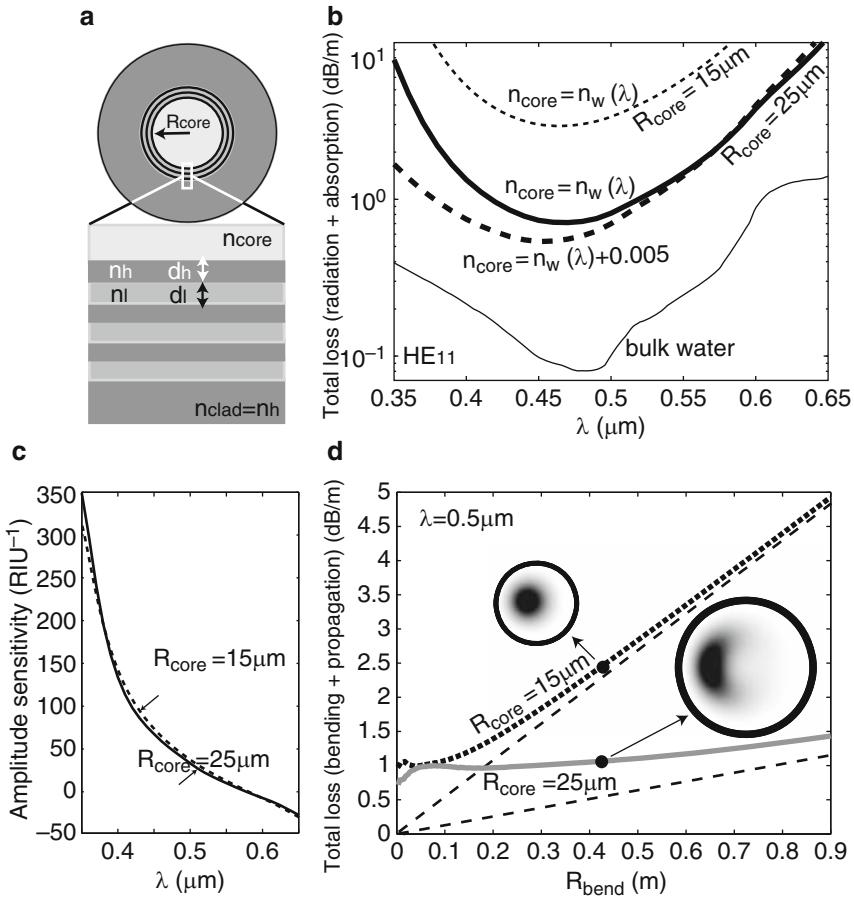


Fig. 3 Refractive index sensors based on hollow-core PBG Bragg fibers. (a) Schematic of a hollow-core Bragg fiber filled with aqueous analyte of refractive index $n_w(\lambda)$. (b) Radiation dominated propagation loss of a core-guided HE_{11} mode for two Bragg fibers with core radii $R_{core} = 25 \mu\text{m}$ (solid curve) and $R_{core} = 15 \mu\text{m}$ (thin dashed curve). When analyte’s refractive index changes, so does the radiation loss of a fiber-core mode (thick dashed curve). For the reference, in thin solid line, I present absorption loss of an aqueous analyte in the visible. (c) Amplitude sensitivity of the analyte filled Bragg fiber-based sensor for two radii of the fiber core. Note that maximal sensitivity is almost independent of the fiber-core radius. (d) Effect of macro-bending on sensor performance, comparison of two Bragg fibers with different core radii. In solid lines, I present total loss (bending + propagation) of a HE_{11} mode as a function of fiber bending radius. For comparison, losses of straight fibers of comparable lengths are presented as dashed lines. Fibers of smaller-core size exhibit stronger propagation losses; however, for the same value of the fiber bending radius, beam quality in smaller-core fibers is greatly superior to that in larger-core fibers

dominated regime; for comparison, bulk absorption loss of water is presented in Fig. 3b in thin solid line. Note that modal propagation loss reaches its minimum at the center of a photonic bandgap at $\sim 0.46 \mu\text{m}$, while increasing rapidly towards

the edges of a bandgap. When changing the real part of the refractive index of an analyte filling the fiber core, resonant condition (13) is no longer satisfied, thus leading to spectral displacement of the fiber bandgap (see dashed lines in Fig. 3b). Therefore, even for small changes in the analyte's refractive index, due to spectral shift in the position of a reflector bandgap, fiber propagation loss can vary substantially. Moreover, due to resonant nature of bandgap guiding, bandgap shift due to changes in the real part of the analyte's refractive index can have a substantially stronger effect on the propagation losses of a core-guided mode than changes in the absorption coefficient of an analyte. Particularly, in (13) one can calculate that at the operational wavelength of $0.5 \mu\text{m}$, $f \simeq 1$, while $f_{\text{rad}} \simeq 2.4 \times 10^{-4}$. Therefore, change of 1 dB/m loss in the analyte absorption coefficient ($\text{Im}(\Delta n_a) \simeq 0.9 \times 10^{-8}$), or change of $\text{Re}(\Delta n_a) \simeq 3.8 \times 10^{-5}$ in the real part of the analyte's refractive index, result in the same 1 dB/m change in the modal propagation loss.

I now investigate amplitude and spectral sensitivities of the hollow-core PBG fiber-based sensors. In Fig. 3c I present amplitude sensitivity (5) of a Bragg fiber-based sensor to changes in the real part of the analyte's refractive index $\delta = \text{Re}(\Delta n_a)$. Note that sensitivity varies strongly as a function of the wavelength of operation, increasing rapidly towards the bandgap edges. Inside of a bandgap and in the vicinity of a design wavelength, amplitude sensitivity is on the order of $S_a \sim 100 \text{ RIU}^{-1}$. Assuming that 1% of change in the amplitude of a transmitted light can be detected reliably, this results in sensor resolution of $\text{Re}(\Delta n_a)_{\text{min}} \sim 10^{-4} \text{ RIU}$. Finally, in the vicinity of a bandgap center at 470 nm the total fiber loss is $\sim 0.7 \text{ dB/m}$, thus defining sensor length to be on the order of $\sim 6 \text{ m}$.

In a similar fashion, spectral sensitivity can be defined using (7) by detecting spectral shift in the bandgap center (wavelength of the fiber lowest loss) resulting in a spectral sensitivity $S_\lambda \sim 5,300 \text{ nm/RIU}$. Assuming that 0.1 nm spectral shift in the position of a bandgap center can be detected reliably, this results in the sensor resolution of $\text{Re}(\Delta n_a)_{\text{min}} \sim 2 \times 10^{-5} \text{ RIU}$, which is comparable to the resolution achieved by the amplitude method.

Interestingly, maximal sensitivity of a resonant hollow-core PBG fiber sensor does not depend strongly on the fiber length. To demonstrate that, in Fig. 3b, I also present losses of an HE_{11} mode of a hollow-core Bragg fiber, with a core radius $R_{\text{core}} = 15 \mu\text{m}$ and otherwise identical parameters to the Bragg fiber with $R_{\text{core}} = 25 \mu\text{m}$. Note that losses of a smaller-core fiber are almost ten times as high as losses of a larger-core fiber. This signifies that the maximal allowed length of a sensor based on a smaller-core fiber is almost ten times shorter than the length of a sensor based on a larger-core fiber. In Fig. 3c, I also plot the maximal sensitivity (5) of a Bragg fiber-based sensor with a core radius $R_{\text{core}} = 15 \mu\text{m}$ and note that it is almost identical to that of a larger-core fiber. This interesting, while somewhat counterintuitive, result is a direct consequence of the fact that in PBG fibers operating in the radiation dominated regime, fiber propagation loss and radiation factor are not independent parameters. Particularly, starting from (12), and assuming that the fiber loss for a neutral analyte is $\alpha_f(\lambda)$, then PBG fiber

absorption loss $\alpha(\Delta n_a, \lambda)$ in the presence of changes in the real part of the analyte's refractive index is described by:

$$\alpha(\Delta n_a, \lambda) = \alpha_f(\lambda) + \frac{4\pi}{\lambda} \text{Re}(\Delta n_a) \cdot f_{\text{rad}}. \quad (14)$$

In the case of Bragg fibers operating in the radiation dominated regime, one generally finds that $f_{\text{rad}} \sim \alpha_f(\lambda)$. Therefore, maximal amplitude sensitivity as defined by (5) will not depend on the fiber loss, and as a consequence, it will not depend on the sensor length. This finding promises a significant advantage of PBG fiber-based resonant sensors compared to their conventional absorption-based counterparts. Particularly, compact and highly sensitive sensors that utilize short PBG fiber pieces and that do not require fiber coiling are more convenient to use, and easier to maintain than their conventional counterparts that utilize long coiled fibers.

3.3 Effect of Fiber Bending on Sensor Performance

I finally comment on the effects of fiber core size and fiber bending on the performance of a hollow-core PBG fiber-based sensor. In fact, the value of a core radius R_{core} influences strongly modal guiding in such fibers. Particularly, core mode propagation losses in a straight fiber decrease rapidly with increase in the hollow core size (typically $\sim R_{\text{core}}^{-3}$), thus allowing, in principle, longer sensor lengths and higher sensitivities (for non-resonant sensing) when using fibers with larger cores. At the same time, mixing of the fundamental core mode with higher-order high-loss modes increases dramatically with increase in the hollow core size. This also results in the degradation of the quality of a guided beam and, potentially, resulting in reduced overlap with analyte. Therefore, while designing hollow-core PBG fiber-based sensors, one has to be aware of the tradeoff between longer sensor lengths versus bending induced beam degradation. As an example, in Fig. 3d, I compare bending losses and beam profiles of the two Bragg fibers having core radii $R_{\text{core}} = 15 \mu\text{m}$ and $R_{\text{core}} = 25 \mu\text{m}$ and featuring the same Bragg reflector as described above. All the simulations are performed at $\lambda = 0.5 \mu\text{m}$. In Fig. 3d, in thick solid lines, I plot total losses of a 90° bend as a function of the bending radius, while in dashed lines, I present, for the sake of comparison, propagation losses of straight fibers of equivalent lengths. Simulations show that in the bending loss dominated regime (fiber bending radius is small), bending loss depends weakly on the fiber core size. However, for larger bending radii, propagation loss is largely determined by the loss of the fundamental core mode of a straight fiber, which increases rapidly when core size decreases. Moreover, for the same value of bending radius, intensity distribution inside of a fiber featuring larger core shows strong mode mixing and pronounced beam profile degradation, while field intensity

distribution in a smaller-core fiber resembles that of a fundamental core mode (see also Fig. 1b).

4 Plasmon-Assisted Sensing Using PCFs

In this section, I describe another type of a resonant sensor operating in the vicinity of a phase-matching point between an easy-to-excite core-guided mode of a waveguide (fiber) with another mode that has strong overlap with analyte region (see Fig. 1b). In the particular case described in what follows, the mode that has strong overlap with analyte is a highly lossy plasmon wave.

Propagating at the metal/dielectric interface, surface plasmons [1] are extremely sensitive to changes in the refractive index of the dielectric. This feature constitutes the core of many SPR sensors. Typically, these sensors are implemented in the Kretschmann–Raether prism geometry where p-polarized light is launched through a glass prism and reflected from a thin metal (Au, Ag) film deposited on the prism facet [34]. The presence of a prism allows phase-matching of an incident electromagnetic wave with a plasmonic wave at the metal/ambient dielectric interface at a specific combination of the angle of incidence and wavelength. Mathematically, phase-matching condition is expressed as an equality between the plasmon wavevector and a projection of the wavevector of an incident wave along the interface. Since plasmon excitation condition depends resonantly on the value of the refractive index of an ambient medium within 100–300 nm from the interface, the method enables, for example, detection, with unprecedented sensitivity, of biological binding events on the metal surface [37]. The course of a biological reaction can then be followed by monitoring angular [37, 39], spectral [65] or phase [20, 29] characteristics of the reflected light. However, the high cost and large size of commercially available systems makes them useful mostly in a laboratory, while many important field and other applications still remain out of the reach for this method.

The use of optical waveguides and fibers instead of bulk prism configuration in plasmonic sensors offers miniaturization, high degree of integration, and remote-sensing capabilities. In fiber and waveguide-based sensors, one launches the light into a waveguide core and then uses coupling of a guided mode with a plasmon mode to probe for the changes in the ambient environment. To excite efficiently a surface plasmon, the phase-matching condition between a plasmon and a waveguide mode has to be satisfied, which mathematically amounts to the equality between their modal propagation constants (effective refractive indices). Over the past decade, driven by the need for miniaturization of SPR sensors, various compact configurations enabling coupling between optical waveguide modes and surface plasmonic waves have been investigated. Among others, metallized single mode, multimode and polarization maintaining waveguides and fibers, metallized tapered fibers, metallized fiber Bragg gratings [2, 3, 9, 12, 17, 21, 25, 26, 40, 41, 43, 56, 58–60, 64] and, recently, solid-core microstructured fibers [19, 24, 35], as well as planar photonic crystal waveguides [51, 52] have been studied. In the majority of

fiber implementations (with an exception of microstructured fibers), one typically strips the fiber polymer jacket and polishes off fiber cladding until the fiber core is exposed; then, a metal layer is deposited directly onto a fiber core. Thus, the functionalized surface of a fiber core is then exposed to an analyte.

Ideally, one would use a single mode fiber or waveguide with all the power traveling in a single Gaussian-like core mode operating near the point of resonant excitation of the plasmon [13, 23, 27, 36, 48, 63]. Gaussian shape of a core mode is important as it is best suited for the excitation by standard Gaussian laser sources. Near the point of phase-matching, most of the energy launched into a waveguide core mode should be efficiently transferred into a plasmon mode. However, in the total internal reflection (TIR) single mode waveguides with low refractive index-contrast, coupling with a plasmon is realized at essentially grazing angles of modal incidence on the metal layer. As follows from the basic SPR theory, coupling at such grazing incidence angles leads to an inevitable decrease of sensitivity of the SPR method. In principle, high index-contrast single mode waveguides (see Fig. 4a) could be employed to increase the angle of modal incidence on the interface. Overall, in the single mode waveguide-based sensors, phase-matching between plasmon and fundamental waveguide mode is typically hard to realize. This is related to the fact that the effective refractive index of a core-guided mode is close to the refractive index of the core material, which is typically larger than 1.45

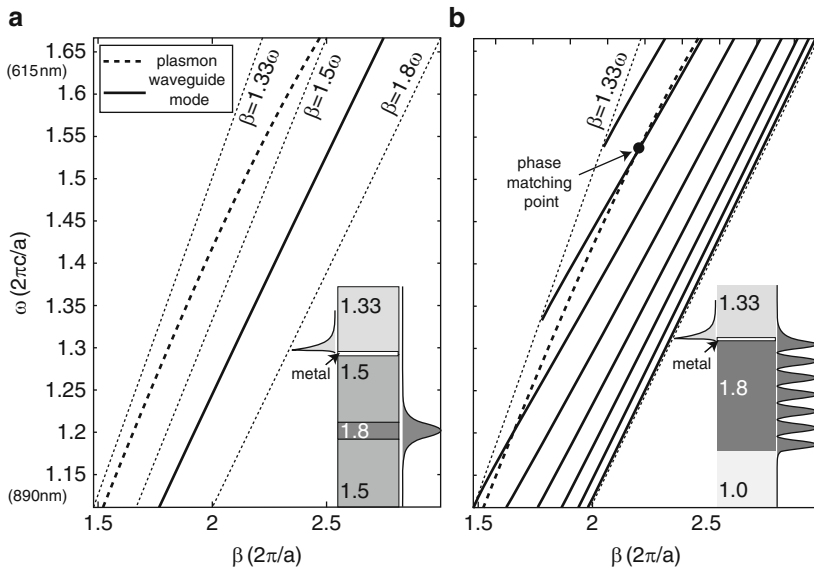


Fig. 4 Band diagrams and schematics of various SPR-based integrated sensor implementations. (a) Single mode waveguide-based sensor. Dispersion relations of a core-guided mode (*solid*) and a plasmon (*thick dashed*). *Inset* – sensor schematic; $|H_{||}|^2$ of a plasmon (*left*) and a core mode (*right*). (b) Multimode waveguide-based sensor. Dispersion relations of the core modes (*solid*) and a plasmon (*thick dashed*). *Inset* – coupler schematic; $|H_{||}|^2$ of a plasmon (*left*) and a high-order mode (*right*) at the phase-matching point (*black circle*)

due to practical material limitations. The effective refractive index of a plasmon is close to the refractive index of an ambient medium, which is typically air $n_a = 1$ (gas sensing) or water $n_a = 1.33$ (biological sensing). Thus, large discrepancy in the effective indices makes phase-matching between the two modes hard to achieve, with an exception of the high frequencies where $\lambda < 650$ nm, where the plasmon dispersion relation deviates towards higher refractive indices. Thus, due to practical limitation on the lowest value of the waveguide core and cladding refractive indices, single mode TIR waveguide-based sensors were demonstrated almost exclusively in the visible region, where phase-matching condition is easier to enforce.

Problems with phase-matching and loss of sensitivity due to shallow angles of incidence could be, in principle, alleviated by using multimode waveguides [10, 17, 21, 58, 64] as presented in Fig. 4b. If launched properly, modal effective propagation angles in such waveguides can be much steeper, also resulting in smaller effective refractive indices. However, in multimode waveguides, only a certain number of higher order modes will be phase-matched with a plasmon. Thus, sensitivity and stability of such sensors depend crucially on launch conditions. Moreover, as spatial field distribution in a Gaussian-like laser source is typically not well matched with the field distribution of a higher order mode of a multimode waveguide, only a small fraction of energy can be launched into such a mode resulting, again, in decreased sensitivity.

In what follows, I detail design principles of a PCF and waveguide-based SPR sensors, and show that they integrate advantages of both the single mode and multimode waveguide-based SPR sensors. Moreover, in PCF and waveguide-based SPR sensors, fundamental Gaussian-like leaky core modes can be phase-matched with a plasmon at any desired wavelength of operation, thus enabling sensing anywhere from the visible to mid-IR. The term “leaky mode” generally refers to the guidance mechanism where the effective refractive index of a propagating mode is smaller than that of the waveguide cladding. Such unusual modes are called leaky modes as, outside of a waveguide core, they do not exhibit a traditional evanescent decay into the cladding, but rather they radiate slowly (leak) into the cladding. Unlike in the case of common TIR waveguides, leaky modes in photonic crystal waveguides are confined by the bandgap of a photonic crystal reflector. As a consequence, the effective refractive index of the fundamental (lowest loss) leaky-core mode can be designed to be arbitrarily smaller than that of a waveguide-core material, thus enabling phase-matching with a plasmon at any desired frequency. Moreover, the lowest loss leaky-core mode typically exhibits a Gaussian-like intensity distribution in the waveguide-core region, thus enabling convenient excitation by a Gaussian beam of an external light source. Using the fundamental (lowest loss) leaky mode for sensing gives the additional advantage of an effectively single mode propagation regime. In particular, when a set of modes is excited at a sensor input, higher-order leaky modes radiate out faster than a fundamental mode. Consequently, after a certain propagation distance, only the fundamental mode is left in the waveguide core. Finally, the effective angle of modal incidence onto a metal film, and hence sensitivity, can be varied by a proper selection of the waveguide core and reflector materials.

4.1 SPR Sensors Using Planar Photonic Bandgap Waveguides

To demonstrate the principles of operation of photonic bandgap waveguide-based SPR sensors, I start by considering plasmon excitation by a Gaussian-like TM polarized mode of a planar photonic crystal waveguide (see Fig. 5a), in which light confinement in a lower refractive index core is achieved by a surrounding multi-layer reflector. TM polarization of the electromagnetic field in a planar multilayer assumes a single magnetic field component $|H_{\parallel}|^2$ directed parallel to the plane of a multilayer, while the electric field component is confined to a plane perpendicular to the multilayer.

The photonic crystal waveguide under consideration consists of 27 alternating layers having refractive indices $n_h = 2.0$, and $n_l = 1.5$. The core layer is layer number 12; having refractive index $n_c = n_l$. Analyte (first cladding) is water $n_a = 1.332$ bordering a 50 nm layer of gold. The substrate refractive index is 1.5. Theory of planar photonic crystal waveguides with infinite reflectors where $n_c = n_l$ [50], predicts that, for a design wavelength λ_c , the effective refractive index $n_{\text{eff}}(\lambda_c)$ of the fundamental TE and TM core-guided modes can be designed, as long as $0 < n_{\text{eff}} < n_l$, by choosing the reflector layer thicknesses as

$$d_{l,h} = \frac{\lambda_c}{4\sqrt{n_{l,h}^2 - n_{\text{eff}}^2}} \quad (15)$$

and by choosing the core layer thickness as $d_c = 2d_l$. Moreover, for this choice of n_c , the field distribution in the core is always Gaussian-like for TE polarized modes, while for TM polarized modes it is Gaussian-like as long as $n_{\text{eff}}^2 > \epsilon_l \epsilon_h / (\epsilon_l + \epsilon_h)$ [50]. By choosing the effective refractive index of a core mode to be that of a plasmon, a desired phase-matching condition is achieved. For a waveguide with a finite reflector, the same design principle holds approximately. Thus, for an operating wavelength of $\lambda = 640$ nm, considered in this example, phase-matching is achieved when the photonic crystal waveguide is designed using $\lambda_c = 635$ nm and $\text{Re}(n_{\text{eff}}(\lambda_c)) = 1.46$ in (15). A reasonable approximation to the $n_{\text{eff}}(\lambda_c)$ is a value of the effective refractive index of a plasmonic wave propagating at a planar gold–analyte interface:

$$n_{\text{eff}}(\lambda_c) = \left(\frac{\epsilon_{\text{gold}}(\lambda_c) \times \epsilon_a(\lambda_c)}{\epsilon_{\text{gold}}(\lambda_c) + \epsilon_a(\lambda_c)} \right)^{1/2}, \quad (16)$$

where ϵ_a is the dielectric constant of an analyte and ϵ_{gold} is the dielectric constant of the gold layer approximated by the Drude model:

$$\epsilon_{\text{gold}}(\lambda_c) = \epsilon_{\infty} - \frac{(\lambda/\lambda_p)^2}{1 + i(\lambda/\lambda_t)}, \quad (17)$$

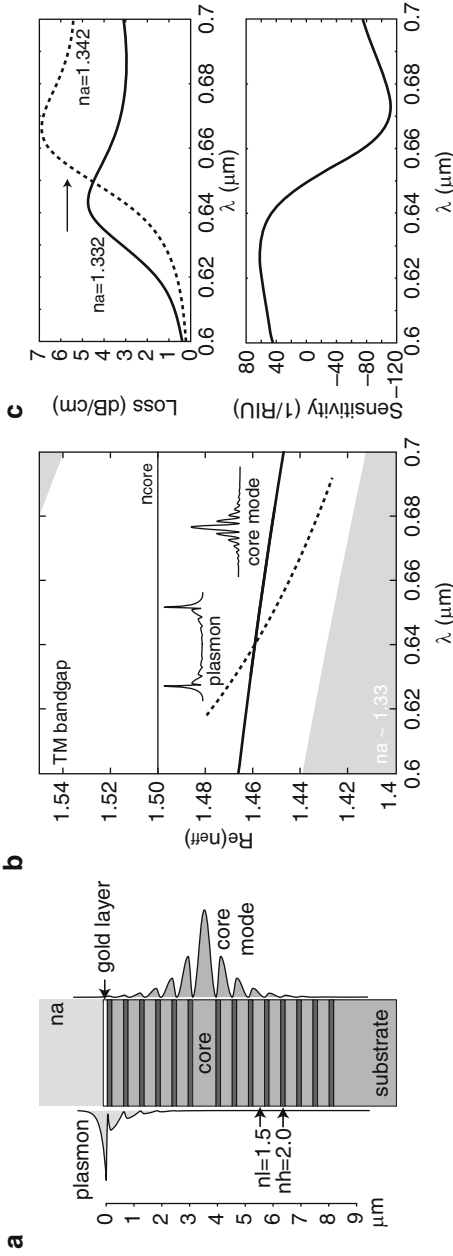


Fig. 5 Planar photonic bandgap waveguide-based SPR sensor. (a) Schematic of a sensor. Low refractive index core is surrounded by the periodic photonic crystal reflector. Top side of the reflector is goldplated for plasmon excitation. Gold layer is bordered by aqueous analyte. $|H_{||}|^2$ field distribution in the fundamental core mode is shown on the *right*, while field distribution in a plasmon mode is shown on the *left* of a sensor schematic. (b) Band diagram of sensor modes. Dispersion relation and field distribution of the fundamental core mode (*thick solid curve*), and plasmon mode (*dashed curve*). TM bandgap of a periodic reflector is shown as a clear region, while *gray* regions correspond to the continuum of the bulk reflector states. By design, the effective refractive index of a core-guided mode can be made significantly smaller than that of the waveguide core material. (c) *Upper part*: *solid curve* shows loss of a waveguide core mode near the phase-matching point with a plasmon at which modal loss peaks. *Dashed line* shows shift of the modal loss curve when refractive index of the analyte is varied. *Lower part*: dependence of the sensor amplitude sensitivity on wavelength

where the choice $\varepsilon_\infty = 9.75$, $\lambda_t = 13 \mu\text{m}$, $\lambda_p = 0.138 \mu\text{m}$ presents one of the many possible fits of the experimental data.

In Fig. 5b, I present band diagram of a planar photonic crystal waveguide-based SPR sensor. All the simulations are performed using standard transfer matrix theory on a complete system that includes both the waveguide and metal layer. Gray regions signify bulk states of a periodic reflector. The clear region in Fig. 5b is a TM bandgap where no extended into the reflector states are found. The thick solid line, which is almost parallel to the band gap edges, marked as “core mode” is a dispersion relation of a Gaussian-like leaky core mode with most of its modal energy concentrated in the low refractive index core. The dashed line marked as “plasmon” represents the dispersion relation of a plasmon mode. Most of the plasmon energy is concentrated at the metal/analyte interface.

Near the phase-matching point, fields of a core-guided mode contain strong plasmonic contribution. As plasmon wave exhibits very high propagation loss, the loss of a core mode (upper plot in Fig. 5c) will also exhibit a sharp increase near the phase-matching point with a plasmon. An important aspect of the proposed setup is the freedom of adjusting the loss of a core mode. As leaky mode decays exponentially fast with respect to distance into the multilayer reflector, coupling strength between the plasmon and core modes can be controlled by changing the number of reflector layers situated between the waveguide core and a metal film. Ultimately, higher coupling strength leads to higher modal losses, hence, shorter sensor length. When the real part of the analyte’s refractive index is varied, the plasmon dispersion relation displaces accordingly, thus leading to a shift in the position of the phase-matching point with a core-guided mode. Consequently, in the vicinity of the phase-matching point, transmission loss of a core-guided mode varies strongly with changes in the analyte’s refractive index; see the upper part of Fig. 5c.

I would like to point out that what is identified as a “core mode” in all the figures in this chapter is in fact a waveguide supermode that includes both the core-guided mode and plasmonic contribution. Since the plasmon mode is extremely lossy, only a small mixing of this mode with the core mode is necessary to achieve sensing. I found pertinent to also show on the graphs what a plasmon mode looks like near the phase-matching point, although this mode by itself is not used in the sensing arrangements. Depending on the designs, the plasmon contribution to the evanescent tail of a core mode is not always visible on the field distribution plots as only the real components of the modes are truly phase-matched.

The simplest mode of operation of a waveguide-based SPR sensor is detection of small changes in the bulk refractive index of an analyte. Similarly to the case of hollow-core PBG fiber-based sensors, there are two main modalities of SPR detection: amplitude-based and spectral-based. In both methodologies, sensing is enabled through detection of changes in the location of a sharp plasmonic loss peak, whose spectral position is strongly dependent on the value of the ambient refractive index. In the amplitude-based approach, all the amplitude measurements are performed at a single wavelength near the center of a plasmonic peak. The advantage of this method is its simplicity and low cost, as no spectral manipulation is required. The disadvantage is a smaller dynamic range and lower sensitivity when compared

to the wavelength interrogation approach, in which the whole transmission spectra are taken and compared before and after the change in the analyte has occurred. I now use expression (5) to define sensor amplitude sensitivity with respect to changes in the real part of an analyte's refractive index. In (5), the measurand δ is $\text{Re}(\Delta n_a)$, and $\alpha(\delta, \lambda)$ is propagation loss of a core-guided mode presented at the top of Fig. 5c. At the bottom of Fig. 5c, I present amplitude sensitivity of a PBG waveguide-based SPR sensor as a function of the wavelength of operation. Maximal sensitivity is achieved at 673 nm and is equal to 112 RIU^{-1} . It is typically a safe assumption that 1% change in the transmitted intensity can be detected reliably, which leads to a sensor resolution of $9 \times 10^{-5} \text{ RIU}$. In the wavelength interrogation mode, changes in the analyte's refractive index are detected by measuring displacement of a plasmonic peak center wavelength λ_p as a function of the value of an analyte's refractive index. Sensor sensitivity is then defined by expression (7), where $\delta = \text{Re}(\Delta n_a)$. I find that the spectral sensitivity of a PBG waveguide-based sensor is $2,300 \text{ nm RIU}^{-1}$. Assuming that a 0.1 nm change in the position of a resonance peak can be detected reliably, sensor resolution of $4.3 \times 10^{-5} \text{ RIU}$ is obtained.

Finally, sensor length is always in the range $L \sim 1/\alpha(\delta, \lambda)$. In the vicinity of plasmonic peak shown in Fig. 5c, the typical sensor length is $L \sim 1 \text{ cm}$. Detailed simulations also show that, similarly to the case of resonant sensing using hollow-core PBG fibers, sensitivity of a PBG waveguide-based plasmonic sensor is only weakly dependent on the sensor length. Particularly, by varying the number of reflector layers separating the waveguide core and gold layer, one can vary the overall sensor length from sub-millimeters to several centimeters without changing significantly the sensor sensitivity.

In the rest of this section, I present theoretical study of SPR sensor designs based on photonic bandgap fibers, rather than planar waveguides. Advantages of fiber-based sensors over their planar counterparts include lower manufacturing cost, possibility of distributed sensing, and incorporation of microfluidics into the fiber structure directly at the fiber drawing step. In what follows I demonstrate an SPR sensor using solid-core PBG Bragg fiber operating at 760 nm, as well as an SPR sensor using honeycomb lattice photonic bandgap fiber operating at 1,060 nm.

4.2 SPR Sensors Using Photonic Bandgap Bragg Fibers

I start by describing solid-core Bragg fiber-based SPR sensor for detection in aqueous analytes. In such a sensor, a thin gold layer is deposited on the outer surface of a Bragg fiber in direct contact with an analyte. By tailoring the dispersion relation of the core-guided mode of a Bragg fiber, phase-matching with a plasmon wave can be obtained at any wavelength in the visible and near-IR. The mode of operation in such a sensor is a Gaussian-like HE_{11} core mode. Effective refractive index of such a mode is matched with that of a plasmon by the proper choice of the

fiber core size. The choice of an HE_{11} mode over the other modes is motivated by the ease of its excitation using common Gaussian laser sources.

As an example, I consider solid-core photonic crystal Bragg fibers made of two materials with refractive indices $n_l = 1.42$ and $n_h = 1.6$. Prototypes of such fibers have been recently fabricated in our group by using a poly(vinylene difluoride) (PVDF)/polycarbonate (PC) material combination [18]. In such fibers, a solid core of refractive index n_l is surrounded by N alternating high and low refractive index reflector layers of thicknesses d_l and d_h (see Fig. 6a). In a manner similar to the planar multilayer waveguides, reflector layer thicknesses are given by the quarter-wave condition (15), where λ_c is an operating wavelength, and $n_{\text{eff}}(\lambda_c)$ is a desired effective refractive index of a core-guided mode at that wavelength. Although such a choice of the reflector parameters guarantees bandgap guidance at λ_c of a mode with effective refractive index $n_{\text{eff}}(\lambda_c)$; however, it does not guarantee existence of such a mode. One way of positioning a core mode dispersion relation inside of the reflector bandgap is by varying the fiber-core diameter d_c , namely, in the large-core diameter Bragg fibers with $d_c \gg \lambda_c$, effective refractive index of the fundamental core mode is close to that of the core material. By decreasing the fiber core size, one can consistently reduce the core mode effective refractive index, and, eventually, position it in the middle of the reflector bandgap. Moreover, in the context of SPR sensing, λ_c also corresponds to the wavelength of phase-matching between plasmon and a core-guided mode. Therefore, a good approximation to $n_{\text{eff}}(\lambda_c)$ of a core-guided mode is that of the effective refractive index of a plasmonic wave propagating at a planar gold-analyte interface given by (16). With these choices of $n_{\text{eff}}(\lambda_c)$ and d_c , one parameter still remains undetermined, which is the number of layers N in the Bragg reflector. In metallized Bragg fibers, guided modes incur additional losses due to high absorption in the metal film. When operating within bandgap of a Bragg fiber reflector, the fields of leaky core modes decay exponentially fast into the reflector. Therefore, modal presence in the metal layer also decreases exponentially fast when increasing the number of reflector layers. Thus, the choice of the number of reflector layers primarily affects the core mode propagation loss and, consequently, the sensor length. As mentioned earlier, PBG fiber-based sensor sensitivity is only weakly dependent on sensor length. Therefore, without the loss of sensitivity, one would choose a small enough number of reflector layers, so that the resultant fiber is short enough to prevent the necessity of coiling and simplify sensor handling.

In Fig. 6, I present an example of a solid-core PBG fiber-based SPR sensor. By choosing the fiber core size to be small, one can considerably reduce the effective refractive index of the core mode. This enables plasmonic excitation at longer wavelengths in the near-IR. In Fig. 6a, I show cross section of a small-core Bragg fiber-based sensor, as well as energy flux distributions in the HE_{11} core mode and plasmon mode. Reflector layer thicknesses are chosen according to (15), where $\lambda_c = 760$ nm, $n_l = 1.42$, $n_h = 1.6$, and $n_{\text{eff}} = 1.39$, thus resulting in $d_l = 654$ nm, $d_h = 240$ nm. The fiber-core diameter is $d_c = 1.8$ μm . The total number of layers is $N = 12$. For the fundamental Gaussian-like mode, the amount of energy in the core is 78%. In Fig. 6b, I present the band diagram of the modes of thus defined

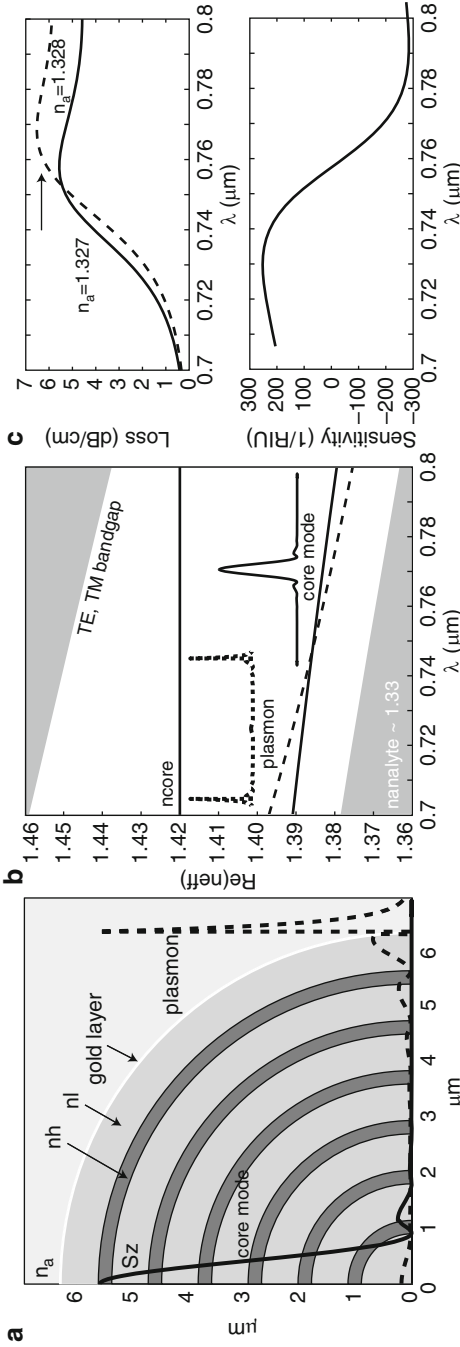


Fig. 6 Small solid-core PBG Bragg fiber-based SPR sensor. (a) Schematic of a sensor. Low refractive index core is surrounded by the concentric photonic crystal reflector. Reflector exterior is goldplated for plasmon excitation. Gold layer is bordered by aqueous analyte. Energy flux distribution across the fiber cross section is shown as a *solid curve* for the fundamental core mode, and as a *dashed curve* for the plasmon mode. (b) Band diagram of the sensor modes. Dispersion relation of the fundamental core mode (*thick solid curve*), and plasmon mode (*dashed curve*), TE, TM bandgap of a periodic planar reflector is shown as a clear region, while *gray* regions correspond to the continuum of bulk reflector states. In a small-core Bragg fiber, effective refractive index of the fundamental core mode can be much smaller than refractive index of the core material. (c) *Upper plot*: solid curve shows loss of the fundamental core mode near the phase-matching point with plasmon. Modal loss reaches its maximum at the phase-matching wavelength. Dashed line corresponds to the shifted modal loss curve when the analyte's refractive index is varied. *Lower plot*: sensor amplitude sensitivity as a function of wavelength (after [19] © 2007 OSA)

Bragg fiber sensor. The common TM, TE bandgap of a corresponding infinitely periodic Bragg reflector is presented as a clear region, while gray regions define a continuum of reflector bulk states. In a small-core Bragg fiber, the effective refractive index of the core-guided HE_{11} mode (thick solid line) can be considerably smaller than the refractive index of a core material (thin solid line). Dispersion relation of a plasmon mode is shown as thick dashed line. In this particular case, the dispersion relation of the core-guided mode is shifted towards the lower edge of the reflector bandgap; therefore, the core mode (solid curve in Fig. 6a) and plasmon mode (dashed curve in Fig. 6a) penetrate significantly into the reflector. Phase-matching between the core and plasmon modes is achieved at 758 nm. In the upper plot of Fig. 6c, propagation loss of the core-guided mode is presented as a function of the wavelength. As seen from this plot, core mode loss peaks at the wavelength of phase-matching with plasmon mode. In the lower plot of Fig. 6c, I present amplitude sensitivity (5) of a solid-core Bragg fiber-based SPR sensor with respect to changes in the real part of the analyte's refractive index. Maximal sensitivity is achieved at 788 nm and is equal to 239 RIU^{-1} . Assuming that a 1% change in the transmitted intensity can be detected reliably, this leads to a sensor resolution of $3.4 \times 10^{-5} \text{ RIU}$. Finally, I find that the corresponding spectral sensitivity (7) is 10^4 nm RIU^{-1} . Assuming that a 0.1 nm change in the position of a resonance peak can be detected reliably, this leads to a sensor resolution of $9.8 \times 10^{-6} \text{ RIU}$. The sensor length in this case is in a 1 cm range.

4.3 SPR Sensors Using Photonic Bandgap Honeycomb Fibers

In the two previous subsections, I have presented design strategies for the SPR sensors based on photonic crystal Bragg fibers. In principle, any photonic bandgap fiber can be used in place of a Bragg fiber to develop such sensors. In this section, I present an example of a SPR sensor based on a solid-core honeycomb PCF.

In Fig. 7a, schematic representation of a honeycomb PCF-based SPR sensor is presented. The design parameters are chosen as follows: the center to center distance between adjacent holes is $\Lambda = 0.77 \mu\text{m}$, the cladding hole diameter is $d = 0.55\Lambda$ and the diameter of the hole in the core center is $d_c = 0.35\Lambda$. The fiber is made of silica glass with a refractive index of $n_{\text{glass}} = 1.45$, the core and cladding holes are filled with air $n_{\text{air}} = 1$, while the large semicircular channels are plated with a 40 - nm - thick layer of gold and filled with an aqueous analyte $n_a = 1.32$. The central hole in the fiber core lowers its effective refractive index compared to that of a silica cladding. Under certain conditions, such a core can support a mode confined by the bandgap of the honeycomb reflector. The core-guided mode in such a fiber is analogous to that of the small solid-core Bragg fiber discussed earlier. Guided by the bandgap of the fiber reflector, the effective refractive index of the core mode can be made much lower than that of the silica material. Moreover, as in the case of photonic crystal Bragg fibers, radiation loss of a bandgap-guided core

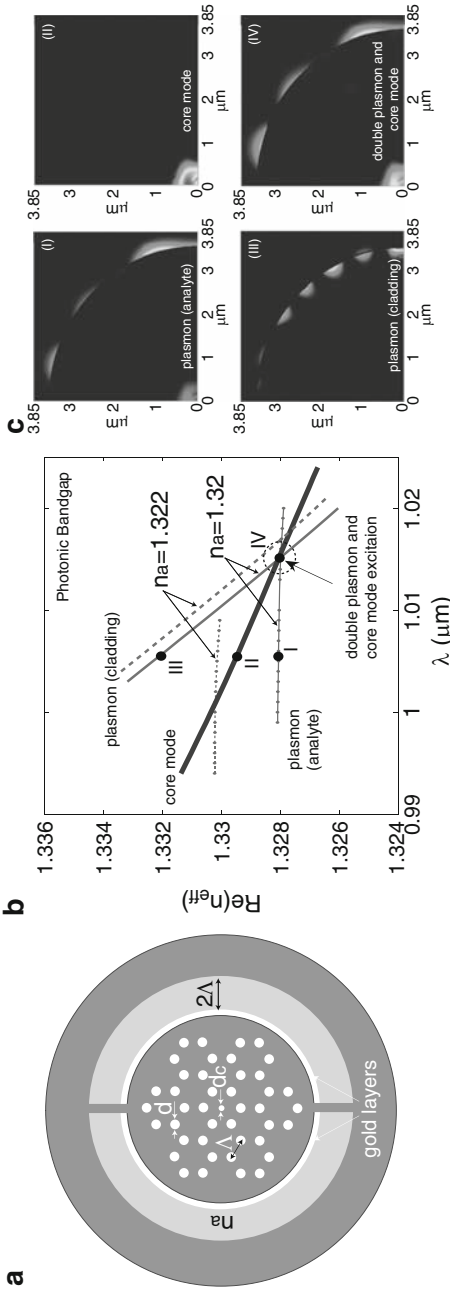


Fig. 7 Solid-core honeycomb photonic crystal fiber-based SPR sensor. (a) Schematic of a sensor. Solid fiber core having a small central hole is surrounded with a honeycomb photonic crystal reflector. Two large channels are integrated to implement analyte access to the fiber reflector region. The channels are goldplated for plasmon excitation. The gold layer is bordered by an aqueous analyte. (b) Band diagram of sensor modes. Dispersion relation of the fundamental core mode (*thick solid curve*), analyte bound plasmon mode (*dashed curve with circles*), and cladding bound plasmon mode (*dashed curve*). The bandgap of an infinitely periodic reflector is shown as a clear region. (c) The energy flux distributions across the fiber cross section are shown for the fundamental core mode (II) as well as the analyte and cladding bound plasmon modes (I,III) outside of the phase-matching region. The energy flux distribution is also shown for the fundamental core mode at the phase-matching point (IV) showing strong mixing of the fundamental core mode with plasmon modes (after [19] © 2007 OSA)

mode can be reduced by adding more layers into the honeycomb reflector. The main reason why I chose a honeycomb structure of the fiber reflector is because it enables a very large photonic bandgap [6, 42], thus simplifying considerably phase-matching of the core-guided and plasmon modes.

Unlike planar metal/dielectric interface that supports a single plasmonic excitation, finite size, microstructured metal layer separating two dielectrics can support multiple plasmon modes [19, 24]. Thus, when tracking losses of a core-guided fiber mode as a function of wavelength, one typically observes several plasmonic peaks corresponding to phase-matching between the core mode and various plasmon modes. Particularly, one of the plasmon modes will have most of its energy concentrated in one of the neighboring dielectrics, while the other plasmonic excitation will have most of its energy concentrated in the other neighboring dielectric. In principle, simultaneous detection of changes in several plasmonic peaks can improve sensor sensitivity; additionally, it gives a natural reference point in the measurements.

In the case of a honeycomb PCF-based sensor, I design the fiber so that two plasmonic peaks are degenerated at 1,009 nm with $n_a = 1.32$. Figure 7b shows the dispersion relations of the Gaussian-like core mode (thick solid line), analyte bound plasmon mode (thin solid line with circles), and cladding bound plasmon mode (thick solid line). These dispersion relations are positioned well inside the bandgap of an infinite honeycomb reflector, which can be confirmed by the plane wave method [6]. Corresponding flux distributions of the core-guided and plasmon modes are presented in Fig. 7c. The core mode loss shows a single plasmonic peak (solid curve in Fig. 8a). When the refractive index of the analyte is varied, this affects the two plasmonic dispersion relations differently. Particularly, the analyte bound plasmon mode is affected much strongly by the changes in the analyte's refractive index than the cladding bound plasmon mode. As a result, degeneracy is lifted, and two closely spaced plasmonic peaks appear in the core mode loss curve (dashed curve in Fig. 8a). For example, a 0.002 change in the analyte's refractive index splits a single plasmonic peak into two peaks separated by 27.5 nm. This permits a novel spectral detection technique, where relative peak separation can be used to characterize changes in the real part of the analyte's refractive index. By defining spectral sensitivity as:

$$S_\lambda = \lim_{\Delta n_a \rightarrow 0} \frac{\lambda_{\text{peak2}}(n_a + \Delta n_a) - \lambda_{\text{peak1}}(n_a + \Delta n_a)}{\Delta n_a}, \quad (18)$$

I find spectral sensitivity of 1.4×10^4 nm RIU⁻¹. It is typically a safe assumption that a 0.1 nm change in the position of a resonance peak can be detected reliably, which results in a sensor resolution of 7.2×10^{-6} RIU, which is, to my knowledge, the highest reported spectral sensitivity of an aqueous fiber-based SPR sensor.

Finally, in Fig. 8b, I present the amplitude sensitivity of the proposed honeycomb PCF-based sensor as defined by (5). The maximal sensitivity is achieved at 1,009 nm and equals to 400 RIU⁻¹. It is typically a safe assumption that a 1% change in the transmitted intensity can be detected reliably, which leads to a sensor

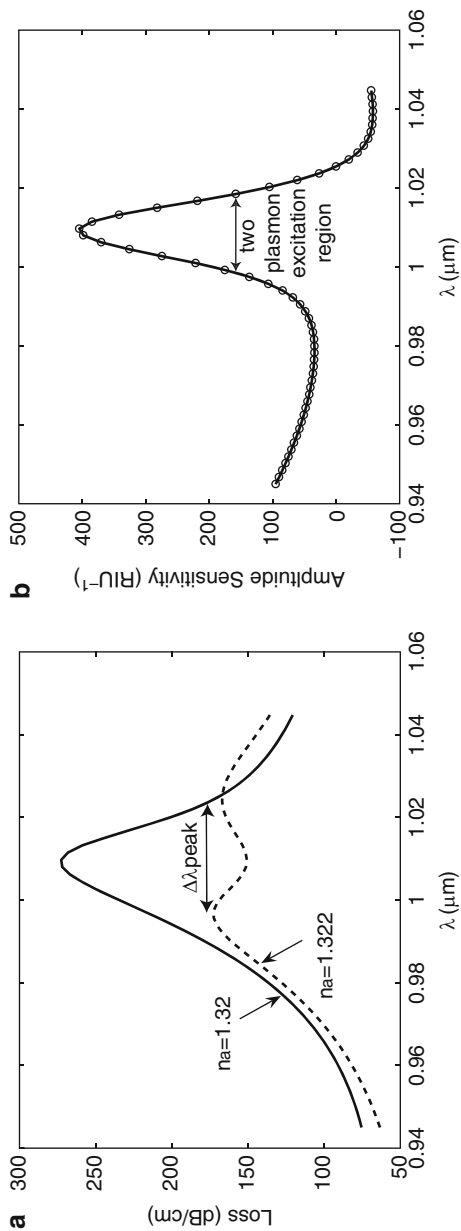


Fig. 8 Sensitivity of the honeycomb photonic crystal fiber-based SPR sensor. (a) The solid curve shows loss of the fundamental core mode near the degenerate phase-matching point with two plasmon modes and $n_a = 1.32$. Due to degeneracy, only one peak is distinguishable in the loss curve. Dashed line shows splitting of the degeneracy in plasmon modes when the analyte's refractive index is changed to $n_a = 1.322$ (b) Dependence of the sensor amplitude sensitivity on wavelength (after [19] © 2007 OSA)

resolution of 2.5×10^{-5} RIU. Note that the sensitivity curve for this sensor design has a single maximum, unlike the sensitivity curves associated with the Bragg fiber designs reported in the preceding section. The sensor length in this case is in 1 mm range.

5 Concluding Remarks

I have described theoretically photonic bandgap (PBG) fiber-based resonant optical sensors of analyte's refractive index. Particularly, I have considered two sensor types. One employed hollow-core photonic bandgap fibers, where core-guided mode is predominantly confined in the analyte-filled core. Another sensor type employed metallized photonic bandgap waveguides and fibers, where core-guided mode was phase-matched with a plasmon wave propagating at the fiber/analyte interface. Both sensor types described in this chapter showed strong resonant dependence of the fiber absorption on the value of the real part of analyte's refractive index, leading to the $10^{-6} - 10^{-4}$ RIU resolution in the real part of the aqueous analyte's refractive index.

References

1. Agranovich VM, Mills DL (1982) Surface polaritons – electromagnetic waves at surfaces and interfaces. North-Holland, Amsterdam
2. Al-Bader SJ, Imaar M (1993) Optical fiber hybrid-surface plasmon polaritons. *J Opt Soc Am B* 10:83–88
3. Alonso R, Subias J, Pelayo J, Villuendas F, Tornos J (1994) Single-mode optical fiber sensors and tunable wavelength filters based on the resonant excitation of metal-clad modes. *Appl Opt* 33:5197–5201
4. Argyros A, van Eijkelenborg MA, Large MCJ, Bassett IM (2006) Hollow-core microstructured polymer optical fiber. *Opt Lett* 31:172–174
5. Balasubramanian S, Sorokulova IB, Vodianov VJ, Simonian AL (2007) Lytic phage as a specific and selective probe for detection of *Staphylococcus aureus* – a surface plasmon resonance study. *Biosens Bioelectron* 22:948–955
6. Barkou SE, Broeng J, Bjarklev A (1999) Silica-air photonic crystal fiber design that permits waveguiding by a true photonic bandgap effect. *Opt Lett* 24:46–49
7. Charlton C, Temelkuran B, Dellemann G, Mizaikoff B (2005) Midinfrared sensors meet nanotechnology Trace gas sensing with quantum cascade lasers inside photonic band-gap hollow waveguides. *Appl Phys Lett* 86:194102
8. Cox FM, Arguros A, Large MCJ (2006) Liquid-filled hollow core microstructured polymer optical fiber. *Opt Express* 14:4135–4140
9. Ctyroky J, Abdelmalek F, Ecke W, Usbeck K (1999a) Modelling of the surface plasmon resonance waveguide sensor with Bragg grating. *Opt Quantum Electron* 31:927–941
10. Ctyroky J, Homola J, Lambeck PV, Musa S, Hoekstra HJWM, Harris RD, Wilkinson JS, Usievich B, Lyndin NM (1999b) Theory and modelling of optical waveguide sensors utilising surface plasmon resonance. *Sensors Actuators B Chem* 54:66–73

11. DeMarco DV, Lim DV (2001) Direct detection of *Escherichia coli* O157:H7 in unpasteurized apple juice with an evanescent wave sensor. *J Rapid Meth Automation Micro* 9:241–257
12. Diez A, Andres MV, Cruz JL (2001) In-line fiber-optic sensors based on the excitation of surface plasma modes in metal-coated tapered fibers. *Sensors Actuators B Chem* 73:95–99
13. Dostalek J, Ctyroky J, Homola J, Brynda E, Skalsky M, Nekvindova P, Spirkova J, Skvor J, Schrofel J (2001) Surface plasmon resonance biosensor based on integrated optical waveguide. *Sensors Actuators B Chem* 76:8–12
14. Fini JM (2004) Microstructure fibres for sensing in gases and liquids. *Meas Sci Technol* 15:1120–1128
15. Jensen JB, Hoiby PE, Emiliyanov G, Bang O, Pedersen LH, Bjarklev A (2005) Selective detection of antibodies in polymer microstructured optical fibers. *Opt Express* 13:5883–5889
16. Johnson SG, Ibanescu M, Skorobogatiy M, Weisberg O, Engeness TD, Soljacic M, Jacobs SA, Joannopoulos JD, Fink Y (2001) Low-loss asymptotically single-mode propagation in large core omniguided fibers. *Opt Express* 9:748–779
17. Jorgenson RC, Yee SS (1993) A fiber-optic chemical sensor based on surface plasmon resonance. *Sensors Actuators B Chem* 12:213–220
18. Gao Y, Guo N, Gauvreau B, Rajabian M, Skorobogata O, Pone E, Zabeida O, Martinu L, Dubois C, Skorobogatiy M (2006) Consecutive solvent evaporation and co-rolling techniques for polymer multilayer hollow fiber preform fabrication. *J Mater Res* 21:2246–2254
19. Gauvreau B, Hassani A, Fehri MF, Kabashin A, Skorobogatiy MA (2007) Photonic bandgap fiber-based Surface Plasmon Resonance sensors. *Opt Express* 15:11413–11426
20. Grigorenko AN, Nikitin P, Kabashin AV (1999) Phase jumps and interferometric surface plasmon resonance imaging. *Appl Phys Lett* 75:3917–3919
21. Gupta BD, Sharma AK (2005) Sensitivity evaluation of a multi-layered surface plasmon resonance-based fiber optic sensor: a theoretical study. *Sensors Actuators B Chem* 107:40–46
22. Harrington JA (2000) A review of IR transmitting hollow waveguides. *Fib Integr Opt* 19:211–227
23. Harris R, Wilkinson JS (1995) Waveguide surface plasmon resonance sensors. *Sensors Actuators B Chem* 29:261–267
24. Hassani A, Skorobogatiy M (2006) Design of the microstructured optical fiber-based surface plasmon resonance sensors with enhanced microfluidics. *Opt Express* 14:11616–11621
25. Homola J (1995) Optical fiber sensor based on surface plasmon resonance excitation. *Sensors Actuators B Chem* 29:401–405
26. Homola J, Slavik R, Ctyroky J (1997a) Interaction between fiber modes and surface plasmon wave spectral properties. *Opt Lett* 22:1403–1405
27. Homola J, Ctyroky J, Skalky M, Hradiliva J, Kolarova P (1997b) A surface plasmon resonance based integrated optical sensor. *Sensors Actuators B Chem* 39:286–296
28. Hoo YL, Jin W, Ho HL, Ju L, Wang DN (2005) Gas diffusion measurement using hollow-core photonic bandgap fiber. *Sensors Actuators B Chem* 105:183–186
29. Kabashin AV, Nikitin P (1998) Surface plasmon resonance interferometer for bio- and chemical-sensors. *Opt Commun* 150:5–8
30. Kim N, Park IS, Kim WY (2007) Salmonella detection with a direct binding optical grating coupler immunosensor. *Sensors Actuators B Chem* 121:606–615
31. Knight JC, Birks TA, Russell RSJ, Rarity JG (1998) Bragg scattering from an obliquely illuminated photonic crystal fiber. *Appl Opt* 37:449–452
32. Konorov SO, Zheltikov AM, Scalora M (2005a) Photonic crystal fiber as a multifunctional optical sensor and sample collector. *Opt Express* 13:3454–3459
33. Konorov SO, Fedotov AB, Zheltikov AM, Miles RB (2005b) Phase-matched four-wave mixing and sensing of water molecules by coherent anti-Stokes Raman scattering in large-core-area hollow photonic-crystal fibers. *J Opt Soc Am B* 22:2049–2053
34. Kretschmann E, Raether H (1968) Radiative decay of non radiative surface plasmons excited by light. *Z Naturforschung A* 23:2135–2142

35. Kuhlmeiy BT, Pathmanandavel K, McPhedran RC (2006) Multipole analysis of photonic crystal fibers with coated inclusions. *Opt Express* 14:10851–10864
36. Lavers CP, Wilkinson JS (1994) A waveguide-coupled surface-plasmon sensor for an aqueous environment. *Sensors Actuators B Chem* 22:475–481
37. Liedberg B, Nylander C, Lundstrom I (1983) Surface plasmon resonance for gas detection and biosensing. *Sensors Actuators B Chem* 4:299–304
38. McLean A (2003) Detection of hydrocarbon fuel spills using a distributed fiber-optic sensor. *Sensors Actuators A Phys* 109:60–67
39. Melendez JL, Carr R, Bartholomew DU, Kukanskis KA, Elkind J, Yee SS, Furlong CE, Woodbury RG (1996) A commercial solution for surface plasmon sensing. *Sensors Actuators B Chem* 35:212–216
40. Monzon-Hernandez D, Villatoro J, Talavera D, Luna-Moreno D (2004) Optical-fiber surface-plasmon resonance sensor with multiple resonance peaks. *Appl Opt* 43:1216–1220
41. Monzon-Hernandez D, Villatoro J (2006) High-resolution refractive index sensing by means of a multiple-peak surface plasmon resonance optical fiber sensor. *Sensors Actuators B Chem* 115:227–231
42. Murao T, Saitoh K, Koshiha M (2006) Design of air-guiding modified honeycomb photonic band-gap fibers for effectively single mode operation. *Opt Express* 14:2404–2412
43. Piliarik M, Homola J, Manikova Z, Ctyroky J (2003) Surface plasmon resonance based on a polarization-maintaining optical fiber. *Sensors Actuators B Chem* 90:236–242
44. Pone E, Dubois C, Dupuis A, Lacroix S, Skorobogatiy M (2006a) Fabrication of the hollow all-polymer Bragg fibers. In: *Proceedings of European Conference on Optical Communication (ECOC)*; We4.4.6, Cannes, France
45. Pone E, Dubois C, Gu N, Gao Y, Dupuis A, Boismenu F, Lacroix S, Skorobogatiy M (2006b) Drawing of the hollow all-polymer Bragg fibers. *Opt Express* 14:5838–5852
46. Russell PSTJ (2006) Photonic crystal fibers. *J Lightwave Technol* 24:4729–4749
47. Shepard JR, Danin-Poleg Y, Kashi Y, Walt DR (2005) Array-based binary analysis for bacterial typing. *Anal Chem* 77:319–326
48. Sheridan AK, Harris RD, Bartlett PN, Wilkinson JS (2004) Phase interrogation of an integrated optical SPR sensor. *Sensors Actuators B Chem* 97:114–121
49. Shi YW, Ito K, Matsuura Y, Miyagi M (2005) Multiwavelength laser light transmission of hollow optical fiber from the visible to the mid-infrared. *Opt Lett* 30:2867–2869
50. Skorobogatiy M (2005) Efficient anti-guiding of TE and TM polarizations in low index core waveguides without the need of omnidirectional reflector. *Opt Lett* 30:2991–2993
51. Skorobogatiy M, Kabashin A (2006a) Plasmon excitation by the Gaussian-like core mode of a photonic crystal waveguide. *Opt Express* 14:8419–8424
52. Skorobogatiy M, Kabashin A (2006b) Photon crystal waveguide-based surface plasmon resonance biosensor. *Appl Phys Lett* 89:211641
53. Smith CM, Venkataraman N, Gallagher MT, Müller D, West JA, Borrelli NF, Allan DC, Koch KW (2003) Low-loss hollow-core silica/air photonic bandgap fibre. *Nature* 424:657–659
54. Smolka S, Barth M, Benson O (2007) Highly efficient fluorescence sensing with hollow core photonic crystal fibers. *Opt Express* 15:12783–12791
55. Snyder AW, Love J (2008) *Optical waveguide theory*, 2nd edn. Springer, London
56. Suzuki H, Sugimoto M, Matsuiand Y, Kondoh J (2006) Fundamental characteristics of a dual-colour fibre optic SPR sensor. *Meas Sci Technol* 17:1547–1552
57. Temelkuran B, Hart SD, Benoit G, Joannopoulos JD, Fink Y (2002) Wavelength-scalable hollow optical fibres with large photonic bandgaps for CO₂ laser transmission. *Nature* 420:650–653
58. Trouillet A, Ronot-Trioli C, Veillas C, Gagnaire H (1996) Chemical sensing by surface plasmon resonance in a multimode optical fibre. *Pure Appl Opt* 5:227–237
59. Tubb AJC, Payne FP, Millington RB, Lowe CR (1997) Single-mode optical fibre surface plasma wave chemical sensor. *Sensors Actuators B Chem* 41:71–79

60. Vidal MB, Lopez R, Alegret S, Alonso-Chamarro J, Garces I, Mateo J (1993) Determination of probable alcohol yield in musts by means of an SPR optical sensor. *Sensors Actuators B Chem* 11:455–459
61. Vienne G, Xu Y, Jakobsen C, Deyerl HJ, Jensen J, Sorensen T, Hansen T, Huang Y, Terrel M, Lee R, Mortensen N, Broeng J, Simonsen H, Bjarklev A, Yariv A (2004) Ultra-large bandwidth hollow-core guiding in all-silica Bragg fibres with nano-supports. *Opt Express* 12:3500–3508
62. Watts H, Lowe C, Pollard-Knight D (1994) Optical biosensor for monitoring microbial cells. *Anal Chem* 66:2465–2470
63. Weiss MN, Srivastava R, Grogner H (1996) Experimental investigation of a surface plasmon-based integrated-optic humidity sensor. *Electron Lett* 32:842–843
64. Weisser M, Menges B, Mittler-Neher S (1999) Refractive index and thickness determination of monolayers by plasmons. *Sensors Actuators B Chem* 56:189–197
65. Zhang LM, Uttamchandani D (1988) Optical chemical sensing employing surface plasmon resonance. *Electron Lett* 23:1469–1470
66. Zourob M, Mohr S, Brown BJT, McDonnell FPR, MB GNJ (2005a) An integrated metal clad leaky waveguide sensor for detection of bacteria. *Anal Chem* 77:232–242
67. Zourob M, Mohr S, Brown BJT, Fielden PR, McDonnell MB, Goddard NJ (2005b) An integrated optical leaky waveguide sensor with electrically induced concentration system for the detection of bacteria. *Lab Chip* 5:1360–1365

Nanophotonic and Subwavelength Structures for Sensing and Biosensing

I. Abdulhalim

Abstract Nanophotonic structures exhibit a large variety of effects on the nanoscale that can be used for biosensing in a biochip format. The resonance nature of these structures then allows high sensitivity to analytes, gases, or other external index perturbations down to the order of 10^{-8} refractive index unit. In this chapter, several configurations of nanophotonic structures and their use for sensing are reviewed with special emphasis on grating-based resonant structures, metallic nanoparticle, and nano apertures.

Keywords Nanophotonics · Biosensors · Sensors · Surface plasmons · Surface enhanced effects · Metallic nanostructures

Contents

1	Introduction	74
2	The Sensing Mechanism Based on Evanescent Waves	78
3	Sensors Based on Resonances in Diffraction Grating Structures	81
3.1	The GMR as a Sensor and Tunable Filter	85
4	Sensing Based on Localized Surface Plasmons and Surface Enhanced Effects	89
4.1	Nano-Enhancement of Surface Plasmon Sensitivity (LSPR Technique)	89
4.2	Resonant Raman Effect and Surface Enhanced Raman Scattering	92
4.3	Surface-Enhanced Fluorescence	95
5	Metallic Nanoapertures as Sensors	97
6	Photonic Crystals for Biosensing	99
7	Concluding Remarks and Future Directions	100
	References	100

I. Abdulhalim

Department of Electrooptic Engineering, Ben Gurion University of the Negev, Beer Sheva 84104
e-mail: abdulhlm@bgu.ac.il

Abbreviations

ARC	Antireflection coating
ATR	Attenuated total reflection
CARS	Coherent anti-Stokes Raman scattering
CCD	Charge coupled device
DNA	Deoxyribonucleic acid
EOT	Enhanced optical transmission
GMR	Guided mode resonance
GWS	Guided wave structure
ITO	Indium tin oxide
LC	Liquid crystal
LSPR	Localized surface plasmon resonance
MR	Micro resonators
PBG	Photonic band gap
PC	Photonic crystal
PCF	Photonic crystal fibers
PL	Photoluminescence
RCWA	Rigorous coupled-wave approximation
RIU	Refractive index unit
RM	Resonant mirror
RRE	Resonant Raman effect
SEF	Surface-enhanced fluorescence
SERRS	Surface-enhanced resonance Raman spectroscopy
SERS	Surface-enhanced Raman scattering
SEW	Surface electromagnetic wave
SPR	Surface plasmon resonance
TE	Transverse electric
TIR	Total internal reflection
TM	Transverse magnetic
WG	Wave guide
WGM	Whispering-gallery modes

1 Introduction

The emerging field of nanophotonics deals with the technology and science that involves the interaction of light with material structures having fine details on the order of 100 nm or smaller. Such structures can appear in the form of nanoparticles having different shapes, nanowires, nanoholes, gratings with nanoslits, porous materials, and sculptured thin films. Photonic effects depend on the materials and the structure used, ranging from enhanced transmission through nano metallic

apertures, resonant reflection or transmission, surface plasmons resonance, surface-enhanced optical effects, such as Raman, fluorescence, and second harmonic generation. Nanophotonic applications have been growing in number and diversity recently due to the advancements in the fabrication possibilities in the nanoscale. The shrinkage of the design rule in the nanoelectronics industry is the main drive in this regard and it is anticipated to shrink down to 16 nm resolution by the year 2020, which would further advance the field by improving system integration. The increased resolution would lead to fabrication methods that are reliable, scalable, power-efficient, and cost-effective. Nanoscale component integration would be feasible, both from the top-down (e.g., fabrication on wafers) and from the bottom-up (e.g., building the system starting at the scale of atoms and molecules).

The field of sensing using optics and photonics has undergone extensive research during the last two decades due to the wide variety of effects and their applications in biology, medicine, environment, and industry for monitoring of parameters, such as temperature, concentration, pressure, and biochemical and biological entities [1]. Sensors based on surface plasmon resonance (SPR) are being used for monitoring fabrication processes of biochemical and pharmaceutical industries [2]. Fiber-based sensors [3] are being used in concrete for stress monitoring, in machinery and industrial areas for monitoring pressure and temperature over kilometers length-scale. Optoelectronic sensors are used for imaging, profiling, auto-focusing, and tracking. In the material side, metal nanoparticles, nanotubes, quantum dots, and porous materials are under extensive studies for biosensing applications due to their unique optical properties. Guided wave structures, such as planar waveguides and optical fibers allow optical sensing based on the interaction between the evanescent field outside the confinement region and the analyte to be sensed. Several important parameters define the quality of a sensor: (1) sensitivity, (2) specificity, and (3) reliability. In order to enhance the sensitivity, several techniques were developed such as the surface-enhanced optical effects near a metal nanoparticle [4], micro-resonators [5], resonant mirror waveguides [6], and other resonance effects in waveguides or other photonic structures [7]. Table 1 summarizes the most common nanophotonic structures and the effects associated with them upon which biosensing relies.

Extensive studies are going on by several research groups who are now exploring alternative strategies for optical biosensing and chemical sensing based on the

Table 1 The most common nanophotonic structures and the associated effects and measurands

Nanophotonic structure	Biosensing based effect	Measurands
Planar metal film on prism, waveguide or grating	SPR	Intensity, angle, phase, wavelength
Metal nanoparticles and nanoshells	LSPR, SERS, SEF	Intensity, angle, emission or scattering spectrum
Porous materials	LSPR, SERS, SEF, effective index variation	Intensity, angle, spectrum, reflectance
Nanoapertures	Enhanced transmission	Intensity, angle, wavelength
Photonic crystals	Resonant reflections, surface waves	Intensity, angle, wavelength, phase

extraordinary optical properties of nanoparticles made of noble metals. A new field of research called plasmonics has emerged which deals with the optics of metallic nanostructures. Nanoscale chemosensors and biosensors can be realized through shifts in the localized surface plasmon resonance (LSPR). An LSPR biosensor, based on LSPR spectroscopy, operates in a manner totally analogous to a SPR sensor by transducing small changes in the refractive index near a noble-metal surface into a measurable wavelength shift. In contrast to the conventional SPR technology, LSPR technology promises multiplexed, high-throughput screening platforms in a highly miniaturized format, requiring small volumes (e.g., attoliters) of analyte solutions. The sensitivity is a few orders of magnitudes better than that of the conventional SPR sensors without metallic nanostructures. In addition, LSPR technology does not require precise controls of the angle of incidence and the ambient temperature, both of which are necessary for the conventional SPR technology. As the measurements are noninvasive in nature, the LSPR platforms are ideal for *in vivo* quantification of chemical species and the monitoring of dynamic processes inside biological cells.

In addition to the LSPR phenomenon near metallic nanoparticles, other interesting effects arise such as the surface enhanced Raman scattering (SERS) and surface enhanced fluorescence (SEF). In SERS, Raman scattering from a compound (or ion) adsorbed on or even within a few Angstroms of a structured metal surface can be enhanced by a factor of 10^3 – 10^{14} compared to the case when it is in a solution. SERS is strongest on a silver surface, but is observable on gold and copper surfaces as well, and it is now known that the shape of the nanoparticle plays a crucial role in determining the enhancement factor. So far, the triangular–pyramid shape has been found to give the strongest enhancement. Electromagnetic simulations confirm that the electric field can be enhanced by factor of 10^3 and so the Raman signal is enhanced by a factor of 10^{12} , because it is proportional to the fourth power of the field while SEF signal can be enhanced by a factor of 10^6 .

Another interesting resonant structure is the newly introduced field of microresonators (MRs). In MRs, resonance in a transparent dielectric microresonator occurs when light, confined by TIR along the inside of the resonator surface, orbits near a recognition particle's surface and returns in phase after each revolution. The sensitivity is improved by several orders of magnitude due to the fact that the light interacts with the same analyte molecule captured by the recognition particle for several thousand times unlike single-pass techniques. The frequencies of the whispering gallery modes (WGMs), characterized by the number of wavelengths within an orbit, are extremely sensitive to added dielectric material on the recognition particle's surface. Just an atomic thickness can lead to a detectable shift of a specific resonance frequency [8]. Optical microresonators have attracted interest during the last few years in the biosensing community, due to (1) their small size requiring analyte solutions in nanoliter volumes, (2) high quality factors, and (3) unprecedented sensitivity. These tiny optical cavities, whose dimmers may vary from a few to several micrometers, deliver quality factors as large as 3×10^9 and beyond. Such enormously high quality factors represent unique performance characteristics: an extremely narrow resonant linewidth, long decay time, and a high energy

density. Optical microresonators have various types of shapes such as cylindrical, spherical, spheroidal/toroidal, and ring-like. The underlying principle is the provision of efficient energy transfer to the resonant circular TIR guided wave, representing the WGM, through the evanescent field of a guided wave or a TIR spot in the coupler. Efficient coupling occurs upon fulfillment of two main conditions: (1) phase synchronization, and (2) significant overlap of the WGM and the coupler mode. Different techniques have been demonstrated for coupling the light into the microresonators including the prism couplers, side-polished optical fiber-couplers, and “pigtailed” couplers utilizing angle-polished fiber tips in which a core-guided wave undergoes TIR.

Vollmer *et al.* [9] demonstrated the use of WGM microsphere biosensors for the detection of protein adsorption: the adsorption of a single layer of bovine serum albumin (BSA) caused the wavelength to shift by approximately 16 ppm. An optical microsphere resonator used for the detection of thrombin using aptamer as the recognition molecule delivered a detection limit on the order of 1 NIH Unit/ml (1 NIH unit of thrombin clots a standard fibrinogen solution in 15 s at 37°C) [10]. A multiplexed platform for DNA quantification was developed with two microsphere cavities evanescently coupled to the same single optical fiber, the sensitivity of this device being as high as 6 pg/mm² mass loading [11]. Boyd *et al.* [12] described the use of WGM disk microresonators for the detection of pathogens using selective recognition receptors, the devices being capable under optimum conditions of detecting as few as 100 molecules.

Another interesting resonant configuration is the resonant mirror (RM) waveguide sensor. The RM is effectively a prism coupler where the air gap has been replaced by a low-index dielectric layer. The RM device structure, usually consisting of a high-index substrate ($n = 1.72$), a thin low-index spacer (about 550 nm of silica), and a very thin monomode waveguiding layer (about 80 nm of Si₃N₄). The high-index resonant layer acts as both a waveguiding and sensing layer. Light incident above the critical angle on the substrate–spacer interface is coupled into the waveguiding layer via the evanescent field in the spacer, when the propagation constants in the substrate and waveguide match. For monochromatic light, this occurs over a very narrow range of incidence angles, typically spanning considerably less than 1°. Alternatively, it can be operated at a fixed incidence angle, and coupling occurs over a narrow range of wavelengths [13]. The RM sensor was developed for immunosensors (for example, the commercially available product IAsys from Affinity Sensors, a company in Cambridge, UK), as it is very sensitive to changes in the refractive index of the interfacial layer caused by the binding of macromolecules such as proteins to immobilized biorecognition species like antibodies [14].

Resonant grating waveguide structures (GWS) or guided mode resonance (GMR) structures have also been used for biosensing. They are very sensitive to the adsorption/desorption of molecules on the waveguide surface and to any change of refractive index of the medium covering the surface of the sensor chip. When the GMR structure is illuminated with an incident light beam, the diffracted light matches the guided-mode condition and interference with the zero-order beams

causes resonant reflection backwards. This happens at a specific wavelength and incidence angle of the incident beam at which the resonance condition is satisfied, whereby the rediffracted beam destructively interferes with the transmitted beam, so that the incident light beam is completely reflected [15–17].

Scattering from nonresonant grating structures is known to be highly sensitive to the grating parameters and to the layers surrounding the grating structure. This property is being used to optically monitor layers thickness, critical dimension, and overlay misregistration, which are crucial parameters to control the fabrication process in the nanoelectronic industry [18]. This field of optical metrology is now known as optical scatterometry. Recently, new investigations [19] showed that optical response of grating-based nanophotonic structures exhibited sensitivity to refractive index variations of an analyte embedded within and on top of the grating structure using the scatterometric approach in nonresonant regime.

2 The Sensing Mechanism Based on Evanescent Waves

Most of the optical sensing techniques are based on the existence of evanescent wave in the region where the analyte to be sensed is located. Examples are: TIR, ATR, SPR, fibers and waveguides, LSPR, microresonators, grating waveguide resonant structures, and resonant mirror sensors. Evanescent waves arise when there is a confinement region in which the majority of the optical density exists; however, outside this region a tail of the optical field exists forming the evanescent wave. Figure 1 shows a general schematic of the confinement region and the two bounding regions called substrate and cover or analyte.

The dielectric function of the structure may be written as:

$$\varepsilon = \begin{cases} n_w^2 & r \in V_w \\ n_{a,s}^2 & r \notin V_w \end{cases}, \quad (1)$$

where n_w , n_a , n_s are the refractive indices in the confinement (waveguide) region, the analyte (cover) region and the substrate region with V_w being the space volume

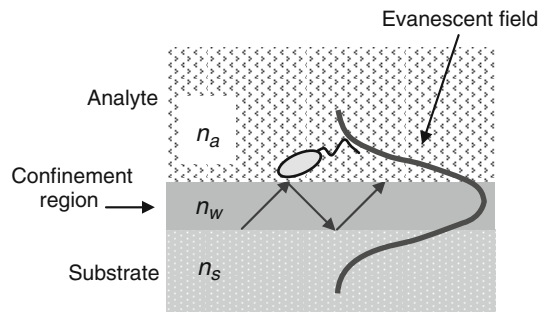


Fig. 1 Schematic of evanescent wave sensor based on planar optical waveguide

of the confinement region. Assuming a particle with refractive index n_p is added to the analyte and caused a variation $\delta\varepsilon = n_a^2 - n_p^2$ in the dielectric function of the analyte within the volume of the particle V_p . The wave equation before the addition of the particle is:

$$\nabla \times \nabla \times \vec{E}_i = k_i^2 \varepsilon \vec{E}_i \quad (2)$$

where \vec{E}_i and k_i are the electric field and the wave number before the addition of the particle. After the addition of the particle, the electric field, the dielectric function and the wave number changes to: \vec{E}_f , $\varepsilon_f = \varepsilon + \delta\varepsilon$, $k_f = k_i + \delta k$ so that the wave equation becomes:

$$\nabla \times \nabla \times \vec{E}_f = k_f^2 \varepsilon_f \vec{E}_f. \quad (3)$$

Multiplying by \vec{E}_i^* , subtracting (2) from (3) and integrating over the entire volume leads to:

$$(k_i^2 - k_f^2) \int \varepsilon \vec{E}_f \cdot \vec{E}_i^* dr = k_f^2 \int_{V_p} \vec{E}_i^* \delta\varepsilon \vec{E}_f dr. \quad (4)$$

Using first-order perturbation theory in δk , we get:

$$\delta k \approx \frac{k_i}{2} \frac{\int_{V_p} \delta\varepsilon \vec{E}_i^* \cdot \vec{E}_p dr}{\int_V \varepsilon \vec{E}_i^* \cdot \vec{E}_i dr}. \quad (5)$$

Hence, the dielectric perturbation in the evanescence region caused a shift in the guided wave number determined by the overlap integral normalized to the mode energy integral. This is the essence of evanescent wave sensing which can then be enhanced by enhancing the field or increasing the interaction volume. To demonstrate this, assume a single spherical dielectric particle is added; then, the electric field within the volume that the particle occupying is given by:

$$\vec{E}_p = \frac{3n_a^2}{2n_a^2 + n_p^2} \vec{E}_a. \quad (6)$$

Inserting this relation into (5) leads to:

$$\frac{\delta k}{k_i} \approx -\frac{3}{2} \times \frac{1 - (n_p/n_a)^2}{2 + (n_p/n_a)^2} v_p, \quad (7)$$

where v_p is the fractional volume of the particle relative to the interaction volume defined as the region where the field E_i extends. It should be noted that the ratio $\delta k/k_i$ can be identified with the relative change in the modal effective refractive

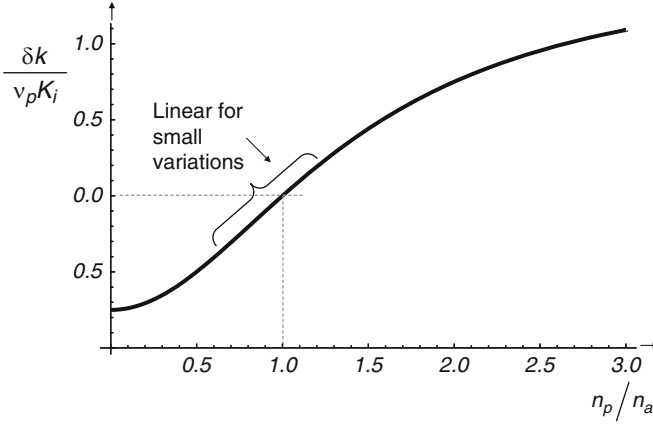


Fig. 2 Variation of the relative change in the modal effective refractive index versus the ratio of the particle index to the analyte index

index $\delta n_{\text{eff}}/n_{\text{eff}}$. Figure 2 shows the behavior of the relative change in the effective index with the ratio n_p/n_a in units of v_p . Note that when v_p is larger, that is, the field is localized near the particle, the modal effective refractive index variation becomes more sensitive to the particle's refractive index, a fact that might have some relation to the surface enhancement of optical effects near metallic nanoparticles. When the particle has a complex-valued dielectric constant $\epsilon_p = n_p^2$, then an enhanced shift is obtained when $\text{Re}\{2\epsilon_a + \epsilon_p\} = 0$, which again explains the enhanced sensing of metallic nanoparticles in the evanescent region.

The sensitivity of the evanescent wave sensors, in particular, the guided waves, is defined by:

$$S = \frac{\partial n_{\text{eff}}}{\partial n_a} \quad (8)$$

and the mode effective refractive index is a function of many parameters:

$$n_{\text{eff}} = f(n_a, n_w, n_s, n_0, n_1, d_g, d_w, \gamma_i, \lambda, \Lambda, l, \rho). \quad (9)$$

The additional parameters, $n_0, n_1, d_g, d_w, \gamma_i, \Lambda, \lambda, l$ and ρ , are respectively defined here as: the refractive indices of the two regions forming the rectangular grating in case of grating coupling, the grating height, the waveguide thickness, the incidence angle, the grating period, the wavelength, the mode number, and mode type with $\rho = 0$ for TE and $\rho = 1$ for TM. The equations describing the sensitivity of planar waveguides were derived by Tiefenthaler and Lukosz [20] for the three-layer waveguide and can be written as follows:

$$S = \frac{n_a \delta_a}{n_{\text{eff}} d_{\text{eff}}} \left[\frac{n_w^2 - n_{\text{eff}}^2}{n_w^2 - n_a^2} \right] \left[2 \frac{n_{\text{eff}}^2}{n_a^2} - 1 \right]^\rho, \quad (10)$$

where $d_{\text{eff}} = d_w + \delta_a + \delta_s$, an effective thickness with $\delta_{s,a}$ being the penetration depths in the substrate and analyte given by:

$$\delta_{s,a} = \frac{1 - \rho}{k\sqrt{n_{\text{eff}}^2 - n_{s,a}^2}} + \frac{\rho \left[(n_{\text{eff}}/n_w)^2 + (n_{\text{eff}}/n_{s,a})^2 - 1 \right]^{-1}}{k\sqrt{n_{\text{eff}}^2 - n_{s,a}^2}}. \quad (11)$$

This parameter defines the extent of the evanescent field inside the substrate or the analyte:

$$E_1(z) = E_1(z_{s,a}) \exp(-z/\delta_{s,a}) \quad (12)$$

with $z_{s,a}$ defining the waveguide–substrate or the waveguide–analyte interfaces. To determine the sensitivity to the analyte index from (10) the mode effective index has to be determined which is a function of n_a itself. Therefore, the sensitivity determination requires first a solution of the mode index dispersion relation determined by the phase matching condition:

$$l\pi = kd_w \sqrt{n_w^2 - n_{\text{eff}}^2} - \arctan \left[\left(\frac{n_w}{n_s} \right)^{2\rho} \left(\frac{n_{\text{eff}}^2 - n_s^2}{n_w^2 - n_{\text{eff}}^2} \right)^{0.5} \right] \\ - \arctan \left[\left(\frac{n_w}{n_s} \right)^{2\rho} \left(\frac{n_{\text{eff}}^2 - n_a^2}{n_w^2 - n_{\text{eff}}^2} \right)^{0.5} \right]. \quad (13)$$

The following consequences can be understood based on these analytic expressions:

- (a) When $n_a \approx n_w$, the analyte is part of the WG and the sensitivity is high.
- (b) When $n_a \approx n_{\text{eff}}$, the penetration depth in the analyte region is high and so the sensitivity is high.
- (c) When $n_a < n_s$, there exists a WG thickness just above the cutoff where the sensitivity is a maximum. At the cutoff $S = 0$, $n_{\text{eff}} = n_s$ because the energy is in the substrate.
- (d) When $n_a > n_s$, the maximum sensitivity is at the cutoff because the field is in the analyte and nothing in the substrate.
- (e) At large d_w , $S \rightarrow 0$ because the energy becomes confined in the waveguide.

3 Sensors Based on Resonances in Diffraction Grating Structures

Diffraction gratings are the basic building block for many photonic structures important for passive and active devices. They exhibit sharp resonances from 1902 called Wood anomalies [21]. There was a debate from 1902 on the nature

of their origin until the distinction between the resonant and nonresonant anomalies was first proposed in 1941 by Fano [22], who found that the former is because of the excitation of guided waves and the latter appearing when some diffraction order is being passed off. In 1965, Hessel and Oliner [23] proposed a phenomenological approach to resonant anomalies that introduces the poles and the zeros of the diffraction efficiency. The pole appears because of guided-wave excitation, which is a result of the solution of the homogeneous problem when a guided wave exists without an incident wave. This solution requires that the scattering matrix that links the diffracted- and the incident-field amplitudes has a zero determinant. In so far as the diffracted amplitudes are inversely proportional to this determinant, they have a singularity, i.e., a complex pole, which equals to the guided wave propagation constant. Because of energy-balance and continuity requirements, this pole must be accompanied by a zero of the amplitudes of the propagating diffraction orders. The values of the poles and the zeros are complex, and their positions in the complex plane depend on grating parameters but not on the angle of incidence. The phenomenological approach (as well as grating anomalies, in general) has been the subject of extensive studies. Several reviews [24, 25] can be found that describe this approach and show how to use its results for predicting the behavior of anomalies. Recently, the subject was again revived [15, 17, 26, 27] in connection with dielectric-grating anomalies when such gratings are used as narrow-band optical filters. In brief, when a waveguide mode is excited in a dielectric grating (usually a corrugated waveguide), the pole leads to a peak and the zero to a dip in the diffraction efficiency and, in particular, in the reflectivity and the transmittivity of the device. When the overall (nonresonant) reflectivity is low, the high (theoretically 100%) and narrow peak in the reflectivity can be used for spectral filtering [28, 29]. Since the propagation constants of the guided wave are polarization dependent, the position of the peak depends strongly on the polarization; thus, the filtering properties are polarization selective.

Guided-mode resonance (GMR) is a peculiar diffraction phenomenon of waveguide gratings with definite parameters and incident light conditions. It refers to a sharp peak in the diffraction efficiency spectrum of waveguide gratings. At resonance, efficient energy exchange between the reflected and transmitted waves occurs in small parameter ranges (for example, wavelength, angle of incidence, or refractive index). Physically, this is due to coupling of the externally propagating diffracted fields to the modes of the waveguide. For a subwavelength grating, the grating period is shorter than the incident wavelength, only the zero-order forward and backward diffracted waves propagate, while all higher-order waves are cut off. High reflection mirrors, filters, and polarization devices, which are widely used in the fields of lasers, optical communication and optoelectronics, can be realized by using the properties of high diffraction efficiency and narrow linewidth of GMR. Moreover, the applications of GMR in biology [30], sensors [31, 32], and medicine [33] have also attracted people's attention. There are many reports of theory and experiments on GMR, which prove the correctness of GMR as well as the feasibility of manufacture. Experimental results verifying the theoretically predicted high resonant efficiencies for reflection filters have also been reported in the millimeter

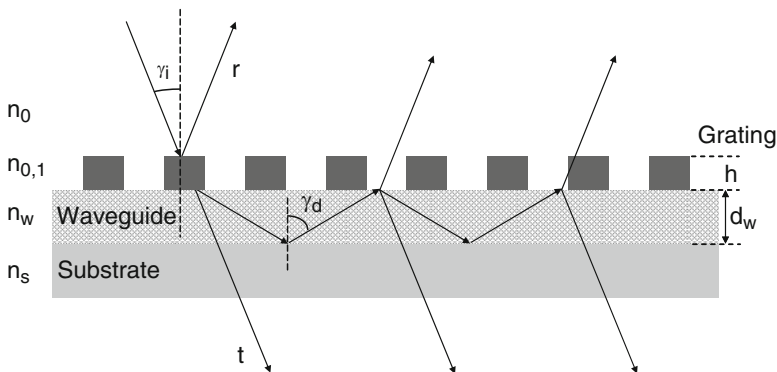


Fig. 3 Schematic of the guided wave resonant structure to elucidate the origin of the resonance in reflection

wave region [34] in the microwave region [35], in the near infrared region [124], and in the visible regions [15].

The basic structure of the GMR device is shown in Fig. 3, where the grating layer is on top of the waveguide layer and the top layer could be the analyte material filling both the spaces between the grating lines and the space above the gratings. A cavity is formed [36, 37] for the diffracted order and a reflection resonance is obtained when the phase difference between the transmitted and reflected waves is multiple of π . To show this, we start from the grating equation:

$$n_0 k \sin \gamma_i + mG = n_w k \sin \gamma_d, \quad (14)$$

where $G = 2\pi/\Lambda$, is the grating vector. When the diffracted beam of order m becomes a guided mode, the effective mode index is then given by:

$$n_{\text{eff}} = n_0 \sin \gamma_i + m\lambda/\Lambda. \quad (15)$$

The phase difference between the transmitted and reflected waves is:

$$\phi_{t-r} = \phi_{0-w} + \phi_{\text{TIR}} + 2\phi_{\text{diff}}, \quad (16)$$

where the phase difference due to pathlength difference is: $\phi_{0-w} = 2k_w d_w$ with $k_w = kn_w$ and the phase difference: $\phi_{\text{diff}} = \phi_{\text{Fresnel}} - \pi/2$ is that due to diffraction and Fresnel reflection at the interfaces. Substituting all this into (16) yields:

$$\phi_{t-r} = 2k_w d_w + \phi_{\text{TIR}} + 2\phi_{\text{Fresnel}} - \pi. \quad (17)$$

The guided wave condition is:

$$2k_w d_w + \phi_{\text{TIR}} + 2\phi_{\text{Fresnel}} = 2\pi l. \quad (18)$$

Combining (17) and (18) leads to:

$$\phi_{t-r} = \pi(2l - 1). \quad (19)$$

Hence, when the diffracted beam is a guided wave, destructive interference occurs between the transmitted and reflected beams leading to resonance in reflection.

The reflected resonant peak shape was shown by [38] to be a Lorentzian. The angular shape of the peak can be written as:

$$R = \frac{|\kappa_a/k|^2}{(n_0 \sin \gamma_i - n_0 \sin \gamma_{i\text{peak}})^2 + (\Gamma/k)^2}, \quad (20)$$

where κ_a represents a coupling constant and Γ is a loss parameter. Note that γ_i here is the incidence angle in the medium above the grating of index n_0 , while if the light is incident from air on this medium, then in terms of the incidence angle in air γ_a , the expression $n_0 \sin \gamma_i = \sin \gamma_a$ should be replaced with $\sin \gamma_a$. The peak location is determined by (15): $n_0 \sin \gamma_{i\text{peak}} = n_{\text{eff}} - m\lambda/\Lambda$, while the width at half the maximum is: $\Delta\gamma_i = (180/\pi)(\lambda\Gamma/(\pi \cos(\gamma_{i\text{peak}})))$. The spectral shape may be written as:

$$R = \frac{|\kappa_w|^2 (\Lambda\lambda_{\text{peak}}/2\pi)^2}{(\lambda - \lambda_{\text{peak}})^2 + \lambda^2 (\Lambda\Gamma/2\pi)^2}, \quad (21)$$

where the peak wavelength is determined by (15): $\lambda_{\text{peak}} = (n_{\text{eff}} - n_0 \sin \gamma_i)\Lambda/m$, while the spectral width is given by: $\Delta\lambda = (\lambda_{\text{peak}}\Lambda\Gamma/\pi)$. Note that $R=1$ when $\kappa_a = \kappa_w = \Gamma$.

The basic parameters for the design of GMR structure can be determined from the equations in the previous section particularly the peak position, shape, and width. The effective index however should be determined from the mode dispersion relation similar to the three layer WG problem described by (13). Since the grating layer is much thinner than a wavelength, it can be ignored and the results in this approach are obtained in good approximation. Alternatively, one can use more rigorous electromagnetic calculation such as the use of the eigen-functions approach, the rigorous coupled wave approximation (RCWA), the Fourier approach or the scattering matrix approach [38]. These approaches can give the resonance spectrum including absorption, exact value of the peak width and its dependence on the grating parameters. A less heavy approach uses the characteristic matrix approach where the grating layer is homogenized to a uniaxial thin film within the effective medium approximations. The 4×4 matrix approach can handle anisotropic layers and it was used recently by the present author [18] to show that the effective mode index calculated this way agrees very well with the rigorous approaches. In order to maximize the peak reflectivity, the grating period should be chosen less than the wavelength so that only the zero order is supported and the first-order diffraction exists in the waveguide (WG) ($m = 1$). The existence of higher modes will decrease the diffraction efficiency and pull part of the energy away into

the higher orders. Losses are a result of absorption, scattering due to imperfections particularly in the WG layer where the interaction region is large and due to imperfect collimation of the incident light beam. As a sensor, the WG index and thickness should be chosen so that the evanescent field extends more in the analyte region. In order to reduce the background reflection outside the resonance region, care should be taken to the design of the layers and perhaps the inclusion of antireflection coating (ARC) in between. As this is not so easy with the rigorous approaches due to the heavy numerical calculation, optimization can be done with thin film design software's or the use of the characteristic matrix approach with the grating film homogenized to uniform uniaxial film. Fine-tuning of the structure parameters can then be done with the rigorous calculation.

3.1 *The GMR as a Sensor and Tunable Filter*

There are several attractive properties of the GMR to be used both as a narrow filter and as a sensor: (1) planar geometry (2) made of standard dielectric materials (3) can be manufactured easily in mass production with Si fabrication technology on the wafer scale and used for multisensing functionality, (4) can be operated at normal incidence, (5) exhibits large sensitivity, at least comparable to the sensitivity of the planar WG sensor, and (6) can be operated both in spectral mode and in angular mode. Figure 4a shows the angular and spectral operation modes of the GMR device. In the angular mode, a single wavelength is used and a beam with a spread of angles, for example, the natural spread from a laser diode. The center of mass of the beam is detected using an array of detectors like a CCD camera. Any shift in the reflection resonant angle will affect the center of mass of the beam. In the spectral mode, a collimated beam is used containing a relatively wide spectral range and the spectrum is analyzed using a spectrometer. Alternatively a tunable source can be used for continuous scanning of the wavelength and a single pixel detector. In Fig. 4b, the normal incidence operation mode is illustrated which is usually preferable, in particular, when multisensing using an array of GMR structures is required. As can be seen from the grating equation, the spectral sensitivity is: $(\partial\lambda_{\text{peak}}/\partial n_a) = (\Lambda/m)(\partial n_{\text{eff}}/\partial n_a)$; therefore, we can conclude that the sensitivity is determined by the sensitivity of n_{eff} in a similar fashion to the sensitivity of a planar waveguide. The largest sensitivity is obtained for the first-order diffraction ($m=1$) and for larger Λ . Note that the sensitivity in the angular mode is slightly less because $\sin\gamma_i < \gamma_i$ except for small angles, where it becomes comparable. The combination of a colorimetric resonant grating and photonic crystal embedded in the plastic surfaces of microtiter plates (96-, 384-, and 1,536-well) has been developed by SRU Biosystems as a label-free, high-throughput, screening platform.

The sensor can detect a shift in wavelength as low as half a picometer. Binding interactions can be quantified with proteins, cells, and small molecules. Sensitivity is quoted in the 0.05 $\mu\text{g/ml}$ to 1 mg/ml range with molecular weights < 200 Da. Corning has also developed a label-free detection platform that contains resonant

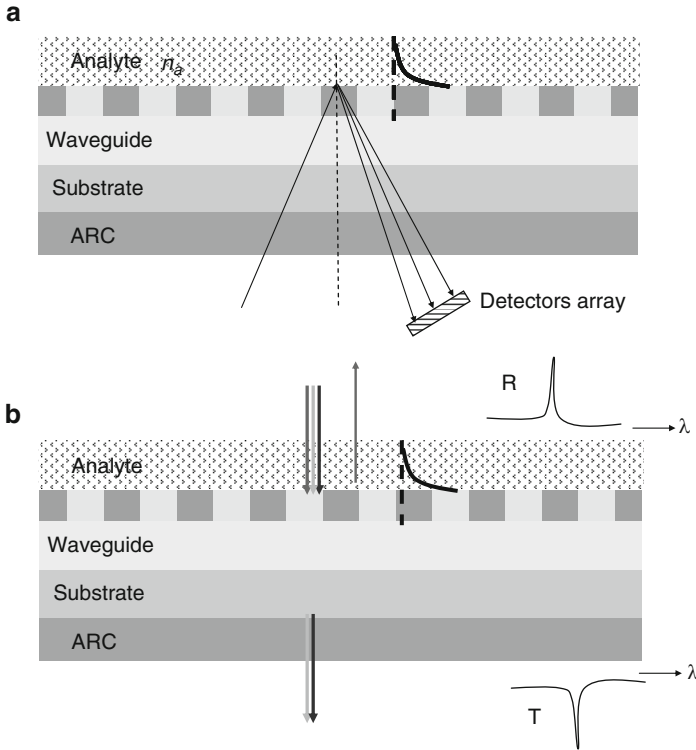


Fig. 4 Schematic of GMR structure as a biosensor in (a) the angular mode and (b) the spectral mode at normal incidence

GWS in the bottoms of 384-well microtiter plates. When illuminated with broadband light, the optical sensors inside each well reflect only a specific wavelength that is a sensitive function of the index of refraction close to the sensor surface. The platform has a sensitivity of 5 pg/mm^2 , which enables the detection of the binding of a 300-Da molecule to a 70-kDa immobilized molecule [29–31].

As an example of a design for water sensor operating at normal incidence, we considered a grating of pitch $\Lambda = 500 \text{ nm}$, having lines of height $h = 100 \text{ nm}$ and refractive index $n_1 = 3.6$, while the spaces are filled by the liquid analyte of index around $n_a = 1.33$ corresponding to water. The waveguide layer has a refractive index and thickness of $n_w = 1.6$ and $d_w = 500 \text{ nm}$, respectively. The sensitivity ($\partial n_{\text{eff}}/\partial n_a$) calculated from the slope is 0.21 for the TM₀ mode and 0.24 for the TE₀ mode, which is comparable to the maximum sensitivity reported for planar waveguides when $n_a < n_s$. The spectral sensitivity then equals: $\Lambda(\partial n_{\text{eff}}/\partial n_a) \approx 100 - 120 \text{ nm/RIU}$; hence, if the system minimum spectral detectability is 1 pm , one can measure refractive index variations of the order of 10^{-5} RIU . For analytes with $n_a > n_s$ and thin waveguide layer, the sensitivity can be enhanced several times, as expected (Fig. 5).

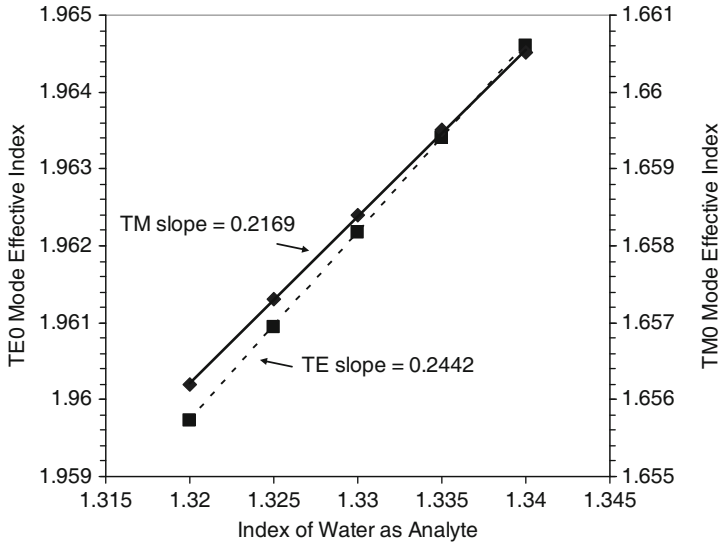


Fig. 5 Calculated sensitivity of water sensor for the zero-order modes. Parameters of the GMR structure are given in the text

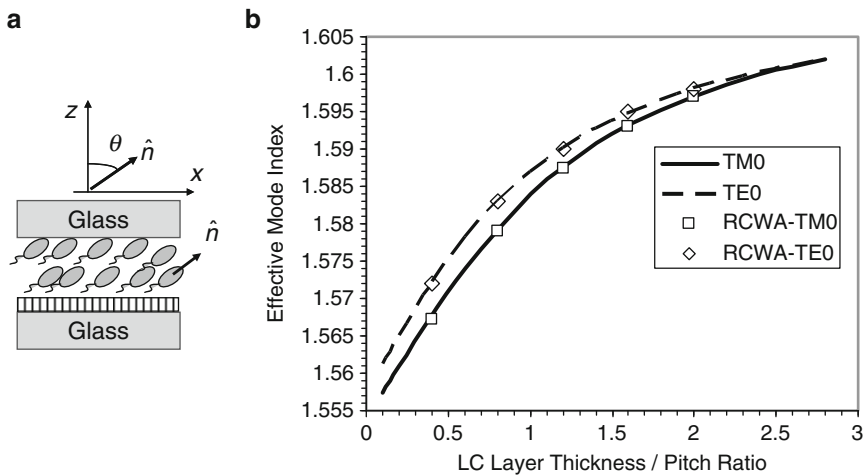


Fig. 6 (a) Schematic of GMR structure with the LC layer acting as the waveguide layer on top of the grating sandwiched between two glass plates. (b) The effective mode index versus the normalized LC layer thickness calculated both using the rigorous RCWA approach and using the analytic 4×4 matrix approach. Structure parameters are given in the text

One of the potential applications of the GMR structure is for tunable filtering and temperature sensing using a liquid crystal (LC) that exhibits large electro-optic and thermo-optic effects. In Fig. 6a, a simplified design is shown where the LC itself is the waveguide on top of the grating. The LC has the refractive indices and tilt angle:

$n_{\perp} = 1.611$, $n_{\parallel} = 1.830$ and $\theta = 90^{\circ}$. The grating refractive indices, height, and fill factor are: $n_H = 1.95$, $n_L = 1.6$, $d_g = 0.1\Lambda$ and $f = 0.5$.

Figure 6b shows comparison of calculated mode effective index using the analytic 4×4 matrix approach [18, 39] and using the rigorous coupled wave approach (RCWA) [40]. The agreement is excellent, hence confirming that it is possible to use the 4×4 matrix approach for the design of GMR structures.

One of the advantages of using liquid crystals is the possibility of tuning the resonance using an ac voltage of few volts applied between the two glass plates. The voltage causes rotation of the molecules towards the normal to the plates hence decreasing the tilt angle θ which in turn causes variation in the effective index. The resonance wavelength at normal incidence is given by $\lambda_{\text{peak}} = \Lambda n_{\text{eff}}$; hence for $\Lambda = 1,000$ nm, the wavelengths fall within the optical telecommunication window.

Figure 7 shows experimental results obtained from a grating structure on Si substrate with a liquid crystal layer on top of it and a voltage applied to the two substrates coated with thin ITO layers. The figure demonstrates tunability over the

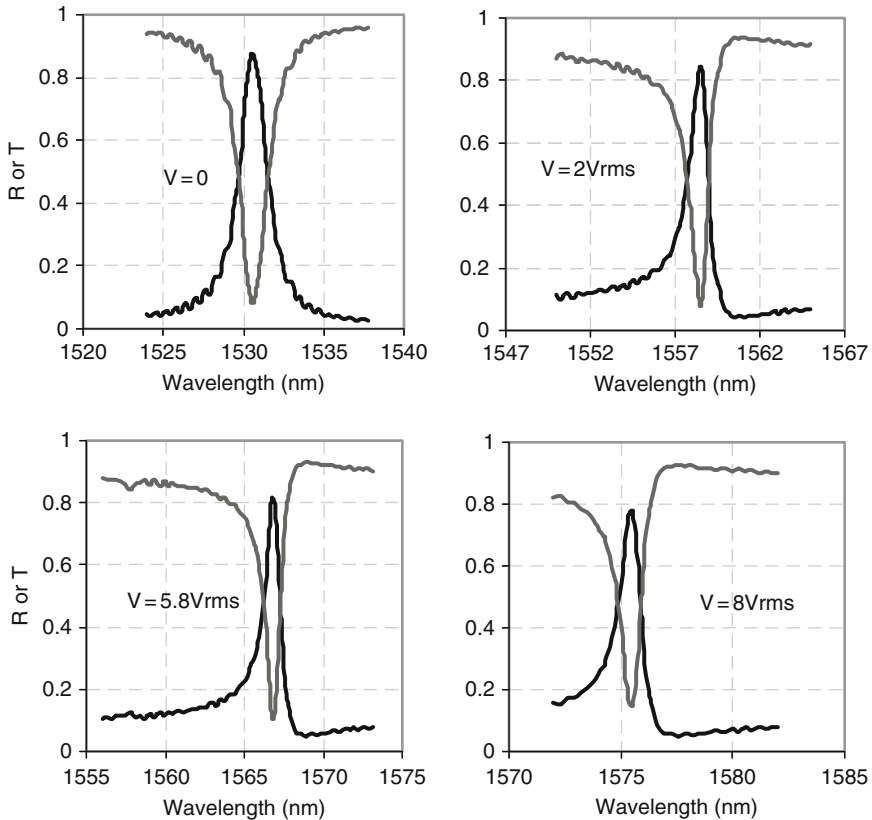


Fig. 7 Experimental reflectance (*peaks*) and transmittance (*dips*) from a guided mode resonant structure with liquid crystal layer used as the analyte and tuned with an applied voltage showing tunability of few tens of nm within less than 10 V on the LC layer

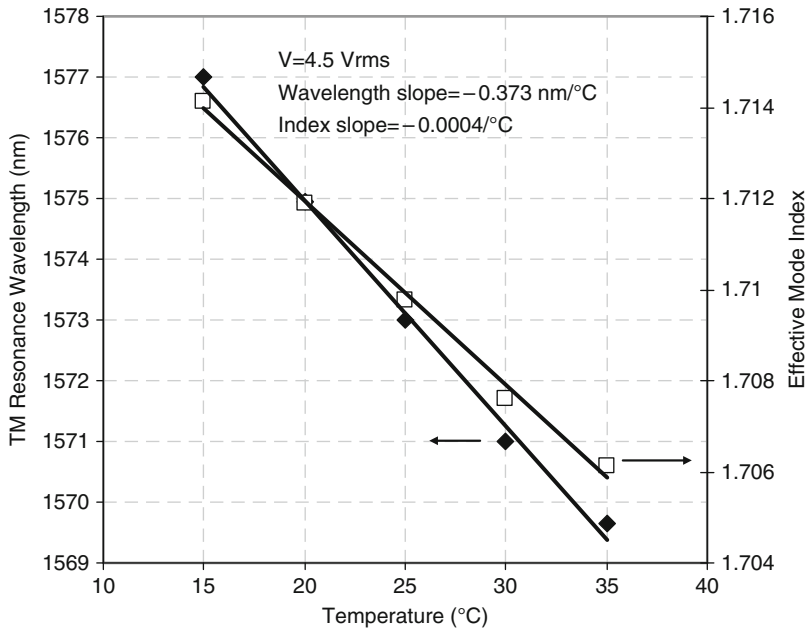


Fig. 8 Measured peak wavelength and effective mode index versus temperature showing linearity and high sensitivity. The sensitivity can be enhanced by more than an order of magnitude near the nematic to isotropic phase transition which is our case occurs at 101°C

C-band of the telecommunication window. The refractive index change for the tuning range of 40 nm is about 0.1; hence, the sensitivity is about 400 nm/RIU. This can be increased further by optimizing the waveguide thickness and grating parameters. Another potential application of the LC layer within the GMR structure is for temperature sensing because the LCs have high thermo-optic coefficient in particular near the phase transition to the isotropic liquid phase. In Fig. 8, we present measured peak wavelength versus temperature around room temperature. It can be shown that near the transition, the temperature sensitivity is of the order of 10 nm/°C, hence sensitivity to 0.0001°C, can be obtained.

4 Sensing Based on Localized Surface Plasmons and Surface Enhanced Effects

4.1 Nano-Enhancement of Surface Plasmon Sensitivity (LSPR Technique)

Several research groups are now exploring alternative strategies for optical biosensing and chemical sensing based on the extraordinary optical properties of

nanoparticles made of noble metals. Nanoscale chemosensors and biosensors can be realized through shifts in the localized SPR (LSPR) [41–45]. A LSPR biosensor, based on LSPR spectroscopy, operates in a manner totally analogous to a SPR sensor by transducing small changes in the refractive index near a noble-metal surface into a measurable wavelength shift as follows [46–48]:

$$\Delta\lambda_{\max} = m(n_{\text{adsorbate}} - n_{\text{blank}}) \left[1 - \exp\left(-\frac{2d_{\text{adsorbate}}}{l_d}\right) \right]. \quad (22)$$

Here, m is the refractive-index sensitivity of the sensor; $n_{\text{adsorbate}}$ and n_{blank} are the refractive indices of the adsorbate (i.e., analyte) and the bulk environment prior to the sensing event, respectively; $d_{\text{adsorbate}}$ is the effective thickness of the adsorbate layer; and l_d is the characteristic electromagnetic field decay length associated with the sensor.

The extinction coefficient within the Mie scattering theory for a spherical particle is given by:

$$\kappa = \frac{24\pi n_a r^3 \varepsilon_m^{3/2}}{\lambda \ln(10)} \left\{ \frac{\varepsilon_i}{(\varepsilon_r + \chi \varepsilon_m)^2 + \varepsilon_i^2} \right\}, \quad (23)$$

where n_a is the number of nanoparticles per unit area, r is their radius, $\varepsilon_{r,i}$ are the real and imaginary parts of the metal dielectric constant and ε_m is the dielectric constant of the surrounding medium. The parameter χ equals 2 for a sphere, but χ is larger than 2 for prolate spheroids ($L > S$) and less than 2 for oblate spheroids ($L < S$) where L and S are the semiaxis of the ellipsoid. For nonspherical particles the term outside the parenthesis in (7) will also be different. SPR greatly increases the local field experienced by a molecule adsorbed on the surface of the nanoparticle, when $\text{Re}\{\varepsilon_r(\omega) + \chi \varepsilon_m(\omega)\} = 0$. One can visualize this phenomenon by considering the nanoparticle as localizing the electric field of a dipole field centered in the sphere, which then decays with the dipole decay law away from the surface in all directions. When χ is greater than 2, the plasmon resonance condition $\text{Re}\{\varepsilon_r(\omega) + \chi \varepsilon_m(\omega)\} = 0$ is satisfied for a wavelength that lies to the red of that for a sphere (due to the fact that the real part of ε_i of metals is, according to (7), more negative for longer wavelengths). Of course, this also means that for oblate spheroids, the resonance is blueshifted relative to a sphere.

However, the resonance described here refers to an incident field with the electric field polarized parallel to the axis of symmetry of the spheroidal nanoparticle. There is another plasmon resonance associated with the incident electric field polarized perpendicular to the symmetry axis. This resonance is identical in frequency to the parallel resonance for a sphere, but it shifts in the opposite direction for a spheroid, i.e., blueshifting for prolate spheroids and redshifting for oblate spheroids. The parameter χ for the two cases of polarization parallel and perpendicular to the axis of the ellipsoid is given by [49]:

$$\chi_{\parallel} = \frac{2}{(\xi^2 - 1) \left[\xi \ln \left(\frac{\xi+1}{\xi-1} \right) - 2 \right]} - 1 \tag{24}$$

$$\chi_{\perp} = \frac{-2}{\xi(\xi^2 - 1) \ln \left(\frac{\xi+1}{\xi-1} \right) - 2\xi^2} - 1 \tag{25}$$

where $\xi = (1 - S^2/L^2)^{-1/2}$.

While the responses of the LSPR and SPR sensors can be described via the same equation, the sensitivities of the two techniques arise from different experimental parameters [50–53]. Figure 9 shows the resonances in the extinction coefficient of ellipsoidal silver particles calculated using (23)–(25) for long and short semiaxis around $L = 500$ nm and $S = 100$ nm showing the strong dependence of the resonances to the dimensions of the nanoparticle. This property might be useful for widening the resonance spectrum, thus allowing resonant enhancements of the local field and other related effects over a wide spectral excitation range.

Flat-surface SPR sensors have a large refractive-index sensitivity ($\sim 2 \times 10^6$ nm/RIU), which is the chief component of their overall sensitivity [54]. LSPR nanosensors have modest refractive-index sensitivity ($\sim 2 \times 10^2$ nm/RIU) [55], in contrast. Nevertheless, both types of sensors have approximately equivalent sensitivity for a given adsorbate. In addition to the difference in refractive-index sensitivity, the electromagnetic field decay length l_d is also different for SPR and LSPR sensors. SPR sensors have a decay length on the order of ~ 200 nm. For LSPR

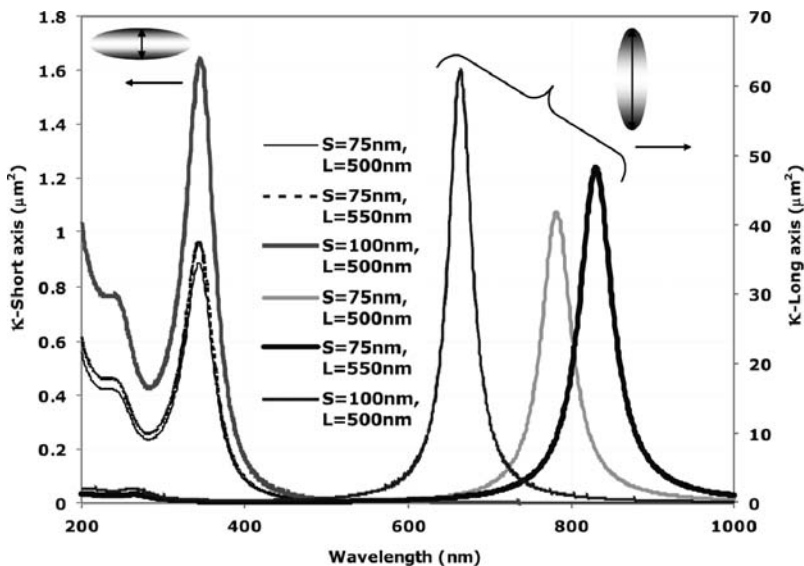


Fig. 9 Calculated extinction coefficient for silver ellipsoidal nanoparticles with different values of the semimajor and semiminor axis both for excitation along the major and the minor axis as indicated in the figure

nanosensors, using noble-metal nanoparticles, a much shorter electromagnetic field decay length (~ 6 nm) has been measured [56]. The shorter decay length is associated with the enhancement of the field near the metal, thus giving rise to a larger overall sensitivity of LSPR nanosensors.

In contrast to the conventional SPR technology, LSPR technology promises multiplexed, high-throughput screening platforms in a highly miniaturized format, requiring small volumes (e.g., attoliters) of analyte solutions. The sensitivity is a few orders of magnitudes better than that of the conventional SPR sensors without metallic nanostructures. In addition, LSPR technology does not require precise controls of the angle of incidence and the ambient temperature, both of which are necessary for the conventional SPR technology. As the measurements are noninvasive in nature, the LSPR platforms are ideal for *in vivo* quantification of chemical species and the monitoring of dynamic processes inside biological cells.

LSPR sensors can be divided into three broad groups: (1) those based on monitoring changes in the relative permittivity of the immediate environment, (2) those based on changes in SP coupling, and (3) those exploiting a combination of these two effects [57]. The first group of LSPR sensors were implemented for the detection of hexadecanethiol down to zeptomolar sensitivity by monitoring changes in the resonant Rayleigh scattering [58]. The second and the third groups were demonstrated for many chemical and biosensing applications by monitoring the changes in LSPR band of metal nanostructures upon analyte binding, using standard spectrophotometric instruments in the transmission mode [49]. The advantage of LSPR sensing in the transmission configuration over conventional SPR sensing is a simple experimental procedure that involves measurement just at one wavelength. This simplicity enables the development of disposable LSPR sensors for personal medicine and field applications.

4.2 Resonant Raman Effect and Surface Enhanced Raman Scattering

Four mechanisms are used to enhance the Raman signal [59–61, 62]: (1) stimulated Raman scattering due to the excitation of analyte molecules by a high energy pulse (optical electric field of strength $\sim 10^9$ V/cm); (2) coherent anti-Stokes Raman scattering (CARS) due to excitation with two strong collinear laser beams having frequency difference equal to the frequency of a Raman peak; (3) resonant Raman effect (RRE) caused by excitation with photon energies corresponding to resonant energies within the electronic spectrum of the analyte molecules; and (4) surface-enhanced Raman scattering, when the analyte molecules in close proximity (fraction of nanometers) of metallic nanoparticles are excited. The last two mechanisms are the ones that are mostly used for optical biosensing.

The RRE increases the intensity of some Raman-active vibrations by a factor of 10^2 – 10^5 . This effect occurs when the excitation-laser frequency is chosen in such a way that it crosses the frequencies of excited electronic states and resonates with

them. The enhancement factor increases when the molecular expansion along its axis of vibration is higher as it absorbs photons.

Formally, one can think of the Raman transition probability being proportional to the elements of the polarizability tensor of a bound electron; as the exciting frequency approaches the resonance frequency, these elements are enhanced in a Lorentz model of the bound electron. A common example of this mechanism is furnished by the ring-breathing (in-plane expansion) modes of porphyrins. Another mechanism, called vibronic enhancement, involves vibrations which couple two electronic excited states. In both mechanisms, the enhancement factors are nearly proportional to the intensities in the absorption spectrum of the adsorbate.

The enhancement does not begin at a sharply defined wavelength. In fact, enhancement by factor of 5–10 is usually observed if the wave number of the exciting laser is only within a few hundred cm^{-1} below the electronic-transition wave number of the analyte molecule.

SERS is the second relevant enhancement mechanism. The Raman scattering from a compound (or ion) adsorbed on or even within a few Angstroms of a structured metal surface can be enhanced by factor of 10^3 – 10^{14} compared to the case when it is in a solution. SERS is strongest on a silver surface [57–59, 62], but is observable on gold and copper surfaces as well, and it is now known that the shape of the nanoparticle plays a crucial role in determining the enhancement factor. So far, the triangular–pyramid shape has been found to give the strongest enhancement [62].

Although a complete understanding of SERS has not been achieved yet, two main mechanisms are widely accepted. The first, called chemical enhancement, involves enhancement of polarizability of the analyte molecule that may occur because of a charge-transfer effect or chemical bond formation between the metal surface and the analyte molecules.

The second is due to the enhanced electromagnetic field produced at the surface of the metal when the wavelength of the incident light matches the SPR wavelength of the metal. Molecules adsorbed or in close proximity to the metal surface experience an exceptionally large electric field. Because the Raman effect is proportional to the fourth power of the field amplitude, the efficiency is enhanced by factors as large as 10^{14} . Molecular vibrational modes normal to the metal surface are most strongly enhanced in comparison to other vibrational modes. Electromagnetic simulations confirm that the electric field can be enhanced [62, 63] by factor of 10^3 and so the Raman signal is enhanced by a factor of 10^{12} .

For a spherical nanoparticle whose radius is much smaller than the wavelength of light, the electric field is uniform across its dimensions, and the electrostatic (Rayleigh) approximation suffices to explain the enhancement. More generally, the field induced at the surface of an ellipsoidal nanoparticle (with major and minor semiaxes of lengths L and S) is related to the applied external field as:

$$\vec{E}_{\parallel, \perp\text{-induced}} = \left(\frac{\varepsilon_1(\omega) - \varepsilon_2(\omega)}{\varepsilon_1(\omega) + \chi_{\parallel, \perp} \varepsilon_2(\omega)} \right) \vec{E}_{\parallel, \perp\text{-laser}}, \quad (26)$$

where $\varepsilon_1(\omega)$ is the complex-valued, frequency-dependent, relative permittivity scalar of the metal, $\varepsilon_2(\omega)$ is that of the ambient material, ω is the angular frequency, and χ is a geometrical factor that depends on the shape of the nanoparticle depending on the incident polarization direction, where $\chi_{||}$ is for polarization parallel to the major axis and χ_{\perp} is for polarization along the minor axis of the ellipsoid. For a sphere: $\chi_{||} = \chi_{\perp} = 2$, but it is larger than 2 for prolate spheroids ($L > S$) and less than 2 for oblate spheroids ($L < S$).

SPR greatly increases the local field experienced by a molecule adsorbed on the surface of the nanoparticle, when $\text{Re}\{\varepsilon_1(\omega) + \chi\varepsilon_2(\omega)\} = 0$. One can visualize this phenomenon by considering the nanoparticle as localizing the electric field of a dipole field centered in the sphere, which then decays with the dipole decay law away from the surface in all directions. In this sense, the nanoparticle acts as an antenna which amplifies the intensity of the scattered light. The signal enhancement is so dramatic that very weak Raman peaks that are unnoticeable in spontaneous Raman spectra can appear prominently enough in SERS spectra. Some trace contaminants can also contribute additional peaks. Moreover, because of chemical interactions with metal surfaces, certain peaks that are strong in conventional Raman spectra might not be present in SERS spectra at all. The nonlinear character of signal intensity as a function of the concentration complicates things even further. Very careful consideration of all physical and chemical factors must be made while interpreting SERS spectra, which makes it extremely impractical.

Because of such complications, the surface-enhanced resonance Raman spectroscopy (SERRS) was developed. As it exploits the best features of both the SERS and the RRE, the resulting enhancement of the Raman signal intensity can be as high as 10^{14} . Additionally, SERRS spectra resemble regular RRE spectra, which make the former much easier to interpret.

SERS was discovered with pyridine. Other aromatic nitrogen- or oxygen-containing compounds, such as aromatic amines or phenols, also display strong enhancement due to SERS. The enhancement can also be seen with other electron-rich analytes such as carboxylic acids. Although SERS allows easy observation of Raman spectra from solutions with concentration in the micromolar (10^{-6}) range, slow adsorption kinetics and competitive adsorption limit its application in analytical chemistry.

The SPR intensity is dependent on many factors, including the wavelength of the incident light and the morphology of the metal surface. The Raman excitation wavelength should match the plasma wavelength of the metal, which is about 382 nm for a 5 μm silver particle but can be as high as 600 nm for larger ellipsoidal silver particles. The plasma wavelength shifts to 650 nm for copper and gold, the other two metals that are used for SERS at wavelengths in the range from 350 to 1,000 nm. The best modality for SPR excitation is the use of either a nanoparticle (<100 nm diameter) or an atomically rough surface.

SERS is used to study monolayers of materials adsorbed on metal substrates. Although the substrates are often used as electrodes, a wide variety of substrate formats have been found to exhibit SERS: electrochemically modified electrodes [64], colloids, island films, particles grafted on silanized glasses [65–67], and more

recently, regular particle arrays. Thin films of tilted nanorods of silver, grown by directing silver vapor obliquely at some planar surface, have been applied recently [68, 128] to virus detection as they exhibited SERS enhancement on the order of 10^8 . This type of nanorod assemblies falls into the category of sculptured thin films [69].

A pH sensor was reported recently [70] using SERS spectra of monolayers of *para*-mercaptobenzoic acid (pMBA) adsorbed on gold nanoshells. The pMBA molecule has a pH-sensitive SERS response. The developed all-optical nanosensor is capable of measuring pH in the vicinity of the molecule continuously over the 5.8–7.6 range at near-infrared wavelengths with accuracy better than 0.1 pH. Magnetic nanoparticles modulated by a rotating magnetic field were shown recently [71] to emit modulated fluorescence signals that may be used to detect analytes dissolved in water. A pH sensing possibility was shown to be possible from the blinking signal.

4.3 Surface-Enhanced Fluorescence

Surface-enhanced fluorescence (SEF) has been known for more than a few decades, [72], but its potential was rediscovered during the last decade due to the emerging developments in the field of optics of metallic nanostructures [73, 74]. SEF is fundamentally interesting because several effects play a role in it, and it can be achieved even with exciting photon energies far from the surface plasmon resonance (SPR). SEF is a very useful phenomenon, with significant applications in biotechnology [73] and life sciences, alongside surface-enhanced Raman scattering (SERS).

When a molecule is excited, there are a variety of processes which will return it to the ground state. If we consider three processes for returning to the ground state (radiationless energy loss, intersystem crossing through the triplet state, and emission of photons), then the efficiency of emission will be a function of the competing rates of these processes:

$$\eta = \frac{K_f}{K_f + K_i + K_x}, \quad (27)$$

where η is efficiency or quantum yield which is a dimensionless quantity given by the ratio between the emitted photon and the number of absorbed photons. The rate constants $K_{f,i,x}$ designate those for fluorescence emission, radiationless energy loss, and intersystem crossing, respectively. The average lifetime of the excited state is inversely related to the fluorescence emission rate: $\tau_f = K_f^{-1}$.

Surface enhanced fluorescence (SEF) takes place in the proximity of metal structures. The effect of fluorescence enhancement has been intensively studied by several groups [74]. In the proximity of metals, the fluorophore radiative properties are modified and an increase in the spontaneous emission rate is observed,

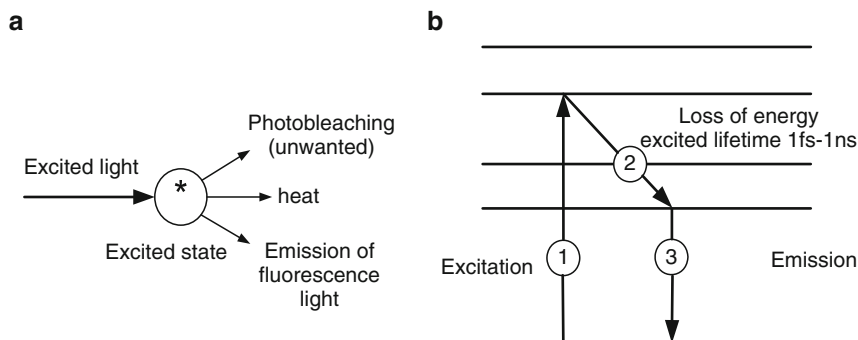


Fig. 10 Fluorescence effect: (a) molecule is excited by light, (b) Schematic explanation of excitation and emission processes, (1) excitation from the ground state, (2) decay to the nearest energy level and (3) photon emission via returning to the ground state

which is associated with a concomitant increase in the radiative quantum efficiency. This results from the shortening of the fluorescence lifetime, which enables faster cycling of the fluorophore. These are given by the following relationships:

$$\eta_{ns} = \frac{K_f + K_{ns}}{K_f + K_{ns} + K_i + K_x}, \quad (28)$$

$$\tau_{ns} = \frac{1}{K_f + K_{ns}}. \quad (29)$$

Here, η_{ns} is the quantum yield, modified by the nanostructure; k_f and k_i are rate constants as in (1); K_{ns} is the additional rate constant induced by the nanostructure; and τ_{ns} is the fluorophore lifetime modified by the nanostructures (Fig. 10).

Several physicochemical effects [75–82] related to the behavior of fluorophores near nanoparticles have been brought into focus by the emerging field of plasmonics. The effect of a surface near an oscillating dipole on its emission properties was first investigated by Chance et al. [72] in what is known now as the CPS theory. The most important consequences of this theory are as follows: (1) The reflected field from a nearby surface interferes with the emitted field and, therefore, can enhance or weaken the fluorescence, depending on the distance between the dipole and the surface. (2) When the nearby surface is reflective, the enhancement factor is larger. (3) Very near a reflective surface, the excited molecule may decay nonradiatively by coupling to lossy modes, surface plasmons, or guided waves. Depending on the nature of the nearby interface, this can cause quenching of the fluorescence when the molecule is touching the surface. (4) At small distances near a metallic surface, the lifetime decreases due to several competing relaxation processes. (5) Surface plasmon cross emission (SPCE) is one of the potential ways for SEF in which the excited surface plasmons couple back to the radiative electromagnetic (EM) mode on the back side of the metal film [83] (Kretschmann configuration or rough metal

surfaces). On top of these effects, localization of the electromagnetic field near nano tips, corners, holes, needles, etc., has been shown to enhance SEF by factors up to few hundreds in what is known as the lightning nanoantenna effect [84].

The quantum efficiency of the photoluminescence (PL) from a bulk noble metal is very low (typically, 10^{-10}). However, in a similar manner to LSPR and SERS, when fluorophores (fluorescent analyte molecules) are in close proximity to metal nanoparticles [85], the fluorescence intensity is enhanced and the fluorescence lifetime is lowered [86, 87, 125]. These surface-enhanced-fluorescence (SEF) effects occur because the excited fluorophores interact with freely mobile electrons in the metal, thereby resulting in increased rates of radiative decay; similar interactions with the LSPR have been the subject of theoretical analysis and are closely related to the SERS mechanisms [88–90]. The effect is now known as the lightning rod effect. SEF has been demonstrated on different fluorophores and suggested as a method to enhance *in vivo* imaging [91]. Enhancement of fluorescence has also been reported on nanoscale ZnO platforms [92]. A red shift for the PL maximum was observed with increasing aspect ratio of the gold nanorods and PL efficiency found to increase with the square of aspect ratio [93]. Rough metal surfaces can be regarded as an ensemble of randomly oriented hemispheroids of nanometer size, and SPR arising from them amplifies the local fields, thereby resulting in the enhancement of photoluminescence. It has been reported that quenching of luminescence occurs when metal nanoparticles are in close proximity to the fluorophores (dyes or semiconductor nanoparticles), whereas enhancement in luminescence is observed when metal nanoparticles are located farther away from the fluorophores [99]. The fluorophore emission intensity depends on the distance between the metal and the fluorophore in a complex fashion. At very close distances (less than several nm), the fluorophore experiences significant nonradiative decay components, and consequently, the emission is strongly quenched. At intermediate distances (e.g., for Ag around 5 nm), the nonradiative decay process subsides and the enhancement effect begins to dominate, producing the overall fluorescence amplification peak, which, for spherical metal nanoparticles, reaches a typical value in the order of 10. For longer distances (10 nm and above), the amplification tapers off, eventually reaching unity.

5 Metallic Nanoapertures as Sensors

Another important application of surface plasmons in nanophotonics is enhanced optical transmission through subwavelength apertures [94]. Usually, when light is transmitted through an aperture having lateral dimensions smaller than half the wavelength, the efficiency is extremely low (0.001 for a hole of 150 nm diameter). The light cannot propagate freely because transmission is possible only via the highly inefficient photon tunneling mechanism [95]. But when these apertures (holes or slits) are fabricated in a metal film, substantial enhancement of transmitted

light at resonant wavelengths could be achieved due to coupling of the incident light with surface plasmons. In the case of a metal film with a periodic array of nanoholes, light transmission much larger than that predicted by classical diffraction theory has been achieved. The enhanced transmission can be larger than normally expected through a large number of nanoholes, suggesting that even the photons impinging between the nanoholes can be transmitted. The incident light is diffracted by the nanoholes to produce evanescent waves [96]. The evanescent waves diffract while tunneling through the nanoholes, resulting in their interference with the incident waves. Although the exact origin of the EOT is not fully understood and still under investigation, the accepted view is that surface plasmons enhance the field associated with the evanescent waves, thereby resulting in the enhancement of the transmitted light intensity. Figure 11 shows theoretically calculated transmittance at normal incidence through nanoslits in silver on glass substrate. The slits are 45 nm wide, the thickness is 45 nm and the period is 450 nm. This structure was designed to operate in the visible range for water sensing. There are two types of peaks in the TM spectrum, one with high sensitivity on the order of 500 nm/RIU, while the other has no sensitivity. Note that in this case there is polarization dependence as the SPR can be excited only with TM waves although recent studies show that there is EOT also with TE waves. In the latter case, the EOT is explained as a result of interference and called cavity modes. To avoid the polarization dependence, two-dimensional gratings were used such as nanoholes in metals and their use for sensing using refractive index changes, absorption [126], SERS [97], or SEF [98]. The attractive features of the EOT-based sensors include (1) normal incidence operation (2) angular or spectroscopic

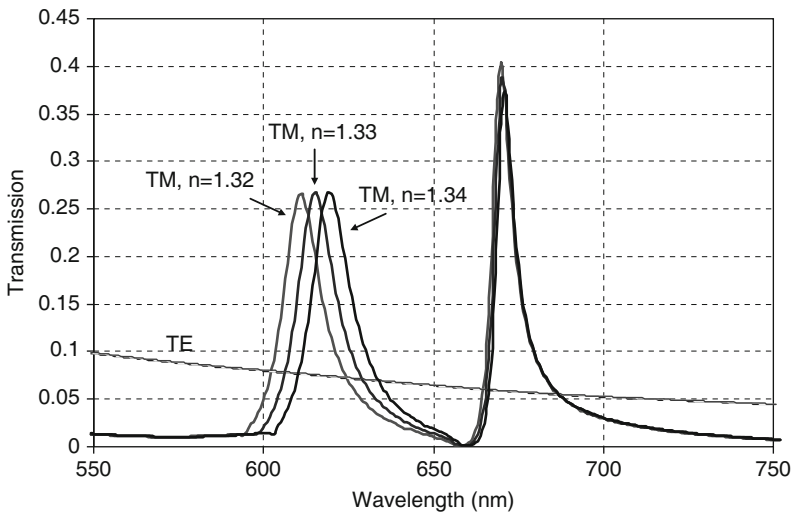


Fig. 11 Theoretical simulation of sensing action using EOT through nanoslits in silver calculated using the rigorous coupled-wave approach

modes of operation and (3) planarity that allows building biochips in a simple planar substrate [99, 127].

6 Photonic Crystals for Biosensing

Recently, a wide range of photonic crystal (PC) sensing devices has been presented in the literature [100, 101]. Photonic crystal fibers (PCF) constitute a class of PC devices that has been demonstrated for refractive index measurements and biosensing [102, 103]. However, these are difficult to implement in a compact, automated system and the fabrication of PCF sensors is rather tedious. So far, the biosensing presented by use of PCF's includes detection of fluorescently labeled objects like DNA and specific antibody detection. Sensors based on planar bulk PCs have also been presented for sensing and biosensing in particular [104]. Here, white light is incident perpendicular to the surface of the crystal and the reflected light is measured. This method has been presented for immobilized protein detection and detection of antibody/antigen multilayers with a reported detection limit of 500 ng/mm^2 . Components based on planar PCs, also referred to as planar PBG components, where the light is guided along defects such as missing rows of holes can be designed to obtain a very high and spatially selective sensitivity to changes in the RI of the surroundings, superior to the planar bulk devices. The sensing properties of PC-WGs have already been exploited for different simple parameters. Recent applications of PC-WGs include nanofluidic tuning, refractive index measurements, and optical characterization of molecule orientation [105, 106]. A PC-WG sensor was presented recently [107] for detection of protein concentrations. Concentrations around $10 \text{ }\mu\text{g/ml}$ ($0.15 \text{ }\mu\text{M}$) were measured with excellent signal-to-noise ratio, and a broad, dynamic refractive index sensing range extending from air to high viscous fluids.

Surface electromagnetic waves (SEWs) in PCs have also been used for sensing particularly in 1D PCs. They are excited at certain incidence and are sensitive to the layer adjacent to the surface [108–110]. Although it is possible to excite SEWs in PCs, coupling through a prism is preferable in order to observe them in measurable incidence angles (Fig. 12).

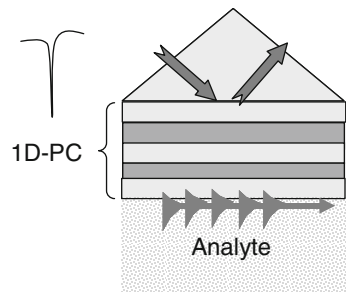


Fig. 12 Scheme for SEW's on PC's sensor

7 Concluding Remarks and Future Directions

Although a tremendous progress was achieved during the last few years in the field of nanophotonics and its biosensing applications, there is still a long way to go. Two very important advantages of nanophotonic structures are under extensive investigations: planarity for biochip development and specificity through the use of Raman and SEF techniques. These two properties will allow the buildup of highly sensitive biochips with specificity alongside with the vast developments in miniature fiber based spectrometers for portable and cheap system development. Surface biological modification is another important topic for specificity and for improving the detection limit as the interaction region is limited to half a wavelength from the surface. Hence, there is still a problem in the detection of biological entities larger than half the wavelength such as bacteria. This problem exists in all evanescent wave sensing schemes; however, with the SPR sensors case in the Kretschmann configuration, it was resolved by the long-range SPR configuration [111] and the use of longer wavelengths in the IR range [112]. The combination of nanophotonic structures with other sensing configurations, such as gratings [113], or nanolayer with high refractive index [114] on top of the metal layer in the Kretschmann configuration was shown to improve the sensitivity. Numerical solutions of Maxwell's equations in nanophotonic structures are at hand these days using commercially available software packages – tools that will help in designing new structures for better sensitivity.

The possibility of miniaturization and the use of optical beams for detection make nanophotonic structures suitable for medical analyte sensors for example to monitor the blood glucose level noninvasively. Another attractive configuration is to attach the nanophotonic structure to the distal end of an optical fiber for remote sensing such as in monitoring water quality.

Another emerging field is the field of nanoporous and sculptured thin films [69]. These films can be prepared in variety of forms: nanorods, nanosprings, nanoblades [115], etc., and from different metallic or dielectric materials. Their use for biosensing started to emerge using SERS [68, 116, 123, 128], SEF [117, 118], SPR [119] and other optical properties [120] showing a great potential as planar beds for biosensing that can be patterned for biochip buildup.

References

1. Abdulhalim I, Zourob M, Lakhtakia A (2007) Overview of optical biosensing techniques. In: Marks RS, Cullen DC, Karube I, Lowe CR, Weetall HH (eds) Handbook of biosensors and biochips. Wiley, New York
2. Abdulhalim I, Zourob M, Lakhtakia A (2008) Surface plasmon resonance for biosensing: a mini-review. *Electromagnetics* 28:214–241
3. Grattan LS, Meggett BT (eds) (2000) Optical fiber sensor technology: advanced applications – Bragg gratings and distributed sensors. Kluwer Academic, Boston

4. Genov DA, Sarychev AK, Shalaev VM, Wei A (2004a) Resonant field enhancements from metal nanoparticle arrays. *Nano Lett* 4:153–158
5. Matsko AB, Savchenkov AA, Strekalov D, Ilchenko VS, Maleki L (2005) Review of applications of whispering-gallery mode resonators in photonics and nonlinear optics, *IPN Progress Report* 42-162 August 15
6. Cush R, Cronin JM, Stewart WJ, Maule CH, Molloy J, Goddard NJ (1994) The resonant mirror: a novel optical biosensor for direct sensing of biomolecular interactions, Part I: Principle of operation and associated instrumentation. *Biosens Bioelectron* 8:347–354
7. Block ID, Chan LL, Cunningham BT (2006) Photonic crystal optical biosensor incorporating structured low-index porous dielectric. *Sensors Actuators B Chem* 120:187–193
8. Vahala K (ed) (2004) *Optical microcavities*. World Scientific, Singapore
9. Vollmer F, Braun D, Libchaber A, Khoshhsima M, Teraoka I, Arnold S (2002) Protein detection by optical shift of a resonant microcavity. *Appl Phys Lett* 80:4057–4059
10. Zhu H, Suter JD, White IM, Fan X (2006) Aptamer based microsphere biosensor for thrombin detection. *Sensors* 6:785–795
11. Vollmer F, Arnold S, Braun D, Teraoka I, Libchaber A (2003) Multiplexed DNA quantification by spectroscopic shift of two microsphere cavities. *Biophys J* 85:145–151
12. Boyd RW, Heebner JE (2001) Sensitive disk resonator photonic biosensor. *Appl Opt* 40:5742–5747
13. Goddard NJ, Pollard-Knight D, Maule CH (1994) Real-time biomolecular interaction analysis using the resonant mirror sensor. *Analyst* 119:583–588
14. Brecht A, Klotz A, Barzen C, Gauglitz G, Harris RD, Quigley GR, Wilkinson JS, Sztajn bok P, Abukensha R, Gascon J, Oubina A, Barcelo D (1998) Optical immunoprobe development for multiresidue monitoring in water. *Anal Chim Acta* 362:69–79
15. Abdulhalim I (2006) Anisotropic layers in waveguides for tuning and tunable filtering. *Proc SPIE* 6135:179–188
16. Sharon A, Rosenblatt D, Friesem AA, Weber HG, Engel H, Steingrueber R (1996) Light modulation with resonant grating-waveguide structures. *Opt Lett* 21:1564–1566
17. Sharon A, Rosenblatt D, Friesem AA (1997) Resonant grating-waveguide structures for visible and near-infrared radiation. *J Opt Soc Am A* 14:2985–2993
18. Abdulhalim I (2007) Simplified optical scatterometry for periodic nano-arrays in the quasi-static limit. *Appl Opt* 46:2219–2229
19. Abdulhalim I, Auslender M, Hava S (2007b) Resonant and scatterometric gratings based nano- photonic structures for biosensing. *J Nanophoton* 1:011680
20. Tiefenthaler K, Lukosz W (1989) Sensitivity of grating couplers as integrated optical chemical sensors. *J Opt Soc Am B* 6:209–220
21. Wood R (1902) On a remarkable case of uneven distribution of light in a diffraction grating spectrum. *Philos Mag* 4:396–402
22. Fano U (1941) The theory of anomalous diffraction gratings and of quasi-stationary waves on metallic surfaces (Sommerfeld's waves). *J Opt Soc Am A* 31:213–222
23. Hessel A, Oliner AA (1965) A new theory of Wood's anomalies on optical gratings. *Appl Opt* 4:1275–1297
24. Nevier M (1980) The homogeneous problem. In: Petit R (ed) *Electromagnetic theory of gratings*, Chap. 5. Springer, Berlin
25. Priambodo PS, Maldonado TA, Magnusson R (2003) Fabrication and characterization of high-quality waveguide-mode resonant optical filters. *Appl Phys Lett* 83:3248–3250
26. Norton SM, Morris GM, Erdogan T (1998) Experimental investigation of resonant-grating filter line shapes in comparison with theoretical models. *J Opt Soc Am A* 15:464–472
27. Tamir T, Zhang S (1997) Resonant scattering by multilayered dielectric gratings. *J Opt Soc Am A* 14:1607–1616
28. Magnusson R, Want SS (1992) New principles of optical filters. *Appl Phys Lett* 61:1022–1024

29. Peng S, Morris G (1996) Experimental demonstration of resonant anomalies in diffraction from two-dimensional gratings. *Opt Lett* 21:549–551
30. Wawro D, Tibuleac S, Magnusson R, Liu H (2000) Optical fiber endface biosensor based on resonances in dielectric waveguide gratings. *Proc SPIE* 39:86
31. Cunningham B, Li P, Lin B, Pepper J (2002) Colorimetric resonant reflection as a direct biochemical assay technique. *Sensors Actuators B Chem* 81:316–328
32. Wang JJ, Chen L, Kwan S, Liu F, Deng X (2005) Resonant grating filters as refractive index sensors for chemical and biological detections. *J Vac Sci Technol B* 23:3006–3010
33. Cooper MA (2002) Optical biosensors in drug discovery. *Nat Rev Drug Disc* 1:515–528
34. Meriakri VV, Nikitin IP, Parkhomenko MP (1996) Frequency-selective properties of modified dielectric gratings. *Int J Infrared Millimeter Waves* 17:769–1778
35. Magnusson R, Wang SS, Black TD, Sohn A (1994) Resonance properties of dielectric waveguide gratings: theory and experiments at 418 GHz. *IEEE Trans Antennas Propag* 42:567–569
36. Glasberg S, Sharon A, Rosenblat D, Friesem AA (1998) Spectral shifts and line shapes asymmetries in the resonant response of grating waveguide structures. *Opt Commun* 145:291–299
37. Rosenblatt D, Sharon A, Friesem AA (1997) Resonant grating waveguide structures. *IEEE J Quant Electron* 33:2038–2059
38. Nevier M, Popov E (2003) Light propagation in periodic media: differential theory and design. Marcel Dekker, New York
39. Abdulhalim I (1999) Analytic propagation matrix method for linear optics of arbitrary biaxial layered media. *J Opt A Pure Appl Opt* 1:646–653
40. Nevier M, Petit R, Cadilhac M (1973) Systematic study of resonances of holographic thin-film couplers. *Opt Commun* 9:48–53
41. Eck D, Helm CA, Wagner NJ, Vaynberg KA (2001) Plasmon resonance measurements of the adsorption and adsorption kinetics of a biopolymer onto gold nanocolloids. *Langmuir* 17:957–960
42. Haes AJ, Chang L, Klein WL, Van Duyne RP (2005) Detection of a biomarker for Alzheimer's disease from synthetic and clinical samples using a nanoscale optical biosensor. *J Am Chem Soc* 127:2264–2271
43. Nath N, Chilkoti A (2002) A colorimetric gold nanoparticle sensor to interrogate biomolecular interactions in real time on a surface. *Anal Chem* 74:504–509
44. Okamoto T, Yamaguchi I, Kobayashi T (2000) Local plasmon sensor with gold colloid monolayers deposited upon glass substrates. *Opt Lett* 25:372–374
45. Storhoff JJ, Lazarides AA, Mucic RC, Mirkin CA, Letsinger RL, Schatz GC (2000) What controls the optical properties of DNA-linked gold nanoparticle assemblies. *J Am Chem Soc* 122:4640–4650
46. Jung LS, Campbell CT, Chinowsky TM, Mar MN, Yee SS (1998) Quantitative interpretation of the response of surface plasmon resonance sensors to adsorbed films. *Langmuir* 14:5636–5648
47. Haes AJ, Van Duyne RP (2002) A nanoscale optical biosensor: sensitivity and selectivity of an approach based on the localized surface plasmon resonance spectroscopy of triangular silver nanoparticles. *J Am Chem Soc* 124:10596–10604
48. Haes AJ, Van Duyne RP (2002) A highly sensitive and selective surface-enhanced nanobiosensor. *Mater Res Soc Sympos Proc* 723:O.31
49. Hutter E, Pileni M-P (2003) Detection of DNA hybridization by gold nanoparticle enhanced transmission surface plasmon resonance spectroscopy. *J Phys Chem B* 107:6497–6499
50. Henglein A, Meisel D (1998) Spectrophotometric observations of the adsorption of organosulfur compounds on colloidal silver nanoparticles. *J Phys Chem B* 102:8364–8366
51. Hilger A, Cuppers N, Tenfelde M, Kreibitz U (2000) Surface and interface effects in the optical properties of silver nanoparticles. *Eur Phys J D* 10:115–118

52. Kalyuzhny G, Vaskevich A, Ashkenasy G, Shanzer A (2000) UV/Vis spectroscopy of metalloporphyrin and metallophthalocyanine monolayers self-assembled on ultrathin gold films. *J Phys Chem B* 104:8238–8344
53. Schuck P (1997) Use of surface plasmon resonance to probe the equilibrium and dynamic aspects of interactions between biological macromolecules. *Annu Rev Biophys Biomol Struct* 26:541–566
54. Homola J, Yee SS, Gauglitz G (1999) Surface plasmon resonance sensors: review. *Sensors Actuators B Chem* 54:3–15
55. Haes AJ, Van Duyne RP (2003) Nanoscale optical biosensors based on localized surface plasmon resonance spectroscopy. *Proc SPIE* 5221:47–58
56. Jung LS, Campbell CT, Chinowsky TM, Mar MN, Yee SS (1998) Quantitative interpretation of the response of surface plasmon resonance sensors to adsorbed films. *Langmuir* 14:5636–5648
57. Lahav M, Vaskevich A, Rubinstein I (2004) Biological sensing using transmission surface plasmon resonance spectroscopy. *Langmuir* 20:7365–7367
58. McFarland AD, Van Duyne RP (2003) Single silver nanoparticles as real-time optical sensors with zeptomole sensitivity. *Nano Lett* 3:1057–1062
59. Cotton TM, Kim J-H, Chumanov GD (2005) Application of surface-enhanced Raman spectroscopy to biological systems. *J Raman Spectrosc* 22:729–742
60. Kerker M (1991) Founding fathers of light scattering and surface enhanced Raman scattering. *Appl Opt* 30:4700–4705
61. Schatz GC, Van Duyne RP (2002) Electromagnetic mechanism of surface-enhanced spectroscopy. In: Chalmers MJ, Griffiths PR (eds) *Handbook of vibrational spectroscopy*. Wiley, Chichester, UK
62. Suchita Kalele A, Neha Tiwari R, Suresh Gosavi W, Sulabha Kulkarni K (2007) Plasmon-assisted photonics at the nanoscale, *Journal of Nanophotonics* 1:012501
63. Genov DA, Sarychev AK, Shalaev VM, Wei A (2004) Resonant field enhancements from metal nanoparticle arrays. *Nano Lett* 4:153–158
64. Shalaev VM (2000) *Nonlinear optics of random media*, Springer, Berlin
65. Jeanmaire DL, van Duyne RP (1977) Surface Raman spectroelectrochemistry, Part 1: Heterocyclic, aromatic, and aliphatic amines adsorbed on the anodized silver electrode. *J Electroanal Chem* 84:1–20
66. Jensen TR, Van Duyne RP, Johnson SA, Maroni VA (2000) Surface-enhanced infrared spectroscopy: a comparison of metal island films with discrete and nondiscrete surface plasmons. *Appl Spectrosc* 54:371–377
67. Willets KA, Van Duyne RP (2007) Localized surface plasmon resonance spectroscopy and sensing. *Ann Rev Phys Chem* 58:267–297
68. Yonzon CR, Stuart DA, Zhang X, McFarland AD, Haynes CL, Van Duyne RP (2005) Towards advanced chemical and biological nanosensors: an overview. *Talanta* 67:438–448
69. Shanmukh S, Jones L, Driskell J, Zhao Y, Dluhy R, Tripp RA (2006) Rapid and sensitive detection of respiratory virus molecular signatures using a silver nanorod array SERS substrate. *Nano Lett* 6:2630–2636
70. Lakhtakia A, Messier R (2005) *Sculptured thin films: nanoengineered morphology and optics*. SPIE Press, Bellingham, WA
71. Bishnoi SW, Rozell CJ, Levin CS, Gheith MK, Johnson BR, Johnson DH, Halas NJ (2006) All-optical nanoscale pH meter. *Nano Lett* 6:1687–1692
72. Roberts TG, Anker JN, Kopelman R (2005) Magnetically modulated optical nanoprobe (MagMOONs) for detection and measurement of biologically important ions against the natural background fluorescence of intracellular environments. *J Magn Magn Mater* 293:715–724
73. Chance RR, Prock A, Sylbey R (1978) Molecular fluorescence and energy transfer near interfaces. *Adv Chem Phys* 37:1–65
74. Aslan K, Gryczynski I, Malicka J, Malveeva E, Lakowics JR, Geddes CD (2005) Metal-enhanced fluorescence: an emerging tool in biotechnology. *Curr Opin Biotechnol* 16:55–62

75. Fort E, Gresillon S (2008) Surface enhanced fluorescence. *J Phys D Appl Phys* 41:013001
76. Lakowicz JR, Shen Y, D'Auria S, Malicka J, Fang J, Gryczynski Z, Gryczynski I (2002) Radiative decay engineering 2. effects of silver island films on fluorescence intensity, lifetimes, and resonance energy transfer. *Anal Biochem* 301:261–277
77. Javier DJ, Nitin N, Roblyer DM, Richards-Kortum R (2008) Metal-based nanorods as molecule-specific contrast agents for reflectance imaging in 3D tissues. *J Nanophoton* 2:023506
78. Goldys EM, Barnett A, Xie F, Drozdowicz-Tomsia K, Gryczynski I, Matveeva EG, Gryczynski Z, Shtoyko T (2007) Plasmon-enhanced fluorescence near metallic nanostructures: biochemical applications. *Appl Phys A* 89:265–271
79. Matveeva E, Gryczynski Z, Malicka J, Gryczynski I, Lakowicz JR (2004) Metal-enhanced fluorescence immunoassays using total internal reflection and silver island-coated surfaces. *Anal Biochem* 334:303–311
80. Tam F, Goodrich GP, Johnson BR, Halas NJ (2007) Plasmonic enhancement of molecular fluorescence. *Nano Lett* 7:496–501
81. Song JH, Atay T, Shi S, Urabe H, Nurmikko AV (2005) Large enhancement of fluorescence efficiency from CdSe/ZnS quantum dots induced by resonant coupling to spatially controlled surface plasmons. *Nano Lett* 5:1557–1561
82. Xie F, Baker MS, Goldys EM (2006) Homogeneous silver-coated nanoparticle substrates for enhanced fluorescence detection. *J Phys Chem B* 110:23085–23091
83. Zhang Y, Aslan K, Previte MJR, Geddes CD (2007) Metal-enhanced fluorescence from copper substrates. *Appl Phys Lett* 90:173116
84. Liebermann T, Knoll W (2000) Surface plasmon field-enhanced fluorescence spectroscopy. *Colloid Surf A* 171:115–130
85. Moskovits M (1985) Surface-enhanced spectroscopy. *Rev Mod Phys* 57:783–826
86. Lee I-YS, Suzuki H, Ito K, Yasuda Y (2004) Surface-enhanced fluorescence and reverse saturable absorption on silver nanoparticles. *J Phys Chem B* 108:19368–19372
87. Lakowicz JR (2001) Radiative decay engineering: biophysical and biomedical applications. *Anal Biochem* 298:1–24
88. Gryczynski I, Malicka J, Shen Y, Gryczynski Z, Lakowicz JR (2002) Multiphoton excitation of fluorescence near metallic particles: enhanced and localized excitation. *J Phys Chem B* 106:2191–2195
89. Yguerabide J, Yguerabide EE (1998) Light-scattering submicroscopic particles as highly fluorescent analogs and their use as tracer labels in clinical and biological applications, 1 Theory. *Anal Biochem* 262:137–156
90. Sokolov K, Chumanov G, Cotton TM (1998) Enhancement of molecular fluorescence near the surface of colloidal metal films. *Anal Chem* 70:3898–3905
91. Kummerlen J, Leitner A, Brunner H, Aussenegg FR, Wokaun A (1993) Enhanced dye fluorescence over silver island films: analysis of the distance dependence. *Mol Phys* 80:1031–1046
92. Malicka J, Gryczynski I, Geddes CD, Lakowicz JR (2003) Metal-enhanced emission from indocyanine green: a new approach to in vivo imaging. *J Biomed Opt* 8:472–478
93. Dorfman A, Kumar N, J-i H (2006) Highly sensitive biomolecular fluorescence detection using nanoscale ZnO platforms. *Langmuir* 22:4890–4895
94. Mohamed MB, Volkov VV, Link S, El-Sayed MB (2000) The 'lightening' gold nanorods: fluorescence enhancement of over a million compared to the gold metal. *Chem Phys Lett* 317:517–523
95. Barnes WL, Dereux A, Ebbesen TW (2003) Surface plasmon subwavelength optics. *Nature* 424:824–830
96. Dintinger J, Degiron A, Ebbesen TW (2005) Enhanced light transmission through subwavelength holes. *MRS Bull* 30:381–384
97. Degiron A, Ebbesen TW (2005) The role of localized surface plasmon modes in the enhanced transmission of periodic subwavelength apertures. *J Opt A Pure Appl Opt* 7: S90–S96

98. Brolo AG, Gordon R, Leathem B, Kavanagh KL (2004) Surface plasmon sensor based on the enhanced light transmission through arrays of nanoholes in gold films. *Langmuir* 20:4813–4815
99. Zhang J, Lakowicz JR (2005) Enhanced luminescence of phenyl-phenalthrindine dye on aggregated small silver nanoparticles. *J Phys Chem B* 109:8701–8706
100. Rigneault H, Capoulade J, Dintinger J, Wenger J, Bonod N, Popov E, Ebbesen TW, Lenne PF (2005) Enhancement of single molecule fluorescence detection in subwavelength apertures. *Phys Rev Lett* 95:117401
101. Lee K-L, Lee C-W, Wang W-S, Wei P-K (2007) Sensitive biosensor array using surface plasmon resonance on metallic nanoslits. *J Biomed Opt* 12:044023
102. Chow E, Grot A, Mirkarimi LW, Sigalas M, Girolami G (2003) Ultracompact biochemical sensor built with two-dimensional photonic crystal microcavity. *Opt Lett* 29:1093–1095
103. Erickson D, Rockwood T, Emery T, Scherer A, Psaltis D (2006) Nanofluidic tuning of photonic crystal circuits. *Opt Lett* 31:59–61
104. Fini JM (2004) Microstructure fibres for optical sensing in gases and liquids. *Meas Sci Technol* 15:1120–1128
105. Jensen JB, Pedersen LH, Hoiby PE, Nielsen LB, Folkenberg JR, Riishede J, Noordegraaf D, Nielsen K, Carlsen A, Bjarklev A (2004) Photonic crystal fiber based evanescent-wave sensor for detection of biomolecules in aqueous solution. *Opt Lett* 29:1974–1976
106. Chan LL, Cunningham BT, Li PY, Puff D (2007) Self-referenced assay method for photonic crystal biosensors: application to small molecule analytes. *Sensors Actuators B Chem* 120:392–398
107. Ferrini R, Martz J, Zuppiroli L, Wild B, Zabelin V, Dunbar LA, Houdre R, Mulot M, Anand S (2006) Planar photonic crystals infiltrated with liquid crystals: optical characterization of molecule orientation. *Opt Lett* 31:1238–1240
108. Topolancik J, Bhattacharya P, Sabarinathan J, Yu PC (2003) Fluid detection with photonic crystal-based multi channel waveguides. *Appl Phys Lett* 82:1143–1145
109. Skivesen N, Têtu A, Kristensen M, Kjems J, Frandsen LH, Borel PI (2007) Photonic-crystal waveguide biosensor. *Opt Express* 15:3169–3176
110. Meade RD, Brommer KD, Rappe AM, Joannopoulos JD (1991) Electromagnetic Bloch waves at the surface of a photonic crystal. *Phys Rev B* 44:10961–10964
111. Robertson WM, May MS (1999) Surface electromagnetic wave excitation on one-dimensional photonic band-gap arrays. *Appl Phys Lett* 74:1800–1802
112. Shinn M, Robertson WM (2005) Surface plasmon-like sensor based on surface electromagnetic waves in a photonic band-gap material. *Sensors Actuators B Chem* 105:360–364
113. Nennering GG, Tobisikab P, Homola J, Yee SS (2001) Long-range surface plasmons for high-resolution surface plasmon resonance sensors. *Sensors Actuators B Chem* 74:145–151
114. Lirtsman V, Ziblat R, Golosovsky M, Davidov D, Pogreb R, Sacks-Granek V, Rishpon J (2005) Surface-plasmon resonance with infrared excitation: studies of phospholipid membrane growth. *J Appl Phys* 98:093506
115. Alleyne CJ, Kirk AG, McPhedran RC, Nicorovici NAP, Maystre D (2007) Enhanced SPR sensitivity using periodic metallic structures. *Opt Express* 15:8163–8169
116. Lahav A, Auslender M, Abdulhalim I (2008) Sensitivity enhancement of guided wave surface plasmon resonance sensors. *Opt Lett* 33:2539–2541
117. Tang F, Parker T, Li H-F, Wang G-C, Lu T-M (2007) Unusual magnesium crystalline nanoblades grown by oblique angle vapor deposition. *J Nanosci Nanotechnol* 7:3239–3244
118. Suzuki M, Maekita W, Wada Y, Nakajima K, Kimura K, Fukuoka T, Mori Y (2006) In-line aligned and bottom-up Ag nanorods for surface-enhanced Raman spectroscopy. *Appl Phys Lett* 88:203121
119. Abdulhalim I, Karabchevsky A, Patzig C, Rauschenbach B, Fuhrmann B (2008) Comparative study of enhanced fluorescence from nano sculptured thin films. *Proc SPIE* 7041:70410G
120. Abdulhalim I, Karabchevsky A, Patzig C, Rauschenbach B, Fuhrmann B, Eltzov E, Marks RS, Xu J, Zhang F, Lakhtakia A (2009) Surface-enhanced fluorescence from metallic sculptured thin films with application to biosensing in water. *Appl Phys Lett* 94:063206

121. Abdulhalim I, Lakhtakia A, Lahav A, Zhang F, Xu J (2008) Porosity effect on surface plasmon resonance from metallic sculptured thin films. *Proc SPIE* 7041:70410C
122. Martin-Palma RJ, Torres-Costa V, Arroyo-Hernández M, Manso M, Pérez-Rigueiro J, Martínez-Duart JM (2004) Porous silicon multilayer stacks for optical biosensing applications. *Microelectron J* 35:45–48
123. Félidj N, Aubard J, Lévi G, Krenn JR, Salerno M, Schider G, Lamprecht B, Leitner A, Aussenegg FR (2002) Controlling the optical response of regular arrays of gold particles for surface-enhanced Raman scattering. *Phys Rev B* 65:075419
124. Popov E (1993) Light diffraction by relief gratings: a microscopic and macroscopic view. In: Wolf E (ed) *Progress in optics*, vol 31. Elsevier, Amsterdam, pp 139–187
125. Lakowicz JR, Shen Y, Gryczynski Z, D'Auria S, Gryczynski I (2001) Intrinsic fluorescence from DNA can be enhanced by metallic particles. *Biochem Biophys Res Commun* 286:875–879
126. Zhang J, Lakowicz JR (2005) Enhanced luminescence of phenyl-phenalthrindine dye on aggregated small silver nanoparticles. *J Phys Chem B* 109:8701–8706
127. Dintinger J, Klein S, Ebbesen TW (2006) Molecule-surface plasmon interactions in hole arrays: enhanced absorption, refractive index changes, and all-optical switching. *Adv Mater* 18:1267–1270
128. Brolo AG, Arctander E, Gordon R, Leathem B, Kavanagh KL (2004) Nano hole enhanced Raman scattering. *Nano Lett* 4:2015–2018
129. Zhao YP, Shanmukh SB, Dluhy RA (2006) Polarized surface enhanced Raman and absorbance spectra of aligned silver nanorod arrays. *J Phys Chem B* 110:3153–3157

Part II
Optical-Fiber Sensors

Fiber-Optic Chemical and Biosensors

Mahmoud El-Sherif

Abstract In the past 15 years, the fiber-optic communication industry has literally revolutionized the telecommunication industry by providing higher performance and more reliable telecommunication links. In parallel to these developments, and due to the high volume production of fiber-optic components at reasonable performance and costs, other industries associated with fiber optics have been developed like the sensors industry. As component prices have fallen and quality improvements have been made, the ability of fiber-optic sensors to displace conventional sensors have become a reality. A major category in fiber-optic sensors is the chemical and biosensors. These sensors can provide numerous advantages over conventional sensors. These advantages are higher performance, light weight, small and compact size, immunity to electromagnetic interference, remote sensing, ability to be multiplexed, and ability to be embedded into various structures and materials. The sensor's sensitivity and selectivity are enhanced by using optical transducers capable of precise detection of surround changes.

This chapter is prepared as an overview on fiber-optic chemical and biosensors. Because of the importance of intrinsic sensors with modified cladding structure, more attention is paid to this type of sensors. The introduction section is focused on some basics for fiber-optic sensors. The introduction is followed by a section on fiber-optic transducers and the transduction mechanisms, mainly absorption, fluorescence, Raman effect, and surface Plasmon effect. In Sect. 3, design guidelines for both extrinsic- and intrinsic-type sensors are presented. Because of the advantages of intrinsic-type sensors, a number of examples are presented and discussed. Sections 4 and 5 are on sensor development, processing, characterization, and optimization, focusing more on the modified cladding type. The manufacturing process is explained in detail and supported by examples on novel applications.

M. El-Sherif

Photonics Laboratories, Inc., 1117 Hillcrest Rd, Narberth PA 19072, USA
e-mail: melsherif@photonicslabs.com

One of the key components in sensor design is the detection technique used for monitoring the sensor output. In addition to the known detection techniques for monitoring of the light intensity, phase, wavelength and others, a new technique, which has recently been developed, based on monitoring the modal power distribution (MPD) and redistribution is presented in Sect. 6. It is based on recording the spatial (2D) intensity modulation (SIM), within the core of multimode fibers. The fundamentals and basic theories are presented as well as the methodology for sensors output measurements. At the end of Sect. 6, an example is presented on the development and successful application of the SIM technique for ammonia detection, which shows significant improvement in the sensor sensitivity in comparison to traditional intensity measurements.

To this end, this chapter is prepared to provide the academic knowledge base for senior and graduate students in the field of chemical and biosensors. Also, it is prepared for industrially qualified researchers for understanding the technology base in this field.

Keywords Fiber optic sensors · Chemical sensors · Biosensors · Evanescent field sensor · Intrinsic fiber optic sensors · Multimode fibers · Modal power analysis · Modal power distribution · Spatial intensity modulation · Optical far-field pattern

Contents

1	Introduction	112
2	Transducers and Transduction Mechanisms	115
2.1	Absorption	115
2.2	Fluorescence	119
2.3	Raman Scattering	120
2.4	Surface Plasmon Resonance	121
2.5	Extrinsic Sensors	123
2.6	Intrinsic Sensors	123
3	Sensors Development and Processing	127
3.1	Selection and Characterization of Chemical Sensitive Materials	127
3.2	Fiber Modification Process	131
4	Sensor Characterization and Optimization	133
4.1	Sensing HCl and NH ₃ Vapors	134
4.2	Sensing Hydrazine Vapor	135
4.3	Sensing DMMP Vapors	136
5	Spatial Intensity Modulation for Sensor Applications	138
5.1	Fundamentals and Basic Theories	139
5.2	Development of Sensor Components	142
5.3	Application of SIM in Chemical Sensors	144
6	Concluding Remarks	147
	References	147

Abbreviations

MPD	Modal power distribution
SIM	Spatial intensity modulation

2D	Two-dimensional
SM	Single mode
MM	Multimode
NA	Numerical aperture
CoCl ₂	Cobalt di-chloride
He-Ne	Helium neon
HCl	Hydrochloric acide
NH ₃	Ammonia
H ₄ N ₂	Hydrazine
H ₂ O ₂	Hydrogen peroxide
DMMP	Dimethyl-methyl phoshopnate
NDSA	Naphthalene-di sulphonic acid
ASQA	Anthraquinone di sulphonic acid
HF	Hydrofluoric acid
LED	Light-emitting diode

Symbols

α	Attenuation coefficient
I_o	Input optical power
I	Output optical power
L	Fiber length
n	Refractive index (n_{core} , n_{co} , n_{clad} , n_{mcl} , n_{cl} , $n_{complex}$, and n_{real})
θ	Acceptance angle
A	Absorbance
I_0	Light intensities transmitted in the absence of the analyte
I	Light intensities transmitted in the presence of the analyte
ε	Absorption coefficient
l	Optical path length
c	Concentration of the absorbing substance
I_{em}	Fluorescence intensity
I_{ex}	Intensity of excitation
ζ	Quantum efficiency of fluorescence
ε	Extension coefficient
k	Constant
c	Concentration of the fluorophore
Q	Quencher concentration
k	Stern-Volmer constant
I_0	Fluorescence intensity in the absence of the quencher
I	Fluorescence intensity in the presence of quencher
k	Imaginary component of the index related to the materials absorbance
R	Sensor response

1 Introduction

An optical fiber is a dielectric cylindrical waveguide, with a central core of transparent material (n_{core}) carrying most of the light energy, surrounded most of the time with a second layer of a slightly lower refractive index (n_{clad}) than the core, called cladding. There is a slight spill of light energy into this cladding layer known as the evanescent field, as shown in Fig. 1. The light is guided through the fiber as a result of total internal reflections on the core/cladding interface. The cladding layer is covered with a layer of a nonoptical material, for mechanical protection and handling.

There are two types of optical fibers: SM and MM fibers. The important parameters characterizing fiber properties are the core and cladding indices, core diameter, attenuation α , and numerical aperture (NA). The attenuation represents optical losses caused by absorption or scattering of light propagating through the fiber per unit length, as:

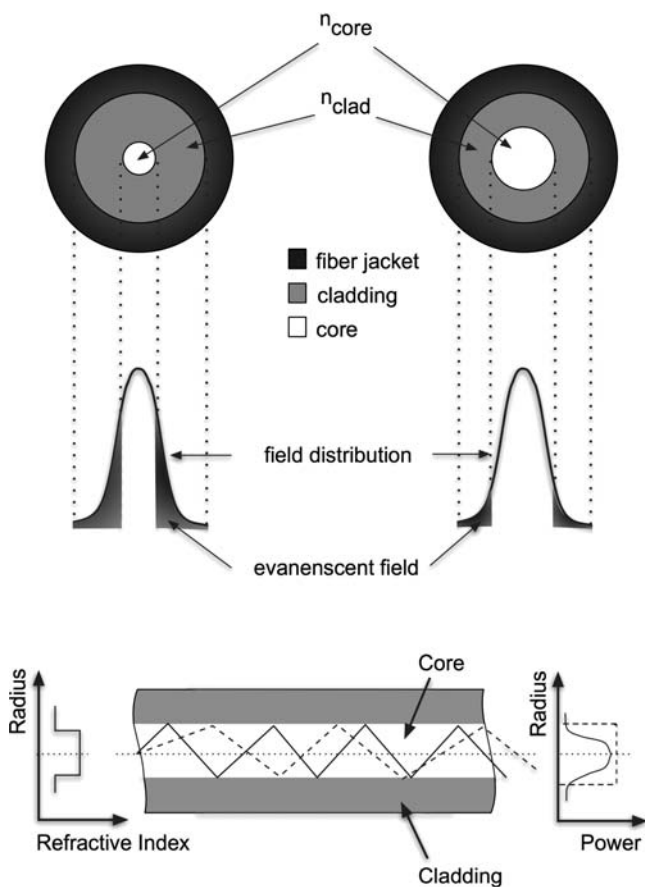


Fig. 1 Schematic structure and principles of optical fibers

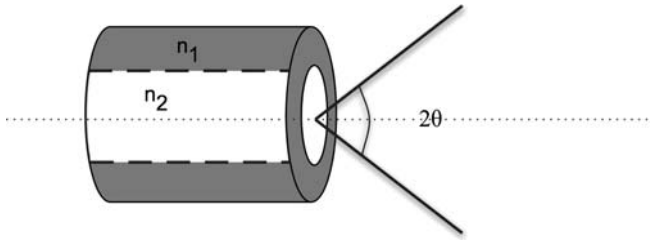


Fig. 2 Illustration of the fiber's numerical aperture

$$\alpha = 10/L \times \log(I_0/I), \quad (1)$$

where I_0 and I are the input and output optical powers, and L is the fiber length. The NA is a function of the core and cladding indices, as shown in Fig. 2, and given by:

$$\text{NA} = (n_{\text{core}}^2 - n_{\text{clad}}^2)^{1/2} = \sin\theta, \quad (2)$$

where θ is known as the light acceptance angle.

Optical fibers were originally designed for transmission of information in telecommunication systems for many years. Such fibers have to be protected from interference or the influence of surrounding environmental conditions.

In contrast to these standard communication fibers, some special fibers are employed not only for passive transmission of signals but also for the generation or processing of information, as in the case of fiber-optic sensors. The fiber can be modified from a passive to an active component or transducer. The function of a sensing fiber is to produce a sensitive response to changes in the fiber surroundings. Thus, advances in optical fibers led not only to their application in communication systems, but also to the realization that these fibers could carry the stimulus of various chemical and physical changes that take place in the vicinity of the fiber, giving way to novel sensing devices.

Fiber-optic sensors have been reported in literatures since 1970s. They have since then been used in chemical [1–4], biochemical [5–8], biomedical and environmental [9–12] sensors applications.

In general, fiber-optic chemical sensors are broadly classified into two categories: an extrinsic- and an intrinsic-type sensor, depending upon the role the optical fiber plays in the sensory device. In the extrinsic-type of sensors, the optical fiber is only used as a means of light transport to an external sensing system, i.e., the fiber structure is not modified in any way for the sensing function. Examples of extrinsic fiber-optic sensors include fibers terminated in active layers, e.g., optode [13], fibers having end face mirrors or fibers confronting other transducer elements or fibers [14]. An example of an extrinsic-type sensor is shown in Fig. 3. The intrinsic fiber-optic sensors differ from extrinsic sensors, where light does not have

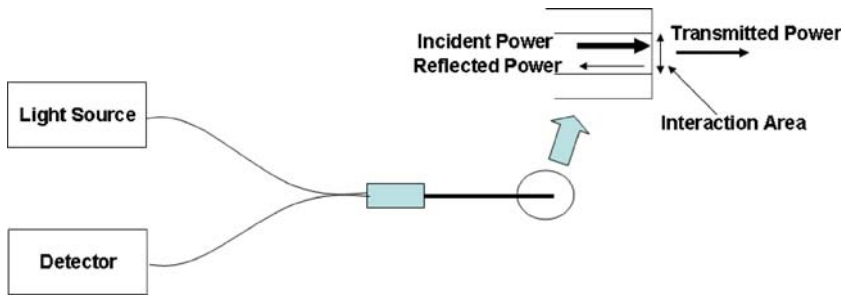


Fig. 3 Schematic diagram of an extrinsic-type sensor (optode)

to leave the optical fiber to perform the sensing function. In the intrinsic fiber-optic sensors, the optical fiber structure is modified and the fiber itself plays an active role in the sensing function.

Fiber modification can be achieved in many ways, such as coating with chemical sensitive materials. Coating represents an integral part of the sensor design, as it makes it possible to tailor the access of the analyte to the detection site. The choice of suitable coating, as a suitable transducer, is an important task in sensor designing. In some cases, a coating should be porous to a certain controllable degree for the penetration of analyte and interaction with the field of optical signals.

In general, fiber-optic sensors provide numerous advantages over conventional sensors, which include immunity to electromagnetic interference, small and compact size, remote sensing, ability to be multiplexed, and the ability to be embedded into various solid and flexible structures, including textiles and fabrics [15].

In sensor applications, the analyte generally modulates one or more of the following five optical properties of the signals propagating in the optical fiber:

- a. *Intensity or Amplitude*: The total intensity of light transmitted through the fiber changes upon interaction with the analyte. Sensors using intensity modulation generally use low-cost incoherent light sources, detectors, and other components, but have limited sensitivity.
- b. *Phase*: The phase of the light wave in the optical fiber changes upon interaction with the analyte. Sensors using phase modulation are interferometer sensors, generally requiring a high cost and stable coherent light sources, single mode, or sometimes polarization maintaining optical fiber. Phase application can be several orders of magnitude more sensitive than intensity-modulated sensors.
- c. *Polarization*: The analyte modulates the polarization of the light in the optical fiber. Polarization is normally used in fiber-optic current sensors. Such sensors require a polarized light and an analyzer at the sensor output for polarization rotation measurements.
- d. *Source Spectrum*: The analyte changes the optical spectrum of the light in the optical fiber. Such sensors require a broadband light source and spectrometer or an optical spectrum analyzer for measuring the changes in the spectral shape of the light.

- e. *SIM*: In MM fibers, the analyte modulates the modal power transmitted in each mode, i.e., the MPD, within the MM optical fibers, resulting in 2D SIM, across the fiber core cross section. This type of sensor is simple and highly sensitive, in comparison to total intensity modulation technique. Also, the sensors are generally inexpensive, because of the use of incoherent light source, and a regular photo-detection that is based on using one or two-dimensional array of photo-detectors. This technique has been developed recently and successfully tested in various sensors applications [16].

Both extrinsic- and intrinsic-type sensors incorporate a transducer element making it an active device. Extrinsic sensors have an external transducer, and the optical fiber just serves the purpose of a light carrier to and from the external transducer; whereas, intrinsic sensors have the structure of the optical fiber modified to incorporate the transducer element. In both cases, the transduction mechanisms change the light properties based on interaction with chemical species.

In this chapter, an overview on fiber-optic chemical and biosensors is presented focusing on transducers and transduction mechanisms, sensor design, sensor development and processing, and sensor characterization and optimization. A few examples are presented on chemical vapor detection and biosensing applications. At the end of the chapter, the theory and application of the newly developed detection technique, which is called the SIM technique, is presented.

2 Transducers and Transduction Mechanisms

There are several optical transduction mechanisms, used in fiber-optic sensors, by which chemical and biological species induce changes in the property of light in the optical fiber. There are four major transduction mechanisms namely, absorbance, fluorescence or chemical luminescence, Raman spectroscopy, and plasmon resonance. The chemical or biospecies can either directly interact with the light in the fiber giving rise to one of the above transduction mechanisms, or change the property of an intermediate sensing layer, which could be an electro-active polymer, an electro-active chromophore in a matrix, or sensitive dye which would in turn change the property of light. The four major transduction mechanisms are discussed next.

2.1 Absorption

Absorption of light is a process by which the energy of a photon is taken up by another entity. The concentration of the analyte is directly proportional to the absorbance “A,” which are related by the Beer–Lambert’s law as

$$A = \log \frac{I_0}{I} = \epsilon/c, \quad (3)$$

where I_0 and I are the light intensities transmitted in the absence and in the presence of the analyte, respectively; ϵ is the absorption coefficient, l is the optical path length and c is the concentration of the absorbing substance.

There are two ways in which the intensity of light in the optical fiber can be modulated by the analyte using absorption, (a) direct absorption by the analyte and (b) indirect absorption, where another material acts as a transducer, such as electro-active polymer or sensitive dye. The analyte interacts with this material layer changing its absorbance, and hence the intensity of light in the optical fiber.

2.1.1 Direct Absorption

Recent research in this area has largely been focused on pushing the wavelength range of this technique into the mid-infrared or the “chemical fingerprint” region of the electromagnetic spectrum. One of the areas in which this type of sensor has found applications is in situ gas diagnostics. The sensor consists of an optical MM fused silica fiber with jacket and cladding removed, and the bare fiber core is in direct contact with the surrounding molecules. Also, evanescent spectroscopic sensing design has also been applied in the area of biosensing for the detection of the *Escherichia coli* bacteria [17]. The sensor described below uses a cladding striped MM fiber as an intensity modulated sensor by evanescent absorption due to the existence of the bacteria.

Figure 4a, b shows a schematic drawing of the biosensor structure and set-up, respectively. The optical source is a 3-mW CW GaAlAs laser with graded-index MM fiber pigtail, emitting at 840 nm. The output fiber is spliced with a bidirectional optical-fiber coupler. Half of the emitted optical power propagates over the probe fiber (sensing element). The light modulated by the growing bacteria, shown in the SEM micrograph (Fig. 4c), exits the fiber and is detected by the photodiode Pd2. The other half of the optical power detected by the photodiode Pd1, form an electrical reference signal. Both electrical signals are amplified and measured by a two-channel calibrated optical-power meter. An AID board controlled by the LabVIEW software digitizes both output signals from the optical power meter by means of its IEEE-488 interface. The AID board collects 800 points per min of both sample and reference recording and storing the respective averages for a period of 24 h per measurement cycle. The developed sensor shows a sensitivity to as low as ten bacteria particles, and it is also calibrated for sensitivity from 10 to 800 bacteria.

2.1.2 Indirect Absorption

Indirect absorption is based on using another material (or medium) as the sensor transducer. The analyte interacts with this material changing its absorbance, and hence, the intensity of light interacting with this material.

Coating-based fibers are the largest class of indirect absorption sensors. In this design, a small section of the optical fiber passive cladding is replaced by an active

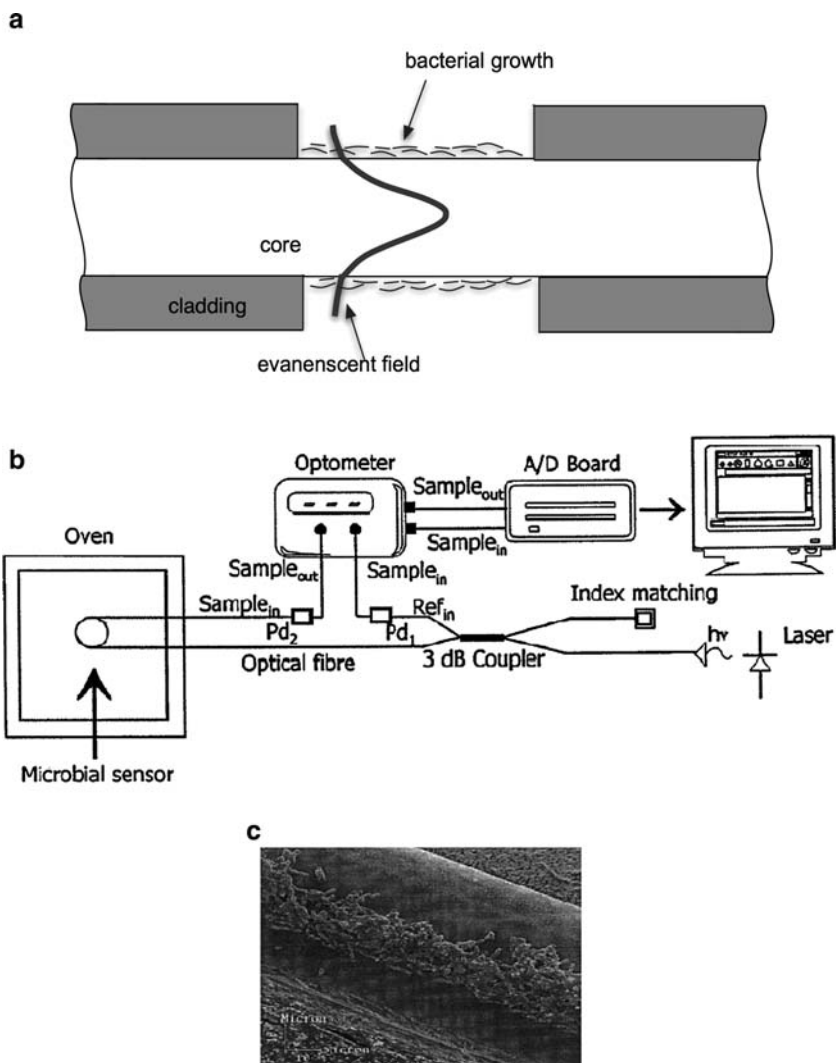


Fig. 4 Schematic diagram of the (a) biosensor structure, (b) the experimental set-up, and (c) the SEM of the growing bacteria [17]

coating or the fiber is immersed in a sensitive solution [18–20]. A coated section of a single fiber can be used as the sensing element (Fig. 5). Also, a pair of fibers oriented in parallel and close to each other, to allow coupling of light from one fiber to another through a chemical sensitive medium, can be used as the sensing element. The pair of parallel fibers can be twisted together to provide close proximity between the fibers without using spacers or fixation materials, as shown in Fig. 6 [18].

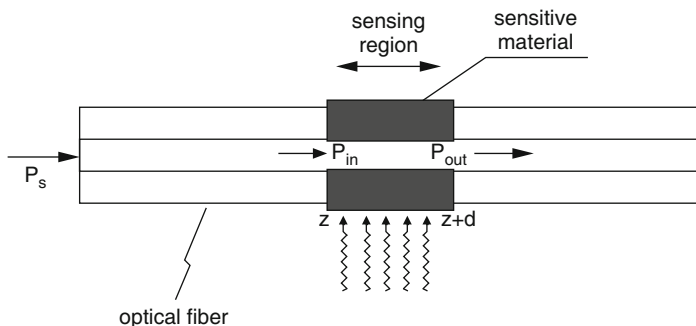


Fig. 5 A modified optical fiber for chemical sensor applications

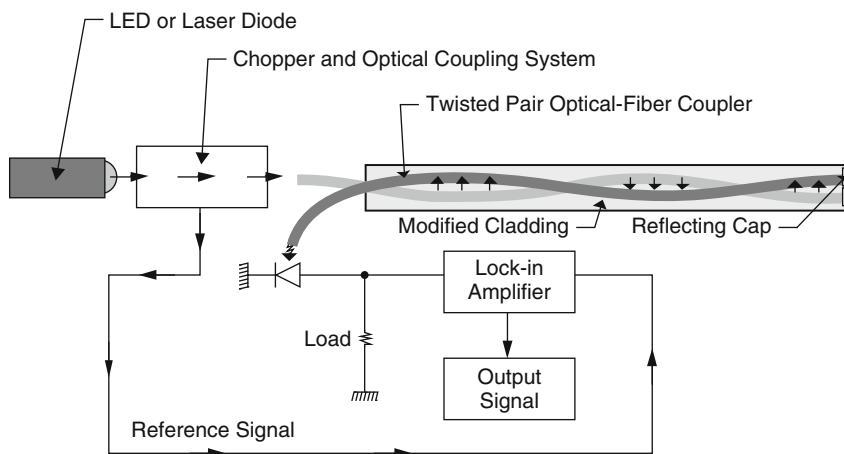


Fig. 6 A schematic diagram of a twisted pair sensing fibers with sensitive modified cladding as well as the sensor components for laboratories measurements

In the case of a modified single fiber, the analyte reacts with the coating to change the optical properties of the coating, i.e., refractive index, absorbance, fluorescence, etc. The changes in the optical property of the modified cladding will change the light transmission conditions through the optical fiber. This fiber sensor design has found numerous applications in chemical and biosensors applications [11, 19, 20]. One of the main chemical sensor designs is based on using electro-active material, such as organic conducting polymers, as the modified cladding. Organic conducting polymers (OCP's), such as polypyrrole, polyaniline, polythiophene, polyindoles, and polyacetylenes, however, have a unique ability to show a reversible change in their electrical resistance and optical properties when exposed to certain toxic vapors.

These conducting polymers are easy to prepare and show excellent ambient stability and very rapid and reversible absorption kinetics. They have, therefore, attracted much attention in the area of chemical and bio sensing. Extensive research

has been conducted on this class of fiber-optic sensors. This class is based on the modified cladding approach, where the passive cladding of the optical fiber is removed from a small section and replaced by a chemo-chromic material [19–22]. This type of sensors will be discussed in detail, in this chapter, and a number of examples will be presented.

In the case of two parallel or twisted fibers, the structure acts as a fiber-optic coupler, where the coupling coefficient is based on the optical properties of the medium between the two fibers, i.e., a chemical sensitive medium. The sensing element is constructed by twisting a small section of two uncladded fibers together, and coating the twisted region with a sensitive material, which is acting as the optical coupling medium. The guided modes propagating in one fiber are coupled to the second one through this coupling medium. This material can be sensitive to the analyte. Instead of coating the twisted fibers, the twisted section can be immersed in a sensitive dye or solution, as shown in Fig. 6.

In the research work performed earlier [18], a twisted pair fiber structure was used for pH measurements. Unclad fibers of PMMA, polystyrene, and nylon were used. The twisted structure was formed in a cylindrical glass tube into which 0.5, 2.0, and 5.0 mM bromothymol blue solution with $3 < \text{pH} < 11$ was introduced. The twisted pair structure suggests that radiation is emitted from one fiber and is received by reciprocity in the other fiber. The twisted pair structure greatly increases the sensitivity of the sensor by having a large interaction area though a long section of modified cladding. As the probe is immersed in a medium with different pH levels, the index of refraction of the sensitive dye, as well as the coupling coefficient, will vary. A simple experimental setup was used, as shown schematically in Fig. 6. The results achieved are reported elsewhere [18]. One of the key observations made with this set-up was that the intensity of the light transmitted from one fiber to the next depended critically on the pitch and number of turns in the twisted pair, in addition to the optical characteristics of the coupling medium. The effective optical path length will have to be calibrated for this structure, but once done, it provides a very convenient configuration for probing various solutions.

It became clear in the study that the twisted structure is the key to the coupling mechanism. The interesting aspect of this investigation is that the response appears to be directly proportional to the geometrical structure and the absorbency of the solution. The role of the absorbency is clear and the twist structure enhances the sensitivity and dynamic range.

2.2 Fluorescence

Fluorescence is a phenomenon in which the molecular absorption of a photon triggers the emission of another photon with a longer wavelength. The energy difference between the absorbed and emitted photons ends up as molecular vibrations or heat. Usually the absorbed photon is in the ultraviolet range, and the emitted light is in the visible range. Optical-fiber sensors based on fluorescence measurements generally

measure the intrinsic fluorescence of the analyte or a change in fluorescence of an indicator dye by the analyte, referred to as the quenching case.

In the intrinsic case, the analyte itself is the fluorescent concentration, where its concentration can be determined using the Parkers Law

$$I_{em} = (2.3k\zeta\varepsilon/c)I_{ex}, \quad (4)$$

where I_{em} is the fluorescence intensity, I_{ex} is the intensity of excitation, ζ is the quantum efficiency of fluorescence, ε is the extension coefficient, l is the path length, k is a constant depending upon the sensor configuration and c is the concentration of the fluorophore.

2.2.1 Quenching

In the quenching case, the indicator dye is immobilized onto a thin polymer film, which is placed at the distal tip or in the evanescent field of the optical fiber. The analyte interacts with this indicator dye by quenching the fluorescence, by forming a complex with the fluorophore. The concentration of the quencher is given by

$$[I_0/I] = 1 + \mathbf{k}[Q], \quad (5)$$

where I_0 is the fluorescence intensity in the absence of the quencher, I is the fluorescence intensity when the quencher is present in a concentration of Q , and \mathbf{k} is the Stern–Volmer constant.

2.2.2 Energy Transfer

Fluorescence can be altered by placing another absorbing species in close proximity to the fluorophore, i.e., the emission spectrum of the fluorophore overlaps the absorption spectrum of the absorbing species. The analyte can, in this case, interact with the absorbing species leading to an overlap with the emission spectrum of the fluorophore. If the distance between the fluorophore and the absorbing species is of an acceptable close proximity, an energy transfer can occur between the fluorophore and the absorbing species, leading to fluorescence quenching of the fluorophore which could also be led by fluorescence from the absorbing species.

2.2.3 Lifetime

Fluorophore lifetime is another method to measure the degree of fluorescence quenching.

2.3 Raman Scattering

Raman scattering provides a vibrational spectroscopic technique in which the monochromatic incident laser light is nonelastically scattered from a sample and

shifted in frequency by the energy of its characteristic molecular vibrations. In the case of conventional Raman scattering, no metal particles are present and the target analyte interacts directly with the incident electromagnetic field. However, in the surface enhanced Raman scattering (SERS) effect, the substrate is coated with metal colloids and the chemical to be examined is on the surface. This metal coating involves the creation of a surface plasmon on the substrate surface, which transfers energy through an electric field to the target molecules allowing otherwise inaccessible vibrational structure to be determined. The signal obtained is much more enhanced in the case of SERS than in conventional Raman scattering.

2.4 Surface Plasmon Resonance

Surface plasmons, also known as surface plasmon polaritons, are surface electromagnetic waves that propagate parallel along a metal/dielectric (or metal/vacuum) interface. Since the wave is on the boundary of the metal and the external medium (air or water for example), these oscillations are very sensitive to any change in the boundary, such as the adsorption of molecules to the metal surface. Surface Plasmon Resonance (SPR) is the most popular method for optical biosensing.

SPR is a phenomenon which occurs when light reflects off thin metal films. A fraction of the light energy incident at a sharply defined angle (SPR angle) can interact with the delocalized electrons in the metal film (plasmon), thus reducing the reflected light intensity. If binding of molecules occurs to the immobilized target, the local refractive index changes, leading to a change in SPR angle, which can be monitored in real-time by detecting changes in the intensity of the reflected light.

The SPR fiber sensor setup is shown in Fig. 7 [23]. The sensor is made of an all silica/silicone fiber with 600 μm diameter. The sensing element is prepared by removing the silicone cladding and coating this section with a 50 nm silver film by thermal evaporation and covering this with thiol and actuator polymer, poly-3,3,3-trifluoropropyl-methylsiloxane and poly-3,3,3-trifluoropropyl-methylsiloxane 50% dimethylsiloxane copolymer. The polymers were deposited by dip coating. Vapors of chlorinated hydrocarbons and of aromatic compounds can be detected using the fluorosiloxane coatings [23]. The sensor developed shows a detection limit of 3,000 ppm for trichloroethylene and about 180 ppm for xylene.

2.4.1 Sensor Design

An optical fiber chemical sensor and biosensor are devices that can selectively detect the presence and concentration of chemical and bio species, respectively. The development of such sensors can be performed in three major steps (or tasks): (a) sensor design; (b) sensor development and processing, which involves (1) selection and characterization of chemical sensitive material, such as polyaniline

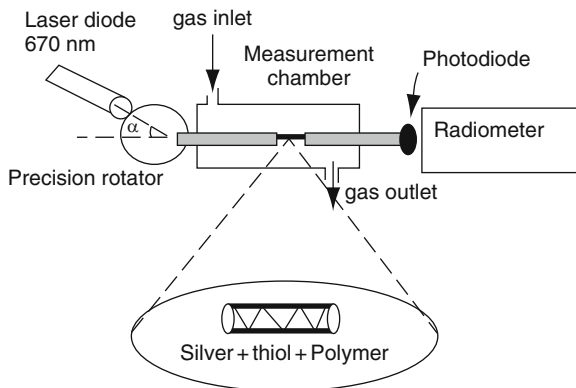


Fig. 7 A schematic of the SPR fiber sensor set-up [23]

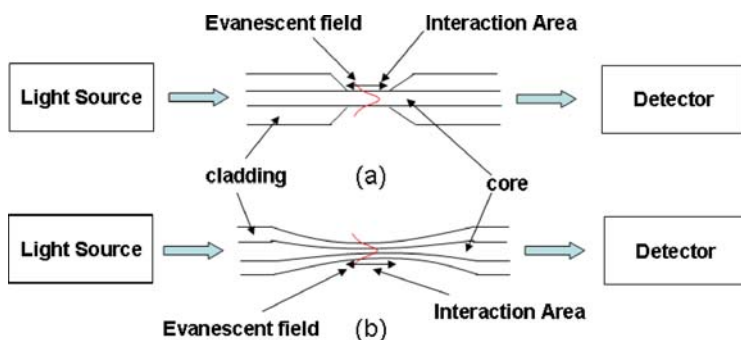


Fig. 8 Schematic diagram of evanescent field sensors

and polypyrrole, and (2) fiber modification process; and (c) sensor characterization and optimization.

There are broadly three ways a chemical or bio species can access the electromagnetic field inside the fiber, which include:

- (1) Direct access to the core of the fiber by means of; hollow waveguides, porous core, or microstructured optical fiber. This type will not be discussed in details in this chapter as it is covered in another chapter
- (2) Access to evanescent field, which can be exposed either by etching the optical fiber cladding or tapering the optical fiber as shown in Fig. 8a,b, and
- (3) Using a modified cladding as the chemical sensitive material. Two types are recorded in many applications: the single fiber structure and the dual fiber (parallel or twisted) structure, as shown before in Figs. 5 and 6. The single fiber structure will be explained in detail in this chapter, with samples of application

It was mentioned before that fiber-optic chemical and biosensors are broadly classified into two categories: extrinsic- and intrinsic-type sensors. In the extrinsic-type sensors, the fiber is acting as a link connecting optical signals to (and from) the active material (medium) positioned at the end of the fiber, such as the Optode case. In the intrinsic-type sensors, the fiber is modified in different ways, through construction of the sensing component, which will be explained next.

2.5 *Extrinsic Sensors*

The basic design consists of a source fiber and a receiver fiber connected to a third optical fiber by a special connector as shown in Fig. 3. The tip of the third fiber is coated with a sensitive material, mostly by the dip coating procedure. The chemical to be sensed may interact with the sensitive tip by changing the absorption, reflection, scattering properties, change in luminescence intensity, change in refractive index, or a change in polarization behavior, hence changing the reflected light properties. This type of sensors are explained elsewhere and not in the focus of this chapter.

2.6 *Intrinsic Sensors*

2.6.1 Core-Based Sensing Fibers

Core-based optical-fiber sensors require the use of special fibers made from porous glass. The core is sensitized by adding chemically sensitive reagents on the surfaces of the pores. The response time of these sensors is very long so this technique finds applications where very fast response is less important than sensitivity. There is very limited literature available for this type of sensors since there are very few research groups working in this area, also the fabrication of porous optical fiber can be a difficult task. In spite of the difficulties in this area, pioneering work has been conducted by Macedo [24], Shahariari [25], and Zhou [26].

A porous sol-gel fiber was prepared by pouring CoCl_2 doped sol-gel solution in a 0.7 mm Tygon tube. After 2 days of gelation, the gels were pushed out of the tubes and air-dried to obtain the CoCl_2 doped sol-gel fiber [27]. The fibers obtained by this technique had pore sizes ranging from submicrometer level to 2 μm . Figure 9 shows an SEM micrograph of the fiber surface. Humidity sensor was constructed by cutting a 0.2 cm length of the porous CoCl_2 doped sol-gel fiber and gluing this section between two commercial silica fibers, with epoxy glue. This sensing element was then connected with a He-Ne laser (630 nm) light source and a photodiode array photo-detector. The sensing element was placed in a climate chamber as shown in Fig. 10, where a controlled amount of humid and dry air was passed for humidity sensing. The sensor results show sensitivity down to 2% relative humidity.

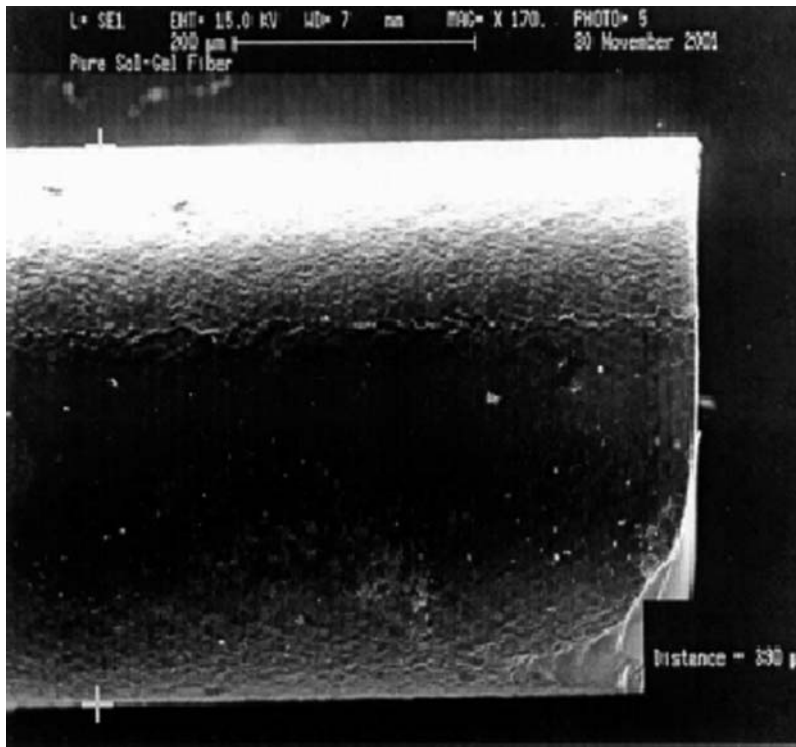


Fig. 9 SEM micrograph of CoCl_2 doped sol-gel fiber [27]

2.6.2 Evanescent Field Sensors

The evanescent spectroscopic sensor design uses the evanescent field associated with the propagation of light in optical fibers. The evanescent fields can be used to transfer energy out of the core to absorbing species in the surrounding medium (evanescent absorption), to create fluorescence in the region outside the core (evanescent excitation), or to couple fluorescence from surrounding medium into the fiber core (evanescent collection). In the evanescent spectroscopic type design, shown in Fig. 8, the change in optical transmission properties is caused by optical absorbance of the analyte. These sensors require the analyte to be optically active in the wavelength range of the light in the optical fiber. Recent research in this area has therefore been focused mainly on pushing the wavelength range of this technique into the mid-infrared or the “chemical fingerprint” region of the electromagnetic spectrum.

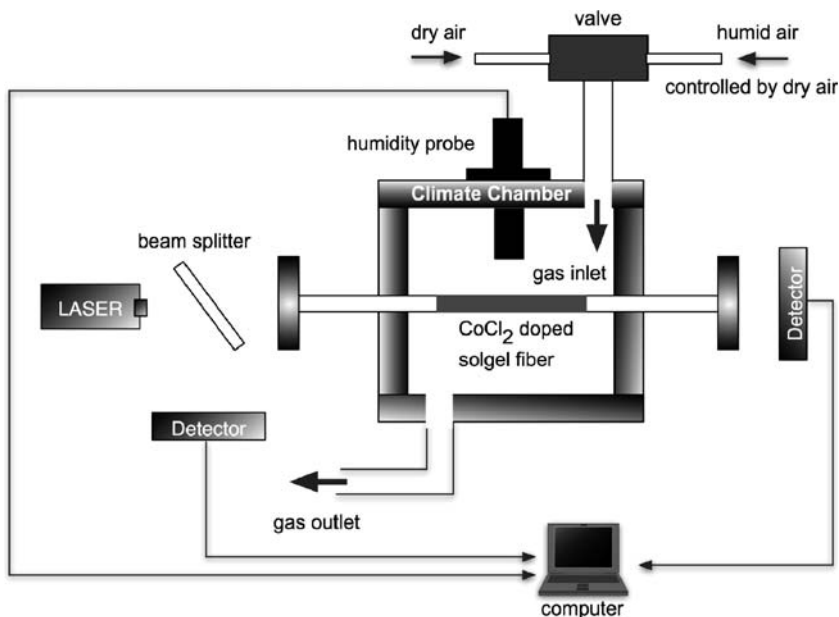


Fig. 10 The experimental set-up for a humidity sensor, using a porous sol-gel fiber

2.6.3 Modified Cladding Fibers

The sensing fibers explained in this section are based on the modified cladding structure [18–20]. The passive cladding of the optical fiber is removed from a small section and is replaced by a chemo-chromic material as shown in Fig. 11. The refractive index is a complex quantity given by

$$n_{\text{complex}} = n_{\text{real}} + ik, \quad (6)$$

where n_{real} is the real part of the refractive index and k is the imaginary part, which is related to the absorbance of the material.

Any change in the real refractive index or the absorbance of the material due to the presence of the analyte changes the transmission properties of the optical fiber. There can be three different modes of operation/propagation (cases 1–3 next) of the sensor depending upon the real part of the refractive index of the modified cladding (n_{mcl}), i.e., the chemo-chromic material, with respect to both the refractive index of the core (n_{core}) and the original cladding (n_{cl}). For example, polypyrrole film refractive index is 1.817 [19], which is much higher than the core refractive index 1.45, and the sensor operation is in the leaky mode principles, i.e., case 2 below.

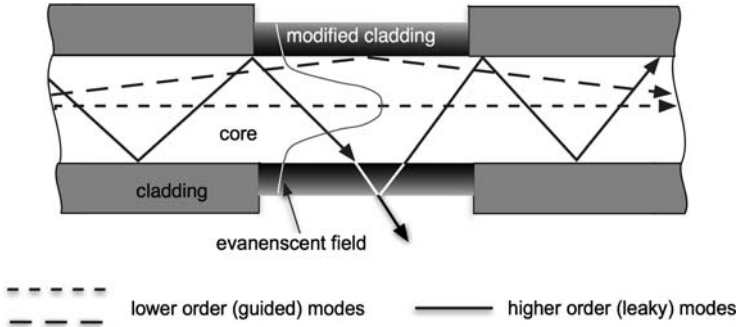


Fig. 11 Schematic of the optical-fiber sensor design showing the modified cladding region

Case 1: Operations on the evanescent mode principles ($n_{cl} = n_{mcl} < n_{co}$)

In this case, since the refractive index of the modified cladding is equal to that of the original cladding, the wave-guiding conditions do not change in the modified region and the light has the same Gaussian intensity profile throughout the fiber. There is an evanescent field penetration in the modified region, as shown in Fig. 11. Any change in the absorbance of the material will result in evanescent absorption, which will lead to intensity modulation.

Case 2: Operations on the leaky mode principles ($n_{mcl} > n_{co} > n_{cl}$)

Since this condition does not satisfy total internal reflection at the interface between the core and the modified cladding, guided modes will be changed to leaky modes in the modified region, as shown in Fig. 11. The boundary between the air and the modified cladding can support total internal reflection and some of the light will propagate in the modified cladding and some is reflected back into the core. Any change in the complex refractive index of the modified cladding due to the analyte can change the waveguide transmission conditions and result in an intensity change. In some cases, a thin layer of the cladding can be left on the core, before coating the sensitive material. This will control the energy in leaky modes, where the fiber has two layers of cladding and operates on the W-shape principles.

Case 3: Operations on the partial leaky mode principles ($n_{cl} < n_{mcl} < n_{co}$)

In this case, the sensor operates in the partial leaky mode, i.e., the critical angle in the modified region is higher than the critical angle for the fiber, so some higher-order modes will leak through the modified cladding and the lower-order modes will continue as guided modes. Any change in the real part or the complex part

(absorbance) of the refractive index can lead to a change in the transmitted intensity.

Sensors based on modified cladding fibers are explained in detail in this chapter. A large number of examples are presented in the following sections on sensors development and processing as well as on sensors characterization and optimization. Also, successful application of these sensors in detecting chemical vapors and toxic substances are presented and discussed.

3 Sensors Development and Processing

In the modified cladding sensors, one of the critical tasks for the successful development of a specific type of sensor is the proper selection of the sensitive material for such application. The material would be applied, as the modified cladding, to the sensing part of the optical fiber.

3.1 Selection and Characterization of Chemical Sensitive Materials

Polyaniline and Polypyrrole represent a new class of conducting polymer, attracting the attention of many researchers for sensors application. In these types of polymers, electrical conductivity is achieved by creating charge carriers through a p-type (holes) or n-type (electrons) doping of the conjugated polymer backbone. These conducting polymers can be doped by a variety of redox processes [28], i.e., chemical or electrochemical partial oxidation or partial reduction. There is also evidence of nonredox doping process [29]. The doping/dedoping process mentioned above results in reversible or irreversible changes in electrical and optical properties of these conducting polymers; hence, these materials have found applications in electro-chromic devices and optical chemical sensors. A large number of gas sensors make use of conducting polymers as their sensing elements since conducting polymers have great design flexibility and are very stable at ambient temperature and pressure. The conductivity and work function of conducting polymers are the two main properties that are used in chemo-electric, chemo-mechanic, and chemo-chromic transduction [30, 31].

3.1.1 Polyaniline

The composition of polyaniline (emeraldine base) is shown in Fig. 12, and consists of alternating reduced and oxidized repeating units. Polyaniline can be switched back and forth from its insulating state to the conducting state by doping with HCl

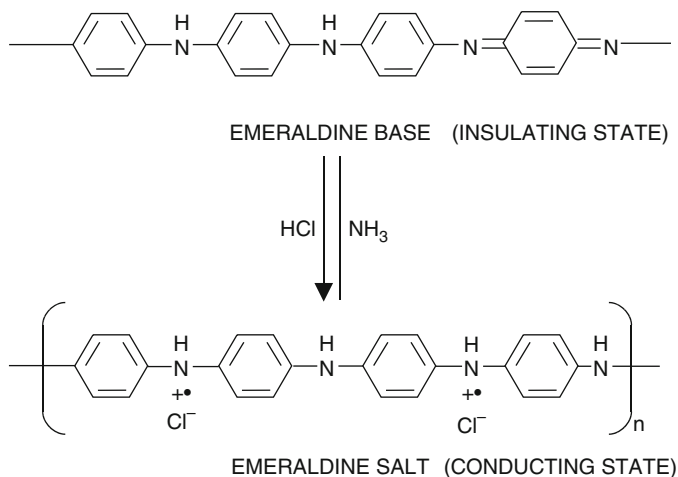


Fig. 12 Switching between emeraldine base (insulating form) and emeraldine salt (conducting form) by HCl and ammonia, respectively

solution or vapor and dedoping with ammonium hydroxide solution or vapor, respectively, as shown in Fig. 12. This change is also accompanied with an optical property change. Therefore, polyaniline was used as the modified fiber cladding material for sensing HCl vapor and NH₃. Thin film coating of 400 nm thickness, using in situ deposition, was used for chemical sensor applications [19].

3.1.2 Polypyrrole

The base unit of polypyrrole is pyrrole, the structure of which is a five member hetero-aromatic ring containing a nitrogen atom, as shown in Fig. 13a. Polypyrrole is synthesized from the pyrrole monomer by mild oxidation, using chemical or electrochemical technique. After the oxidation of the monomer, a black solid polymer is precipitated from the solution. The polypyrrole structure in its oxidized form is shown in Fig. 13b. Film thicknesses on the order of 1–1.5 μm , using in situ deposition, were obtained for our application [19].

3.1.3 Materials Characterization

For a polyaniline film, the light absorption measurements were conducted after the film was exposed to HCl and NH₃ vapors, respectively, as shown in Fig. 14 [19]. The difference in the spectra indicated that HCl and NH₃ vapors induced a different band structure and conformation of the polymer. Therefore, the optical property of the film changed when the film switched from one state (doped by HCl) to another (dedoped by NH₃). The refractive index measurement by ellipsometry showed that the refractive index changed from 2.43 (doped by HCl) to 1.95 (dedoped by NH₃).

Fig. 13 (a) Polypyrrole structure and (b) Polypyrrole structure in its oxidized form

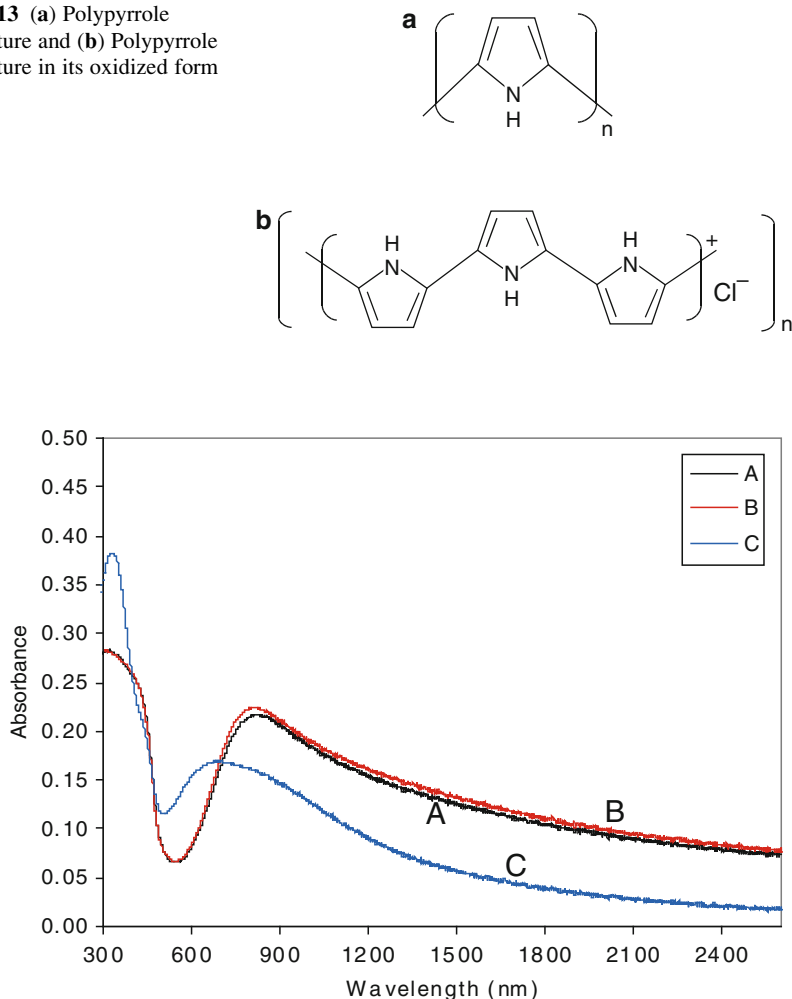


Fig. 14 Polyaniline film response to: (a) as deposited, (b) after exposure to HCl, and (c) after exposure to NH_3

For a polypyrrole film [19], measurements were conducted before and after the film was exposed to hydrazine (H_4N_2) and hydrogen peroxide (H_2O_2), as shown in Fig. 15. The measured refractive indices are 1.82 (before exposure to hydrazine) and 1.71 (after exposure to hydrazine).

For biosensor applications, it is reported that a change in polypyrrole absorbance is induced when the material is exposed to dimethyl–methyl phosphonate (DMMP) [32], as shown in Fig. 16, where 40% reduction occurred in the UV/Vis absorbance band. DMMP is a chemical precursor to the nerve agent sarin. It is reported that the DMMP interacts electronically with the polypyrrole to increase the amount of free

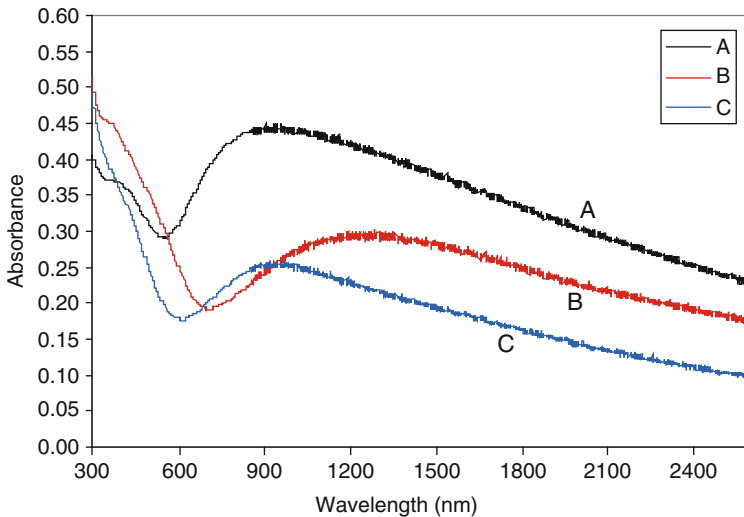


Fig. 15 Polypyrrole film response to: (a) as deposited, (b) after exposure to hydrazine, (c) after exposure to hydrogen peroxide

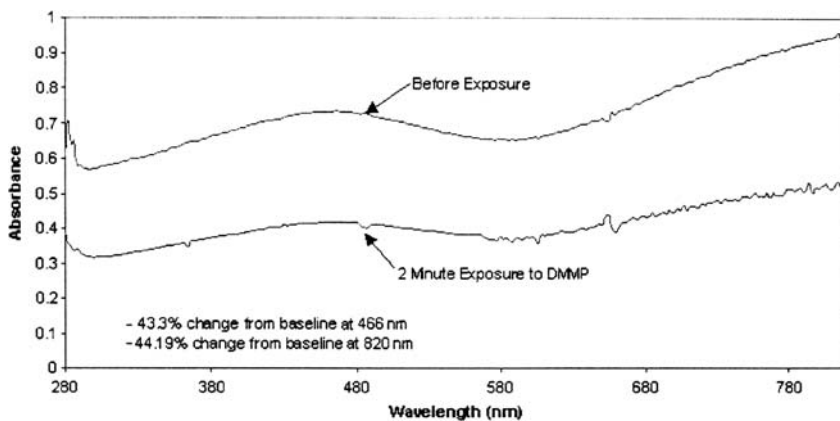


Fig. 16 Polypyrrole film response to DMMP

mobile holes charge carriers [30]. Also, additional drop in the resistance of polypyrrole thin films can be achieved when the film is doped with naphthalene-disulphonic acid (NDSA), before exposure to DMMP vapor [30]. The change in resistivity implies a change in the refractive index of the polypyrrole. A change in the refractive index and absorbance of the modified cladding will lead to a change in the propagation of the light through the sensing element which results in optical intensity modulation. Therefore, the optical property change in both polymer

(polyaniline and polypyrrole) films are attributed to changes in bulk conductivity and absorbance properties, because of the porous nature of both polymer thin films.

3.2 Fiber Modification Process

The modification of the optical fiber involves two major steps, for chemical sensor application [19, 20]: (1) removal of the passive cladding (fiber etching) and (2) application of active cladding (fiber coating). The etching and coating processes are explained next. An all-silica MM fiber with core/cladding/jacket dimension of 105/125/250 μm was selected for such application.

3.2.1 Fiber Etching

A meter length of optical fiber was used and a small section (1 cm) of the jacket was stripped off the center of the optical fiber. The exposed section of the fiber is immersed in HF (hydrofluoric acid) solution, which etches and removes the glass cladding of the optical fiber. The etching process is performed under real-time monitoring, as shown in the experimental set-up, Fig. 17. While the fiber is immersed in etching solution (HF), the fiber is connected to a He-Ne (wavelength 633 nm) light source and a Silicon photo-detector (Newport 818 SL wavelength range 400–1,100 nm), and the power is continuously monitored. The optical power transmitted through the fiber remains constant as long as the glass cladding

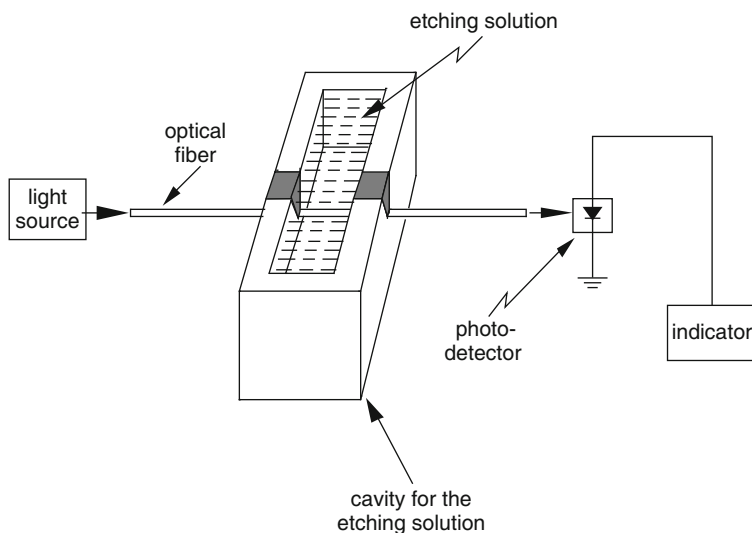


Fig. 17 Schematic drawing of the set-up for monitoring the cladding etching process, in HF solution

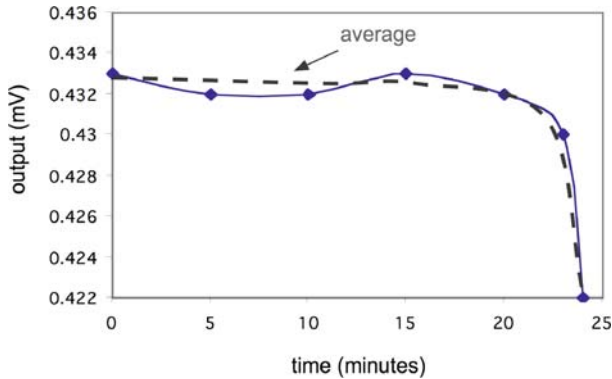


Fig. 18 Change of the output power during the fiber cladding etching process

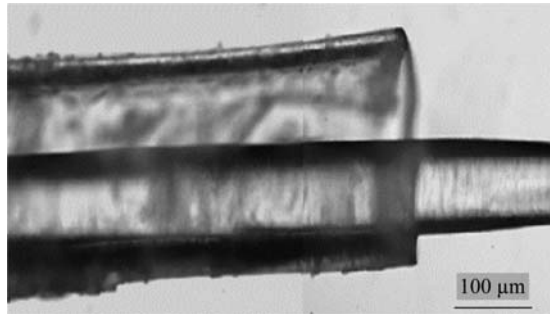


Fig. 19 Micrograph of an optical fiber after the etching process has been completed, for an improper etching

thickness is larger than the evanescent field penetration. Then, a sudden drop in the power is observed, as the remaining cladding thickness is thin or completely removed, as seen in the etching plot in Fig. 18. A concentration of about 16.3% HF will take 30 min to etch away a 10 μm thick cladding.

The etching process has been calibrated to prevent overetching and protect the fiber core from being etched too. Figure 19 is an example of improper etching. The proper etching process can be achieved by calibrating the etching process, for a certain HF concentration. Once this calibration had been achieved, a fixed acid concentration and a fixed time of etching were used to give exact core diameter, which is confirmed for many samples, using optical microscopy. An example of a properly etched fiber is shown in Fig. 20.

3.2.2 Coating of Conducting Polymers

Several techniques, such as casting, spin-casting, and in situ deposition methods, can be used to produce polymer coated thin films, such as polyaniline and

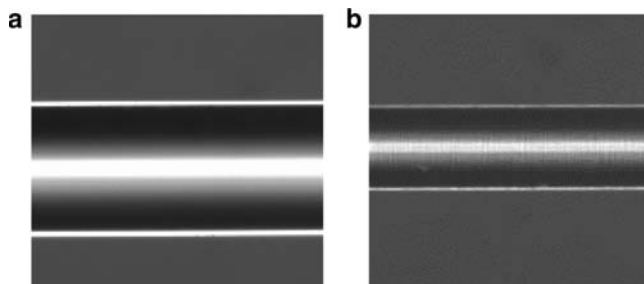


Fig. 20 Micrographs of an optical fiber after a proper etching process has been completed; (a) before the cladding was etched (140 μm in diameter), and (b) after the cladding was etched (100 μm in diameter)

polypyrrole thin films. Both spin-cast and in situ deposition methods were used to coat the cladding-removed fiber region with the conducting polymers [19, 20, 33]. For spin-cast method, the spinning time, spin-rate, and the viscosity of the solution have to be properly controlled to get a uniform thin film. For in situ deposition method, the polymerization process and fiber deposition time have to be determined to obtain a homogeneous coating.

4 Sensor Characterization and Optimization

After the modified part of the fiber is coated with the chemical sensitive material, the optical fiber is integrated with other proper sensor's components, such as light source, photo-detector, data processing electronics, and data recording devices. In sensing applications, the sensing part of the fiber is exposed to the analyte vapor (or liquid). The output intensity is measured by a power meter, which is connected to an oscilloscope for real-time measurement and recording. A general experimental setup is shown in Fig. 21. A triggering circuit, which consists of a LED–detector combination, is used to record the exposure time (cuts the light to the detector) during the analyte exposure period. The sensor response time is measured as the time lapse between the trigger and the beginning of intensity drop in the fiber.

The developed fiber-optic sensors were tested for their sensitivity towards vapors of HCl and ammonia, in the case of using Polyaniline as the modified cladding; and vapors of DMMP, hydrazine and hydrogen peroxide, in the case of using Polypyrrole as the modified cladding. Using total light intensity modulation method, the sensors showed very reasonable responses. However, using the SIM technique, we were able to achieve reasonable improvement in the sensor sensitivity. This is achieved by shifting more light to higher-order modes, which have more interaction with the sensitive material, than lower-order modes, at the core/cladding interface.

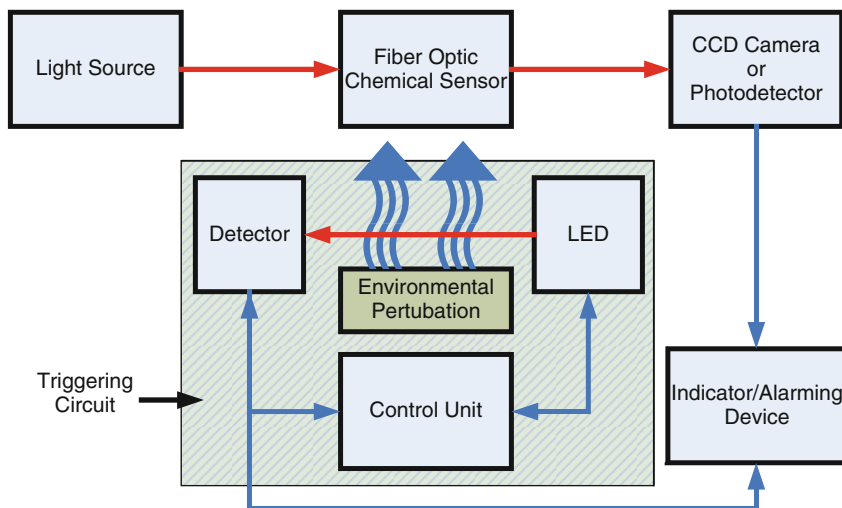


Fig. 21 A Schematic diagram of the experimental set-up

4.1 Sensing HCl and NH_3 Vapors

When polyaniline was used as the modified cladding layer, HCl and NH_3 vapors could be detected immediately upon their exposure to the fiber sensing region. It is known that polyaniline can be easily doped by acid (such as HCl) and dedoped by base (such as NH_3). The doping and dedoping processes are reversible. It was found that after the polymer was doped, it was stable in the air. However, after the dedoping chemical was moved away, the polymer gradually returned to the doped state. The polyaniline was doped after in situ deposition and the optical property of polyaniline changed from the doped state to the dedoped state. When the sensing region of the optical fiber, which was coated with polyaniline, was exposed to acid vapor (HCl) or base vapor (NH_3), the output intensity of optical signal changed. Figure 22 shows the sensor output change, based on total intensity measurement, when it was exposed to the chemical vapors [19]. The signal response (R) is calculated based on the following equation:

$$R = \{(I_0 - I)/I_0\} \times 100, \quad (7)$$

where I_0 is the average light intensity before gas exposure and I is the average light intensity after gas exposure. The response was 50% for NH_3 vapor and 12% for HCl vapor.

In Fig. 22, at the time of 15 s, the sensing fiber was exposed to NH_3 vapors, which induced the power-drop from 1.75 to 0.87 V. After 60 s, the NH_3 vapor was

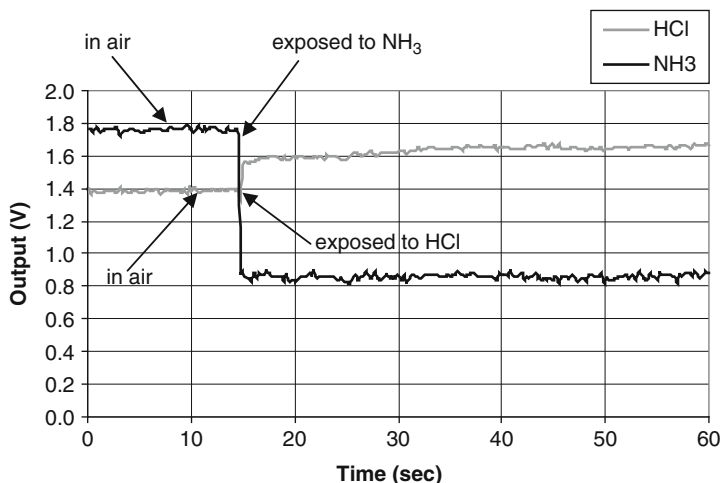


Fig. 22 Sensor response to chemical vapors of HCl and NH₃, where the sensing fiber was coated polyaniline by in situ deposition. The deposition time was 30 min

moved away. It was found that the polyaniline partially went back to the HCl doped state with the output power increasing to 1.4 V. The sensor was then exposed to HCl vapor, which resulted in the power increase by 12%. More experiments indicated that the response of the sensing signal did not show significant influence by a film deposition time from 7 to 30 min, i.e., different film thickness; however, any imperfections in the structure of the deposited layer decreased the signal response of the sensor.

4.2 Sensing Hydrazine Vapor

Polypyrrole was used as the modified cladding layer to detect hydrazine vapor. The sensing fiber was coated with polypyrrole by in situ deposition. The deposition time was 15 and 30 min, respectively. When hydrazine vapor was exposed to the sensing region, the optical signal decreased (based on (7)) to 91% and 64% for 15 and 30 min deposited samples, respectively, as shown in Fig. 23 [19]. The difference in the response may be induced by the thickness, uniformity, and conformation of the polymer layer. After the polypyrrole region was exposed to hydrazine, it was exposed to hydrogen peroxide vapor and hydrazine vapor again as shown in Fig. 24. The output increased, when exposed to hydrogen peroxide vapor, to 28% and decreased to 86%, when exposed to hydrazine vapor. It was found that the sensor can only be used for a few times, since an irreversible change occurred in polypyrrole after it was exposed to hydrazine.

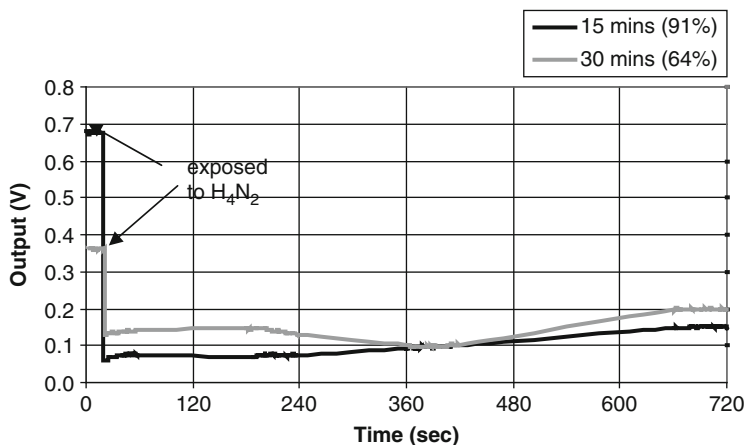


Fig. 23 Sensor response to chemical vapor of hydrazine (H_4N_2)

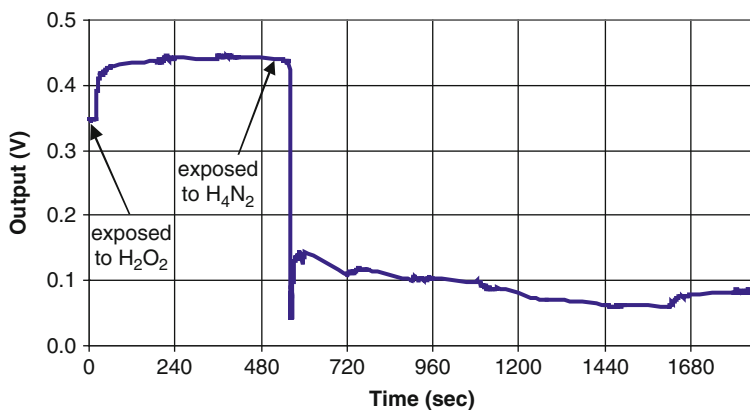


Fig. 24 Sensor response to chemical vapors of hydrogen peroxide (H_2O_2) and hydrazine (H_4N_2)

4.3 Sensing DMMP Vapors

The sensor response to DMMP vapor exposure (without any added dopant) is shown in Fig. 25. A percentage-response of approximately 2.1% was obtained, and the response time was 2 s [20]. This response is attributed to the leaking of the higher-order modes through the modified cladding of the fiber, due to the increased conductivity in polypyrrole film due to DMMP absorption.

To enhance the response of the polypyrrole sensor towards DMMP, acid dopants were added to the polypyrrole structure. The rationale for doping polypyrrole was to introduce secondary doping sites for DMMP in the structure. Secondary doping

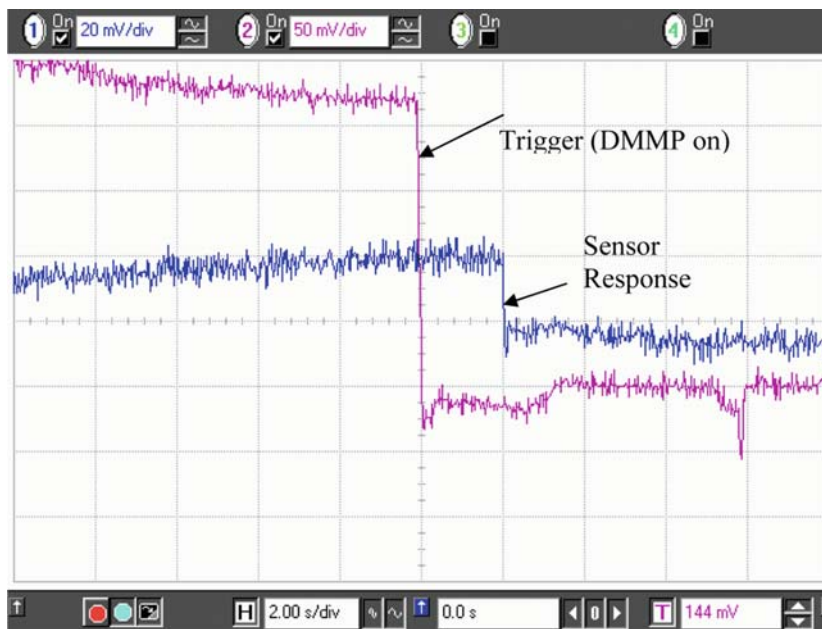


Fig. 25 Sensor response for polypyrrole coated fiber upon DMMP exposure

sites are sites where an interaction with DMMP would lead to conformational change in the polypyrrole structure leading to an optical property change.

To improve the response to DMMP, several sensors were prepared by coating the sensing part of the fiber with differently doped polypyrrole. Three different dopants – HCl, NDSA and ASQA – were added during the polymerization stage, during the synthesis of polypyrrole. Optical fiber samples were coated for 5 min by in situ deposition. The concentration of the dopant acid varied (0.1 ml, 0.5 ml, 1 ml, 1.5 ml of 1 Molar (M) dopant solution in 100 ml oxidant solution) to investigate the influence of doping concentration on the sensor response. The choice of the three particular dopants is made on the bases of their reported sensitivities to DMMP [30]. Figure 26(a–c) depicts the waveforms obtained for 0.5 ml of HCl, NDSA, and ASQA doping to polypyrrole respectively.

The upper waveform is the sensor response and the lower waveform is the trigger, i.e., the start of the exposure of DMMP. It can be seen that the doping polypyrrole results in a dramatic change in the percentage of sensor response from just 2.1% for undoped polypyrrole to 15.75% for HCl, 15.75% for NDSA doped, and 4.21% for ASQA doped polypyrrole. This increase in the sensor response to DMMP in doped polypyrrole may be attributed to conformational changes, which may occur in doped polypyrrole due to DMMP adsorption [30, 34]. These conformational changes may further increase the conductivity change upon DMMP exposure, resulting in an enhanced sensor response.

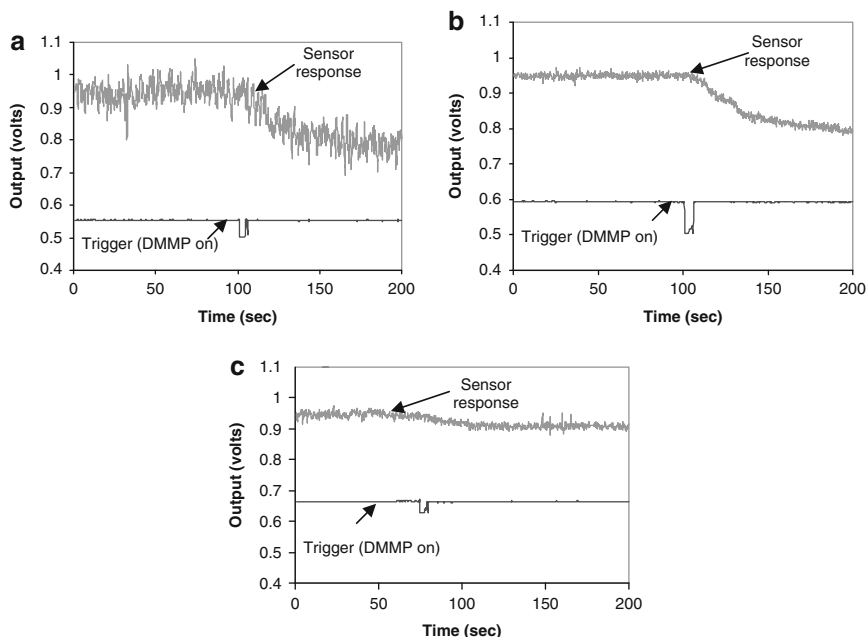


Fig. 26 Sensor response of doped polypyrrole for (a) HCl, (b) NDSA, and (c) ASQA dopants

It is found that as the amount of dopant is increased the sensor response in the case of HCl and NDSA increases up to 0.5 ml of 1 M concentration and decreases as the dopant amount is increased further. For ASQA doping, the sensor response is almost constant up to 0.5 ml dopant concentration and then there is a gradual decrease observed, with increased dopant concentration. X-ray diffraction studies indicate an increase in crystallinity of the polymer when the primary doping is increased [35]. This increase in crystallinity at higher doping concentrations may be responsible for lower sensor response. The best response time is observed in the ASQA (0.5 ml) doped sample, but the percentage of sensor response is low (4.03%) as compared to the other two dopants, i.e., NDSA and HCL which give a sensor response of 15.75%, as shown in Fig. 26. The optimal dopant and dopant concentration is 0.5 ml of 1 M NDSA in 100 ml oxidant solution with a percentage of sensor response of 15.75% and a response time of 7 s.

5 Spatial Intensity Modulation for Sensor Applications

Current research in fiber-optic sensors relates perturbations to change in the total intensity of the light signal transmitted through the optical fiber. Other methods involve launching coherent polarized light through an optical fiber and observing the changes in the polarization or phase of the launched signal with the applied external perturbation. Sensors based on total intensity modulation are simple and

cost-effective. However, they provide limited sensitivity. Phase and polarization modulation type sensors provide much better sensitivity, but they are bulky and require laser sources and expensive techniques for detection. To overcome these limitations, a novel technique, based on monitoring the MPD in MM fibers, was developed. This technique provides a new methodology to improve the sensors sensitivity, using inexpensive and miniature components, for chemical and biosensors applications [36–38]. The fundamentals and basic theories, the detection technique, and the sensors application are explained in this section and an example of a chemical sensor application is presented.

5.1 Fundamentals and Basic Theories

The principle of operation of the developed technique is based on SIM of the modal power in MM fibers. Within a MM optical fiber, optical signals propagate according to the modal structure of the fiber and the boundary conditions. Altering the boundary conditions of an optical fiber induces modal coupling and results in modal power redistribution, i.e., MPD modulation. The coupled-mode theory can be employed for the analysis of the MPD modulation [16, 38, 39]. The MPD within a MM fiber is a function of the geometry (size) and the optical properties (core and cladding indices) of the fiber and the light launching conditions. Deforming the fiber by any form of perturbation, results in modal power modulation, which can be exploited for sensing the source of perturbation.

Based on the theories of geometric and wave optics, light propagates within optical fibers in the form of orthogonal modes. The light power distribution, in MM fibers, can be analyzed and characterized by using geometric and wave optics. In order to evaluate the MPD, within MM fibers, the wave equation, which is a second-order differential equation, has to be solved in cylindrical coordinate system. A summary of the MPD analysis is presented next, with an example on application to chemical and biosensors.

Assuming that the propagation is in the z -direction, the electric field E is given in the following form

$$\vec{E} = \vec{E}_0(r, \phi) \exp(-j\beta z) \quad (8)$$

where r , ϕ , and z are for the cylindrical coordinates, and β is the propagation constant.

Knowing that the Helmholtz wave equations for E_z are:

$$\nabla_t^2 E_{z1} + (n_{core}^2 k_0^2 - \beta^2) E_{z1} = 0, \quad r \leq a, \quad (9)$$

$$\nabla_t^2 E_{z2} + (n_{clad}^2 k_0^2 - \beta^2) E_{z2} = 0, \quad r \geq a, \quad (10)$$

we obtain

$$E_z = \begin{cases} AJ_q(ur/a) \sin(q\phi) \exp(-j\beta z), & r \leq a \\ CK_q(wr/a) \sin(q\phi) \exp(-j\beta z), & r \geq a \end{cases}, \quad (11)$$

where J_q and K_q are ordinary and modified Bessel functions of order q ;

$$V^2 = u^2 + w^2, \quad (12)$$

$$u = a\sqrt{n_{\text{core}}^2 k_0^2 - \beta^2}, \quad (13)$$

$$w = a\sqrt{\beta^2 - n_{\text{clad}}^2 k_0^2}, \quad (14)$$

$$\beta = \sqrt{n_{\text{core}}^2 \left(\frac{2\pi}{\lambda_0}\right)^2 - \left(\frac{u}{a}\right)^2}, \quad (15)$$

where a is the core radius and λ_0 is the free space optical wavelength; n_{core} and n_{clad} are core and cladding refractive indices, respectively; V is the fiber V number, which embodies fiber structural parameters in it; u and w are normalized propagation and attenuation constants; and β is the mode propagation constant or phase constant.

This analysis results in

$$\begin{aligned} & \left(\frac{J'_q}{uJ_q(u)} + \frac{K'_q(w)}{wJ_q(w)} \right) \left(\frac{n_{\text{core}}^2}{n_{\text{clad}}^2} \frac{J'_q(u)'}{uJ_q(u)} + \frac{K'_q(w)}{wJ_q(w)} \right) \\ & = q^2 \left(\frac{1}{u^2} + \frac{1}{w^2} \right) \left(\frac{n_{\text{core}}^2}{n_{\text{clad}}^2} \frac{1}{u^2} + \frac{1}{w^2} \right). \end{aligned} \quad (16)$$

By using weakly guidance approximation, equation (16) can be reduced to the following form:

$$\frac{J'_q}{uJ_q(u)} + \frac{K'_q(w)}{wJ_q(w)} = \pm \left(\frac{1}{u^2} + \frac{1}{w^2} \right). \quad (17)$$

After using the numerical solution of the eigenvalues equation, the radial electric field in the direction of polarization is found as:

$$E_{\text{LP}_{lm}} = 2E_0 J_l \left(\frac{ur}{a} \right) \sin l\phi, \quad r \leq a, \quad (18)$$

$$E_{LP_m} = 2E_0 \frac{J_l(u)}{K_l(w)} K_l\left(\frac{wr}{a}\right) \sin l\phi, \quad r \geq a. \tag{19}$$

The corresponding intensity distribution can be calculated for each mode as:

$$I_{lm} = I_0 J_l^2\left(\frac{ur}{a}\right) \sin^2(l\phi), \quad r \leq a, \tag{20}$$

$$I_{lm} = I_0 \left(\frac{J_l(u)}{K_l(u)}\right)^2 K_l^2\left(\frac{wr}{a}\right) \sin^2(l\phi), \quad r \geq a. \tag{21}$$

An example of MPD, i.e., the light intensity plots for the LP₃₁ mode, is shown in Fig. 27.

Based on this analysis and from (20) and (21), it is clear that for sensors application, any change in the core or cladding indices as well as the fiber geometry will result in modal power redistribution, which can be exploited for chemical and biosensing applications.

As an example of sensor applications, for an optical fiber with a core diameter 20 μm, $n_{\text{clad}} = 1.45$, and $n_{\text{core}} = 1.46$, the field of the modal power for LP_{lm} modes is shown in Fig. 28a,b for the modal orders $l = 6$ and $l = 13$, at an optical wavelength $\lambda = 0.75 \mu\text{m}$. In the presence of external perturbations applied to the fiber, resulted in changing the cladding index to $n_{\text{clad}} = 1.455$, the modal power redistribution of $l = 6$ and $l = 13$ modes is shown in Fig. 28c, d. This theoretical analysis is based on the use of a single frequency (laser) light source.

To take advantage of the MPD technique for sensors applications, a special setup has been developed for measuring the MPD and redistribution in real time, as explained in the next section.

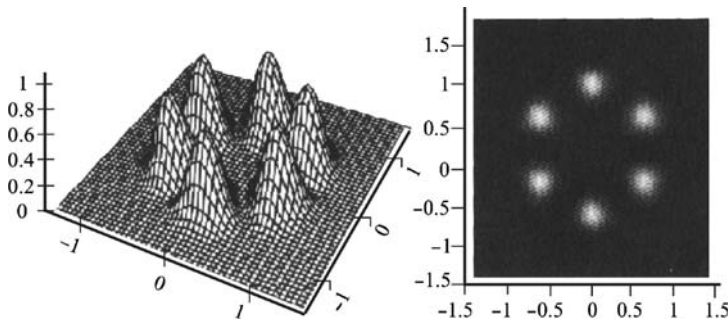
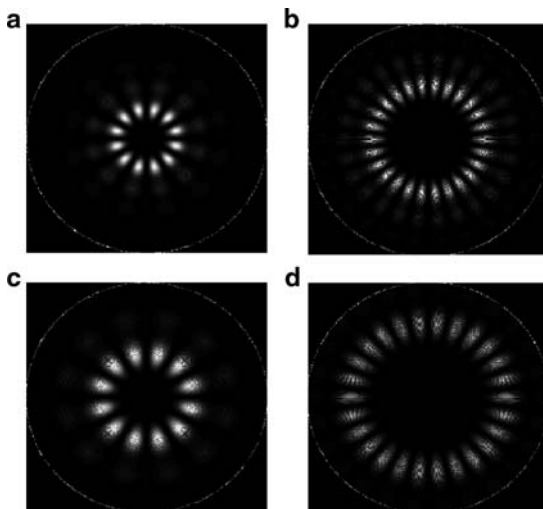


Fig. 27 Light intensity distribution within the fiber core for the mode LP₃₁

Fig. 28 The LP_{lm} modal structure of a multimode fiber having; $n_{\text{core}} = 1.46$ and; (a) $l = 6, n_{\text{clad}} = 1.45$, (b) $l = 13, n_{\text{clad}} = 1.45$, (c) $l = 6, n_{\text{clad}} = 1.455$, and (d) $l = 13, n_{\text{clad}} = 1.455$



5.2 Development of Sensor Components

The measurements of the distribution and the subsequent redistribution of the modal power can be accomplished by scanning the far-field pattern at the fiber end using a CCD camera or by using one or more photodetectors positioned at a specific location in the far-field zone, as shown in Fig. 29. The modal launcher is a single or array of LEDs, used to excite a limited group of modes within the MM optical fiber, and the modal analyzer is the detection system of the modal power positioned at the output end of the optical fiber, in the far-field zone.

Based on the theoretical analysis presented before, the modal power redistribution of $l = 6$ and $l = 13$ modes shown in Fig. 28c, d, were for a light source having a single frequency, i.e., laser source. However, when a light-emitting diode (LED) is used, the modal power structure will have a continuous intensity distribution. Through selective excitation, a limited number of propagating modes can be excited. This method can be applied by exciting the optical fiber with a beam of light off-axis.

For example, a step index silica fiber of 100- μm -diameter was excited at 10° off-axis. The 2D far-field pattern (MPD) and intensity profile were scanned and recorded by a CCD camera as shown in Fig. 30a. When the fiber was under perturbation, the recorded far-field pattern showed intermodal coupling and redistribution of the modal power (Fig. 30b). As the perturbation level was increased, considerable rearrangement of the modal power was recorded in a similar way. This experiment indicates that continuous variation of the applied perturbation results in a respective change in the MPD, in a very sensitive manner.

For a simple approach and cost-effective sensor configuration, the CCD camera can be replaced by photo-detectors located at key positions in the far field.

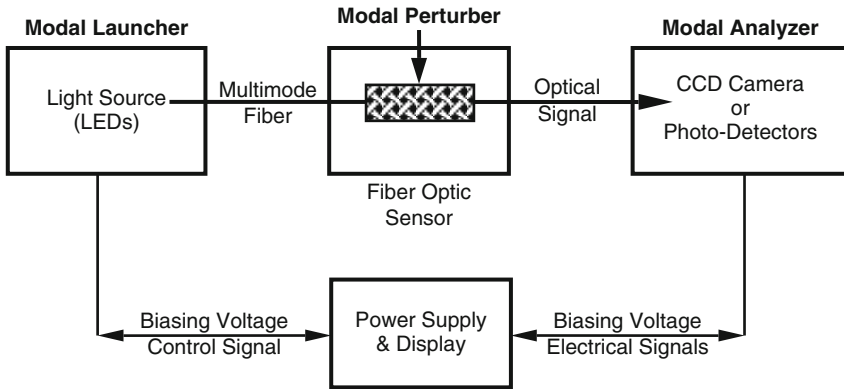


Fig. 29 The general block diagram of the developed MPD sensor characterization method

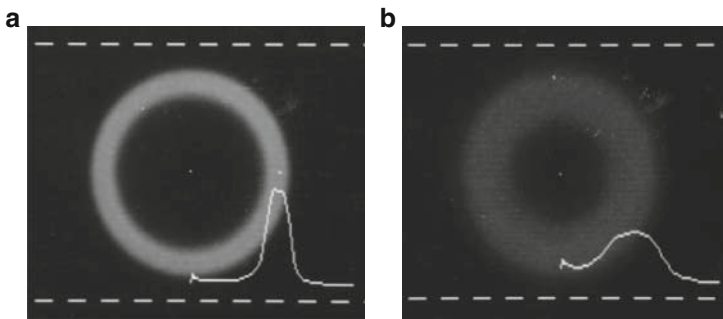


Fig. 30 The 2D image and the horizontal intensity profile of the far-field pattern measured at the center before (a) and after (b) the presence of perturbation

Therefore, using a light-emitting diode as the light source and regular photodiodes for detection will provide a sensitive, inexpensive, and miniature sensor. These advantages make the MPD technique as the most suitable technique for the chemical and biosensor applications.

The sensitivity and the dynamic range of this type of sensor are related to the modal structure of the fiber, and to the behavior of the materials surrounding it. Therefore, the developed SIM technique can provide a compatible methodology suitable for sensors applications. Experimental and theoretical feasibility studies show that the developed sensing technique is sensitive, inexpensive, and can be manufactured in microstructure components. A simple example on using the SIM technique for chemical sensors application is presented in the next section.

5.3 Application of SIM in Chemical Sensors

The SIM technique uses the intensity information in two dimensions (2D), which can enhance the sensor detection sensitivity. The intensity distribution in 2D is the function of the optical excitation and the boundary conditions of the optical fiber, whereby changing the boundary conditions results in intensity modulation in 2D [36]. It is known that in SIM technique applications, higher-order modes are excited by off-axis illumination of the optical fiber [16, 38]. Those modes have more interactions with the core/cladding interface; therefore, they are more sensitive to changes in the refractive index of the cladding material.

For the evaluation of the SIM technique in chemical sensors application, an experimental set-up was developed as shown in Fig. 31. A fiber-optic chemical sensor was prepared, using polyaniline as the modified cladding for a short MM sensing fiber. The spin-casting method was used for coating a thin layer of polyaniline material on the fiber core surface. Then, the modified fiber was tested for the detection of HCl vapor and NH₃ gas. The sensor was tested by both the total intensity modulation and the SIM techniques.

5.3.1 Total Intensity Measurements

In the case of total intensity measurements, it was decided to test the sensor at three different light wavelengths. This approach will provide critical information on the important of the light wavelength on the sensor sensitivity, and on the final selection of the light source for proper application.

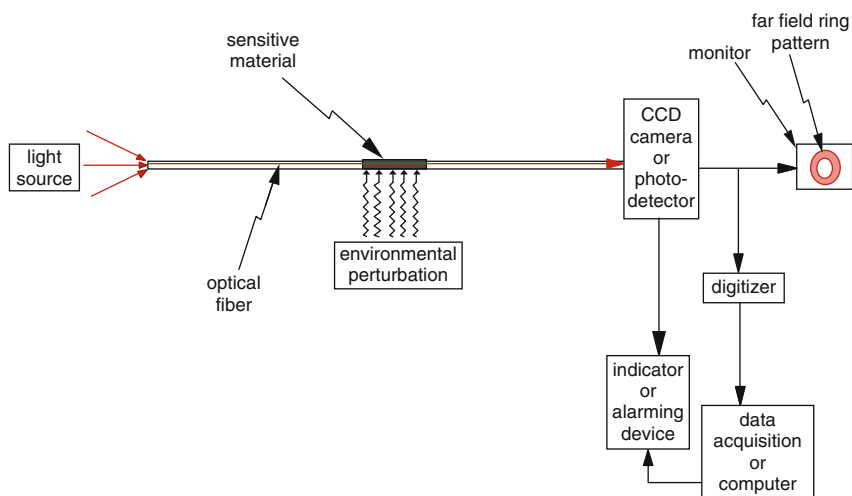


Fig. 31 Schematic diagram of the experimental set-up, for both the total intensity and the spatial intensity measurements

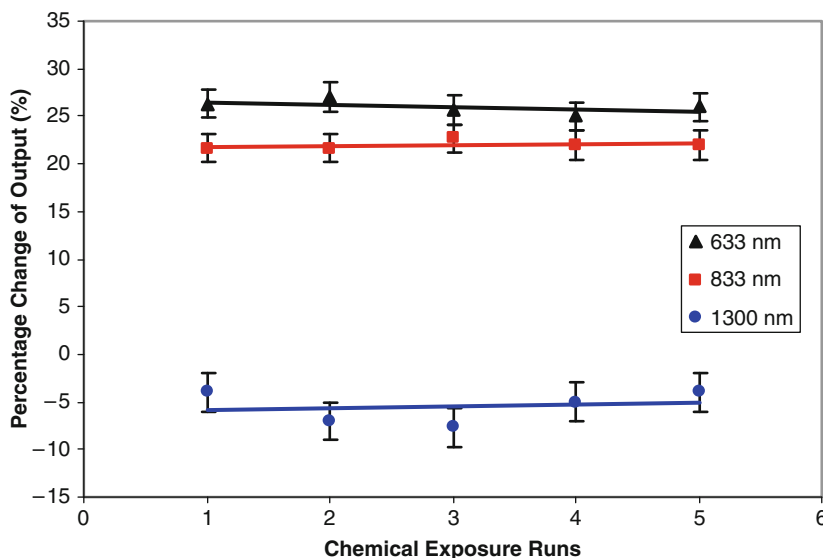


Fig. 32 Change of the sensor output power (total intensity) when three different light sources (633 nm, 833 nm, and 1,300 nm) used

Three light sources, with wavelengths of 633 nm, 833 nm, and 1,300 nm were used, respectively, for testing the sensor sensitivity, as well as, the influence of the light wavelength, with total intensity measurements. When the sensors exposed to HCl vapor and NH₃ gas, the percentage change of the transmitted light at the three wavelengths is shown in Fig. 32, for several testing cycles [19]. The results show that the changes of the output are 26%, 22%, and -6% for light sources with wavelengths of 633 nm, 850 nm, and 1,300 nm, respectively. Significantly, the change of the optical output at 1,300 nm is not only small, but also negative. The negative sign means that the output power increases when the sensor exposed to NH₃. At the wavelength of 1,300 nm, the polyaniline has lower absorption when exposed to NH₃ gas. That is just opposite from the case when light sources with wavelength of 633 nm and 833 nm are used. This experiment shows that the highest change in the sensor output was 26% at the wavelengths of 633 nm. Also, it shows that the sensitivity of the sensor is highly dependent on the wavelength of the light sources.

5.3.2 Spatial Intensity Measurements

In the previous section, the results on using the total intensity modulation technique are recorded. In this section, the improvement of the sensor sensitivity, when the MPD method is applied, is presented. Based on the results achieved before, when total intensity technique was used, a He-Ne laser with wavelength of 633 nm was

selected as the light source. The optical fiber was excited with an off-axis laser beam, and the far-field pattern was detected using a CCD camera, as shown in Fig. 31. Figure 33 presents a sample of the far-field pattern before and after the sensor was exposed to HCl vapor and NH_3 gas. The ring looked much brighter when the sensor was exposed to HCl vapor, Fig. 33 (left). The whole ring became darker when the sensor was exposed to NH_3 gas, Fig. 33 (right). The normalized radial intensity profiles of the ring patterns are shown in Fig. 34. The change of the output reached 67% between exposure to HCl and NH_3 chemical vapors, compared with 26% change for the same sensor with total intensity method used before. This experiment shows the dramatic improvement of the sensor sensitivity (more than double), when the SIM method is applied.

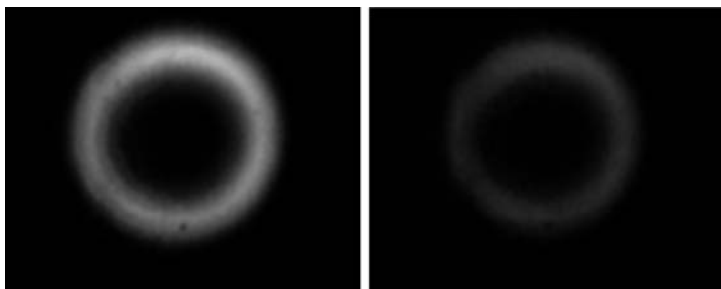


Fig. 33 Far-field ring pattern of MPD: *left* – after sensor exposed to HCl and *right* – after sensor exposed to NH_3

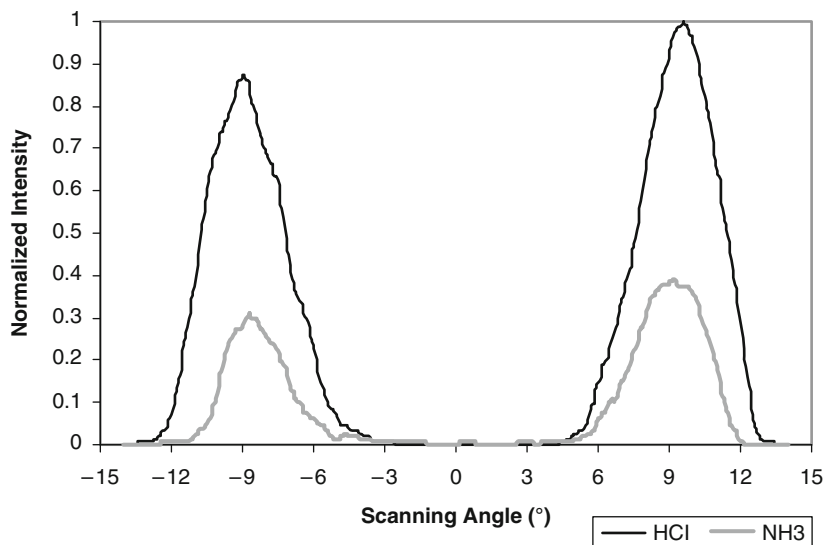


Fig. 34 Normalized intensity profiles of the 2D ring pattern of Fig. 33

6 Concluding Remarks

The intention of the author of this chapter was to provide an introductory knowledge base on the application of fiber optics in chemical and biosensors. The field of fiber-optic sensors is progressing very rapidly, with significant new research being continuously reported for various sensors applications.

In this chapter, a general introduction to fiber-optic sensors is presented, followed by sections on the principle of sensors design and sensors development and processing, as well as on sensors characterization and optimization. The technical feasibility and viability of fiber optics in chemical and biosensors applications have been demonstrated with a number of examples and a list of references on successfully reported research. Also, an overview on state-of-the-art research is presented, which is still under development and requires more work before the ultimate limits imposed by fiber optics science and technologies are reached.

Because of the numerous advantages in fiber-optic sensors, it is expected that the market of chemical and biosensors will be expanding day after day, and because of the rapid changes in fiber optics technologies, it is expected more expansion in the near future in applications to chemical and biosensors. The pace of research in fiber-optic chemical and biosensors has continued to be expanding in recent years, especially in the field of intrinsic-type sensors. This was considered during the preparation of the scientific information presented in this chapter. It is prepared for researchers and graduate students who are interested in learning and understanding the fundamentals in fiber-optic sensors, which provides them with the required knowledge base for future research.

References

1. Chan K, Ito H, Inable H (1984) An optical fiber based gas sensor for remote adsorption measurement of low level methane gas in near infrared region. *J Lightwave Technol* 2:234–237
2. Stewart G, Jin W, Culshaw B (1997) Prospects for fiber optic evanescent field gas sensors using absorption in the near infrared. *Sensors Actuators B Chem* 38:42–47
3. Wolfbeis OS (1992) *Fiber optic chemical sensors and biosensors*, vols 1 and 2. CRC, Boca Raton, FL
4. Wolfbeis OS, Posch HE (1986) Fiber optic fluorescing sensor for ammonia. *Anal Chim Acta* 185:321–324
5. Baker SLR, Kopelman R, Meyer TE, Cusanovich MA (1998) Fiber optic nitric oxide selective biosensors and nanosensors. *Anal Chem* 70:971–976
6. Healy BG, Li L, Walt DR (1997) Multianalyte biosensors on optical imaging bundles. *Biosens Bioelectron* 12:521–529
7. Ferguson JA, Boyles TC, Adams CP, Walt DR (1996) Fiber optic DNA biosensor microarray for the analysis of gene expression. *Nat Biotechnol* 14:1681–1684
8. Rowe-Taitt CA, Ligler FS (2001) Fiber optic biosensors. In: Lopez-Higuera JM (ed) *Handbook of optical fiber sensing technology*. Wiley, New York, pp 687–700
9. Dietrich AM (1996) Measurement of pollutants: chemical species. *Water Environ Res* 68:391–406

10. Holst G, Mizaikoff B (2001) Fiber optic sensors for environmental sensing. In: Lopez-Higuera JM (ed) Handbook of optical fiber sensing technology. Wiley, New York, pp 729–749
11. Mizaikoff B et al (1995) Infrared fiber optic gas sensor for chlorofluorohydrocarbons. *Vib Spectrosc* 8:103–108
12. Schwotzer G (1997) Optical sensing of hydrocarbons in air or in water using UV absorption in the evanescent field of fibers. *Sensors Actuators B Chem* 38:150–153
13. Anderson FP, Miller WG (1988) Fiber optic immunochemical sensor for continuous, reversible measurement of phenytoin. *Clin Chem* 34:1417–1427
14. Riberio ABL, Jackson DA (1993) Low coherence fiber optic system for remote sensors illuminated by a 1.3 μm multimode laser diode. *Rev Sci Instrum* 64:2974–2977
15. El-Sherif MA (2003) Smart textiles created with embedded sensors. *MRS Bull Technol Adv* 28:101–102
16. Radhakrishnan J (1996) Real time characterization of composite materials using fiber optics techniques. PhD Thesis, Drexel University, Pennsylvania, USA
17. Ferreira A, Werneck MM, Ribeiro RM (2001) Development of an evanescent-field fibre optic sensor for *Escherichia coli* O157:H7. *Biosens Bioelectron* 16:399–408
18. El-Sherif MA, Zemel JN (1985) Twisted pair optical fiber pH sensors. Technical Digest, IEEE Third International Conference on Solid-State Sensors and Actuators, pp 434–437
19. Yuan J (2001) Polymer materials as modified optical fiber cladding for chemical sensors. PhD Thesis, Drexel University, Pennsylvania, USA
20. Bansal L (2004) Development of a fiber optic chemical sensor for detection of toxic vapor. PhD Thesis, Drexel University, Pennsylvania, USA
21. El-Sherif MA, Yuan J, MacDiarmid A (2000) Fiber optic sensors and smart fabrics. *J Intell Mater Syst Struct* 2:407–414
22. Yuan J, El-Sherif MA (2003) Fiber-optic chemical sensor using polyaniline as modified cladding material. *IEEE Sens J* 3:5–12
23. Abdelghani A, Jaffrezic-Renault N (2001) SPR fibre sensor sensitized by fluorosiloxane polymers. *Sensors Actuators B Chem* 74:117–123
24. Macedo PB, Barkatt A, Feng X, Finger SM, Hojaji H, Laberge N, Mohr R, Penafiel M, Saad E (1989) Development of porous glass fiber sensors, Fiber optic structures and smart skins. *Proc SPIE* 986:200–205
25. Shahriari MR, Zhou Q, Sigel GH (1988) Porous optical fibers for high-sensitivity ammonia vapor sensors. *Opt Lett* 13:407–409
26. Zhou Q, Sigel GH (1998) Detection of carbon monoxide with a porous polymer optical fiber. *Int J Optoelectron* 4:415–523
27. Tao S, Winstead CB, Singh JP, Jindal R (2002) Porous sol-gel fiber as a transducer for highly sensitive chemical sensing. *Opt Lett* 27:1382–1384
28. MacDiarmid AG (1991) Sciences and technology of conducting polymers. In: Prasad PN, Nikam JK (eds) *Frontiers of polymer research*. Plenum, New York, pp 259–269
29. MacDiarmid AG (2001) Synthetic metals: a novel role for organic polymers. *Synth Met* 125:11–22
30. Collins GE, Buckley LJ (1996) Conductive polymer-coated fabrics for chemical sensing. *Synth Met* 78:93–101
31. Potje-Kamloth K (2002) Chemical gas sensors based on organic semiconductor polypyrrole. *Crit Rev Anal Chem* 32:121–140
32. Bansal L, Khalil S, El-Sherif M (2002) Fiber optic neurotoxin sensor. Proceedings of the IEEE 28th Annual Northeast Philadelphia, pp 20–21
33. Yuan J, El-Sherif MA, MacDiarmid AG, Jones W (2001) Fiber optic chemical sensors using modified conducting polymer cladding. *Proc SPIE* 4205:170–179
34. MacDiarmid AG (1995) Secondary doping in polyaniline. *Synth Met* 69:85–92
35. Liu J, Wan M (2001) Polypyrrole doped with 1, 5-naphthalenedisulphonic acid. *Synth Met* 124:317–321
36. El-Sherif MA (1989) On-fiber sensor and modulator. *IEEE Trans Instrum Meas* 38:595–598

37. El-Sherif MA (2001) The Final Technical Report on Sensors and Smart Fabrics. The MURI-ARO (Army Research Office) project on Functionally Tailored Textiles, Contract #DAAH 01-96-1-0018
38. Radhakrishnan J, El-Sherif MA (1996) Analysis on spatial intensity modulation for fiber optic sensor applications. *J Opt Fiber Technol* 2:114–126
39. Snyder A, Love J (1983) *Optical waveguide theory*. Chapman and Hall, New York

Applications of Fiber Gratings in Chemical and Biochemical Sensing

Tinko Eftimov

Abstract The basic idea of using fiber gratings for chemical and biochemical sensing is presented in this chapter. The physical nature and practical applications of regular and tilted fiber Bragg (FBG) as well as long-period (LPG) gratings and the associated LPG-based interferometers are discussed. Sensitivity characteristics and methods of fabrication are considered. Various chemical and biochemical sensing applications are described and compared.

Keywords Fiber- optic sensors · Tilted fiber Bragg gratings (TFBG) · Long-period gratings (LPG) · LPG-based interferometers · Chemical and biochemical sensing

Contents

1	Introduction	153
2	Fiber Bragg Gratings and Long-Period Gratings	154
2.1	Physical Principles and Characteristics	154
2.2	Fabrication, Interrogation and Multiplexing Techniques	160
3	Chemical and Biochemical Sensing Applications	161
3.1	Straight and Tilted FBG-Based Sensors	161
3.2	LPG-Based Sensors	164
3.3	Intermodal Interference-Based Sensors	172
4	Concluding Remarks	173
	References	174

Abbreviations

CCD	Charge-coupled device
DNA	Deoxyribonucleic acid

T. Eftimov

Faculty of Physics, Plovdiv University "Paisii Hilendarski", Plovdiv 4000, Bulgaria
e-mail: teftimov@uni-plovdiv.bg.

DNP	Dinitrophenyl compound
FBG	Fiber Bragg grating
FM	Fundamental mode
HIV	Human immunodeficiency virus
HOCM	Higher-order cladding mode
ISAM	Ionic self-assembled multilayers
LPG	Long-period grating
MSFBG	Microstructured FBG
MSOF	Microstructured optical fibers
OSA	Optical spectrum analyzer
PAH	Poly(alamine hydrochloride)
POC	Point-of-care
PVA–PAA	Polyvinyl alcohol–polyacrylic acid
RIU	Refractive index unit
SDM	Space division multiplexing
SRI	Surrounding refractive index
TAP	Turnaround point
TDM	Time division multiplexing
TFBG	Tilted fiber Bragg grating
UV	Ultraviolet
WDM	Wavelength division multiplexing

Symbols

b	Radius of fiber cladding
J_0	Bessel function
N	Number of pitches along a grating
n	Higher refractive index of the periodic structure
n_0	Lower refractive index of the periodic structure
n_1	Fiber core refractive index
n_2	Fiber cladding refractive index
n_a	Ambient refractive index (SRI)
n'_a	Ambient refractive index (SRI) after a change δn_a is introduced
n_{air}	Refractive index of air
n_c	Effective refractive index of the fundamental core mode
n_{cl}	Effective refractive index of the higher-order cladding mode
n_e	Effective refractive index of the fiber
$n_{e,i}$	Effective refractive index of the core mode at λ_i
n_i	Effective refractive index of the cladding mode at λ_i
n_m	Effective refractive index of the m -th HOCM of an LPG
β_c	Propagation constant of the fundamental core mode
β_{cl}	Propagation constant of the higher-order cladding core mode
δn_a	A change in the SRI

Λ	Actual pitch length for a straight LPG or effective pitch length in a tilted LPG
Λ_g	Actual pitch length in tilted LPG
λ	Wavelength
λ_B	Resonance Bragg wavelength
λ_i	Resonance wavelengths of the HOCMs of a TFBG
$\lambda_{m,LPG}$	LPG resonance wavelength corresponding to the m -th HOCM
$\delta\lambda$	Center wavelength shift
$\Delta\lambda$	Finite center wavelength shift
K_ε	FBG strain sensitivity coefficient
K_T	FBG temperature sensitivity coefficient
K_p	FBG pressure sensitivity coefficient
$K_{\varepsilon,m}$	LPG strain sensitivity coefficient for the m -th HOCM
$K_{T,m}$	LPG temperature sensitivity coefficient for the m -th HOCM
$K_{p,m}$	LPG pressure sensitivity coefficient for the m -th HOCM
$K_{b,m}$	LPG bending sensitivity coefficient for the m -th HOCM
$K_{\tau,m}$	LPG sensitivity coefficient to torsion for the m -th HOCM
$K_{n,m}$	LPG sensitivity coefficient to SRI for the m -th HOCM
S_ε	Strain sensitivity
S_T	Temperature sensitivity
S_p	Pressure sensitivity
u_∞	The m -th root of the Bessel function J_0

1 Introduction

Fiber gratings are structures consisting of a periodic perturbation of the optical and/or geometrical properties of an optical fiber. Depending on the pitch Λ of the perturbation, fiber gratings can be subdivided into two distinct categories: short-period gratings, known as fiber bragg gratings (FBGs) introduced 30 years ago [20], and long-period gratings (LPGs), proposed about 18 years later [44]. Fiber gratings have initially and mostly been used as components in the fiber-optic communication area. It was, however, quickly realized that because of their spectral characteristics and sensitivities to a variety of external physical fields, fiber gratings have a huge potential in the fiber sensor technology area. Fiber grating sensor applications have been largely widened with the advent of micro structured optical fibers (MSOFs). While most of the fiber-grating-sensor research and applications have been in the field of strain- and temperature-sensing using multiplexed sensor networks, the development of etched regular FBGs, tilted FBGs, and LPGs, and their sensitivities to changes in the SRI have opened unprecedented opportunities for the development of fiber-optic refractometers.

This chapter is dedicated to the application of fiber gratings for the development of chemical and biochemical sensors on the basis of their sensitivity to SRI changes.

Section 2 introduces the basic idea, the properties, and sensitivities of regular, tilted FBGs and LPGs, as well as the fabrication, multiplexing, and interrogation techniques. Section 3 is devoted to the proposed applications of fiber gratings in the development of chemical and biochemical sensors.

2 Fiber Bragg Gratings and Long-Period Gratings

2.1 Physical Principles and Characteristics

2.1.1 Straight and Tilted FBGs

Principle of operation. Let us consider a distributed periodic structure consisting of a series of transitions from a lower refractive n_0 to a higher refractive index n as shown in Fig. 1. This is a grating structure with a period Λ and a refractive index modulation Δn . Waves reflected at each interface will interfere with one another and for a given period Λ constructive interference due to phase matching will be observed only for a particular resonance wavelength such that $\lambda/2 = n_0\Lambda$, where λ denotes the wavelength. Such a structure is known as a Bragg grating and is characterized by its resonance Bragg wavelength $\lambda_B = 2n_0\Lambda$ at which the reflectance (R) reaches a maximum and the transmittance (T) a minimum.

Let us now consider an optical fiber which uses total internal reflection to guide light waves. Its core has a higher refractive index n_1 compared to that of the cladding n_2 . Wave structures called “modes” travel along the fiber. When the core supports only one mode, the fiber is single-mode. This fundamental mode (FM) of the core has a propagation constant β_c such that $kn_2 < \beta_c = kn_c < kn_1$, where $k=2\pi/\lambda$ is the free space wave number and n_c is the modal effective refractive index. A periodic structure like the one shown in Fig. 1b will cause the forward propagating core FM to couple to a backward propagating core FM, described by a coupling coefficient q , as well as to backward propagating higher-order cladding modes (HOCMs) shown in Fig. 2, with propagation constants β_{cl} such that $kn_{air} < \beta_{cl} = kn_{cl} < kn_2$, and n_{cl} is the cladding mode effective index. The basic idea beyond an FBG is thus counter-directional coupling.

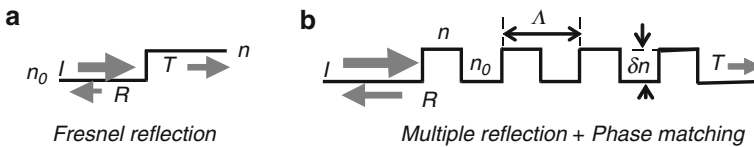


Fig. 1 (a) Fresnel reflection at the interface of two media. (b) Reflection from a periodic structure at a particular resonance wavelength λ_B

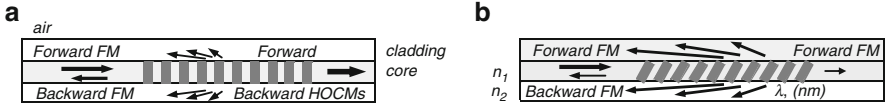


Fig. 2 In an FBG, the forward FM is coupled to a backward FM and to HOCMs (a) regular BFG with strong coupling to a backward FM and weak coupling to a multitude of HOCMs; (b) a tilted FBG with weak coupling to a backward FM and a strong coupling to a multitude of HOCMs

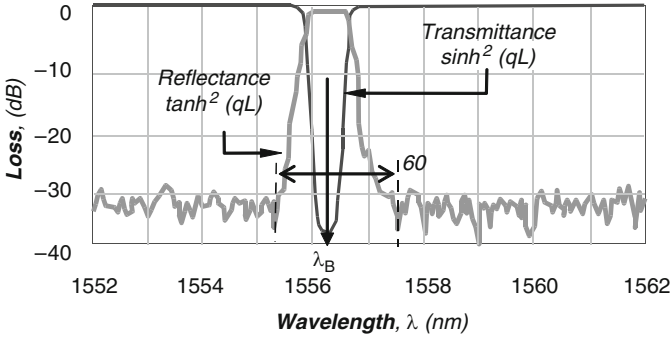


Fig. 3 Reflectance and transmittance spectra at the central wavelength λ_B of a strong apodized regular FBG. The much weaker spectra of the HOCMs situated at lower wavelengths are not shown

Spectral characteristics. In an FBG, coupling is to a backward core FM at λ_B , and to HOCM at a multitude of wavelengths λ_i ($i = 1$ to n). We thus observe both a peak of maximum reflectance and corresponding attenuation minima at λ_B and λ_i (Fig. 3). The central Bragg wavelength λ_B is given as:

$$\lambda_B = 2n_e\Lambda, \tag{1}$$

where n_e is the effective refractive index of the fiber, while the pitch Λ is typically about half a micron.

In a tilted (slanted) FBG, most of the optical power of the forward core FM is back-coupled to a multitude of HOCMs [13], whose fields propagate in the cladding. Therefore, the higher the mode order, the more the modal field “feels” the changes in the SRI. This implies that we can obtain different sensitivity to SRI for each HOCM.

The resonance Bragg wavelength is again given by (1), but Λ is the projection of the actual grating period Λ_g along the fiber axis due to the tilt angle θ and $\Lambda = \Lambda_g \cos\theta$. The resonance wavelength λ_i of the i -th cladding mode can be found as [27]:

$$\lambda_i = (n_{e,i} + n_i)\Lambda, \tag{2}$$

Table 1 Classification of FBS depending on the modulation type of their refractive indices









<p>❖ Weak: small Δn <i>Reflectivity is 10 to 40 % maximum</i></p> 	<p>○ Strong: large Δn <i>Reflectivity is > 40 %</i></p> 
<p>❖ Uniform: $\Delta n = \text{const}$ <i>Strong side lobes</i></p> 	<p>○ Apodized: Δn varies <i>Side lobes suppressed</i></p> 
<p>❖ Regular: $\Lambda = \text{const}$ <i>Narrow bandwidth and low dispersion</i></p> 	<p>○ Chirped: Λ varies <i>Broad bandwidth and high dispersion</i></p> 
<p>❖ Straight FBGs <i>Back-couples to a core mode</i></p> 	<p>○ Tilted <i>Back-couples to radiation modes</i></p> 

Table 2 Typical values for the sensitivities of FBGs

λ	S_ϵ (pm/ $\mu\epsilon$)	S_T (pm/ $^\circ\text{C}$)	S_p (pm/bar)
850 nm	≈ 0.6	7–7.84	–
1,300 nm	1.051	10.5	–
1,550 nm	1.254	12.5	≈ 0.43

where $n_{e,i}$ is the effective refractive index of the core mode at λ_i and n_i is the effective refractive index of the cladding mode at the same wavelength. If a tilted FBG is additionally etched and hence the cladding diameter is reduced, the number of HOCMs is consequently reduced and the spectral response changes as well [7].

Depending on the optical and geometric parameters Δn and Λ , various types of FBGs exist and the most important are summarized in Table 1.

Sensitivities to external fields. Sensor applications of FBGs are dependent on the sensitivities to external physical fields. The relative center wavelength shift of silica-fiber-based Bragg gratings can be written as:

$$\delta\lambda/\lambda_B = K_\epsilon\delta\epsilon + K_T\delta T + K_p\delta p, \tag{3}$$

where K_ϵ , K_T , and K_p are the strain, temperature [24], and pressure coefficients. The corresponding sensitivities $S_\epsilon = \lambda_B K_\epsilon$, $S_T = \lambda_B K_T$, and $S_p = \lambda_B K_p$ at three different wavelengths are given in Table 2.

There is also a very weak dependence on magnetic field which, for the usual ambient conditions, is negligible.

Etched FBGs. FBGs are practically insensitive to bending and twisting, and since the FM is strongly confined in the fiber core and not in the cladding, there is practically no sensitivity to changes in the surrounding refractive index (SRI). However, if the grating region is etched, then the tails of the FM distribution get closer to the fiber/air interface and the center wavelength position becomes

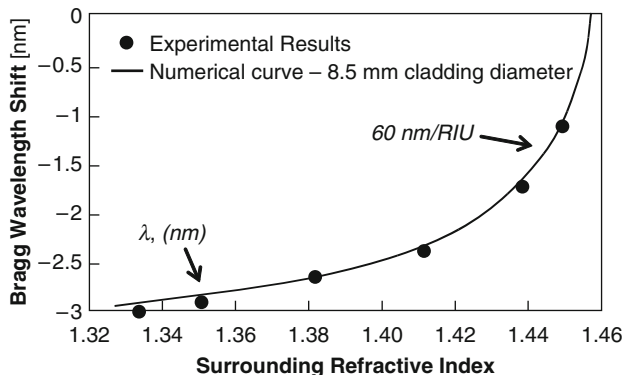


Fig. 4 Center-wavelength shift of the reflected spectrum of a thinned Bragg grating with a cladding diameter of 8.5 μm . Reprinted with permission from [10]

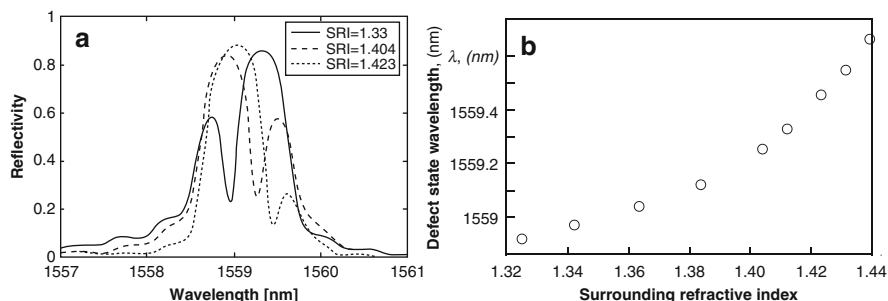


Fig. 5 Spectral response of an MSFBG to SRI changes: (a) Positions of the dip wavelength λ_D for three different SRIs; (b) Dependence of λ_D on the SRI. Reprinted with permission from [22]

sensitive to the ambient refractive index changes [10, 21], as shown in Fig. 4. The sensitivity is largely dependent on the diameter of the thinned section and on SRI. For an 8.5 μm cladding diameter of an FBG written in the standard SMF-28 communication fiber, the sensitivities range from 8.8 nm/RIU around $n = 1.36$ to about 60 nm/RIU or more for $n = 1.45$, which is close to the value of the cladding refractive index. As the minimum detectable wavelength shift is of the order of 1 pm, only temperature and strain sensing is then of practical importance for a straight FBG.

Iadicicco et al. [21, 22] also proposed a microstructured FBG (MSFBG) design, in which case, the FBG cladding is not etched over the entire length L but only in the central part $L_{th} < L$, to a diameter $D_{th} < D_{clad}$. The net effect of this partial etching is that the constructive interference along the FBG that gives rise to the reflected signal is broken because of the introduced defect in the grating structure and, as a result, the reflection spectrum exhibits a narrow dip at a center wavelength λ_D (defect state wavelength). Changes in the SRI induce a shift of λ_D within the bandwidth of the MSFBG, as illustrated in Fig. 5.

By analyzing both the shifts of λ_D and the relative intensity changes of the spectral response, SRI changes within the ranges 1.391–1.420 and 1.364–1.40 with resolutions of respectively 4×10^{-5} RIU and 6×10^{-5} RIU [21].

Tilted FBGs. For a tilted FBG (TFBG), the center wavelength of the reflected FM is not dependent of the SRI and can be used as a reference. Therefore, the differential shift of each cladding mode $\lambda_B - \lambda_i$ is caused by the dispersion of the cladding modal refractive index. The sensitivity to SRI changes are found to be:

$$\Delta(\lambda_B - \lambda_i)/\Delta n = -\Lambda \partial n_i / \partial n. \tag{4}$$

Laffont and Ferdinand [27] tested TFBGs with tilt angles from 8° to 16° , lengths of about 8 mm and $\lambda_B = 1,530$ nm. For SRI changes between 1.0 and 1.3, a total red shift $\Delta\lambda_i \approx 200$ pm takes place without noticeable changes in the attenuation. Varying SRI from 1.3 to 1.43 leads to changes in both wavelength and attenuation, because the SRI approaches the effective refractive index of the HOCMs. These changes were used to show that a resolution of 10^{-4} can be achieved with this type of refractometer. Chen et al. [7] showed that the same resolution can be obtained from individual tracing of the transmission minima for the HOCMs, each one of them exhibiting different sensitivity to SRI changes.

2.1.2 Long-Period Gratings

Principle of operation, spectral characteristics, and sensitivities. For LPGs, $\lambda_{m,LPG}$ is a separate resonance wavelength corresponding to each HOCM. The higher the mode order m , the greater the difference $n_0 - n_m$ and hence, the higher the resonance wavelength $\lambda_{m,LPG}$ as shown in Fig. 6.

The center wavelength of an LPG is cladding mode order dependent and is given by:

$$\lambda_m = \Delta n_m \Delta, \tag{5}$$

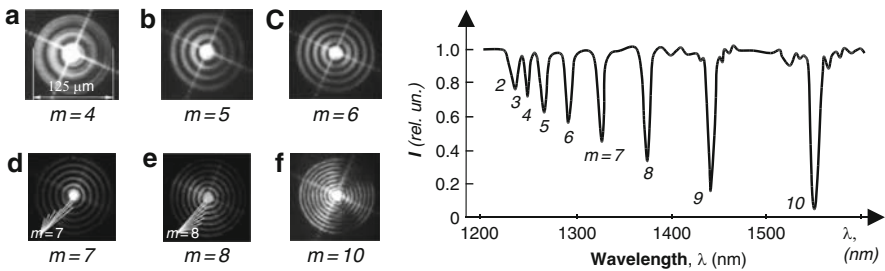


Fig. 6 Near-field distributions of the higher order HE_{1m} cladding modes and the corresponding spectral response of the LPG [42]

where $\Delta n_m = n_0 - n_m$ is the difference between the effective refractive indices of the core FM and of the m -th HOCM. For LPGs, the pitch ranges from 250 to 750 μm .

Because coupling is HOCMs, the center wavelength is dependent not only on strain ε and temperature T , but also on hydrostatic pressure p , bending b , torsion τ and most importantly to the SRI n_a ; thus,

$$\delta\lambda/\lambda_m = K_{T,m}\delta T + K_{\varepsilon,m}\delta\varepsilon + K_{p,m}\delta p + K_{b,m}\delta b + K_{\tau,m}\delta\tau + K_{n,m}\delta n, \quad (6)$$

where the coefficients $K_{i,m}$ ($i = \varepsilon, T, p, b, \tau$ and n) are dependent on the mode order, wavelength, and technology.

The foregoing expression means that if we are interested in refractive index measurements special care must be taken to eliminate all other perturbations. Chiang et al. [8] found that, for an LPG, the wavelength shift due to SRI change from n_a to $n_a' = n_a + \delta n_a$ is given by the expression

$$\delta\lambda \approx \frac{u_\infty^2 \lambda_m^3 \Lambda}{8\pi^3 b^3} \left[\frac{1}{\sqrt{n_{cl}^2 - n_a^2}} - \frac{1}{\sqrt{n_{cl}^2 - n_a'^2}} \right], \quad (7)$$

where n_{cl} is the cladding refractive index, b is the cladding radius, and u_∞ is the m -th root of the Bessel function J_0 . For small changes δn_a of the external refractive index n , after some manipulations, (5) can be rewritten as:

$$\frac{\delta\lambda}{\lambda_m} \approx K_{n,m}\delta n = -\frac{u_\infty^2 \lambda_m^2 \Lambda}{8\pi^3 b^3} \frac{n}{(n_{cl}^2 - n_a^2)^{3/2}} \delta n \quad (8)$$

from where it follows that the sensitivity coefficient $K_{n,m}$ depends on the resonance wavelength λ_m , the SRI, and the cladding radius. As the SRI approaches n_{cl} , the wavelength decreases. The thinner the cladding and the closer the SRI to the refractive index of the cladding, the greater is the sensitivity. Thus, etching an LPG would additionally enhance sensitivity to SRI changes. Chiang et al. [8] proved experimentally the validity of (5) and found that if cladding diameter of an LPG is reduced from 125 to 118 μm , the wavelength shift for SRI variations from 1 to 1.457 increases from 20 to about 50 nm, i.e., by a factor of 2.5.

2.1.3 Core-Cladding Intermodal Interferometers and Cascaded LPGs

Core-cladding intermodal interference. In a stripped fiber, both the core FM and HOCMs can propagate. These two modes interfere and if a spatial filter is used at the output, an intermodal interferometric response will be taken.

There are two ways to obtain such structures. One is to splice two dissimilar fibers, for example, a piece of photonic crystal fiber PCF is spliced between two

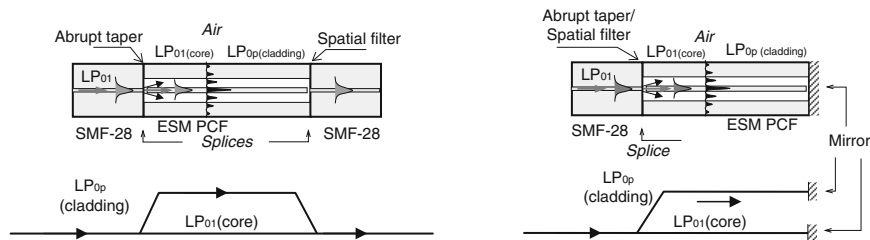


Fig. 7 Equivalent Mach-Zener arrangement of an intermodal interferometer or two cascaded LPGs

Corning SMF-28 fibers in which case the first splice is an abrupt taper and excited HOCMs in the PCF, while the second splice acts as a spatial filter. The other is to fabricate two weak (3 dB) LPGs in series on the same fiber separated by a section of a certain length. The first LPG actually splits the FM into an FM and several HOCMs, while the second recombines them. These constructions are known as cascaded LPGs and equivalently can be represented as a Mach-Zener arrangement as shown in Fig. 7.

Spectral characteristics of intermodal interferometers. An intermodal interferometer has a cosine response. In the case of cascaded LPGs, the spectrum of a single LPG is periodically modulated by the intermodal sine response. So, instead of a broad spectral dip, we have several spikes which are narrower and, thus, wavelength shifts can be detected with greater precision. There are two schemes for intermodal interferometers: the Mach-Zener arrangement and the Michelson arrangement. In the latter, only one splice or LPG is used in combination with a mirror, as shown in Fig. 7b. The light thus traverses the two-mode area twice.

2.2 Fabrication, Interrogation and Multiplexing Techniques

2.2.1 FBG Fabrication Techniques

As the periodicity of FBGs and TFBGs is about half a micron, the only way to fabricate is by making use of photosensitivity, the essence of which is UV-induced changes of the refractive index, in combination with either an interferometer or a phase mask. The project periodic modulation of the light beam is projected on the fiber inducing the desired refractive index changes. The lasers used are then 488 nm and 514 nm Ar-ion, 248 nm KrF-excimer, frequency-doubled 244 nm and 257 nm Ar-ion, frequency doubled XeCl-pumped dye, 197 nm ArF-excimer, and 157 nm F₂ laser. Photosensitivity of the fiber is largely increased by H₂ loading at high pressure. The photo-imprinted grating is stabilized by additional thermal treatment.

LPGs have hundreds of times larger periodicity and UV illumination is just one of the methods. Periodic index modulation can also be achieved using localized

thermal treatment of the fiber by heating to temperatures up to 1,000°C. Using either a CO₂ (or CO) laser, or electric arc-discharge with a conventional splicer. These methods are cheaper and more available than the far more complicated UV photo-imprinting method.

2.2.2 Grating Sensor Interrogation Techniques

There are several commonly used fiber-grating interrogation techniques which allow the precise determination of the resonance wavelength. For laboratory purposes, OSA are used and they allow 0.1 nm wavelength shifts to be easily detected.

The other interrogation schemes are based on the use of linear filters, matched gratings, interferometers (Michelson, Mach-Zender, Fabry-Perot), and CCD arrays in combination with diffraction gratings. The best resolution attainable after averaging is about 1 pm. LPGs, however, have a wider spectrum and their wavelength shifts are detected with smaller resolution.

2.2.3 Multiplexing Techniques

The great advantage of fiber gratings is that the changes of the measurand are spectrally encoded. Therefore, the most evident multiplexing technique is wavelength division multiplexing (WDM). The other two techniques are spatial and time division multiplexing (SDM and TDM). In more sophisticated networks, combinations of the above techniques are used to increase the number of multiplexed gratings.

3 Chemical and Biochemical Sensing Applications

3.1 *Straight and Tilted FBG-Based Sensors*

3.1.1 FBG-Based Transducers

pH sensing. While most of the applications of fiber gratings are based on refractive index measurements, it is possible to develop transducers that convert a chemical response into a geometrical change of the FBG and thus, cause wavelength shifts. An FBG based transducer [41] converts pH changes in a solution into volume changes of a hydrogel actuator. Polyvinyl alcohol–polyacrylic acid (PVA–PAA) copolymer is used as a hydrogel, because of large volume variations and small hysteresis in response to pH changes from 3.0 to 5.0. The changes in the hydrogel volume cause elongation of the FBG for an alkaline environment having a high pH

level and low presence of H^+ ions. The polymeric chain gets negatively charged, thus causing repulsion and expansion. In an acid environment with high level of H^+ ions, repulsion is reduced and elongation diminishes. With a FBG interrogation sensitivity of 1 pm, pH variations between 3.0 and 6.0 can be detected with a resolution of 10^{-2} .

Hydrogen detection. Detection of hydrogen (H_2) is based on its high solubility in palladium. H_2 -induced lattice expansion of Pd causes the latter to swell, changes its conductivity and refractive index. The swelling effect can be sensed with FBGs in strain sensing mode.

Peng et al. [32] deposited a 70 nm *Ti* layer followed by a 1 μm *Pd* layer on an FBG. They observed wavelength shifts of maximum 240 pm for 0.6% concentration of H_2 in nitrogen and exposure of 4 h with response times on the order of minutes. H_2 was then purged out with N_2 for another 4 h. This procedure was repeated up to 24 times. A degradation of the responses was observed with the number of cycles expressed in a decrease of maximum wavelength shift and an increase of the response time. The sensor was found to recover after air heat treatment.

Maier et al. [29] used two FBGs in series of which the first senses temperature and the other is coated with Pd to sense H_2 in nitrogen at atmospheric pressure. They reported a sensitivity of 0.7 pm/ppm of H_2 . Increase of temperature was found to diminish sensitivity.

3.1.2 Sensing Applications of Etched Straight FBGs

Concentration measurement of propylene glycol and sugar solutions. As FBGs are sensitive to temperature changes, special measures must be taken to compensate for thermal effects. An interesting approach for efficient temperature compensation has been suggested by Sang et al. [35] by fabricating a half-etched strong FBG having an initial center wavelength at 1,552.04 nm and a reflection of 99.6%. The spectrum of the half-etched FBG splits into two peaks, the lower corresponding to the etched half (Fig. 8). The two halves have the same sensitivities to temperature, but only the thinned one is sensitive to ambient refractive index changes. Thus, the wavelength separation $\Delta\lambda$ depends on the external refractive index alone. Two FBGs with diameters of the etched regions of 6.5 μm and 8.1 μm correspondingly have been fabricated and tested. Sensitivities of 15 pm/% and 11 pm/% in propylene glycol solutions and of 37 pm/% and 27 pm/% for sugar solutions have been reported [35].

Alcohol sensing. An etched FBG was used [28] to discriminate between methanol ($n = 1.326$), ethanol ($n = 1.359$), and isopropyl alcohol (IPA) ($n = 1.378$) (Fig. 9). The FBG was written using a KrF excimer laser (248 nm) with a length of 2.5 mm. It was etched down to 15 μm diameter using a 52% solution of hydrofluoric (HF) acid and then to a diameter of 6 μm with a 13% HF solution. The plot of the center wavelengths of the thinned FBG vs ambient refractive index is shown in the next figure.

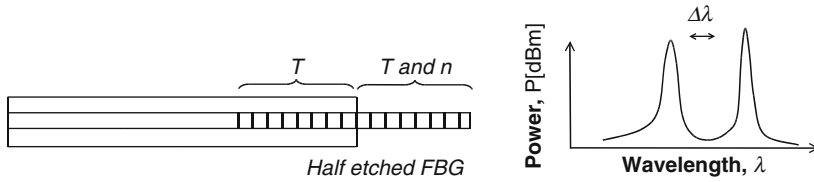


Fig. 8 Construction of a temperature-independent half-etched Bragg grating and the corresponding spectral response of each half

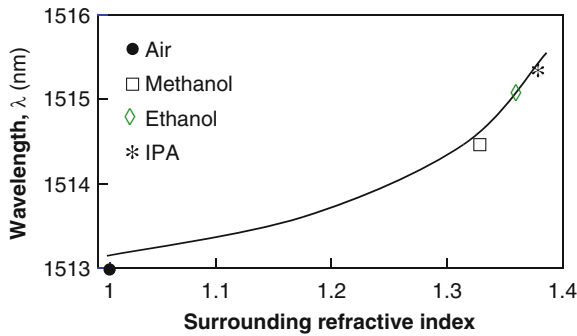


Fig. 9 Center wavelength shifts for methanol, ethanol and IPA obtained with a thinned Bragg grating with a cladding diameter of 6 μm . Reprinted with permission from [28]

3.1.3 Sensing Applications of Tilted FBGs

Sucrose solution. Chen et al. [7], showed that there are two ways to increase the sensitivity of a TFBG refractometer at lower values of the SRI. The first is to generate even HOCMs by increasing the tilt angle, and the second is to overlay the cladding with a thin film whose refractive index is higher than that of silica. The use of several HOCM resonances improves accuracy.

3.1.4 Gold-Coated TFBGs and SPR Sensing Applications

Sucrose solutions. Shevchenko and Albert [36] observed surface plasmon resonances in gold-coated TFBGs in which HOCMs are incident at different angles to the outer surface, thus realizing a fiber-optic version of the Kretschmann configuration. The gold coating modifies the cladding resonances and for some of them the phase-matching condition is met which leads to their tunneling. The change of SRI lead to wavelength shifts with a slope of $454 \text{ pm}/10^{-3} \text{ RIU}$.

DNA target detection. In a very recent paper, Shevchenko et al. [37] reported the deposition of a 20 nm gold coating on TFBGs with a tilt angle of 10° . The sensor

was inserted in a buffer solution. Then a single-strand DNA sequence containing 15 bases and an attached thiol group at the end of the chain was immobilized on the gold plated surface, which lead to a wavelength shift. The estimated length of this DNA sequence was 5 nm and its refractive index around 1.5. The sensor was then immersed into a similar buffer solution containing a single-stranded target DNA complimentary to the previously immobilized one. This led to a decrease by 60% of the observed resonance peak. This was indicative of the formation of a DNA monolayer in aqueous solutions.

3.2 LPG-Based Sensors

3.2.1 Bare LPGs as Chemo- and Biochemical Sensors

Petroleum hydrocarbon detection. Leakage monitoring or fluid identification is of practical importance in pipelines transporting petroleum products. In such systems, avoiding electrical sparks is crucial because of evident safety considerations. Therefore, the use of fiber grating sensors presents a serious advantage. The different refractive indices of the hydrocarbon compounds, such as commercial gasoline ($n = 1.4240$), pure gasoline (1.4470), naphtha (1.4059), and solvents like thinner (1.4652), turpentine (1.4411), and alcohol (1.3665) make it possible to distinguish them easily [25] as well as to perform quality control and detect illegal admixture proportions and thus prevent malpractices. Falate et al. [14, 15] have used arc-induced LPGs for gasoline blend and solvent mixture characterization (LPG₁: $\lambda = 1,586.4$ nm, $\Lambda = 649$ μ m, $N = 53$) and for butane–propane mixtures (LPG₂: $\lambda_1 = 1,559$ nm and $\lambda_2 = 1,573$ nm, $\Lambda = 604$ μ m, $N = 60$). As alcohol and naphtha have lower refractive indices compared to commercial gasoline, they shift resonance LPG wavelengths to higher values. On the contrary, turpentine and especially thinner have higher indices of refraction, and shift the center wavelengths to lower values. The same research group has studied LPG spectral responses in water polluted with gasoline, diesel, turpentine, kerosene, and thinner. Wavelength shifts from 5 nm for gasoline detection, up to 49 nm for kerosene detection were reported which is higher than the temperature induced shifts over the 20–60°C interval. As the wavelength shift caused by pollutants is instantaneous, this opens a possibility for real-time monitoring of water pollution.

Concentration measurements of aqueous solutions of salt, sugar, antifreeze etc. Quality control of a number of industrial processes requires checking the concentration stability of different solutions and water soluble fluids. The off-line use of Abbe refractometers is sometimes an obstacle to real-time process control. Several researchers have tested different types of LPGs for the measurement of concentrations of aqueous solutions of sugar, salts, and antifreeze. Falciai et al. [16] used a UV written LPG ($\lambda = 1,530$ nm, $\Lambda = 400$ μ m) to measure concentrations of aqueous solutions of sodium chloride (NaCl) and calcium chloride (CaCl₂) having refractive indices in the 1.32–1.42 range. In a later paper, Falciai et al. [17] also measured

concentrations of aqueous solutions of ethylene glycol $(\text{CH}_2\text{OH})_2$. They have monitored the transmission spectrum and its first derivative for a more accurate determination of wavelength shifts. The curves for the wavelength shift vs SRI and vs concentration were taken and it was found that the minimum concentration variations that can be measured are from 20 g/l for highly diluted to 4 g/l for highly concentrated NaCl solutions; from 10 g/l for highly diluted to 3 g/l for highly concentrated CaCl_2 solutions and from 20 g/l for highly diluted to 10 g/l for highly concentrated $(\text{CH}_2\text{OH})_2$ solutions. Compared with the results obtained with a conventional Abbe refractometer, these resolutions were found to be comparable for the low-concentrated solutions and 3–5 times better for the highly concentrated solutions. Thus, on the whole, the LPG sensor had the same or higher resolution than the conventional Abbe refractometer.

Patrick et al. [31] used seven LPGs, UV-written (KrF excimer laser) in a dispersion shifted fiber, with periods ranging from $\Lambda = 200$ to $\Lambda = 350$ μm , to measure antifreeze concentration in water. They have shown that the resonance wavelengths are not only mode order dependent, but strongly dependent on the grating periodicity Λ , namely the shorter the period, the greater the wavelength. The spectral responses of the 275 μm LPG to the concentration of antifreeze in water is shown in Fig. 10, the total shift in the 1.33–1.44 range being 24 nm.

Similarly, Chong et al. [9] tested CO_2 laser written LPGs with a period of 420 μm to measure concentrations of aqueous solutions of sugar, salt, and ethylene glycol and observed 6 nm decrease of resonance wavelength for SRI varying from 1.33 to 1.42.

Shu and Huang [38] used the wavelength separation between two neighboring resonance wavelengths of a 100 μm UV laser (KrF) written LPG. As SRI increases, the peak-to-peak separation increases and the total change observed from 0% to 60% solution of cane sugar in water was 229.2 nm, which allowed an average resolution of 4.8×10^{-5} RIU in the 1.33–1.44 range. This made it possible to detect a minimum concentration of 0.01% of cane sugar in water.

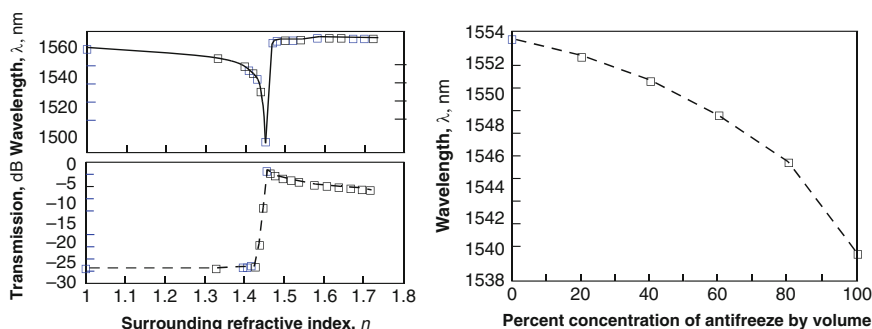
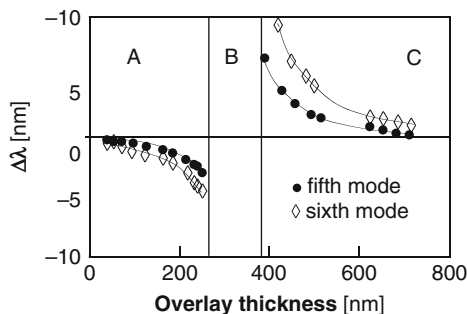


Fig. 10 Response to solutions of antifreeze in water for an LPG with $\Lambda = 275$ μm : (a) Wavelength shift and transmission changes as a function of SRI; (b) Wavelength shift as function of the percent concentration of antifreeze in water. Reprinted with permission from [31]

Fig. 11 Wavelength shifts vs. overlay thickness for coupling to two different cladding modes. Reprinted with permission from [33]



Chen et al. [6] used LPGs written in an etched D-shaped highly birefringent fiber. In this case, the fiber core is elliptic and the cladding boundary is flat on the one side parallel to the major core axis. The fields of the cladding modes are then closely exposed to changes in the SRI. The authors have tested spectral responses in aqueous solutions of sugar in the 0% to 60% range and have obtained a sensitivity of 0.2% with a standard interrogation technique of spectral resolution 0.1 nm.

Detection of aromatic organic compounds. Allsop et al. [1] used LPGs to detect small changes in the concentration of organic compounds like xylene in heptane (paraffin) solutions. The authors have used the fact that different cladding modes exhibit different wavelength shifts for the same changes in the SRI and the higher the mode, the higher the sensitivity. Six LPGs with different lengths and pitches varying from 34 to 550 μm were tested to couple power to the cladding mode with the highest sensitivity to SRI. Best sensitivity was observed with the 16th HOCM of an LPG of $A = 111 \mu\text{m}$ and a total length of $L = 160 \text{ mm}$ written in a B/Ge codoped single mode fiber. For this mode $d\lambda/dn = 439.7 \text{ nm/RIU}$. At lower concentrations (0.1–0.3%) of the xylene in heptane, a sensitivity of 0.07% corresponding to $\Delta n = \sim \pm 1.8 \times 10^{-4}$ was achieved, while at higher concentrations, (0.4–1%) the sensitivity was 0.004% corresponding to $\Delta n = \sim \pm 6 \times 10^{-5}$.

Chloride ion detection for corrosion monitoring. Tang and Wang [40] measured chloride ions in a typical concrete sample immersed in saltwater solutions with different weight concentrations ranging from 0% to 25%. The LPG sensor exhibited a linear decrease in the transmission loss and resonance wavelength shift when the concentration increased. The measurement accuracy for the concentration of salt in water solution was estimated to be 0.6% and the limit of detection for chloride ions was about 0.04%.

3.2.2 Overlaid and Coated LPGs for Improved Chemo- and Biochemical Sensing

Nanolayers on LPGs. The highest sensitivity of LPGs to SRI is within the 1.44–1.456 range. This presents one major problem: higher refractive indices (HRI) cannot be measured with the highest possible sensitivity. Another issue is that in

biosensing it is desirable to deposit thin films on the LPG which bind to an analyte that has to be sensed. This poses the question as to how the response and the sensitivity of the LPG are changed when layers with HRI are deposited on the LPG surface.

The issue was initially studied by Rees et al. [33] who used the Langmuir–Blodgett technique to deposit nanometer-thick overlays on the LPG surface. The technique allows a layer-by-layer deposition of organic molecules to form nanolayers on a substrate. The obtained results showed a strong dependence of the center wavelength shift with the thickness of an overlay film whose refractive index is higher than that of silica (1.456). The shape of the wavelength shift curves vs overlay thickness d exhibited three characteristic regimes: (A) $d < 250$ nm for which the shift is decreasing and negative reaching a maximum of about 5 nm; (B) $250 \text{ nm} < d < 380$ nm with no coupling wavelengths and (C) $d > 250$ nm in which the shift is positive and decreasing from about +10 nm as shown in (Fig. 11).

Cusano et al. [11, 12] studied theoretically and experimentally the responses and sensitivities of overlaid LPGs for optochemical sensing applications. The numerical results showed that the HRI coating leads to an increase in the effective refractive index of the cladding modes and in turn, a decrease in the resonance wavelengths and in the peak loss which are mode dependent as illustrated in the Fig. 12 and Fig. 13.

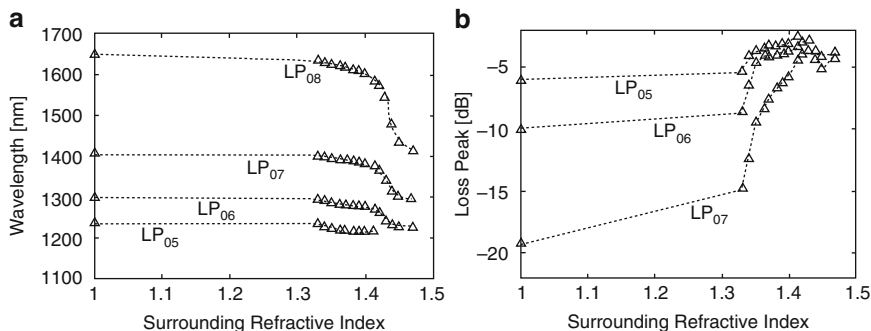


Fig. 12 Response to SRI changes for different HOCMs of an LPG coated with a 150 nm thick sPS layer: (a) wavelength shifts; (b) loss peak changes. Reprinted with permission from [12]

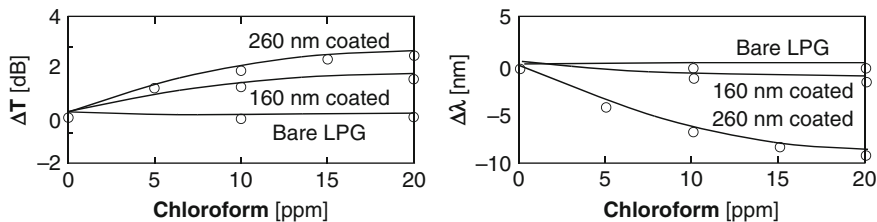


Fig. 13 Response to chloroform concentration changes for bare and coated LPGs: (a) changes in transmission; (b) wavelength shifts. Reprinted with permission from [11]

The presence of the HRI overlay causes modifications in the cladding mode distribution, and thus interaction between the evanescent wave and the surrounding medium is enhanced. This leads an increase in sensitivity to SRI changes and within the transition region around 1.43, the enhancement can be by a factor from 5 to 40. The latter result is of crucial importance for chemical and biochemical sensing applications.

Detection of aromatic compounds. In another work, Cusano et al. [10] performed a series of experiments to detect chloroform dissolved in water using a 30 mm LPG with $\Lambda = 340 \mu\text{m}$ and dip-coated with the δ -form of sPS polymorph semicrystalline polymer having a higher than silica refractive index of 1.578. This form of sPS was chosen for its nanoporous structure allowing the reversible adsorption of a number of analytes, the shape and size of which can fit into the nanocavities and establish host-guest interactions when placed in vapor and liquid environments. The overlay thickness was 150 nm and thus well into regime A described above. The sorption of the analyte (chloroform) into the nanocavities of the sPS promotes an increase in the polymer-layer refractive index. This, in turn, causes changes in the LPG spectrum. Comparison for the changes in transmission and wavelength between a bare LPG and LPGs with 160 nm and 260 nm sPS coatings as a function of the chloroform concentration water is presented in Fig. 13. It is evident from these figures that there are practically no changes in a bare LPG, while the presence of an HRI coating causes peak losses and center wavelength shifts. For a 160 nm coating, sensitivities of 0.163 dB/ppm and -0.130 nm/ppm within the range of 0–10 ppm were found. For the thicker 260 nm coating, these figures become 0.26 dB/ppm and -0.85 nm/ppm , correspondingly. These results show that the HRI coating is clearly responsible for the increase of sensitivity up to a few parts per million of chloroform in water.

Ionic self-assembled multilayers (ISAM). A technologically simple and flexible way to modify the LPG coating effective refractive index is to use ISAMs. As the HOCM field penetrates to about 100–200 nm into the surrounding medium, a multilayer with a typical thickness of 20–30 nm and a refractive index higher than that of silica surrounded by air will cause the mode field to “feel” an average SRI lower than that of silica. The deposition of ISAMs is based on the consecutive immersion–rinsing–immersion process following which the electrostatically charged substrate is first dipped in an aqueous solution of a polyanions, rinsed in deionized water, and then dipped into a solution of polycations. This leads to the adsorption of nanometer-thick monolayers after each dip-and-rinse step. Thus, multilayers of alternating surface charges are deposited and a solid substrate driven by electrostatic forces is formed as shown in Fig. 14a. The advantages of this technique are its ability to fine tune LPG resonances, its suitability to fiber-optic index sensors, and applications to biosensing.

Wang et al. [43] used poly(alamine hydrochloride) (PAH) as polycation and poly{1-[4-(3-carboxy-4-hydroxy-phenylazo) benzenesulphonamido]-1,2-ethanediyl, sodium salt} (PCBS) as polyanion. Wavelength shifts greater than 60 nm have been observed after deposition about 60 nm-thick multilayer film and record shifts of 40 nm have been observed with 25 nm films in an LPG of $\Lambda = 116 \mu\text{m}$ and a length of $L = 50 \text{ mm}$.

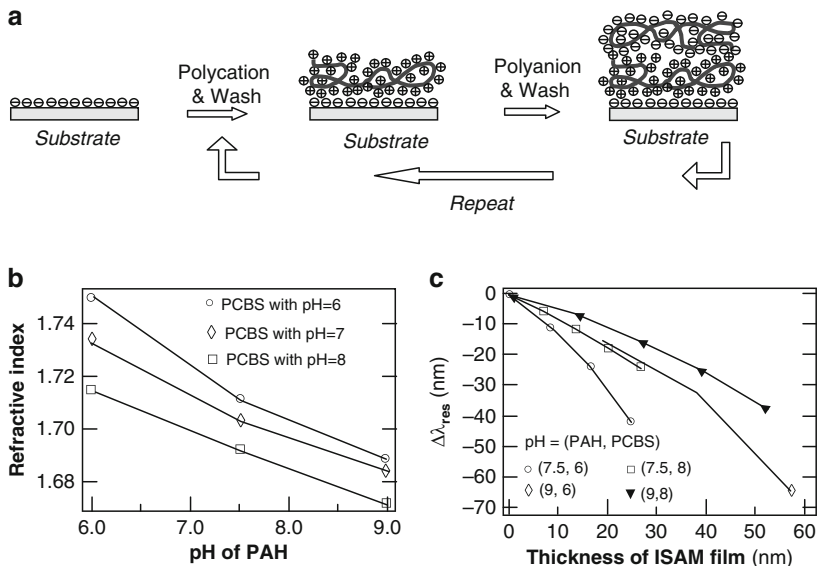


Fig. 14 ISAMs on LPGs: (a) deposition technology; (b) refractive index versus pH of the PAH of a 20 layer PAH/PCBS ISAM film; (c) resonance wavelength shift as a function of the ISAM film thickness. Reprinted with permission from [43]

Gifford et al. [18] used another approach to increase sensitivity to SRI. They first made use of an LPG around a TAP, where the slope $d\tilde{\Lambda}/d\lambda_{res}$ of the phase-matching curve reaches a maximum and switches from positive to negative. Such TAP LPGs are more sensitive to SRI and the thickness of overlays which makes them more suitable for biosensing. Besides, TAP LPGs manifest their sensitivity not in wavelength shifts but in changes of the strength of broadband attenuation which results in simpler detection schemes. If a TAP LPG is etched, the two resonance peaks around 1,300 nm and 1,500 nm tend to merge into one broader minimum around 1,400 nm which changes strength with SRI variations. To test such an LPG as a biosensor, 1.5 bilayers of PAH/PCBS ISAM film have been deposited onto a fiber after with the B-vitamin biotin deposited on top of the film as the probe molecule. Increasing concentrations of the protein streptavidin (SA), which is specifically recognized by biotin, were then deposited as the target molecule. The increase in the concentration of SA leads to an increase in the strength of the attenuation of the LPG. After the concentration of streptavidin became larger than 0.075 mg/ml, the single broadband attenuation peak was observed to split into two separate peaks. The arrangement was tested with 1.5 bilayers of ISAM film deposited on the LPG at TAP in air which lead to an increase in the attenuation strength. Further, deposition of anthrax PA antibody as a probe molecule onto the LPG leads to an increase of attenuation at the resonance wavelength. When the target molecules of anthrax PA protein at a concentration of 0.1 mg/ml were exposed to the fiber and detected by the antibody (probe

molecule), an approximately 50% decrease in the transmitted power was observed. These experiments show that highly sensitive and inexpensive biosensors can be developed on the basis of TAP LPGs.

DNA monolayer thickness sensing. While LPGs induced in conventional fibers can be coated externally, fiber gratings based on photonic crystal fibers can have the inner walls of their holes overlaid with specific films. This approach was used by Rindorf et al. [34] to show the possibility of using a PCF-based LPG for biochemical sensing (Fig. 15). An LPG with $\Lambda = 700 \mu\text{m}$ was induced by a CO_2 -laser in a large mode area PCF fiber with holes spaced at a pitch of $\Lambda_{\text{LPG}} = 7.2 \mu\text{m}$ and $d/\Lambda_{\text{LPG}} = 0.47$ where d is the holes' diameter. The authors have studied the effect of DNA deposition on the wavelength shift of the LPG. Negatively charged DNA molecules were deposited using electrostatic self-assembly technique. Since the fiber surface is negatively charged, a binding intermediate layer of positively charged poly-L-lysine is deposited on the inner side of the PCF. The resonant wavelength of the LPG with air filled holes was $\lambda_{\text{air}} = 753.6 \text{ nm}$. Initially the fiber was flushed with phosphate buffered saline (PBS) solution for 30 min, which shifted the center wavelength by $\Delta\lambda_{\text{PBS}} = 88.9 \text{ nm}$. The immobilization of the PLL added an additional shift of $\Delta\lambda_{\text{PLL}} = 6.7 \text{ nm}$, while the deposition of the DNA layer – a third shift of $\Delta\lambda_{\text{DNA}} = 2.3 \text{ nm}$. Measurements with an atomic force microscope showed 7 nm of thickness for the PLL layer and 2 nm for the DNA double helix. These experiments showed that PCF-based LPGs can be used for the development of a biomolecule lab-on-a chip sensor.

Sucrose solutions and biosensing. Tang et al. [39] used LPGs with self-assembled gold colloids to measure concentrations of sucrose solutions. Both wavelength shifts and transmission changes (in dB) were found to be linearly dependent with the SRI changes. Similarly, when the colloidal gold surface was modified with a dinitrophenyl compound (DNP), experimental results showed a linear increase of signal with the concentration of the analyte, and the detection limit of the sensor for anti-DNP was reported to be $1.4 \times 10^{-7} \text{ g/ml}$ or $9.5 \times 10^{-10} \text{ M}$.

Hydrogen sensing. Unlike FBG-based H_2 sensing, which relies on hydrogen-induced mechanical expansion, Pd-coated LPGs can sense hydrogen because of the induced refractive index changes explained earlier. Maier et al. [29] studied 40-nm-thick Pd layer uniformly deposited on a CO_2 laser-induced LPG with $\Lambda = 450 \mu\text{m}$ and $L = 5 \text{ cm}$. For H_2 concentrations of up to 10,000 ppm the about 115 pm wavelength shifts of the highest order resonance were observed at 26°C . With the interrogation system capable of resolving 2 pm shifts, the sensitivities obtained were 66 ppm for concentrations less than 625 ppm, and 270 ppm for concentrations in excess of 5,000 ppm. The sensitivities were found to decrease with temperature.

Sol-gel coating for ethanol detection. Another way of creating a suitable coating for LPGs is the use of sol-gel technology which has a number of advantages over traditional chemical vapor deposition and vacuum evaporation techniques, such as low-cost, easier control of doping level, and a porous structure suitable for gas sensing. Gu and Xu [19] used an SnO_2 solution in pure ethanol through which the fiber gratings were drawn and further temperature treated. The film thickness obtained after double dipping was about 200 nm measured with a scanning electron

microscope. Its refractive index was between 1.74 and 1.76. The LPGs used had $L = 18$ mm and $\Lambda = 450$ μm and were excimer laser-written. The response of the sensor was evaluated by measuring the transmission T in air and in a test gas $\text{C}_2\text{H}_5\text{OH}$. A downshift of 2 nm for a 200 ppm and a 20% relative change of transmissivity were observed. Maximum operating temperature of the sensor was 500°C.

Biomedical applications. In a review, Carville [4] enumerated many biomedical applications of LPG-sensing platforms that make use of specific affinity coatings or swellable polymers permitting selective, quantitative changes in the refractive index when target analytes are present.

Luna Analytics (Blacksburg, VA) used specially designed affinity coatings, including monoclonal antibodies, in order to absorb selectively the target molecule and provide real-time monitoring of disease pathogens. Clinical applications already tested using the LPG system include drug discovery, diagnostic applications, and POC testing.

Another example is detection of HIV proteins at levels less than 1 ng/ml and for studying other protein–protein interactions. Also, the overall viral load may be quantitated from the calibration curve. For example, different concentrations of the p24 HIV protein were quantitated by using monoclonal antibodies coated onto the biosensor fiber and by plotting the wavelength shifts, that are related to analyte concentration.

Coating LPGs with an affinity purified anti- β -galactosidase antibody allows their use for monitoring microbial activity. Sensors are exposed to the samples and washed to remove unbound material and the net increase in wavelength is caused by microbial activity that is determined by the concentration of bound β -galactosidase (the target analyte). It produced a wavelength shift of ~ 0.6 nm, while the positive control produced a wavelength shift of ~ 2.8 nm. This technology can be expanded to utilize specific microbial components, such as membrane antigens, capsular antigens, and antibodies for monitoring both gram-negative and gram-positive bacterial activity.

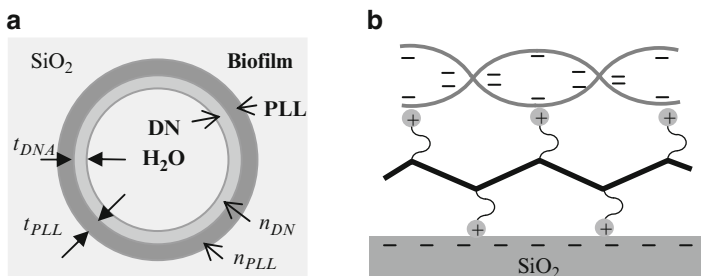


Fig. 15 (a) A hole of a photonic crystal fiber with inner side coated with poly-L-lysine (PLL) and DNA in monolayers of thicknesses t_{DNA} , t_{PLL} and refractive indices n_{DNA} , n_{PLL} . (b) The molecular structure of poly-L-lysine with positive charges immobilized onto the negatively charged silica surface (SiO_2). The negatively charged DNA is immobilized on the PLL. Reprinted from [34]

3.3 Intermodal Interference-Based Sensors

3.3.1 Intermodal Interference in Photonic Crystal Fibers

Hydrogen concentration measurement. Minkovich et al. [30] tested hydrogen sensing with a PCF-based intermodal interferometer. To fabricate it, a large-mode-area microstructured optical fiber (MOF) with core/outer diameter 11/125 μm , average hole diameter $d = 2.7 \mu\text{m}$, and average hole spacing $\Lambda_{\text{MOF}} = 5.45 \mu\text{m}$ was used. This fiber is single mode from 600 nm. A part of the MSOF was tapered which collapses the air holes to a diameter of $d_0 = 28 \mu\text{m}$ and the tapered region of length 10 mm becomes a glass/air multimode waveguide as shown in Fig. 16.

The FM of the MSOF fiber excites several higher-order modes in the tapered region, while the second tapered region acts as a spatial filter for the intermodal interference. An 8 nm Pd thin film deposited in a vacuum chamber on the LPG formed the sensor. Its responses to different concentrations of H_2 in nitrogen are shown in Fig. 17a, b, which summarizes the dependence of the intensity changes on the H_2 concentration. The response time of the sensor to reach a 0.9 level of transmission change was found to be about 10 s.

As is evident from the results, the sensitivity to H_2 increases with wavelength.

3.3.2 Cascaded LPGs

Cascaded LPGs forming a Mach-Zehnder interferometer have been shown to be suitable for high-sensitivity refractometers. Allsop et al. [2] used a phase generated

Fig. 16 Schematic representation of the MOF tapered intermodal interferometer. The shaded area represents the gas-permeable thin film layer

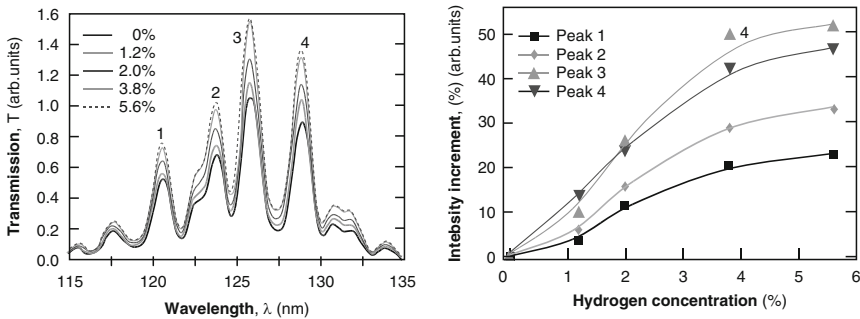
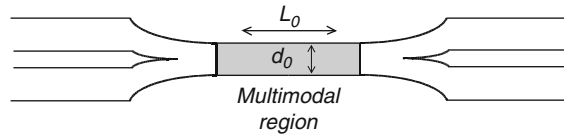


Fig. 17 Responses of the Pd coated intermodal interferometer: (a) spectral curves; (b) intensity increments for each of the four maxima in (a) vs. H_2 concentration in nitrogen

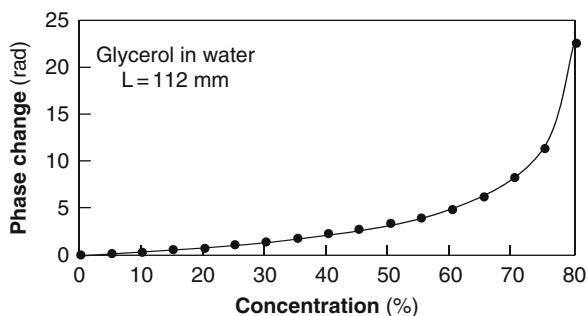


Fig. 18 Accumulated phase difference in a LPG-based Michelson interferometer [3]

carrier technique to interrogate a cascaded LPG interferometer having a LPG separation of 20 cm. A small frequency modulation is applied to the laser illuminating the LPG interferometer and the frequency modulation is converted to a phase modulation by the path difference within the interferometer. Using synchronous detection, the first and second harmonics are extracted and the ratio of their amplitudes is related to the accumulated phase difference. For SRI variations from 1.3 to 1.43, the total accumulated phase was about 45 rad. Ultimately, this translated into a minimum detectable SRI change of $\Delta n \approx 1.8 \times 10^{-6}$, which is the highest resolution obtained with LPG-based fiber device.

For immersion into liquids, however, a Michelson arrangement is more suitable. The response of a LPG-based Michelson interferometer to concentration changes of glycerol in water (corresponding to SRI changes from 1.33 to 1.45) has been reported by Brakel [3] (Fig. 18) and is similar to that of the Mach-Zender arrangement studied by Allsop et al., but the accumulated phase is twice smaller.

Kamikawachi et al. [23] studied in detail the responses of a LPG-based Mach-Zender interferometer depending on whether the LPGs or the LPGS with the cavity in between were immersed in the liquid under test. The results clearly showed that immersing both the LPGs and the cavity gives the highest center wavelength shift (about 35 nm) for a SRI change from 1 to 1.43. The refractive indices of air, water, ethanol, naphta, thinner, turpentine, and kerosene were discernable with a wide margin, which implies the possibility for detection pollution of water with hydrocarbons.

4 Concluding Remarks

This overview of the applications of fiber gratings in chemical and biochemical sensing has outlined the variety of sensing schemes and implementations based as a whole on their specific refractometric and transmission responses.

While simple sensors can be constructed using FBGs and LPGs, considerably more opportunities are opened when fiber gratings are additionally modified by

either etching, or overlaying them with thin films using sol-gel, ISAM, Langmuir-Blodgett, and other techniques. Both approaches lead to an increased sensitivity. However, thin film overlays add selectivity of the LPG sensor to particular analytes which is of importance for chemical and biochemical sensing applications.

LPGs based intermodal interferometers in Michelson and Mach-Zehnder arrangement have been shown to offer even greater sensitivities, but for the moment, their full potential appears to be underexploited.

References

- Allsop T, Zhang L, Bennion I (2001) Detection of organic aromatic compounds in paraffin by a long-period fiber grating optical sensor with optimized sensitivity. *Opt Commun* 191:181–190
- Allsop T, Reeves R, Webb DJ, Bennion I (2002) A high sensitivity refractometer based upon a long period grating Mach-Zehnder interferometer. *Rev Sci Instrum* 73:1702
- Brakel A (2004) Sensing characteristics of an optical fibre long-period grating Michelson refractometer. Ph.D. thesis, Rand Afrikaans University, p 317
- Carville DGM (2002) Fiber optics for the detection of clinical analytes, *IVD Technology* January 2002, <http://www.devicelink.com/ivdt/archive/02/01/003.html>
- Chan C, Chen C, Jafan A, Laronche A, Thomson D, Albert J (2007) Optical fiber refractometer using narrowband cladding mode resonances shifts. *Appl Opt* 46(7):1142–1149
- Chen X, Zhou K, Zhang L, Bennion I (2004) Optical chemsensors utilizing long-period fiber gratings UV-inscribed in D-fiber with enhanced sensitivity through cladding etching. *IEEE Photonics Technol Lett* 16(5):1352–1354
- Chen C, Caucheteur C, Mégret P, Albert J (2007) The sensitivity characteristics of tilted fibre Bragg grating sensors with different cladding thicknesses. *Meas Sci Technol* 18:3117–3122
- Chiang KS, Liu Y, Ng MN, Dong X (2000) Analysis of etched long-period fiber gratings and its response to external refractive index. *Electron Lett* 36(11):966–967
- Chong J, Shum P, Haryono H, Yohana A, Rao M, Lu C, Zhu Y (2004) Measurements of refractive index sensitivity using long-period grating refractometer. *Opt Commun* 229:65–69
- Cusano A, Iadicicco A, Campopiano S, Giordano M, Cutolo A (2005) Thinned and microstructured fiber bragg gratings: towards new all fiber high sensitivity chemical sensors. *J Opt A Pure Appl Opt* 7:734–741
- Cusano A, Iadicicco A, Pilla P, Contessa L, Campopiano S, Cutolo A, Giordano M, Guerra G (2006) Coated long-period fiber gratings as high-sensitivity optochemical sensors. *J Lightwave Technol* 24:1776–1786
- Cusano A, Iadicicco A, Pilla P, Contessa L, Campopiano S, Cutolo A, Giordano M (2006) Mode transition in high refractive index coated long period gratings. *Opt Express* 14:19–34
- Erdogan T (1997) Fiber grating spectra. *J Lightwave Technol* 15:1277–1294
- Falate R, Kamikawachi RC, Fabris J, Müller M, Kalinowski H (2004) Fiber optic hydrocarbon sensors based long period gratings. *J Microwave Optoelectron* 3(5):47–55
- Falate R, Kamikawachi RC, Müller M, Kalinowski HJ, Fabris JL (2005) Fiber optic sensors for hydrocarbon detection. *Sensors Actuators B Chem* 105:430–436
- Falciai R, Mignani AG, Vannini A (1998) Solution concentration measurements by means of optical fibre long-period gratings. *Proc SPIE* 3483:95–98
- Falciai R, Mignani AG, Vannini A (2001) Long-period gratings as solution concentration sensors. *Sensors Actuators B Chem* 74:74–77

18. Gifford E, Wang Z, Ramachandran S, Heflin JR (2007) Sensitivity control of optical fiber biosensors utilizing turnaround point long period gratings with self-assembled polymer coatings. *Proc SPIE* 6659:66590D
19. Gu Zh, Xu Y (2007) Design optimization of a long-period fiber grating with sol-gel coating for a gas sensor. *Meas Sci Technol* 18:3530–3536
20. Hill KO, Fujii Y, Johnson DC, Kawasaki BS (1978) Photosensitivity in optical waveguides: application to reflection filter fabrication. *Appl Phys Lett* 32:647–649
21. Iadicicco A, Campopiano S, Giordano M, Cutolo A, Cusano A (2005) Structured fiber Bragg gratings for sensing applications. In: First international conference on sensing technology, Palmerston North, New Zealand, 21–23 November 2005, pp 248–253
22. Iadicicco A, Campopiano S, Paladino D, Cutolo A, Cusano A (2007) Micro-structured fiber Bragg gratings: optimization of the fabrication process. *Opt Express* 15:15011–15021
23. Kamikawachi R, Possetti G, Muller M, Fabris J (2007) Influence of the surrounding refractive index on the thermal and strain sensitivities of a cascaded long period grating. *Meas Sci Technol* 18:3111–3116
24. Kersey A, Davis M, Patrick H, LeBlanc M, Koo K, Askins C, Putnam M, Friebele E (1997) Fiber grating sensors. *J Lightwave Technol* 15:1442–1463
25. Klemba F, Gusso Rosado R H, Kamikawachi RC, Muller M, Fabris JL (2006) Optical fiber sensors for petroleum hydrocarbon detection in pipelines. XXIX Encontro Nacional de Física da Matéria Condensada, 2006, São Lourenço-Brazil. *Optics Technical Digest*, ID 559
26. Laffont G, Ferdinand P (2000) Fiber Bragg grating-induced coupling to cladding modes for refractive index measurements. In: Proceedings 14-th international conference on optical fiber sensors, 4185, Venice, Italy, 11–13 October 2000, pp. 326–329
27. Laffont G, Ferdinand P (2001) Tilted short-period fiber Bragg grating-induced coupling to cladding modes for accurate refractometry. *Meas Sci Technol* 12:765–770
28. Liang W, Huang Y, Xu Y, Lee R., and Yariv A (2005) Highly sensitive fiber Bragg grating refractive index sensors. *Appl Phys Lett* 86:151122
29. Maier R, Jones B, Barton J, McCulloch S, Allsop T, Jones J, Bennion I (2007) Fibre optics in palladium-based hydrogen sensing. *J Opt A Pure Appl Opt* 9:S45–S49
30. Minkovich V, Hernandez D, Villatorr J, Badenness G (2006) Microstructured optical fiber coated with thin films for gas and chemical sensing. *Opt Express* 14(18):8413–8418
31. Patrick HJ, Kersey AD, Bucholtz F (1998) Analysis of the response of long period fiber gratings to external index of refraction. *J Lightwave Technol* 16:1606–1612
32. Peng YT, Tang Y, Sirkis JS (1999) Hydrogen sensors based on palladium electroplated fiber Bragg gratings (FBG). In: Proceedings 13-th international conference on optical fiber sensors, 3746, Kyongju, Korea, 12–16 April 1999, pp. 171–174
33. Rees ND, James SW, Tatam RP, Ashwell GJ (2002) Optical fiber long-period gratings with Langmuir-Blodgett thin-film overlays. *Opt Lett* 27:686–688
34. Rindorf L, Jensen JB, Dufva M, Pedersen LH, Høiby PE, Bang O (2006) Photonic crystal fiber long-period gratings for biochemical sensing. *Opt Express* 14:8224–8231
35. Sang X, Yu C, Maytevarunyoo T, Wang K, Zhang Q, Chu P (2007) Temperature insensitive chemical sensor based on a fiber Bragg grating. *Sensors Actuators B Chem* 120:754–757
36. Shevchenko Y, Albert J (2007) Plasmon resonances in gold-coated tilted fiber Bragg gratings. *Opt Lett* 32(2):211–213
37. Shevchenko Y, Blair D, Derosa M, Albert J (2008) DNA target detection using gold-coated tilted fiber Bragg gratings in aqueous media In: Conference on lasers and electro-optics, CLEO-2008, San Jose, CA, 4–9 May 2008, paper CMJ4
38. Shu X, Huang D (1999) Highly sensitive chemical sensor based on the measurement of the separation of dual resonant peaks in a 100- μm period fiber grating. *Opt Commun* 171:65–69
39. Tang J-L, Cheng Sh-F, Hsu W-T, Chiang Ts-Y, Chau L-K (2006) Fiber-optic biochemical sensing with a colloidal gold-modified long period fiber grating. *Sensors Actuators B Chem* 119(1):105–109

40. Tang J-L, Wang JN (2007) Measurement of chloride ion concentration long-period grating technology. *Smart Mater Struct* 16:665–672
41. Triques A, Silva M, Gonzalez D, Celnik J, Schiller VG, D'Almeida A, Pereira F, Valente L, Braga A, Dias M (2004) Fiber Bragg grating sensing for indirect evaluation of corrosion in oil and gas facilities. *Proc SPIE* 5502:283–286
42. Vasiliev S, Medvedkov O (2000) Long period refractive index fiber gratings: properties, applications, and fabrication techniques. *Proc SPIE* 4082:212–223
43. Wang Zh, Heflin JR, Stolen RH, Ramachandran S (2005) Highly Sensitive Optical Response of Optical Fiber Long Period Gratings to Nanometer-thick Ionic Self-assembled Multilayers. *Appl Phys Lett* 86(1–3):223104
44. Vengsarkar AM, Lemaire PJ, Judkins JB, Bhatia V, Sipe JE, Ergodan TE (1996) Long-period fiber gratings as band-rejection filters. *J Lightwave Technol* 14:58–65

Hollow-Optical Fiber Probes for Biomedical Spectroscopy

Yuji Matsuura

Abstract Thin and flexible probes made with hollow-optical fibers may be useful for remote spectroscopy. Experimental results showed that these probes are useful for endoscopic measurements of infrared and Raman spectroscopy. A hollow-fiber probe has been used for remote FT-IR spectroscopy in the form of endoscopic measurement of infrared reflectometry spectra inside the body. This measurement was made possible by the hollow-fiber probe's flexibility, durability, nontoxicity, and low transmission loss. A hollow-fiber probe with a ball lens at the end works as a confocal system for Raman spectroscopy. It can thus detect the molecular structure of biotissues with a high signal-to-noise ratio. Owing to their small diameter, the probes are useful for in vivo, noninvasive analysis using a flexible endoscope.

Keywords Hollow-optical fibers · Infrared spectroscopy · Raman spectroscopy · Endoscopes · FT-IR · Raman probes

Contents

1	Introduction	178
2	Design and Fabrication of Hollow-Optical Fibers	179
3	Fiber Probe for FT-IR Spectroscopy	184
4	Hollow-Fiber Raman Probe	187
5	Concluding Remarks	191
	References	192

Y. Matsuura

Graduate School of Biomedical Engineering, Tohoku University, 6-6-05 Aoba, Sendai 980-8579, Japan

e-mail: yuji@ecei.tohoku.ac.jp

Abbreviations

ATR	Attenuated total reflection
COP	Cyclic olefin polymer
FT-IR	Fourier transform infrared spectroscopy
NA	Numerical aperture
TE mode	Transverse electric mode

Symbols

d	Thickness of dielectric layer
j	Imaginary unit
k	Extinction coefficient
k_0	Wavenumber in vacuum
n	Refractive index
p_0	Far-field profile of the incident beam
R	Power reflection coefficient
r	Reflection coefficient
T	Inner radius of circular hollow waveguide
α	Half of the power attenuation constant
ϕ	Phase factor of reflection coefficient
φ	Angle of incidence
λ	Wavelength
θ	Angle of incidence
ρ	Amplitude factor of reflection coefficient
σ	Root-mean-square height of irregular surface

1 Introduction

Least invasive surgery and diagnosis with a thin, flexible, and multifunctional endoscope can minimize risk and consequently reduce recovery time and medical costs. Surgery using a high-power laser beam and optical biopsy using a fiber probe are seen as substitutes to conventional endoscopic surgery. In such surgery and diagnostics, one can use very thin and flexible endoscopes because forceps and other large mechanical extractors are unnecessary.

Infrared and Raman spectroscopies are commonly used for analysis and determination of molecules including those of biological tissues. Infrared and Raman spectroscopies are sometimes complementarily used, because they are based on different mechanisms. The method chosen should be the one that is most suitable for the objective molecules and structures.

Spectroscopic analysis detecting infrared absorption and Raman scattering are useful for diagnosis of early-stage tumors and other diseases; however, it has been

difficult till now to use an endoscope for these analyses because a practical and useful fiber-optic probe does not exist for both applications. Recently, a thin and flexible probe that is applicable to both infrared and Raman spectroscopies was developed. The probe is based on a hollow-optical fiber that has a low transmission loss and high flexibility, and the fiber is thin enough to be inserted into the working channel of endoscopes.

For FT-IR spectroscopy, several commercial products using fiber-optic probes are available [5]. Mainly, two types of infrared fiber are used for transmission of mid-infrared light, which cannot be transmitted by silica-glass fibers. One is an optical fiber made of chalcogenide glasses, which are transparent in the mid-infrared region around wavenumbers of 1,500–5,000 cm^{-1} [13]. Although their transmission efficiency is high and they have high mechanical and chemical durability, chalcogenide-glass fibers suffer from the problem of toxicity, so they are unusable for medical applications. Other materials used in infrared fibers are metal halides. Infrared fibers with metal halides are called “polycrystalline fibers,” and they are usually produced by extrusion of a mixed crystal of silver chloride and bromide through a die [4, 12]. Polycrystalline fibers do not suffer from the toxicity problem; however, they are photosensitive and have poor chemical stability.

A hollow-optical fiber is a prospective fiber-optic probe for infrared spectroscopy in medicine, owing to its nontoxicity and high mechanical and chemical stability [5]. However, it has been difficult to use it for remote spectroscopy because of its relatively high bending losses. Accordingly, the transmission efficiency should be improved by optimizing the fabrication conditions.

2 Design and Fabrication of Hollow-Optical Fibers

In hollow-optical fibers for laser delivery, usually only some low order modes are excited because of small divergence angle of incident laser beam. In contrast, many high order modes are excited in hollow-optical fibers for spectroscopic applications because usually an incoherent light source like an arc lamp is used as the light source. Therefore, ray optic theory that can handle a wide divergence beam is used for evaluation of optical properties in this section.

Let us consider a circular hollow waveguide whose inner radius T is much larger than the wavelength of the light. The light is assumed to be incoherent and randomly polarized. Figure 1 shows a ray model for calculating the transmission loss.

When the angle of incidence θ is small enough, transmission losses for skew rays are equal in the first-order approximation to those for meridional rays with the same θ [9]. Therefore, only meridional rays are considered in the present analysis. For the meridional ray, a power attenuation constant $2\alpha(\theta)$ is calculated as

$$2\alpha(\theta) = \frac{1 - R(\theta)}{2T \cot \theta}, \quad (1)$$

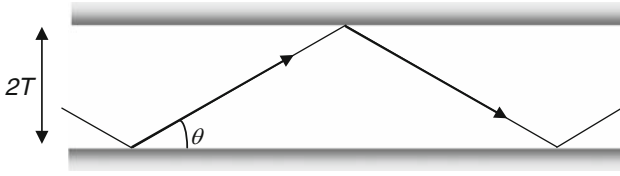


Fig. 1 Ray model for theoretical evaluation

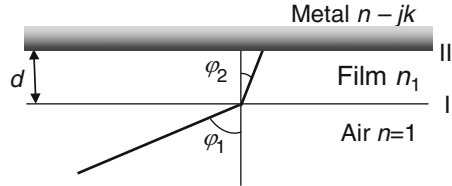


Fig. 2 Reflection on a dielectric-coated metal surface

where $R(\theta)$ denotes a power reflection coefficient of the light and is assumed to be an average of those for p - and s -polarized lights:

$$R(\theta) = \frac{R_s(\theta) + R_p(\theta)}{2}. \tag{2}$$

Let us next consider a metal hollow-optical fiber with dielectric inner coating. When the coating thickness is properly designed, the dielectric layer enhances reflection in a specific wavelength range owing to the interference effect. Let us consider a metal surface coated with a dielectric film of thickness d as shown in Fig. 2. From Fresnel’s formula, the reflection coefficient of the electric field on boundary I is expressed as

$$r_{1p} = \frac{n_1 \cos \phi_1 - \cos \phi_2}{n_1 \cos \phi_1 + \cos \phi_2} \tag{3a}$$

for the p -polarization,

$$r_{1s} = \frac{\cos \phi_1 - n_1 \cos \phi_2}{\cos \phi_1 + n_1 \cos \phi_2} \tag{3b}$$

and for the s -polarization, where ϕ_1 and ϕ_2 denote angles of incidence and refraction, respectively, and n_1 denotes the refractive index of the dielectric film.

On boundary II, a reflection coefficient r_2 is expressed with two parameters, ρ_2 and ϕ_2 as follows:

$$r_2 = \rho_2 \exp(j\phi_2). \tag{4}$$

For the p - and s -polarizations, ρ_2 and ϕ_2 are derived as follows:

$$\rho_{2p}^2 = \frac{[(n^2 - k^2) \cos \varphi_2 - n_1 u]^2 + (2nk \cos \varphi_2 - n_1 v)^2}{[(n^2 - k^2) \cos \varphi_2 + n_1 u]^2 + (2nk \cos \varphi_2 + n_1 v)^2}, \quad (5)$$

$$\phi_{2p} = \tan^{-1} \left[2n_1 \cos \varphi_2 \frac{-2nku - (n^2 - k^2)v}{(n^2 + k^2)^2 \cos^2 \varphi_2 - n_1^2(u^2 + v^2)} \right], \quad (6)$$

$$\rho_{2s}^2 = \frac{(n_1 \cos \varphi_2 - u)^2 + v^2}{(n_1 \cos \varphi_2 + u)^2 + v^2}, \quad (7)$$

$$\phi_{2s} = \tan^{-1} \left[\frac{-2vn_1 \cos \varphi_2}{u^2 + v^2 - n_1^2 \cos^2 \varphi_2} \right], \quad (8)$$

where n and k are the real and imaginary parts of the complex refractive index $n - jk$ of the metal, and

$$u^2 = \frac{1}{2} \left[n^2 - k^2 - n_1^2 \sin^2 \varphi_2 + \sqrt{(n^2 - k^2 - n_1^2 \sin^2 \varphi_2)^2 + 4n^2 k^2} \right], \quad (9)$$

$$v^2 = \frac{1}{2} \left[-(n^2 - k^2 - n_1^2 \sin^2 \varphi_2) + \sqrt{(n^2 - k^2 - n_1^2 \sin^2 \varphi_2)^2 + 4n^2 k^2} \right], \quad (10)$$

Using r_1 and r_2 one can evaluate the reflection coefficient r of the film-coated metal surface for p - or s -polarized light as follows [2]

$$r = \frac{r_1 + r_2 \exp(-j2\Gamma)}{1 + r_1 r_2 \exp(-j2\Gamma)} = \frac{r_1 + \rho_2 \exp[j(\varphi_2 - 2\Gamma)]}{1 + r_1 \rho_2 \exp[j(\varphi_2 - 2\Gamma)]}, \quad (11)$$

where

$$\Gamma = k_0 n_1 d \cos \varphi_2 \quad (12)$$

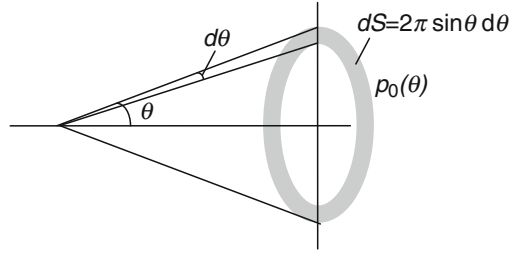
and k_0 is the wavenumber in vacuum. Therefore, the power reflection coefficient $R = |r|^2$ can be expressed as

$$R = \frac{r_1^2 + \rho_2^2 + 2r_1 \rho_2 \cos(\varphi_2 - 2\Gamma)}{1 + r_1^2 \rho_2^2 + 2r_1 \rho_2 \cos(\varphi_2 - 2\Gamma)}. \quad (13)$$

In the absence of dielectric film, the power reflection coefficient can also be calculated from (13) by setting $n_1 = 1$.

Since the power reflection coefficient is dependent on θ , a launching condition should be considered correctly. When an angular distribution, or a far-field profile,

Fig. 3 Illustration of considering an angular distribution of incident rays. The far field distribution $p_0(\theta)$ should be weighed by $\sin\theta$, since the shaded area is proportional to $\sin\theta$



of the incident beam is expressed as $p_0(\theta)$, solid-angle considerations require that it be weighted by $\sin \theta$ to obtain a total intensity of θ -directional rays, as can be inferred from Fig. 3. Hence, for a waveguide of length z , the transmitted power $P(z)$ is given by

$$\begin{aligned} P(z) &= \int_0^{\theta_{\max}} p_0(\theta) \exp[-2\alpha(\theta)z] \sin \theta \, d\theta, \\ &= \int_0^{\theta_{\max}} p_0(\theta) \exp\left[-\frac{1-R(\theta)}{2T \cot \theta} z\right] \sin \theta \, d\theta, \end{aligned} \quad (14)$$

where θ_{\max} denotes a maximum launching angle. With (14), a power attenuation can be evaluated theoretically.

Let us next consider the effect of surface irregularities on transmission losses. When a light of wavelength λ impinges upon an irregular surface at a glancing angle θ ($=\pi/2-\varphi$), the power reflection coefficient $R'(\theta)$ becomes

$$R'(\theta) = R(\theta) \exp\left[-\left(\frac{4\pi n_i \sigma \sin \theta}{\lambda}\right)^2\right], \quad (15)$$

where $R(\theta)$ denotes the power reflection coefficient of light at a flat surface, n_i is refractive index of the medium of incidence, σ is the root-mean-square height of the surface irregularities [1], and λ is the wavelength of light. Equation (15) is valid for both metallic and dielectric surfaces. Using $R'(\theta)$ in place of $R(\theta)$ in (1), one can calculate the attenuation constant for a waveguide with surface irregularities. However, at the rough surface, the angle of some of the scattered light becomes smaller or larger than that of the incident light. When the angle is smaller (larger) than the angle of incidence, the reflection coefficient increases (decreases). Therefore, a complicated estimation and information on the scattering pattern are required for a precise evaluation of the attenuation. In the results shown below, for simplicity, only the decrease in reflectivity at the specular angle is taken into account.

In hollow-core metal waveguides, when excited with linearly polarized light, TE modes are dominant because reflection coefficients of metals are much higher for the s -polarization state. To reduce the loss for a randomly polarized incoherent light

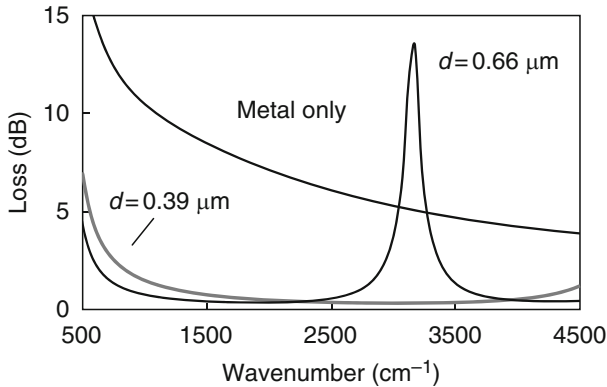


Fig. 4 Calculated loss spectra of metal and dielectric-coated metal hollow-fibers

source, it is essential to enhance reflection of the *p*-polarization as shown in (2). Loading a dielectric film on the inside of metal hollow waveguides is effective because, by choosing a proper thickness, reflection of *p*-polarized light is enhanced and as a result, the arithmetical mean of reflection coefficients of the *p*- and *s*-polarizations is maximized.

The optimum dielectric layer thickness d_{opt} is given by multiplying quarter wave thickness, which is the optimum for the *p*-polarization, by an adjustment factor [10]; thus,

$$d_{opt} = \frac{\lambda}{4\sqrt{n_1^2 - 1}} \frac{1}{\pi} 2\tan^{-1} \left[\frac{n_1}{4\sqrt{n_1^2 - 1}} \right]. \tag{16}$$

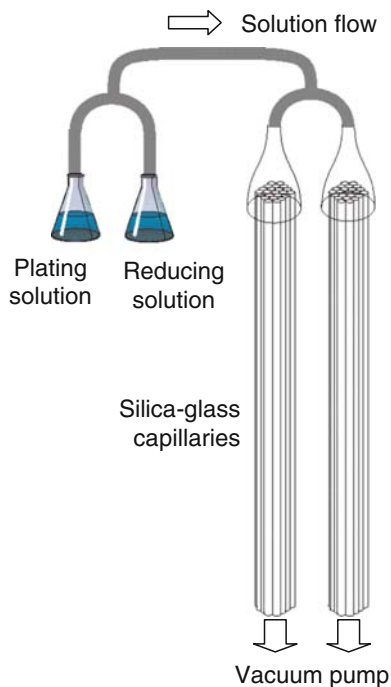
Figure 4 shows theoretical losses of (1) silver hollow-optical fiber, (2) dielectric-coated silver hollow-fiber with coating thickness of 0.39 μm , and (3) $d = 0.66 \mu\text{m}$. The thickness of 0.39 μm is the optimized value for $\lambda = 3 \mu\text{m}$ and 0.66 μm is the one for $\lambda = 5 \mu\text{m}$. Parameters used in the calculation are $n_1 = 1.53$, $z = 1 \text{ m}$, $2T = 1 \text{ mm}$, and $\sigma = 0$ and complex refractive index of silver is taken from literature [11]. In the calculation, a Gaussian beam with the divergence angle of 6° in full-width-half-maximum is assumed as an input beam. As seen from the calculated spectra, one can obtain a low loss region around the optimized wavelength.

The polymer-coated hollow-fibers employ a silica–glass capillary tube as the substrate. Since the wall of the glass is thinner than 40 μm , it is highly flexible, and the minimum bending radius is less than 5 mm for a 320- μm -bore glass tube.

A cyclic olefin polymer (COP) is chosen as the inner polymer film because of its low absorption coefficient in the mid-infrared region and its relatively high heat resistivity ($\sim 140^\circ\text{C}$). The thickness of the silver film is around 0.1 μm , and the thickness of the polymer film is controlled to be a designed value which gives high reflectivity at the desired wavelength range.

Polymer-coated hollow-fibers with a length of 1–2 m and inner diameters of 0.32–1 mm are fabricated by modifying the process of coating the silver and polymer films. Firstly, a thin film of silver is deposited on the inner surface of the

Fig. 5 Fabrication setup for silver coating



glass tube by using a conventional mirror-plating technique. The coating setup is shown schematically in Fig. 5. A silver nitrate solution and a reducing solution are mixed and then injected into the capillary tube. To keep the flow speed of the solutions high enough for sufficient mixing, the two bundles of capillaries are coated in parallel. Each bundle contains 5–20 capillaries. The use of bundles makes the conductance of the solution high and, as a result, the flow rates become high enough for depositing silver film that is uniform in length of up to 2 m. Another advantage of this process is the capability for mass production.

Following the silver-coating process, a COP thin film is coated on the silver layer by use of a liquid-phase polymer coating technique [14]. In this process, a polymer solution diluted with cyclohexane is used for film deposition. After a small amount of the polymer solution is injected into the capillaries, the tubes are gradually heated to 180 °C for 2 h with a constant flow of nitrogen gas. This process dries the solution that remains on the inside of the tubes.

3 Fiber Probe for FT-IR Spectroscopy

Figure 6 shows the measurement setup for remote infrared reflectometry using hollow-optical fibers. A Fourier-transfer infrared spectrometer with an external detector of HgCdTe was used in the experiment. Mid-infrared light from the

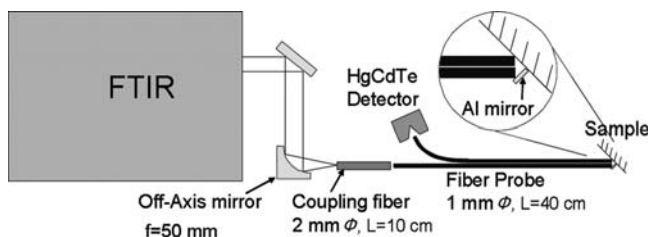


Fig. 6 Measurement setup for remote infrared reflectometry using hollow-optical fibers

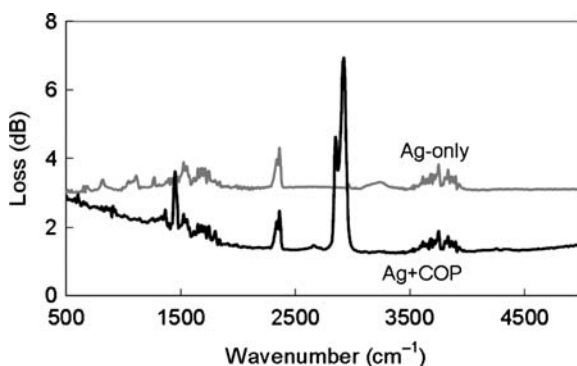
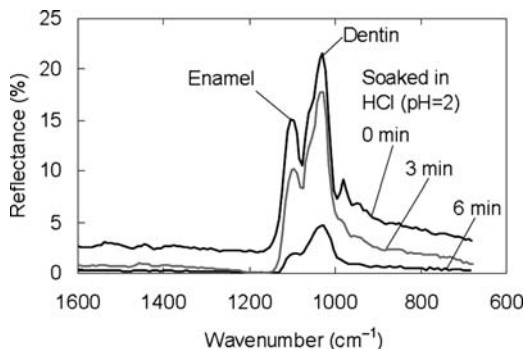


Fig. 7 Measured loss spectra of silver-coated hollow-fiber optics with COP inner coating. The length is 50 cm and the inner diameter is 1.0 mm

spectrometer is focused on the input end of a hollow transmission fiber with 1.0-mm inner diameter and 50-cm length. Light through the transmission fiber is first reflected by a small aluminum mirror and then reflected on the sample surface with an angle of incidence of 45° . The reflected light is also delivered to a detector by the hollow-fiber. The coupling efficiency to the fiber probe is roughly 20% because the incoherent light source with a large source area is difficult to focus onto a small spot and the beam size at the input end of the fiber is around 3 mm.

Silver-only coated hollow-fibers and dielectric-coated silver hollow-fibers were tested as fiber probes. Figure 7 shows the measured loss spectra of these two types of hollow-optical fiber. The inner diameter of the fibers is 1 mm and the length is 50 cm. The silver-only coated fiber exhibits a broadly flat spectrum at wavenumbers from 500 to $5,000\text{ cm}^{-1}$. The small peaks on the spectrum are due to absorptive CO_2 and water vapor in air. This flat spectrum is advantageous for a spectrometry probe. By forming a polymer cover layer on the silver, the loss can be reduced by using the interference effect. In Fig. 7, the effect of the polymer layer is clearly seen; losses are largely reduced, especially at short wavelengths. Although the absorption peaks of the COP appear at wavelengths around $1,400$ and $2,800\text{ cm}^{-1}$, they do not significantly affect the infrared spectroscopy because they can be subtracted when using the spectra as references.

Fig. 8 Measured reflectance spectra of an exfoliated deciduous tooth before and after being soaked in hydrochloric acid



In the first test, the changes in the reflectance of a tooth (which shows relatively high reflectivity) are measured. Figure 8 shows measured reflectance spectra of a primary tooth before and after it was soaked in a solution of hydrochloric acid ($\text{pH} = 2$). Before soaking, the peaks of dentin and enamel are clearly observed in the reflected spectrum. These peaks originated from calcium phosphate contained in hydroxyapatite, and a difference in the crystallinities (higher in enamel) causes the wavelength shift of the peaks. After soaking the tooth in acid, the enamel layer dissolved, and only the peak of enamel diminished. Optimizing the coupling conditions to improve the sensitivity of the probe will enable detection of early dental caries, which are usually invisible.

A common fiber probe using a chalcogenide or crystalline fiber usually cannot be used as a reflectance-measurement probe without a lens at the output end. This is because of the large beam divergence from the fiber optics (with a high NA). Therefore, attenuated-total-reflection (ATR) probes are usually used for reflectance measurements. However, ATR probes should be touched on the measured surface, and the contact pressure must be kept constant to obtain a stable detection signal. This sometimes becomes a problem when using the probe for measuring biological samples, especially *in vivo*. In contrast, the beam divergence from hollow-fibers is usually as small as a few degrees; therefore, hollow-fibers are good for direct measurement of surface reflectance without using a lens.

Figure 9 shows the reflectance of human oral mucosa measured before and after meal ingestion. Although the measured reflectance is lower than 0.5%, it was measured with a signal-to-noise ratio that is good enough to recognize absorption peaks of protein and lipid. From these spectra, changes in blood elements are easily detected with high accuracy because oral mucosa is much closer to blood-vessel networks than the skin surface.

By attaching a prism to the end of the fibers, the probe can also be used for ATR spectroscopy. As shown in the inset of Fig. 10, a silicon flat prism with a thickness of 1.5 mm and a bottom width of 3 mm was attached at the end of the fibers by a metal holder. The apex angle of the prism is 90° , so that it brings a single reflection at the end surface of the prism. Although around 65% of the incident energy is lost due to surface reflection at the surfaces of the prism and limited coupling efficiency,

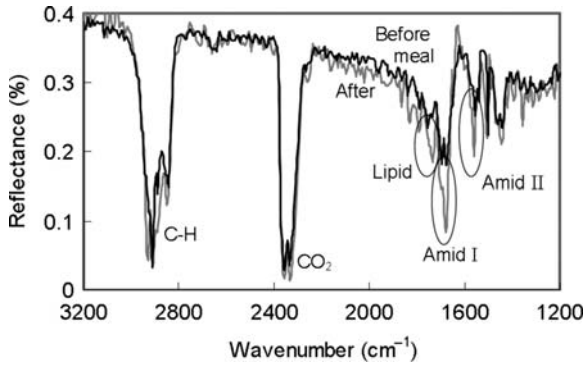


Fig. 9 Reflectance of human oral mucosa measured in vivo before and after meal was ingested

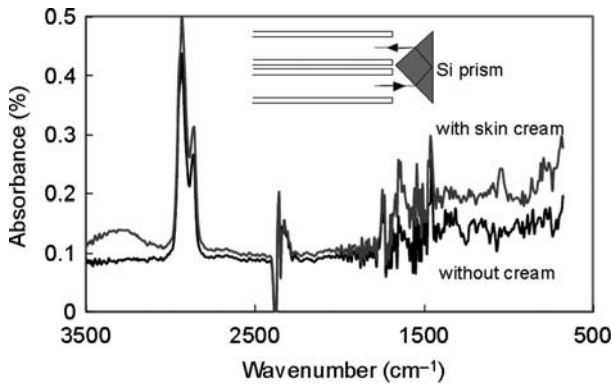


Fig. 10 ATR absorption spectra of skin surface with and without skin cream applied

the detected energy is much higher in the ATR probe because its operation is based on total reflection.

Figure 10 shows the attenuation spectra of the surface of human skin with and without a skin cream applied. Traces of the cream can be seen in the 1,500–1,700 cm^{-1} region as absorptions of organics, and the peak for water can be seen around 3,300 cm^{-1} . Because of the high throughput of the probe, these spectra can be easily taken by simply touching the prism on the sample surface.

4 Hollow-Fiber Raman Probe

In Raman spectroscopy, usually, both the excitation and signal light beams are in visible or near-infrared wavelengths. Therefore, silica-glass fibers, which are commonly used in optical communications, are basically applicable as a flexible

probe. However, a fundamental problem in regards to Raman-scattering measurements using optical-fiber probes is Raman scattering in the silica-glass fiber itself, caused by transmission of the excitation and signal light beams. To eliminate such Raman background noise, two different optical filters should be attached to the output end of the excitation-light-transmitting fiber and signal-collection fiber [3, 7, 8]. This complex configuration makes the probe diameter large and limits its flexibility. Moreover, the filter or probe itself should be changed when changing the excitation wavelength.

Hollow-optical fibers are proposed as a fiber Raman probe [7, 8]. Hollow-fibers provide “clean” transmission, that is, they generate no Raman background noise, and thus, only a single hollow-fiber is necessary for both excitation and signal collection. However, the transmission losses of hollow-optical fibers are usually higher than those of silica-glass fibers, especially when the fibers are bent. Furthermore, the NA of hollow-fibers is much smaller than that of glass fibers, thereby limiting the acceptance angle of scattered light from the sample. Attaching a focusing lens at the end of hollow-fibers is effective to enhance the energy density of the output beam and to compensate the loss and the low NA of the hollow-fiber. It was also shown that the hollow-fiber probe with a ball lens works in a nearly confocal mode owing to mode selectivity of hollow-optical fibers [6]. The output beam from the hollow-fiber is almost parallel and thus, scattered light from other than the focal point is converted into rays having some angle to the fiber axis. These rays coming back to the hollow-fiber are coupled to high-order modes and fade out within a short transmitting length. Functioning as a cap, the lens seals the open end of the hollow-fiber and keeps fluid and fumes from penetrating the bore.

Figure 11 shows the appearance and structure of the focusing-lens cap using a ball lens attached to the end of a hollow-fiber. The diameter of the cap is small (i.e., 0.64 mm), so the fiber with the cap is easily inserted into the working channel (whose inner diameter is usually larger than 1 mm) of a thin endoscope.

Figure 12 shows the measurement setup using a hollow-fiber probe. A hollow-optical fiber (700- μm core diameter and 1-m length) was fabricated by coating a

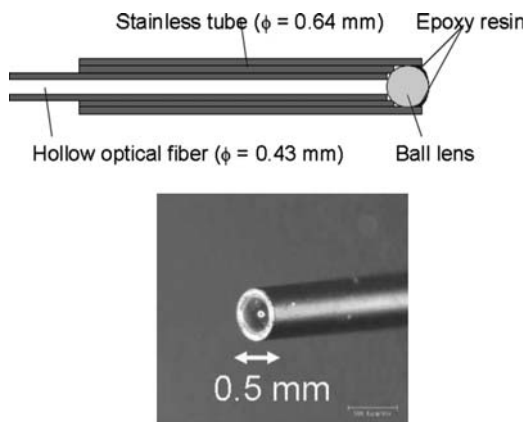


Fig.11 Appearance and structure of the cap with ball lens

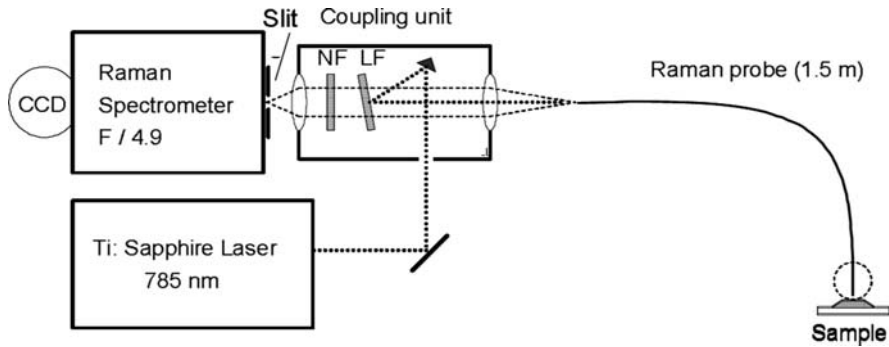


Fig. 12 Measurement setup for Raman spectroscopy. NF is a notch filter for 785 nm and LF is a long-path filter

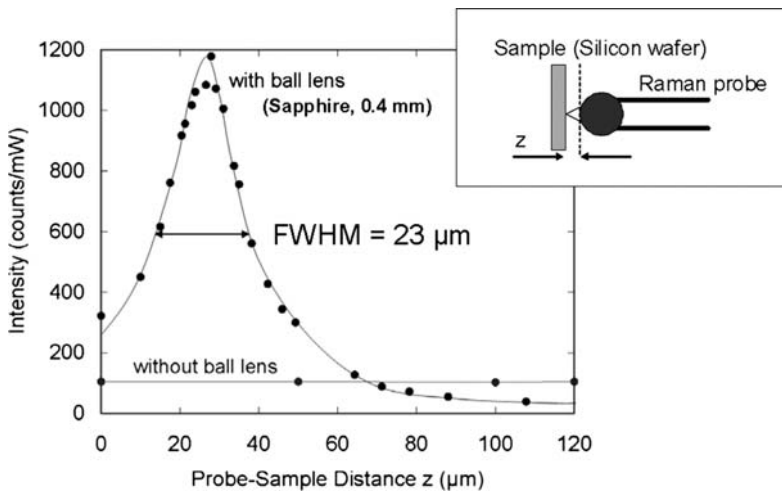


Fig. 13 Intensity of Raman signal from silicon measured by using a hollow-fiber probe with a ball lens

thin silver film on the inner surface of a flexible glass capillary tube. A 785-nm excitation light beam from a Ti:sapphire laser acts as input into the fiber via a lens with a focal length of 150 mm. The Raman-scattered light of the sample is transmitted into the fiber and then collimated by the lens. It passes through a long-pass filter and a 785-nm notch filter to detect only the Raman signal. The Raman spectra are taken by a single polychromatic Raman spectrometer with a cooled CCD.

Figure 13 shows the intensity of the Raman signal from a silicon wafer measured with and without the lens cap to evaluate the depth resolution of the Raman probe. The intensity is measured while changing the distance between the sample and the

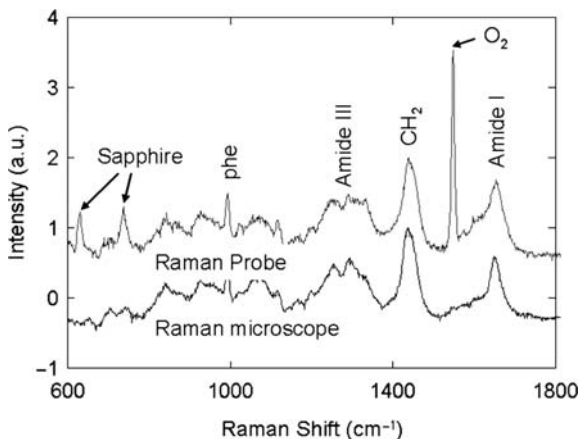


Fig. 14 Raman spectra of rat stomach measured ex vivo using hollow-fiber probe and Raman microscope

lens surface (as shown in the inset). According to this measurement result, it is found that the lens fiber works as a confocal probe with a resolution of around 25 μm . The confocal effect enhances the sensitivity of the probe; namely, it is roughly ten-times higher than that of a probe without a lens. The results of other experiments show that attaching a ball lens at the end of the hollow-fiber increases the signal-to-noise ratio by around 6 dB.

Figure 14 shows the Raman spectrum of a rat stomach measured ex vivo using the hollow-fiber probe. A spectrum taken by using a Raman microscope is also shown for comparison. The excitation power was 29 mW, and the exposure time for the measurement was 60 s. Although Raman peaks of the sapphire-ball lens at 630 and 738 cm^{-1} and oxygen in the bore of the fiber at 1,548 cm^{-1} appear in the spectrum measured with the hollow-fiber probe, they are sharp and do not affect other Raman signals of interest. The spectrum has a high signal-to-noise ratio that is comparable to the one measured by a Raman microscope. This is because of the confocal effect of the ball lens attached at the end of the hollow-fiber.

The fiber probe was used for in vivo measurement of a rat stomach. In the experiment, a rat was anesthetized and intubated; then, a thin endoscope (2-mm in diameter) was inserted into its stomach. The stomach was washed before Raman measurement to remove saburra (which emits strong fluorescence). Finally, the fiber probe was inserted into the working channel, and a Raman signal was detected by touching the probe onto the mucosa of the stomach.

Figure 15 shows the Raman spectra of the rat stomach measured in vivo with a hollow-fiber Raman probe. Although the Raman signals are much lower than the fluorescence background (Fig. 15a), the signal peaks clearly appear when the background is numerically subtracted (Fig. 15b). This is the first in vivo detection of the Raman spectra from the stomach of a living animal.

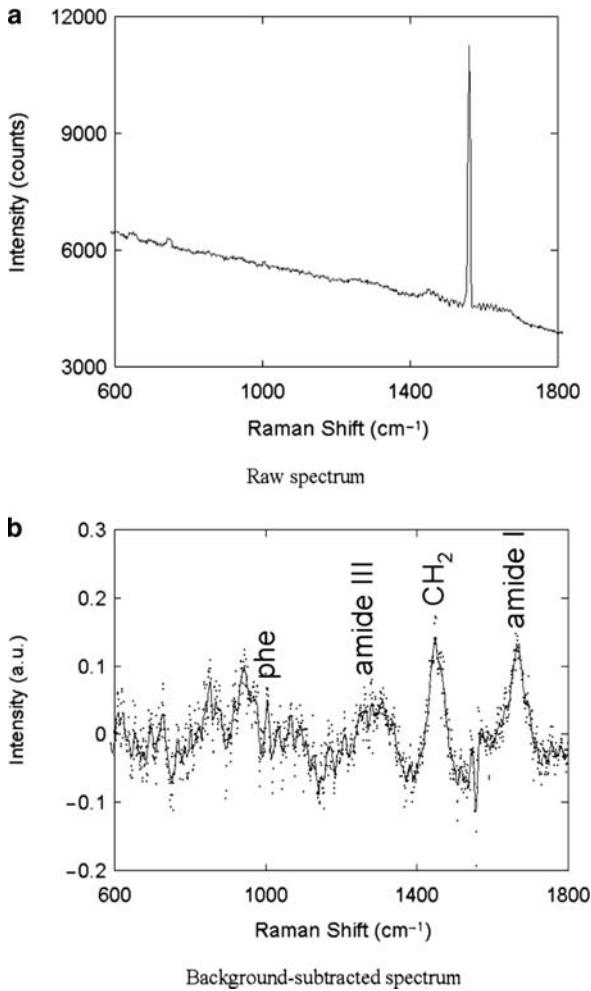


Fig. 15 Raman spectra of rat stomach measured in vivo with hollow-fiber Raman probe

5 Concluding Remarks

Optical probes based on hollow-fiber optics are proposed for remote infrared and Raman spectroscopies. For infrared spectroscopy, hollow-fibers with metal and polymer internal coatings are used as a probe for reflectometry. Because of the flexibility, nontoxicity, and small diameter of the probe, it is applicable to in vivo FT-IR spectroscopy using an endoscope. The flexibility and handling of the probe can be improved by using a single fiber for both transmitting and receiving infrared light. As for Raman spectroscopy, a hollow-fiber probe with a ball lens at the end works as a confocal system and can detect the molecular structure of biotissues with

a high signal-to-noise ratio. Owing to its small diameter, the probe is useful for *in vivo* and noninvasive analysis using a flexible endoscope. Raman spectra of a rat stomach have been successfully measured *in vivo* for the first time.

References

1. Bennet HE (1963) Specular reflectance of aluminized ground glass and the height distribution of surface irregularities. *J Opt Soc Am* 53:1389–1394
2. Born M, Wolf E (1985) Principles of optics. Pergamon, New York, pp 36–66
3. Cooney TF, Schoen CL, Sharma K, Carey DM (1993) Rare-earth-doped glass fiber for background rejection in remote fiber-optic Raman probes: theory and analysis of holmium-bearing glass. *Appl Spectrosc* 47:1683–1692
4. Grigorjeva L, Millers D, Kotomin E, Eglitis R, Lerman AA (1996) Optical properties of silver halide fibres: ageing studies. *Appl Phys* 29:578–583
5. Harrington JA (2003) Infrared fibers and their applications, Chap 1. SPIE, Bellingham, WA
6. Katagiri T, Komachi Y, Hattori Y, Matsuura Y, Miyagi M, Tashiro H, Sato H (2006) Hollow-optical fiber probe for confocal Raman endoscopy. *Proc SPIE* 6083:60830
7. Komachi Y, Sato H, Aizawa K, Tashiro H (2005) Micro-optical fiber probe for use in an intravascular Raman endoscope. *Appl Opt* 44:4722–4732
8. Komachi Y, Sato H, Matsuura Y, Miyagi M, Tashiro H (2005) Raman probe using a single hollow waveguide. *Opt Lett* 30:2942–2944
9. Miyagi M (1985) Waveguide loss evaluation in circular hollow waveguides and its ray optical treatment. *IEEE J Lightwave Technol* 3:303–307
10. Miyagi M, Kawakami S (1984) Design theory of dielectric-coated circular metallic waveguides for infrared transmission. *IEEE J Lightwave Technol* 2:116–126
11. Palik ED (1985) Handbook of optical constants of solids. Academic, Orlando, FL, pp 749–763
12. Pinnow DA, Gentile AL, Standlee AG, Timper AJ, Hobrock LM (1978) Polycrystalline fiber optical waveguides for infrared transmission. *Appl Phys Lett* 33:28–29
13. Seddon AB (1995) Chalcogenide glasses: a review of their preparation, properties, and applications. *J Non-Cryst Sol* 184:44–50
14. Shi Y, Wang Y, Abe Y, Matsuura Y, Miyagi M, Sato S, Taniwaki M, Uyama H (1998) Cyclic olefin polymer-coated silver hollow glass waveguides for the infrared. *Appl Opt* 37:7758–7762

Part III
Hollow-Waveguide and
Micro-Resonator Sensors

Liquid-Core Waveguide Sensors

Holger Schmidt

Abstract Much of chemistry and biology involves liquid substances. It is, therefore, not surprising that a strong need for instruments that can sense the presence, absence, or properties of liquids and their constituents exists in both of these vast fields. The miniaturization paradigm that has driven many industrial developments, including the area of sensors, provides a strong push to use optical waveguides for implementing sensing functions in compact, robust, and convenient form. The most direct approach is the use of liquid-core waveguides, in which both light and liquids are guided through the same physical space, thus providing the most efficient interaction between the two. Fueled by recent developments of novel types of liquid-core waveguides, these devices are rapidly moving to the forefront of research and development of biological and chemical sensors. Here, we take a closer look at liquid-core waveguides by discussing the physical principles underlying the most important waveguide types, discussing the most popular optical sensing modalities, and reviewing representative examples for liquid-core waveguide-based chemical and biological sensors.

Keywords Absorption · ARROW waveguide · Biosensor · Chemical sensor · Confinement · Dielectrics · Evanescent field · Fiber optics · Fluorescence · Hollow core · Liquid-core · Loss · Optical mode · Photonic crystal · Refractive index · Resolution · Scattering · Sensitivity · Total internal reflection · Waveguide

Contents

1	Introduction	197
2	Liquid-Core Waveguiding Principles	199
2.1	Total Internal Reflection-Based Waveguides	199

H. Schmidt
School of Engineering, University of California, Santa Cruz, 1156 High St., Santa Cruz,
CA 95064, USA
e-mail: hschmidt@soe.ucsc.edu

2.2	Non-TIR-Based Waveguides	202
2.3	Interference-Based Waveguides	205
3	Sensor Applications	209
3.1	Absorption	209
3.2	Fluorescence	210
3.3	Scattering	212
3.4	Refractive Index Changes	213
3.5	Polarization Changes	215
4	Concluding Remarks	215
	References	216

Abbreviations

ARGOW	Antiresonant guided optical wave
ARROW	Antiresonant reflecting optical waveguide
FOCap	Fiber-optical capillary
HC-PCF	Hollow-core photonic-crystal fiber
LCORR	Liquid-core optical ring resonators
LCWG	Liquid-core waveguides
RIU	Refractive index units
TIR	Total-internal reflection
ZMWG	Zero-mode waveguides

Symbols

α	Waveguide loss
λ	Wavelength
ω	Angular frequency
d	Waveguide core dimension
L	Interaction length
n	Refractive index
n_c	Waveguide core index
n_{cl}	Waveguide cladding index
R	Reflectivity
K	Bloch wave vector
β	Wave vector
θ_c	Critical angle of incidence
P_{in}	Input power
P_{out}	Output power

1 Introduction

Conceptually, an optical waveguide represents a physical structure capable of directing light along a well-defined path in space by confining the photon energy to a cross section of finite size. This is accomplished by assembling dielectric materials in a suitable fashion around the direction of light propagation. Typically, waveguides exhibit translational invariance along the propagation direction and possess various degrees of symmetry in the cross-sectional planes. The simplest example of such geometry is that of a glass optical fiber illustrated in Fig. 1. Composed of two materials with different refractive indices n_1 and n_2 , its geometry is cylindrical with propagation direction along z as indicated by the dashed line in Fig. 1a and circular cross section as shown in Fig. 1b. In order to guide light efficiently along the cylinder axis, the refractive index near the cylinder axis is higher than far away from it (Fig. 1c). The region closest to the point of inversion symmetry of the waveguide is called the waveguide core and the surrounding materials are referred to as cladding materials. The material comprising the core can be solid, liquid or gaseous, but here we will consider exclusively the case of liquid cores.

Interest in liquid-core waveguides (LCWGs) has developed for numerous reasons. Quite notably, glass fibers filled with high-index liquids, such as hexachlorobutadiene were serious contenders for long-haul telecommunications in the early 1970s [1, 2]. Good performance with light transmission along several kilometers of fiber was demonstrated, but liquid-core waveguides were soon to be abandoned in favor of all-solid silica fiber after the material properties of the silica cores had improved sufficiently to provide ultralow loss.

Subsequently, the emphasis in using liquid-core waveguides has shifted to much more natural uses as sensors for chemicals and biological substances. Liquids play a prominent role in both fields, and optical methods are often used to study either the carrier liquid itself or substances contained therein. LCWGs provide a natural opportunity for creating an environment in which the light can interact with the substance of interest in a well-defined, small volume over possibly long distances. In essence, guiding both light and liquid through the same physical volume maximizes the interaction and should allow for very powerful, i.e., extremely sensitive, optical sensors. This concept is to be distinguished from a complementary class of sensors for which the waveguide core is a solid material and where interaction with

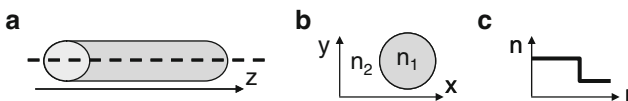


Fig. 1 Waveguide geometry. (a) Cylindrical waveguide with light propagation direction z , (b) circular cross section with refractive indices n_1 and n_2 , (c) corresponding refractive index profile for total internal reflection guiding

light occurs predominantly at surfaces and interfaces between the core and its surroundings. Both chemical and biological sensors using surface interactions with excellent characteristics have been developed. The most popular types include evanescent field sensors and surface plasmon resonance sensors, and the interested reader is referred to the literature (e.g., [3, 4]) for more information on this approach.

Aside from the possibility of higher efficiency due to coinciding light guiding and sample volumes, waveguide-based sensors offer additional benefits that provide strong incentives for their development with a view towards future commercialization. Only very small analyte volumes in the range of pico- to nanoliters depending on the waveguide details are required, which is useful for rapid response and for the ability to sense and detect trace amounts of biological and chemical substances. Moreover, waveguides, whether in the form of fibers or lithographically defined on a chip, can be combined with other integrated optical elements, including on-chip light sources, filters, spectrometers, and photodetectors [5]. They are, therefore, ideally suited for lab-on-chip or micro total analysis (μ -TAS) sensing approaches.

Why, then, have liquid-core waveguides not played a more dominant role as sensors for chemical and biological substances? The answer lies in the nature of the light guiding mechanism. In the past, waveguides including the ubiquitous silica fiber used in telecommunications were mainly constructed by surrounding the core with a cladding material of lower refractive index. Table 1, which displays the refractive indices of a number of relevant liquids and solids, shows that solids tend to have higher refractive indices than most liquids. This means that only certain material combinations lend themselves well to conventional waveguiding. In

Table 1 Refractive indices of liquid and solid materials at 632nm unless noted otherwise

Phase	Material	Refractive index
Liquid	Methanol	1.326 (589 nm)
	Water	1.33
	Acetone	1.357
	Ethanol	1.359 (589nm)
	Propyl alcohol	1.383
	Ethylene glycol	1.43
	CaCl ₂ (40% conc.)	1.44
	Trichlorethylene (TCE)	1.48
	Toluene	1.494
	Hexachlorobutadiene	1.556 (1,000 nm)
Solid	Teflon AF	1.29–1.31
	Teflon FEP	1.34
	Teflon PTFE	1.35
	Polydimethylsiloxane (PDMS)	1.43
	Fused silica	1.45
	Quartz	1.54
	Silicon nitride (Si ₃ N ₄)	2.02
	Silicon	3.92
GaAs	3.84	

particular, water has a lower index than almost all listed solids which presents a challenge for biosensors in which the solvent is typically water-based.

Fortunately, a number of clever approaches to liquid-core waveguiding have been developed, and these concepts have been translated successfully into sensing platforms all the way to single molecule detection sensitivity. In the remainder of this chapter, we will first present an overview of the different types of liquid-core waveguides and their optical characteristics. This discussion will be followed by a section on sensor applications of these waveguides in the fields of chemical and biological detection, organized by the optical sensing mechanism. Due to the large body of literature in this field, the discussion is meant to be representative rather than exhaustive. We will close by summarizing the status of liquid-core waveguide sensors and taking a look at current trends and future directions.

2 Liquid-Core Waveguiding Principles

2.1 Total Internal Reflection-Based Waveguides

The most preferable way to form liquid-core waveguides would be to rely on the principle of total internal reflection that is used in fiber-optic communications. Figure 2a illustrates this concept and introduces the conventions used throughout this chapter. The waveguide core (dark gray, refractive index n_c) is shown in a longitudinal cross section, i.e., the direction of light propagation is assumed to be along z . It is surrounded by a cladding material (light gray) composed of lower refractive index n_{cl} . Intuitively, a ray of light propagating in the core will be guided without propagation loss in the z -direction if the angle of incidence on the core-cladding interface exceeds the critical angle

$$\theta_c = \arcsin\left(\frac{n_{cl}}{n_c}\right). \quad (1)$$

The allowed angles can be determined by imposing a phase condition for the transverse wave vector component k_y in the core [6], and the corresponding modes and electric field patterns can be found from standard electromagnetic field theory [7]. The main advantage of these waveguides is that propagation based on total internal reflection is lossless, i.e., energy is only transported along the desired z -direction, but not along y . Any energy loss observed in an actual device is due to imperfections such as absorption or roughness scattering [8]. Even during the early stages of liquid-core waveguide development, losses as low as 10 dB/km [2] were achieved in hexachlorobutadiene-filled glass fiber. The biggest disadvantage is the index requirement of $n_{cl} < n_c$, as discussed in the introduction. As seen in Table 1, this substantially narrows down the possible combinations of liquid-core materials that can be used in conjunction with common cladding materials, such as

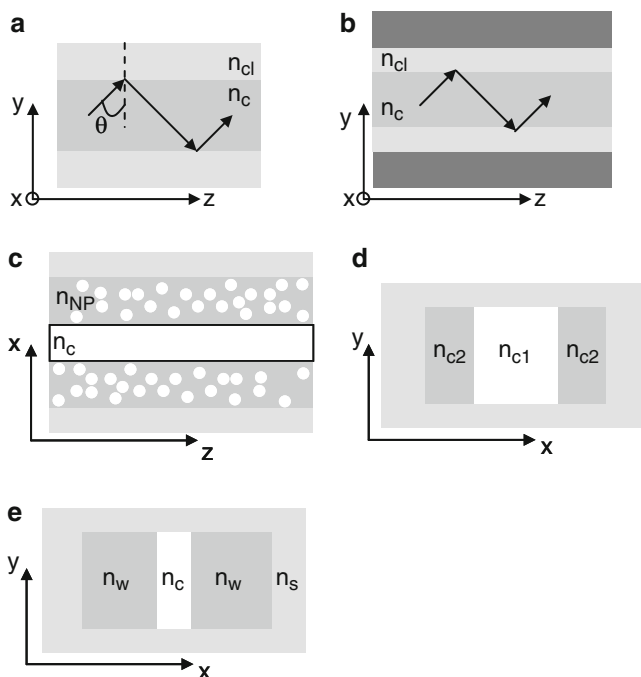


Fig. 2 Total-internal reflection (TIR) based waveguides. **(a)** TIR principle of ray propagating in core medium with index n_c , surrounded by cladding with index n_{cl} , **(b)** LCWG, **(c)** nanoporous cladding waveguide, **(d)** liquid–liquid (L^2) waveguide, **(e)** slot waveguide

glass, silicon nitride, or PDMS in this simplest implementation with a single, homogeneous cladding layer. This problem is particularly severe for water which is the basis for most biological analytes. Several variations of TIR-based waveguides have been developed over the past years to alleviate some of the concerns.

2.1.1 Liquid-Core Waveguides

TIR-guiding in water can be accomplished by using a class of fluorinated polymers, such as Teflon AF, as cladding material. This material is applied as a relatively thin layer on the inside of a higher index material as illustrated in Fig. 2b to form LCWGs. Teflon AF has an index of 1.29 and has been incorporated both in cylindrical tubes and on materials that were wafer-bonded to form a rectangular-shaped hollow cross section [9, 10]. To date, LCWGs have been fabricated with large core diameters of 200–500 μm and Teflon AF cladding thicknesses on the order of a few microns with relatively large fluctuations. In addition, the softness and moderate optical properties of these fluoropolymers limits their utility as materials for sensor chips [11].

2.1.2 Nanoporous Cladding Waveguides

Another way to form a low-index cladding material is to start with a high-index solid material and add air pores until the average index is low enough to facilitate waveguiding. This has the advantage that the cladding index can be tuned by varying the air fraction and that some of the adhesion problems that Teflon AF exhibits can potentially be overcome. Figure 2c shows a schematic image of a slab waveguide that has a nanoporous cladding with index $n_{NP} < n_C$ embedded within a high index substrate. To date, nanoporous claddings have been implemented using a “sacrificial porogen” approach in which an organic phase is removed from a phase-separated polymer hybrid [12]. Only one-dimensional confinement in transverse (x) direction has been demonstrated using this method. However, the existence of low loss modes and the wide tuning range of the cladding index ($1.15 < n_{NP} < 1.37$) make this a very promising technology if a way to create a lateral nanoporous cladding for complete mode confinement can be developed.

2.1.3 Liquid–Liquid-Core Waveguides

A clever way to circumvent the problem of finding a low-index solid cladding material is to use two different liquids with different refractive indices inside a larger fluidic channel. A cross section of such a liquid–liquid or L^2 waveguide is shown in Fig. 2d. As long as the index of the cladding liquid (index n_c) is smaller than that of the core liquid (index n_c) and the cladding layer is thicker than a few micrometers, index guiding in x -direction can be achieved. This concept was first demonstrated using CaCl_2 ($n_c = 1.445$) and water as core/cladding liquids, respectively, embedded in PDMS ($n = 1.4$) [13]. The liquids were introduced into the channel through separate fluidic inlets and exhibited relatively slow mixing along the channel due to the laminar flow conditions. The L^2 waveguide concept is very attractive for sensor applications as in this case control over the fluidic properties allows dynamic modification of the optical performance. Another inherent advantage of L^2 waveguides is that the propagation loss should be independent of the channel roughness (at least along the x -direction) although actual loss values of these waveguides have not been published yet. One limitation of L^2 waveguides aside from intermixing of core and cladding liquids is the fact that up to now, L^2 -guiding has only been implemented along one dimension (x). In the other direction (y), the same considerations with respect to the choice of core and cladding materials that were mentioned above need to be made. This issue, however, can be addressed by using hybrid approaches ([14], see also Sect. 2.3.4).

2.1.4 Slot Waveguides

The recently proposed and demonstrated slot waveguide is an alternative in which index guiding can be realized in nanoscale cross sections, thereby providing an

opportunity for extending waveguide-based sensing into the nanofluidic regime with picoliter or subpicoliter sample volumes [15, 16]. The cross section of a slot waveguide as shown in Fig. 2e appears quite similar to that of the L^2 waveguide. Here, however, the core medium has the lowest index (n_C) in the structure. The immediately adjacent medium has the highest index (n_W) and guided mode solutions exist for this structure. A substantial portion of the optical power can be confined in the low-index core if the width of the core is smaller than the penetration depth of the evanescent wave in the core medium, and if x -polarized light is used. The latter choice results in a discontinuity of the electric field (TM mode) at the core-cladding interface which increases the electric field strength in the core by a factor of n_W^2/n_C^2 . Up to 30% of the optical power can be confined in a 100 nm narrow core for a high index contrast system, such as Si/air with a large enhancement factor of 12 [15, 16]. This field enhancement is somewhat reduced for aqueous cores (7 for a Si cladding, 1.2 for PDMS ($n = 1.45$)). Additional limitations could arise from molecular interactions with the walls due to the large surface-to-volume ratio of the nanofluidic channels.

2.2 Non-TIR-Based Waveguides

2.2.1 Capillary “Waveguide”

One way of dealing with the difficulty of finding suitable materials for TIR guiding is to ignore it and try to guide light along a low-index medium surrounded by a high-index cladding material [17]. This situation is illustrated in Fig. 3a where the propagating ray of light is now partially refracted into the cladding at each dielectric interface, leading to radiation loss perpendicular to the desired propagation direction. Such a structure can still be considered as a waveguide as there is a net flow of energy along the z -direction. Its advantage is that it is easily realized with a wide range of materials, e.g., a hollow glass capillary. It makes, however, for a very poor waveguide due to the high propagation loss given by

$$\alpha = \frac{\lambda^2}{n_c d^3 \sqrt{n_{cl}^2 - n_c^2}}, \quad (2)$$

where α describes the attenuation of light power after a propagation distance L along the waveguide by a factor $e^{-\alpha L}$ according to the Lambert–Beer law. The dependence of the loss of the (one-dimensional) capillary waveguide structure is shown as the top line in Fig. 4 for water as the core material ($n_c = 1.33$) and a glass cladding ($n_{cl} = 1.45$) at a wavelength of 632 nm. The graph shows an important characteristic of the waveguide loss, namely the inverse dependence on the third power of the core diameter d . Since a loss of 1 cm^{-1} corresponds to a reduction of the optical power by 63% over a distance of 1 cm, it is evident that

Fig. 3 Non-TIR-based waveguides. (a) leaky waveguide with light ray being refracted into high-index cladding material, (b) metal-clad waveguide, (c) waveguide with guiding in cladding (all-dielectric), (d) waveguide with guiding in cladding (metal outer coating), (e) Fresnel fiber cross section, (f) zero-mode waveguide cross section showing nanoscale holes of width w and height h

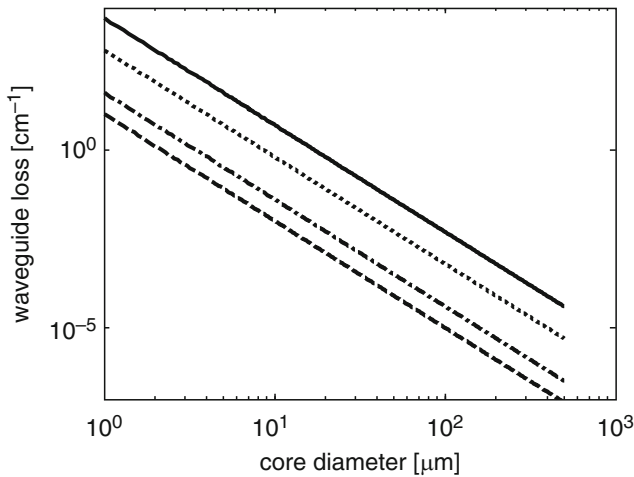
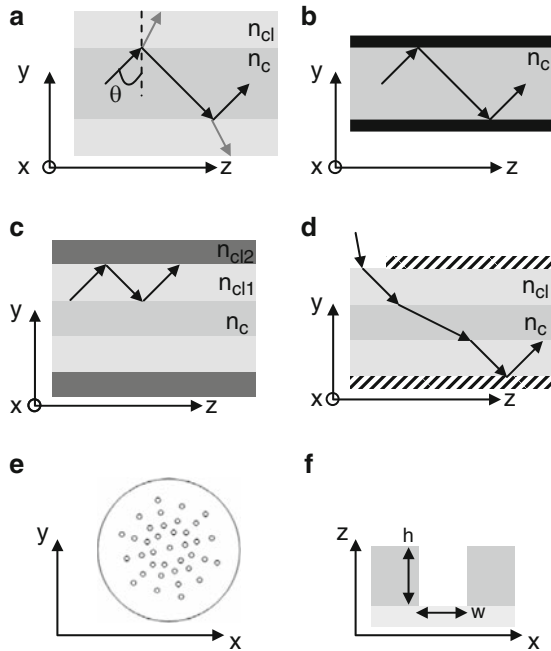


Fig. 4 Propagation loss versus core dimension for different (one-dimensional) waveguide types: leaky capillary waveguide (*solid line*), metal-clad waveguide (*dash-dotted line*), ARROW waveguide with one (*dotted line*) and five (*dashed line*) ARROW layers

the waveguide loss becomes intolerable very quickly as the core dimensions are reduced. (The loss in dB/cm can be obtained by multiplying the values in Fig. 4 with 4.34.)

2.2.2 Metal-Clad Waveguides

An intuitively simple way to reduce the loss due to refraction into the cladding material is to coat the inside of the cladding with a highly reflective metal as shown in Fig. 3b. This approach results in a metal waveguide for which the outer dielectric material does not affect the guiding properties as long as the metal layer thickness exceeds the skin depth [18]. The resulting waveguide loss for a parallel-plate waveguide in the ray optics picture can be calculated from the power loss due to the finite reflection from the metal at the appropriate mode angle [6]. The expression for the loss is then

$$\alpha = \frac{(1 - R)\lambda}{2n_c d^2}, \quad (3)$$

where R is the water/metal reflectivity at the mode propagation angle. The dependence on the core diameter is illustrated in Fig. 4 for a silver coating at 632 nm. We see that the loss is approximately two orders of magnitude lower than for the capillary waveguide, and that it shows the same characteristic d^{-3} behavior (note that the reflectivity is d -dependent). Metal-clad waveguides have been realized in practice by coating glass tubes (inner diameters 250 μm) with silver layers of several hundred nanometers thickness. Optical measurements on 50-cm-long air-filled fibers were made which showed an attenuation of 10^{-3} cm^{-1} at a wavelength of 800 nm [19]. Guiding could also be accomplished if they were filled with low-index fluids. The major limitations of this approach are difficulties in developing a suitable coating process for on-chip waveguides and substantially higher experimental loss due to imperfections of the metal coating due to surface roughness [20]. These nonidealities tend to dominate the waveguide performance, resulting in a factual improvement over leaky capillary waveguides only for very small diameters ($\lesssim 20 \mu\text{m}$) [11].

2.2.3 Waveguides with Cladding Guiding

Another nonconventional approach to liquid-core waveguiding is shown in Fig. 3c,d. Here, a dielectric cladding is sandwiched between the liquid core and another cladding layer. In one implementation (Fig. 3c), the wave is guided by TIR in the cladding layer, and the sensing mechanism in the liquid core relies on the well-known evanescent field coupling. This was implemented in “fiber-optic capillary” (FOCap) waveguides [21] (core diameter 50–150 μm) using methanol as the core liquid and fused silica and doped fused silica ($n = 1.441$) as the first and second dielectric claddings, respectively. Figure 3d, however, shows how under an appropriate propagation angle the light can traverse the liquid core repeatedly, despite not being actually guided in it. Highly efficient reflection from the outer cladding interface ensures good overall guiding. This can be achieved either by using an outside metal

layer [22] or a dielectric material [21, 23]. Silver-coated glass capillaries (inner/outer diameter of 75/364 μm) were made with a 40-fold increase of the path length compared to a single pass liquid cell. ARGOWs (antiresonant guided optical wave) used glass slides as the cladding and air as the outer cladding. Here, the relative path length and therefore interaction wavelength within the liquid core is maximized if the ray hits the glass/liquid interface at a near-critical angle and if the core thickness is increased. Relative confinement factors near 60% in a 160 μm thick water layer were demonstrated [23].

2.2.4 Fresnel Waveguides

Fresnel waveguides appear to be similar to the photonic crystal fibers discussed in Sect. 2.3 in that they incorporate a distribution of holes over the cross section of a solid fiber [24], see Fig. 3e. Here, however, the whole distribution acts as a Fresnel zone plate to confine the light. Light confined in such a way has interesting properties, such as the generation of multiple foci at the fiber output due to wave interference [25]. Fresnel fibers made of silica with holes of ~ 5 μm diameter were fabricated and showed good waveguiding properties when the central hole was filled with water [24]. The potential utility of such an approach for chemical and biological sensors was pointed out, but has not been realized yet.

2.2.5 Zero-Mode Waveguides

The final example for atypical liquid-core waveguides are zero-mode waveguides (ZMWGs) [26]. The side view of a ZMWG in Fig. 3f shows that its defining elements are nanoscale holes within a metal layer whose width is so small that even optical frequencies are below the cutoff frequency of this metal waveguide [18]. In a sense, the goal is to create a non-waveguiding structure where only an evanescent tail of the electric field will penetrate into the hole. This leads to extremely small optical excitation volumes on the order of zeptoliters (10^{-21} l) inside the hole. Arrays of ZMWGs were fabricated in an aluminum film (89 nm height) on fused silica substrates using standard nanofabrication methods, resulting in millions of holes with diameters ranging from 30 to 80 nm.

2.3 *Interference-Based Waveguides*

It was already pointed out that single or multilayer dielectric coatings can reduce the loss of a leaky capillary waveguide substantially, but that it was difficult to see this improvement in practice due to fabrication imperfections [11]. Advances in fabrication technology have helped improve these imperfections. In addition, a strong need for liquid-core waveguides with small cross sections of a few microns

or even nanometer dimensions has developed due to the possibility of single molecule sensing in subpicoliter excitation volumes. Finally, new waveguide types – in particular, photonic crystal-based – that rely on spatial structure of the waveguide cladding have been introduced. Based on all these factors, liquid-core waveguides based on wave interference have become a very active field of research, both from a conceptual standpoint and with a view for sensor applications. They represent perhaps the most promising approach towards efficient liquid-core waveguiding due to their favorable balance of low loss, fabrication complexity, and integration potential.

The underlying common principle of these waveguides is the use of wave interferences to localize the electromagnetic wave. The refractive index profile of the cladding is structured in the (x – y) cross section of the waveguide to create multiple reflections of the electric field that can interfere constructively or destructively. The key idea in the present context is that near-perfect reflection into the original medium can be achieved even if that medium has a lower index than all of the cladding layer materials.

2.3.1 Bragg Fibers

A very important implementation of interference-based waveguiding is the special case where dielectric cladding layers are repeated periodically and extended to infinity. The partial reflections are then equivalent to the Bragg reflections that are well known from X-ray analysis of crystalline materials. In complete analogy, the electric field propagating inside the periodic medium can be described by a Bloch wave vector \mathbf{K} that reflects the periodicity of the structure (period Λ) and depends on Λ , the wave frequency ω , and the indices of the dielectric materials. Real (imaginary) values of \mathbf{K} correspond to propagating (evanescent) solutions and lead to allowed (forbidden) regions, so-called bands, if \mathbf{K} is plotted in an ω – β diagram where β is the magnitude of the wave vector along the waveguide axis. Two conditions need to be fulfilled for realizing a liquid-core Bragg waveguide. First, the Bragg lattice has to be highly reflective, i.e., one has to operate within a forbidden region of \mathbf{K} . Secondly, the transverse component of the wavevector β has to fulfill the same phase resonance condition as in the case of index guiding to allow for transport of energy along the propagation (z) direction. Bragg slab waveguides were first proposed by Yeh and Yariv in 1978 [27], and a more comprehensive review including an analysis of the polarization dependence is given in [28]. The cross section of a cylindrical Bragg fiber is shown in Fig. 5a and illustrates how the periodic layers surround a circular low index core resulting in an index profile that depends on the radial distance from the core center. Cylindrical Bragg fibers were first analyzed by Yeh et al. [29] and later refined by Xu et al. [30]. The first experimental demonstrations of light guiding in an air-core Bragg fiber were given by Fink et al. [31] using a large ~ 2 mm air core surrounded by alternating layers of tellurium and polymer, followed by 275 μm -core As_2Se_3 /PES-fibers for infrared guiding [32]. If the Bragg layers are designed to be reflective for all angles

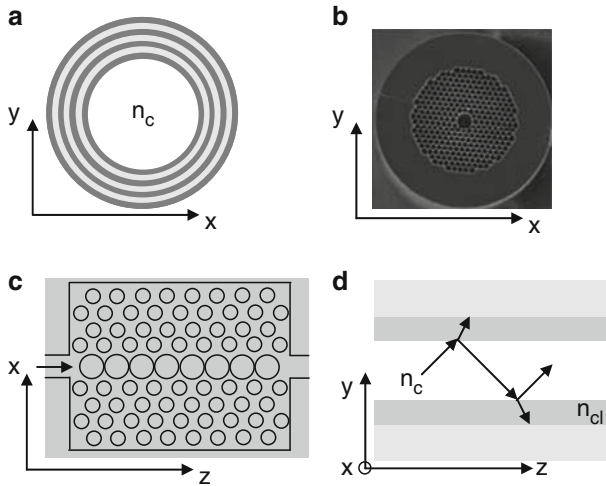


Fig. 5 Interference-based waveguides. (a) Bragg fiber cross section, (b) HC-PCF cross section, (c) top view of two-dimensional photonic crystal waveguide, (d) ARROW

of incidence (omnidirectional guiding [33]), light can even propagate around bends with very low loss. This concept has been successfully developed into medical instruments for CO₂ laser delivery for otolaryngology and pulmonology (see www.omni-guide.com).

2.3.2 Hollow-Core Photonic Crystal Fiber

The photonic crystal concept is not restricted to one-dimensional index periodicity. In fact, dielectric structures with two-dimensional periodicity currently play a bigger role in liquid-core waveguiding. Figure 5b shows the cross section of a hollow-core photonic crystal fiber (HC-PCF) [34, 35]. In this case, a hollow core with typical diameters between 5 and 20 μm is surrounded by a periodic arrangement of holes inside a silica network. As in the one-dimensional case, the spatial structure of the air/silica index variation determines the propagation properties of the hollow fiber along the z -direction. Waveguiding in liquid-core HC-PCFs has successfully been demonstrated by several groups [36–38]. The main areas of concern for utilizing HC-PCFs in commercial sensors are side access to the fiber and the multimode nature for propagation [39]. As discussed in Sect. 3, current approaches insert both light and liquid at the open ends of the fiber which prohibits splicing the fiber to a conventional solid-core fiber. Accessing the inside of the fiber from the side through slots made with focused ion beam lithography is one possible solution [39]. In addition, commercial HC-PCFs are highly multimode in nature which eliminates their use for interferometric purposes. The number of modes can be reduced by filling the cladding holes with a suitable liquid [39].

2.3.3 2D Photonic Crystal-Waveguides

The third approach to utilizing a photonic band gap structure for low-index waveguiding is schematically depicted in Fig. 5c. Light propagation in the direction of the arrow is achieved by Bragg reflection (2D photonic crystal) in the x - z plane [40] and conventional index guiding in the third dimension. This concept was first realized using a central solid core silicon waveguide surrounded by periodic air holes to facilitate light guiding around tight bends [41]. A compelling feature of these PC-waveguides compared to their fiber counterparts is their planarity which is highly attractive for planar optofluidic integration. Nanofluidic tuning of the optical properties of a photonic crystal waveguide with this geometry was also demonstrated [37]. By using multilayer integration of the optical waveguide layer and a fluidic delivery layer, it was possible to address (fill) individual holes in the 2D PC-waveguide, in particular, the central guiding row with the larger holes. The nanoscale spatial control and level of higher level integration in this platform is encouraging for future developments of fluidically controlled optics [42]. 2D PC waveguides have not been used with liquid guiding channels. Conceptually, this should also be possible and would open up this approach to optical analysis of sample analytes in a liquid-core waveguide.

2.3.4 Antiresonant Reflecting Optical Waveguides

The last type of interference-based liquid-core waveguides is antiresonant reflecting optical waveguides (ARROWs). ARROWs are also based on an interference effect, but do not require the periodicity of a photonic crystal that results in the description of light propagation by means of Bloch wave vectors and allowed/forbidden bands. Consequently, a single dielectric layer is sufficient to provide low-loss propagation as illustrated in Fig. 5d. A light ray impinging from the low-index core on the high index ARROW layer (index n_{cl}) is refracted into the ARROW layer due to the absence of total internal reflection. However, if the thickness of the ARROW layer is chosen such that the round trip phase shift Φ_{RT} of the transverse (y) wave component in medium n_{cl} fulfills an antiresonance condition $\Phi_{RT} = m\pi$ (m odd), light is reflected back into the core with high efficiency and enables low loss light propagation in the low-index core. Of course, the waveguide is still a leaky one and has finite propagation loss. Analytical approximations for the loss in the case of optimized cladding layer thicknesses were derived by Archambault et al. [43]. In the simple case of two alternating cladding materials, the loss (TE mode) as a function of core thickness and number of cladding layers N is given by

$$\alpha = \frac{\lambda^2}{n_c d^3 \sqrt{n_{cl1}^2 - n_c^2}} \sqrt{\frac{n_{cl2}^2 - n_c^2}{n_{cl1}^2 - n_c^2}}^N. \quad (4)$$

The similarity with (2) is striking and not coincidental. The functional dependence on both wavelength and core thickness is the same. To the extent that the extra factor under the square-root is less than one, the loss decreases rapidly with increasing number of ARROW cladding layers. This trend is exemplified in Fig. 4 for $N = 1$ and $N = 5$ with silicon nitride as the second cladding material. We see that a few layers are sufficient to achieve better performance than with metal claddings, and that the loss is low enough to make cores of a few microns' width technologically interesting.

The ARROW concept was first implemented in solid-state waveguides to guide light through silicon dioxide on top of a silicon substrate using a silicon ARROW layer [44]. ARROWs were later used for semiconductor laser applications [45, 46]. The use of hollow-core ARROWs was first demonstrated by Delonge and Fouckhardt [47], who used alternating TiO_2 and SiO_2 ARROW layers to confine light in capillaries with $20 \times 20 \mu\text{m}^2$ cross section. More recently, liquid-core waveguides with ARROW confinement using silicon nitride and silicon dioxide were built using silicon microfabrication technology. Both large multimode ($d > 100 \mu\text{m}$) [48] and (quasi) single-mode ($d < 10 \mu\text{m}$) [49] ARROWs have been demonstrated using wafer bonding and sacrificial layer techniques, respectively. Losses as low as 0.26 cm^{-1} were demonstrated in waveguides with a mode area of only $7.4 \mu\text{m}^2$ [50].

One property of ARROWs that is particularly relevant to on-chip sensors is that they can be designed to enable simultaneous guiding of light in a solid- and a liquid-core waveguide. This enables the transfer of light in and out of fluidic channels to produce fully planar optical architectures. The concept of intersecting solid and liquid waveguides was theoretically proposed and later demonstrated by single molecule fluorescence detection using planar beam geometry [51, 52].

3 Sensor Applications

The biggest advantage of optical sensors is their inherent versatility. There are numerous sensing modalities on which to base detection, and sometimes several can be implemented at the same time, resulting in a multidimensional sensing process. Coupled with the added ability to optically *control* the substances of interest via optical traps and tweezers [53], waveguide-based optical sensors are among the most powerful detection methods for a nearly unlimited number of substances. The most important sensing modalities are absorption, fluorescence, scattering, refractive index, and polarization changes. In the following sections, we will discuss the basic properties of these detection mechanisms, and give examples for their implementation in liquid-core waveguides for both chemical and biological sensing.

3.1 Absorption

The simplest method to optically detect a substance is to measure the amount of light transmitted through a defined length of this substance. If the wavelength of the

light coincides with one of the (electronic) resonances of the material, photons will be absorbed, and the optical power will decrease along the length of the sample according to the Lambert–Beer law

$$P_{\text{out}} = P_{\text{in}} e^{-\alpha(\lambda)L}, \quad (5)$$

where $\alpha(\lambda)$ is the wavelength-dependent absorption coefficient and L is the sample length. Since α depends on the sample concentration, the concentration of a known substance can be determined in a sensor with a known absorption length. Sensor performance improves with sample length which can be a problem for miniaturized sensors where the goal is to keep overall dimensions small. A good solution to this problem is to extend the light–sample interaction length. Resonant structures, but also the metal-clad or ARGOW waveguides described in the previous section, can be used to achieve this. It is, however, extremely challenging to measure small substance quantities in absorption due to the minute changes in optical power although single molecule absorption has been detected [54].

Absorption detection has been more commonly used for chemical sensing purposes. Liquid-core waveguides as described in Sect. 2.1.1 using various low-index fluoropolymer claddings (PTFE, PFA, FEP) were used for detection of ammonia by color changes in bromothymol blue (BTB) and for detection of trichloroethylene (TCE) using pyridine chemistry [55]. In this case, the waveguide membrane could also be used as the sampling element. Silver-coated capillary waveguides were used as multipass absorption cells for capillary electrophoresis [22]. Due to a fortyfold increase in the absorption path length L , a concentration detection limit of 65 nM for brilliant green was demonstrated. FOCap waveguides of up to 50 m length were used as chemical sensors by deducing pH changes from the absorption spectrum of fluorescein [21]. In this case, however, it turned out that evanescent detection, i.e., light propagation in the solid cladding, was more sensitive than the liquid-core waveguide mode of the FOCaps. Recently, mid-infrared absorption sensing using photonic bandgap fiber (omniguide) was demonstrated [56]. This wavelength range has substantial technical importance for process and environmental monitoring, surveillance applications, and biomedicine. Here, detection of ethyl chloride concentrations as low as 30 ppb were shown.

3.2 Fluorescence

A method that is extremely versatile and can be applied to sensing of minute quantities of a substance of interest is optical fluorescence. In this case, molecules absorb light at one wavelength and reemit light at a different wavelength after a fraction of the electron energy is lost, typically to molecular vibrations and rotations. The reemitted light spectrum is highly characteristic of the fluorescing molecule, and fluorescent emitters with very high quantum efficiency (= fraction of reemitted

light) are available for different spectral ranges. It is, therefore, possible to identify the substance of interest by the fluorescence it emits (autofluorescence), or by using particularly efficient fluorescent molecules (fluorophores) that bind selectively to the target substance. Fluorescence spectroscopy is capable of resolving signals from single molecules [57] within small optical excitation volumes, and has led to several modifications of the basic principle that have found applications in sensing. Fluorescence or Förster resonance energy transfer describes a method in which two fluorescent dyes are attached to the same particle [58]. One of the two dyes is optically excited and loses some of this energy to the second dye molecule. Since the efficiency of this transfer is strongly distance-dependent, the inter-dye distance can be detected by monitoring the relative intensity of the dye fluorescence signals. This can be used to track motion in particles. In fluorescence correlation spectroscopy, one monitors not the fluorescence signal itself, but its fluctuations over time. By looking for correlations in the fluctuation signals, numerous properties of the labeled particles can be extracted, including concentration, kinetic parameters, binding processes, and more [59]. Fluorescence lifetime imaging microscopy describes a time-resolved method in which the temporal evolution of the fluorescence signal is tracked on a nano to microsecond time scale. Changes in the decay time (lifetime) of the fluorescence signal are then used to monitor changes in the environment, e.g., pH changes [58].

Numerous types of liquid-core waveguides have been used for fluorescence detection. In this case, applications lie predominantly in biological sensing. Teflon AF-coated liquid-core waveguides of 200–500 μm core dimensions were shown to be capable of fluorescence detection of dye with nanomolar concentration [10]. Fluorescing nanobeads were detected in liquid-core waveguides with nanoporous claddings (index as low as 1.15) [12]. Similarly, the enhanced optical path length in ARGOW waveguides was exploited for excitation and detection of fluorescent molecules [23]. Fluorescence has also been excited in L^2 waveguides in which the core liquid was ethylene glycol and the cladding liquid was water [60]. Rhodamine 6G molecules contained in the glycol core were optically excited and acted as a de facto on-chip light source as their emission was captured and guided by the L^2 waveguide. The limits of fluorescence detection sensitivity are being pushed mainly by interference-based waveguides. Dye concentrations in the nanomolar range were detected in hollow-core photonic crystal fibers in which the core hole was selectively coated with Rhodamine 6G [61]. Completely waveguide-based single-molecule fluorescence detection was shown in intersecting solid-core and liquid-core ARROWS, where the waveguide intersection helped define a sub-picoliter excitation volume on the order of 115 fl [52]. The addition of fluidic reservoirs to these waveguide structures allowed for the addition of electrical control and the use of various water-based biological buffer solutions. Subsequently, single liposomes and bacteriophages were detected and analyzed on an ARROW-based chip [62, 63]. In this context, fluorescence correlation spectroscopy proved to be an extremely useful and sensitive technique with unique characteristics when implemented in a waveguide geometry [64]. FCS has also been used to observe single DNA polymerase molecules and their activity in zero-mode

waveguides [26]. The extremely small excitation volume in the nanoscale holes allowed for single molecule sensitivity in unusually high (micromolar) concentrations. ZMWGs have subsequently been used for fluorescence studies of lipid membranes to extract the binding constant of a toxin at high concentration [65]. They also provide a highly promising approach to rapid DNA sequencing (<http://www.pacificbiosciences.com>).

3.3 Scattering

If the light reemission process does not involve a resonant absorption process, we deal with scattering events. These can be divided into elastic and inelastic scattering where the scattered wavelength is the same as or differs from the incident wavelength, respectively. Elastic scattering processes include Rayleigh scattering in the case of particles that are much smaller than the probing wavelength, and Mie scattering for large particles. The most important inelastic process for liquid-core sensors is Raman scattering. In this case, incident and scattered photons differ in wavelength. A Stokes process refers to longer emitted wavelength, and an anti-Stokes process to the opposite. The difference in photon energy is transferred to (Stokes) or taken from (anti-Stokes) the scattering molecule as vibrational quanta (phonons). These quantized vibrations are molecule-specific and are the reason for the attractiveness of Raman scattering as a sensing mechanism. The Raman process provides a unique fingerprint for the molecule, and in addition, does not necessitate labeling with a fluorescent dye. The major downside of this technique is its inefficiency which is many orders smaller than that of a fluorescence process. By binding the molecules to a metal surface or nanoparticle (surface-enhanced Raman scattering), the process can be made more effective, and single molecule detection based on this principle has been reported [66].

Liquid-core waveguides can be applied to sensing both elastic and inelastic scattering processes. Elastic scattering is often detected in flow cytometers where cells with sizes on the order of a few to tens of microns provide a large enough cross section [67]. A waveguide-based flow cytometer was demonstrated using polymer chips with leaky hollow-waveguide channels of $50 \times 50 \mu\text{m}^2$ cross section [68]. Microbeads were moved through the channels and interrogation and detection was accomplished via in-plane solid waveguides. While the detection mechanism of choice in this example was fluorescence, the experiment could also easily be carried out using Rayleigh scattering, alluding to the potential of liquid-core waveguide based cytometric detection. This is further supported by recent demonstrations of optically induced transport in both photonic crystal fiber [69] and ARROWs [70]. This additional optical control enabled by the light-guiding structures adds another level of control to sensing of particles suspended in a carrier liquid.

The first report on liquid-core waveguide based Raman sensing described the detection of acetonitrile ($n = 1.34$) in Teflon-AF coated capillaries in both forward

and backward scattering geometries [71]. Currently, Raman sensing is predominantly carried out in interference-based waveguides. The first such demonstration was reported in 2006 when surface-enhanced Raman scattering from Rhodamine B molecules bound to gold nanoparticles was measured. The nanoparticles were immobilized on the walls of the photonic-crystal fiber air holes, and the entire system was sensitive to a concentration of about 10 μM of rhodamine molecules [38]. In a subsequent study, only the central core hole was filled with liquid and Raman scattering from rhodamine 6G, insulin, and tryptophan was detected with a sensitivity of $\sim 10^{-5}$ M [72]. Rhodamine 6G molecules bound to silver nanoparticles for enhanced Raman scattering were also detected in liquid-core ARROW waveguides [73]. In this case, high sensitivity down to 30 nM R6G concentration could be shown. Single molecule Raman detection in liquid-core waveguides, however, has remained elusive to date.

3.4 Refractive Index Changes

The fourth widely used optical sensing method is detection and analysis of refractive index changes by the presence of a liquid or molecules of interest. Many optical interactions depend on the refractive indices involved, for example, reflection coefficients or angles of refraction. The index of refraction of a liquid can change due to a number of reasons, such as a change in temperature, changes in composition, or addition of molecules. Since these changes are typically rather small (on the order of 1 part in 10^3 – 10^4), refractometers are often based on resonant structures in which a small change still causes a large effect. Figure 6 illustrates this fact by depicting two generic transmission curves through a Fabry–Perot resonator-like structure with different indices in the optical path. Here, the sensing mechanism would be to detect the change in transmission at a fixed wavelength resulting from a variation in index. It is evident that the sensitivity improves as the transmission peaks get sharper. The sharpness is characterized by the quality factor (Q -factor) of the resonator, and large Q -values are clearly desirable.

Refractometric liquid-core waveguide sensors show excellent performance, in particular, when using interferometry to enhance the effect of an index change. Another possibility to introduce a dependence on refractive index is to take advantage of mode beating in a multimode waveguide. In [74], small liquid channels ($2.6 \times 3.9 \mu\text{m}$) were defined between two Ge-doped silica waveguides clad by borophosphosilicate glass. The channels were lithographically aligned with single silica waveguides that provided an optical interface with the ends of the chip. The output power of a 16 mm long liquid-core section depends on the beat length between the two lowest order modes of the waveguide. This beat length in turn is directly related to the refractive index of the liquid. Measurements of throughput versus core index revealed a sensitivity of $\sim 1.1 \times 10^{-4}$ refractive index units (RIU). Hollow-core photonic crystal fibers were turned into a refractometric sensor by inscribing long-period gratings (700 nm period, total length 18.2 mm) into the

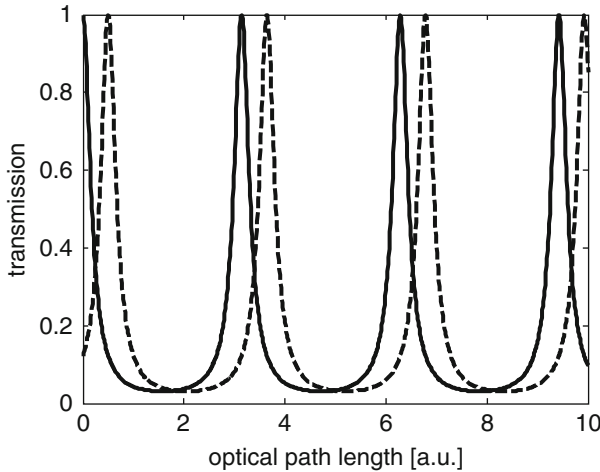


Fig. 6 Transmission through Fabry–Perot etalon versus optical path length. The *two curves* correspond, for example, to different refractive indices of the etalon material and show a characteristic resonance behavior

fiber cladding [75]. Filling the fiber holes with a liquid affected the effective index of the cladding mode and altered the resonant wavelength of the grating which itself depends on the difference between the effective indices of the core and cladding modes. The sensitivity of this device is on the order of 10^{-4} RIU. Biochemical sensing was then demonstrated by detecting the wavelength shift induced by DNA molecules that bound to a monolayer of poly-L-lysine inside the PCF holes. Refractometric sensitivity to index changes on the order of 10% was shown in planar two-dimensional photonic crystals by selectively filling the holes along the center waveguide with liquids of different index [37]. This sensor was integrated within a nanofluidic chip that featured separate control, flow, and photonic layers. Large-core ARROW waveguides ($150 \times 150 \mu\text{m}$ core dimensions) were filled with liquids of different index and showed a dependence of the transmission spectrum on the liquid-core index that corresponds to a sensitivity of 9×10^{-4} RIU [76]. The core dimensions were chosen to match those of multimode optical fiber which could be inserted directly into the ARROW core. Finally, excellent refractometric sensitivity on the order of 10^{-7} RIU has recently been demonstrated in liquid-core optical ring resonators (LCORRs) [77, 78]. In these structures, the light does not propagate through a liquid core. Instead, the whispering gallery modes of the capillary surrounding the liquid are used to form a resonator that can be coupled to a nearby bus waveguide. Due to the high sensitivity afforded by the resonator design and the possibility for on-chip integration with solid-core waveguides, LCORRs are an attractive class of sensors. Both chemical sensing of ethanol and hexane and label-free biological sensing of DNA has been demonstrated [79, 80].

3.5 Polarization Changes

Polarization describes the orientation of the electric and magnetic fields that constitute a propagating electromagnetic wave. It can be the basis of a liquid-core waveguide sensor if the polarization is suitably altered by the substance to be detected. Numerous chemical and biological substances are known to be *optically active*, i.e., they rotate the direction of the electric field by an amount proportional to the substance concentration and propagation length. When implemented in an interferometer geometry, polarimetric sensors can have sensitivities that exceed those of amplitude-based interferometers by a few orders of magnitude [81]. On the downside, the requirements for the waveguides are more demanding as they need to maintain polarizations over distances long enough for the sensing process. The use of liquid-core waveguides for polarimetry is still in its infancy, but offers attractive advantages, such as long interaction length for compounding small polarization rotations and the absence of polarization scrambling in conventional silica fiber. A first demonstration of such a polarimeter was implemented in silica capillaries (core diameter 150 μm) filled with different chiral high-index liquids, including limonene, carvone, and α -pinene [82]. Detection sensitivities of 0.3 mM for the limonene solutions in a 27-cm-long liquid-core fiber were achieved. In addition, it was possible to curl the fibers in a suitable pattern to produce a compact sensor footprint without causing birefringence effects to introduce unwanted polarization rotation.

4 Concluding Remarks

The preceding sections have provided a glimpse into the wealth of research in the field of liquid-core waveguide sensors. The ability to employ different waveguide principles for different sensing modalities creates a nearly unlimited number of sensor types, some with rather impressive detection sensitivities. The specific requirements of substances to be detected, their chemical nature, and constraints arising from the sensing instrument, such as size or cost, will ultimately dictate which waveguide type fits each situation best. Nevertheless, a few clear trends in sensor development can be observed. First, the lab-on-a-chip concept drives the integration of small sensors with other elements of a larger instrument, e.g., sample preparation sections or nonoptical sensing components. This field provides a fertile ground for development of liquid-core optical waveguides. Second, the detection limits of waveguide-based sensors are continuously being pushed towards single particle resolution. This is particularly evident in fluorescence detection of biological molecules and particles. Aside from representing an impressive technological feat, single molecule detection and sensing have very concrete real-world applications, such as rapid sequencing of genomes and proteins. Undoubtedly, future refinements and innovations in liquid-core waveguides will help to push the boundaries in chemical and biological sensing.

References

1. Stone J (1972) Optical transmission in liquid-core quartz fibers. *Appl Phys Lett* 20:239–240
2. Payne DN, Gambling WA (1972) New low-loss liquid-core fibre waveguide. *Electron Lett* 8:374–376
3. Homola J, Yee SS, Gauglitz G (1999) Surface plasmon resonance sensors: review. *Sensors Actuators A Phys* 54:3–15
4. Sharma AK, Jha R, Gupta BD (2007) Fiber-optic sensors based on surface plasmon resonance: a comprehensive review. *IEEE Sens J* 7:1118–1129
5. Balslev S, Jorgensen AM, Bilenberg B, Mogensen KB, Snakenborg D, Geschke O, Kutter JP, Kristensen A (2006) Lab-on-a-chip with integrated optical transducers. *Lab on a Chip* 6:213
6. Yeh P (2005) *Optical waves in layered media*, 2nd edn. Wiley, New York
7. Okamoto K (2005) *Fundamentals of optical waveguides*, 2nd edn. Academic, London
8. Hunsperger RG (2002) *Integrated optics*, 5th edn. Springer, Berlin
9. Schelle B, Dreß P, Franke H, Klein KF, Slupek J (1999) Physical characterization of light-guide capillary cells. *J Phys D Appl Phys* 32:3157–3163
10. Datta A, Eom I, Dhar A, Kuban P, Manor R, Ahmad I, Gangopadhyay S, Dallas T, Holtz M, Temkin H, Dasgupta P (2003) Microfabrication and characterization of Teflon AF-coated liquid core waveguide channels in silicon. *IEEE Sens J* 3:788–795
11. Grewe M, Grosse A, Fouckhardt H (2000) Theoretical and experimental investigations of the optical waveguiding properties of on-chip microfabricated capillaries. *Appl Phys B* 70: S839–S847
12. Risk WP, Kim HC, Miller RD, Temkin H, Gangopadhyay S (2004) Optical waveguides with an aqueous core and a low-index nanoporous cladding. *Opt Express* 12:6446–6455
13. Wolfe DB, Conroy RS, Garstecki P, Mayers BT, Fischbach MA, Paul KE, Prentiss M, Whitesides GM (2004) Dynamic control of liquid-core/liquid-cladding optical waveguides. *Proc Natl Acad Sci USA* 101:12434–12438
14. Bernini R, DeNuccio E, Minardo A, Zeni L, Sarro PM (2008) Liquid-core/liquid-cladding integrated silicon ARROW waveguides. *Opt Commun* 281:2062–2066
15. Almeida VR, Xu Q, Barrios CA, Lipson M (2004) Guiding and confining light in void nanostructures. *Opt Lett* 29:1209–1211
16. Xu Q, Almeida VR, Panepucci RR, Lipson M (2004) Experimental demonstration of guiding and confining light in nanometer-size low-refractive-index material. *Opt Lett* 29:1626–1628
17. Marcatili EAJ, Schmeltzer RA (1964) *Bell Syst Tech J* 43:1783
18. Jackson JD (1998) *Classical electrodynamics*, 3rd edn. Wiley, New York
19. Mohebbi M, Fedosejevs R, Gopal V, Harrington JA (2002) Silver-coated hollow-glass waveguide for applications at 800nm. *Appl Opt* 41:7031–7035
20. Saleh BEA, Teich MC (2007) *Fundamentals of photonics*. Wiley, New York
21. Keller BK, DeGrandpre MD, Palmer CP (2007) Waveguiding properties of fiber-optic capillaries for chemical sensing applications. *Sensors Actuators B Chem* 125:360–371
22. Wang T, Aiken JH, Huie CW, Hartwick RA (1991) Nanoliter-scale multireflection cell for absorption detection in capillary electrophoresis. *Anal Chem* 63:1372–1376
23. Schmidt O, Bassler M, Kiesel P, Johnson NM, Doehler GH (2006) Guiding light in fluids. *Appl Phys Lett* 88:151109
24. Martelli C, Canning J, Lyytikainen K, Groothoff N (2005) Water-core Fresnel fiber. *Opt Express* 13:3890–3895
25. Canning J, Buckley E, Lyytikainen K (2003) Propagation in air by field superposition of scattered light within a Fresnel fiber. *Opt Lett* 28:230–232
26. Levene MJ, Korlach J, Turner SW, Fouquet M, Craighead HG, Webb WW (2003) Zero-mode waveguides for single-molecule analysis at high concentrations. *Science* 299:682–686
27. Yeh P, Yariv A (1978) Bragg reflection waveguides. *Opt Commun* 19:427–430

28. Yeh P, Yariv A, Hong C (1977) Electromagnetic propagation in periodic stratified media. I. General theory. *J Opt Soc Am* 67:423–438
29. Yeh P, Yariv A, Maron E (1978) Theory of Bragg fiber. *J Opt Soc Am* 68:1196–1201
30. Xu Y, Lee RK, Yariv A (2000) Asymptotic analysis of Bragg fiber. *Opt Lett* 25:1756–1758
31. Fink Y, Ripin DJ, Fan S, Chen C, Joannopoulos JD, Thomas EL (1999) Guiding optical light in air using an all-dielectric structure. *J Lightwave Technol* 17:2039–2041
32. Temelkuran B, Hart SD, Benoit G, Joannopoulos JD, Fink Y (2002) Wavelength-scalable hollow optical fibres with large photonic bandgaps for CO₂ laser transmission. *Nature* 420:650–653
33. Winn JN, Fink J, Fan S, Joannopoulos JD (1998) Omnidirectional reflection from a one-dimensional photonic crystal. *Opt Lett* 23:1573
34. Cregan RF, Mangan BJ, Knight JC, Birks TA, Russell PSJ, Roberts PJ, Allan DC (1999) Single-mode photonic band gap guidance of light in air. *Science* 285:1537–1539
35. Russell P (2003) Photonic crystal fiber. *Science* 299:358–362
36. Mach P, Dolinski M, Baldwin KW, Rogers JA, Kerbage C, Windeler RS, Eggleton BJ (2002) Tunable microfluidic optical fiber. *Appl Phys Lett* 80:4294–4296
37. Erickson D, Rockwood T, Emery T, Scherer A, Psaltis D (2006) Nanofluidic tuning of photonic crystal circuits. *Opt Lett* 31:59–61
38. Yan H, Gu C, Yang C, Liu J, Jin G, Zhang J, Hou L, Yao Y (2006) Hollow core photonic crystal fiber surface-enhanced Raman probe. *Appl Phys Lett* 89:204101
39. Cordeiro CMB, de Matos CJS, dos Santos EM, Bozolan A, Ong JSK, Facincani T, Chesini G, Vaz AR, Brito Cruz CH (2007) Towards practical liquid and gas sensing with photonic crystal fibres: side access to the fibre microstructure and single-mode liquid-core fibre. *Meas Sci Technol* 18:3075–3081
40. Joannopoulos JD, Meade RD, Winn JN (1995) *Molding the flow of light: photonic crystals*. Princeton University Press, Princeton
41. Loncar M, Nedeljkovic D, Doll T, Vuckovic J, Scherer A, Pearsall TP (2000) Waveguiding in planar photonic crystals. *Appl Phys Lett* 77:1937–1939
42. McNab S, Moll N, Vlasov Y (2003) Ultra-low loss photonic integrated circuit with membrane-type photonic crystal waveguides. *Opt Express* 11:2927–2939
43. Archambault JL, Black RJ, Lacroix S, Bures J (1993) Loss calculations for antiresonant waveguides. *J Lightwave Technol* 11:416–423
44. Duguay MA, Kokubun Y, Koch T, Pfeiffer L (1986) Antiresonant reflecting optical waveguides in SiO₂-Si multilayer structures. *Appl Phys Lett* 49:13–15
45. Mawst LJ, Botez D, Zmudzinski C, Tu C (1992) Design optimization of ARROW-type diode lasers. *IEEE Photon Technol Lett* 4:1204–1206
46. Patterson SG, Petrich SG, Ram RJ, Kolodziejski R (1999) Continuous-wave room temperature operation of bipolar cascade laser. *Electron Lett* 35:397–397
47. Delonge T, Fouckhardt H (1995) Integrated optical detection cell based on Bragg reflecting waveguides. *J Chromatogr A* 716:135–139
48. Bernini R, Campopiano S, Zeni L, Sarro PM (2004) ARROW optical waveguides based sensors. *Sensors Actuators B Chem* 100:143–146
49. Yin D, Barber JP, Hawkins AR, Deamer DW, Schmidt H (2004) Integrated optical waveguides with liquid cores. *Appl Phys Lett* 85:3477–3479
50. Yin D, Barber JP, Lunt EJ, Hawkins AR, Schmidt H (2005) Optical characterization of arch-shaped ARROW waveguides with liquid cores. *Opt Express* 13:10564–10569
51. Schmidt H, Yin D, Barber JP, Hawkins AR (2005) Hollow-core waveguides and 2D waveguide arrays for integrated optics of gases and liquids. *IEEE J Sel Top Quantum Electron* 11:519–527
52. Yin D, Barber JP, Deamer DW, Hawkins AR, Schmidt H (2006) Single-molecule detection sensitivity using planar integrated optics on a chip. *Opt Lett* 31:2136–2138
53. Ashkin A (1994) Optical trapping and manipulation of neutral particles using lasers. *Proc Natl Acad Sci USA* 94:4853–4860

54. Gerhardt I, Wrigge G, Agio M, Bushev P, Zumofen G, Sandoghdar V (2007) Scanning near-field optical coherent spectroscopy of single molecules at 1.4 K. *Opt Lett* 32:1420–1422
55. Hong K, Burgess LW (1994) Liquid-core waveguides for chemical sensing. *Proc SPIE* 2293:71–79
56. Mizaikoff B, Young C, Charlton C, Temelkuran B, Delleman G, Giovannini M, Faist J (2006) Trace sensing with miniaturized mid-infrared sensors. *IEEE Sens Daegu, (Korea)*:331–333
57. Shera EB, Seitzinger NK, Davis LM, Keller RA, Soper SA (1990) Detection of single fluorescent molecules. *Chem Phys Lett* 174:553
58. Lakowicz JR (2006) Principles of fluorescence spectroscopy, 3rd edn. Springer, Berlin
59. Rigler R, Elson ES (2001) Fluorescence correlation spectroscopy, 1st edn. Springer, Berlin
60. Vezenov DB, Mayers BT, Wolfe DB, Whitesides GM (2005) Integrated fluorescent light source for optofluidic applications. *Appl Phys Lett* 86:041104
61. Smolka S, Barth M, Benson O (2007) Selectively coated photonic crystal fiber for highly sensitive fluorescence detection. *Appl Phys Lett* 90:111101
62. Yin D, Lunt EJ, Barman A, Hawkins AR, Schmidt H (2007) Microphotonic control of single molecule fluorescence correlation spectroscopy using planar optofluidics. *Opt Express* 15:7290–7295
63. Rudenko MI, Kühn S, Lunt EJ, Deamer DW, Hawkins AR, Schmidt H (2009) Ultrasensitive Q β Phage analysis using fluorescence correlation spectroscopy on an optofluidic chip. *Biosensors and Bioelectronics* 24:3258–3263
64. Yin D, Lunt EJ, Rudenko MI, Deamer DW, Hawkins AR, Schmidt H (2007) Planar optofluidic chip for single particle detection, manipulation, and analysis. *Lab Chip* 7:1171
65. Samiee KT, Moran-Mirabal JM, Cheung YK, Craighead HG (2006) Zero mode waveguides for single-molecule spectroscopy on lipid membranes. *Biophys J* 90:3288–3299
66. Kneipp K, Wang Y, Kneipp H, Perelman LT, Itzkan I, Dasari RR, Feld MS (1997) Single molecule detection using surface-enhanced Raman scattering. *Phys Rev Lett* 78:1667–1670
67. Shapiro HM (1995) Practical flow cytometry, 3rd edn. Wiley, New York
68. Lien V, Zhao K, Lo Y (2005) Fluidic photonic circuit for in-line detection. *Appl Phys Lett* 87:194106
69. Mandal S, Erickson D (2007) Optofluidic transport in liquid core waveguiding structures. *Appl Phys Lett* 90:184103
70. Measor P, Kühn S, Lunt EJ, Phillips BS, Hawkins AR, Schmidt H (2008) Hollow-core waveguide characterization by optically induced particle transport. *Opt Lett* 33:672–674
71. Altkorn R, Koev I, Van Duyne RP, Litorja M (1997) Low-loss liquid-core optical fiber for low-refractive index liquids: fabrication, characterization, and application in Raman spectroscopy. *Appl Opt* 36:8992–8998
72. Zhang Y, Shi C, Gu C, Seballos L, Zhang JZ (2007) Liquid-core photonic crystal fiber sensor based on surface-enhanced Raman scattering. *Appl Phys Lett* 90:193504
73. Measor P, Lunt EJ, Seballos L, Yin D, Zhang JZ, Hawkins AR, Schmidt H (2007) On-chip Surface-enhanced Raman scattering (SERS) detection using integrated liquid-core waveguides. *Appl Phys Lett* 90:211107
74. Dumais P, Callender CL, Noad JP, Ledderhof CJ (2006) Liquid-core modal interferometer integrated with silica waveguides. *IEEE Photon Technol Lett* 18:746–748
75. Rindorf L, Jensen JB, Dufva M, Pedersen LH, Høiby PE, Bang O (2006) Photonic crystal fiber long-period gratings for biochemical sensing. *Opt Exp* 14:8224–8231
76. Campopiano S, Bernini R, Zeni R, Sarro PM (2004) Microfluidic sensor based on integrated optical hollow waveguides. *Opt Lett* 29:1894–1896
77. White IM, Oveys H, Fan X (2006) Liquid-core optical ring-resonator sensors. *Opt Lett* 31:1319–1321
78. White IM, Zhu H, Suter JD, Hanumegowda NM, Oveys H, Zourob M, Fan X (2007) Refractometric sensors for lab-on-a-chip based on optical ring resonators. *IEEE Sens J* 7:28–35

79. Sun Y, Shopova SI, Frye-Mason G, Fan X (2008) Rapid chemical-vapor sensing using optofluidic ring resonators. *Opt Lett* 33:788–790
80. Suter JD, White IM, Zhu H, Shi H, Caldwell CW, Fan X (2008) Label-free quantitative DNA detection using the liquid-core optical ring resonator. *Biosens Bioelectron* 23:1003–1009
81. Potyrailo RA, Hobbs SE, Hieftje GM (1998) Optical waveguide sensors in analytical chemistry: today's instrumentation, applications, and trends for future development. *Fresenius J Anal Chem* 362:349–373
82. Preston T, Jones ND, Stille S, Mittler S (2006) Simple liquid-core waveguide polarimetry. *Appl Phys Lett* 89:253509

Capillary Waveguide Biosensor Platform

Harbans S. Dhadwal

Abstract The design and characterization of a fully automated and portable capillary waveguide biosensor are discussed in this chapter. Highly specific target recognition is achieved through hybridization of fluid-borne single-stranded DNA sequences extracted from natural targets to the complimentary nucleic acid sequence (“capture probe”) bound to the inner surface of a capillary. The product of hybridization is enumerated through the use of fluorescent labeling. A novel instantaneous normalization scheme based on two photodetectors, together with the use of a standard reference material, enables independent measurements by the instrument. The probability of false-positive target detection is quantified through the development of a target detection error rate. The instrument exhibits low detection limits ($\sim 10^{-13}$ M) and repeatability of 6%. The sensor can be rearmed through a denaturing step allowing for sequential detection over an extended time period.

Keywords Biosensor · Capillary waveguide · Hollow fibers · Nucleic acid detection · Hybridization

Contents

1	Introduction	223
2	Optical Design	224
2.1	Modal Concepts in Optical Waveguides	225
2.2	Leaky Optical Waveguides	229
2.3	Methods of Excitation	231
2.4	Photon Emission from Fluorescent Molecules	233
2.5	Optimal Capillary for the Prototype CWBP	237

H.S. Dhadwal

Department of Electrical and Computer Engineering, Stony Brook University, Stony Brook, NY 11794-2350, USA

e-mail: dhadwal@ece.sunysb.edu

3	Practical Implementation of a CWBP	242
3.1	Detection Limit	243
3.2	The Capillary Waveguide Biosensor Platform	246
4	Results and Discussion	249
4.1	Precision and Accuracy	250
4.2	Hybridization	252
5	Concluding Remarks	255
	References	256

Abbreviations

CWBP	Capillary waveguide biosensor platform
DNA	Deoxyribonucleic acid
MMF	Multimode fiber
NA	Numerical aperture
PMT	Photomultiplier tube
SMF	Singlemode fiber
SNR	Signal to noise ratio
TDER	Target detection error rate

Symbols

A_v	Avogadro's number
(r, θ, z)	Cylindrical coordinates
(x, y, z)	Cartesian coordinates
c	Concentration
$E_{e, t}$	Events
$\Gamma_{em, ex, nd, hnp, bp}$	Transmission coefficient
$H_{nd, hnp, bp}$	Transfer functions
k	Propagation vector
L	Capillary length
$m_{det, em, ex}$	Photon count
$M_{PM, TM}$	Number of molecules
$n_0, 1, 2, 3$	Refractive index
$N_{S, B}$	Normalized count
p	Probability
$P_{clad, core, tot}$	Optical power
q	Mode number
Q	Number of waveguide modes
$r_1, 2, 3, 4, p$	Radius
R_d	Ratio of capillary outer to inner diameter
T	Time interval

V	Normalized frequency of a waveguide
V_{sen}	Sensing volume
W_{M}	Molecular weight
α	Attenuation coefficient
β_{q}	Propagation coefficient
δy	Coating layer thickness
ε	Molar extinction
$\Phi_{0, \text{ex, em}}$	Photon flux
$\eta_{\text{em, ex, col, mol, bk, L, H}}$	Efficiency
κ	Extinction ratio
$\lambda_{\text{o, ex, em}}$	Wavelength
ν	Frequency
$\theta_{0,1,2,3,1c}$	Angle
$\sigma_{\text{S, n, B}}$	Standard deviation
τ_{H}	Hybridization time

1 Introduction

Hollow-waveguide structures have been recognized for their unique properties in transmission of high energy optical pulses, as resonant cavities for lasers and more recently in the development of photonic crystal fibers. Capillaries are a natural choice for optical sensors requiring copropagation of an interrogating optical field and a fluid-borne target. Capillary-based sensor applications are on the rise, including many diverse application areas, such as environmental monitoring, forensic analysis, detection of retroviruses, diagnosis of genetic disorders, cancer diagnosis, and microbiological analysis of foods. Any meaningful review of the subject matter is beyond the scope of this chapter and will not be attempted. It suffices to identify some of the current technologies at the forefront of analytical instruments, such as flow cytometers, microarray biochip technology both in its planar format and 3D capillary arrays, single-molecule imaging systems, and capillary waveguide sensors.

A capillary waveguide biosensor platform (CWBP) is a mobile analytical instrument, which provides detection and quantification of microbial populations in natural marine samples. High level of target specificity is possible through hybridization between a single-stranded nucleic acid oligonucleotide “probe” sequence and a sample “target” sequence extracted from an organism. The product of hybridization is detected and quantified through the use of fluorescence spectroscopy, which has the lowest detection limit among various analytical techniques.

The central component of the system is a glass capillary which serves as a reaction chamber for hybridization and as an optical waveguide for the transport of both the excitation and emission photons. The interior surface of the capillary, which is chemically modified to support probe sequence molecules, forms a reusable transducer for repeated detection of target sequences. After hybridization

and detection, the transducer region can be reactivated through a denaturing step which breaks the probe–target bonds. Other parts of the CWBP include a fully automated fluid-transport system, a graphical user interface, and an electronics module for overall control and data acquisition. A novel dual photo-detector scheme provides a unique microenvironment independent instantaneous normalization of the real-time data. This normalization is critical for improving system sensitivity and enabling concentration measurements based on absolute fluorescent intensity.

Detection of bacterial species in natural samples, though not reported here, can be achieved through a filtering step to extract and resuspend bacterial matter. Bacterial cells are subsequently lysed to extract sDNA or rRNA target molecules. During this process, a PCR step may be necessary to amplify the target population, that is, to increase the number of copies per cell. However, preliminary data indicate that the amplification step may not be needed. The sDNA or rRNA target sequences are loaded into the capillary for hybridization with the complementary sDNA probe sequence immobilized on the inner capillary surface. Any one of the standardized techniques, such as single- or dual-probe hybridization may be used. In the processing of natural samples, competitive hybridization may be needed to quantify concentration of target molecules. An earlier version of the CWBP reported detection of SAR11 clade organism from environmental samples taken from the Gulf of Papua [1]. Some of the material in the chapter is drawn, with permission from the publisher, from our prior published work [2, 3].

Optimal design of the CWBP must consider all parameters that are likely to compromise performance of the system. The goal is to achieve a balance between theoretical possibilities and practical realities, keeping in mind that the weakest link determines system efficacy. As many configurations are possible, it is important to use a priority assignment to each of the design variables. For instance, a particular CWBP that will be described in this chapter was designed within the framework of the following prioritized constraints:

- Portable for use in the field
- Detect and quantify bacteria targets extracted from marine samples
- Reusable and easily replaceable capillary
- Low detection limit ($<10 \text{ pg mL}^{-1}$)
- High sensitivity
- Wide dynamic range
- A graphical user interface (GUI)
- Manual and batch mode of operation
- Temperature control (20–70°C)

2 Optical Design

A capillary is essentially a tube with a large ratio of outer to inner diameters. It is drawn to the correct dimensions starting from a larger preform of fused synthetic silica which is heated in an induction furnace to its softening temperature and pulled

to the final dimensions under strict dimensional control. During the manufacturing process, a polymer or metallic coating is applied to the outer surface for strength and flexibility. Some capillaries enhance optical guiding properties of the wall by adding a second cladding layer with a slightly lower refractive index. Capillaries are available in a broad range of diameters, with inner diameter in the range of 1–2,000 μm, and outer diameter between 90 μm and 3,500 μm (<http://www.polymicro.com>).

Optical characteristics of the CWBP are determined by the capillary, the method of excitation, and the geometry used for detection of fluorescent emission. Invariably, coaxial paths for excitation and emission are not conducive for achieving low limits of detection because of the high background excitation [3]. Orthogonal paths for excitation and detection are preferred as they provide considerable spatial rejection of the excitation, with the added benefit that the optimization of excitation and detection geometries can be treated independently. Optical properties of the capillary are dependent on its dimensions and refractive index profile. As most of the commercially available capillaries are made from fused synthetic glass, the refractive index of the capillary wall is a fixed parameter, while that of the interior region is determined by the transport fluid. The structure should provide good performance for a broad range of fluids. Essentially, the inner diameter, the wall thickness, and the length of the capillary are the only design variables for determining the optimal capillary. Optimization of these design variables is determined by the methods used for excitation and detection. For instance, numerical aperture is a single most critical parameter for the retro-reflective geometry used in microarray and epifluorescence systems.

2.1 Modal Concepts in Optical Waveguides

As depicted in Fig. 1, the capillary is a cylindrical waveguide with an inhomogeneous transverse refractive index profile described by

$$n(r) = \begin{cases} n_1, & |r| \leq r_1, & \text{liquid core} \\ n_2, & r_1 < |r| \leq r_2, & \text{probe layer} \\ n_3, & r_2 < |r| \leq r_3, & \text{wall} \\ n_4, & r_3 < |r| \leq r_4, & \text{cladding} \end{cases} \quad (1)$$

In the case of $n_1 > n_2$ and $r_2 = r_3 = r_4$, the structure becomes a step-index optical fiber, as illustrated in Fig. 2. The propagation properties of fibers can be fully characterized by solving Maxwell’s equations under the proper boundary conditions [4]. However, a combination of ray and wave optics can be used for obtaining an understanding of the modal concepts if the core diameter is much larger than the wavelength of the source. An optical ray can be modeled by a scalar monochromatic plane wave traveling in a direction defined by the propagation vector \mathbf{k} as

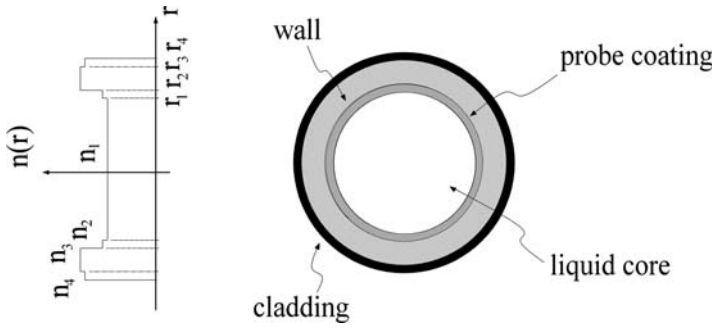


Fig. 1 Cross section of a microcapillary waveguide. $n_{1, 2, 3, 4}$ – refractive indices of various layers

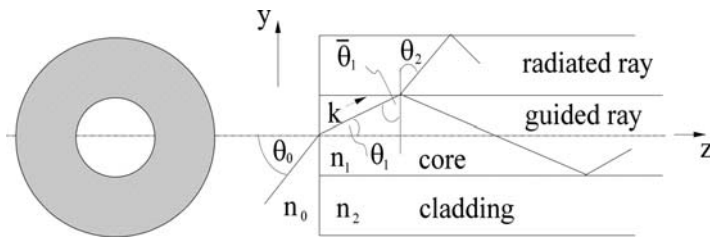


Fig. 2 Longitudinal section view of an optical fiber showing ray propagation

$$E(x, y, z; t) = E_0 \cos(2\pi vt - \mathbf{k} \cdot \mathbf{r}), \tag{2}$$

where the magnitude of \mathbf{k} is $k = nk_0 = n \frac{2\pi}{\lambda_0}$, n is the refractive index of the medium and λ_0 is the free space wavelength. Applying Snel’s law at the ray entrance and core/cladding interfaces leads to the following two equations:

$$n_0 \sin(\theta_0) = n_1 \sin(\theta_1), \tag{3}$$

$$n_1 \sin(\bar{\theta}_1) = n_2 \sin(\theta_2), \tag{4}$$

where the bar denotes the complement of the angle. All rays inside the core which satisfy the condition that $\theta_1 \leq \theta_{1c}$ will be guided along the core by total internal reflection at the core/cladding interface. The critical angle θ_{1c} is given by

$$\cos(\theta_{1c}) = \frac{n_2}{n_1}, \tag{5}$$

Rays with angles greater than the critical angle enter the cladding region and are considered to be radiated, or lost from the perspective of communications.

The critical angle condition translates into a source launching condition, which can be expressed as a numerical aperture (NA) of the fiber as follows:

$$NA = n_0 \sin(\theta_0) = n_0 \sqrt{n_1^2 - n_2^2}. \tag{6}$$

The light collecting power of the fiber, or other optical systems, increases as the square of NA. However, the above simple ray model fails to accurately predict the propagation of light through optical fibers, particularly, in single-mode fibers. In general, reflection at the core/cladding interface is accompanied by a complex reflection coefficient, which is a function of both the ray angle and polarization. Based on the solution of the Maxwell’s equations and boundary conditions at the dielectric/dielectric interface, the complex reflection coefficients, known by Fresnel coefficients, can be derived for the two orthogonal states of polarization [5]. According to these equations, the reflected wave suffers an amplitude and phase change at the dielectric/dielectric interface. The finite transverse dimension imposes a self-consistency condition on the twice-reflected wave, that is, a phase shift of $2q\pi$. Consideration of this leads to the result that the core region can support a finite and discrete set of bounce angles θ_q up to the critical angle θ_{1c} . Each integer value of q defines a *guided mode*, which can be viewed as a superposition of two plane waves with bounce angles $+\theta_q$ and $-\theta_q$ (reflected). Each mode has a stationary spatial transverse distribution, which is independent of the distance along the optical axis.

As depicted in Fig. 3, each guided mode in the core region is accompanied by an exponentially decaying evanescent wave in the cladding region. The depth of penetration and the power carried by the evanescent wave are functions of the mode order and waveguide parameters. According to full electromagnetic wave analysis of optical fibers, the ratio of power in the cladding P_{clad} , to the total power P_{tot} , of a multimode fiber is given by [6]

$$\frac{P_{\text{clad}}}{P_{\text{tot}}} = \frac{4}{3} \frac{1}{\sqrt{Q}}, \tag{7}$$

where $Q = V^2/2$ is the number of guided modes in a multimode fiber and the normalized frequency V is given by

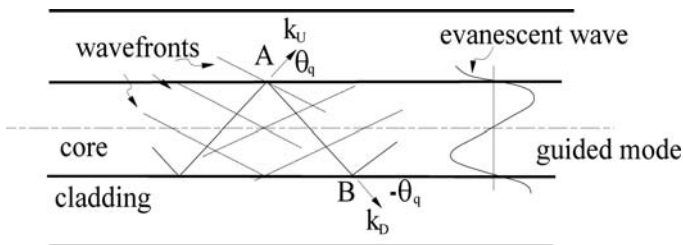


Fig. 3 Propagation of guided modes in the core and evanescent waves in the cladding

$$V = \frac{2\pi r_1}{\lambda_0} [n_1^2 - n_2^2]^{\frac{1}{2}} = \frac{2\pi r_1}{\lambda_0} (\text{NA}). \tag{8}$$

It should be noted that the total power in the cladding is inversely proportional to the V -value of the fiber. Fibers with small V -values can have significant energy in the evanescent wave. Single-mode ($V < 2.405$) and tapered fibers have found considerable utility in fiber optic sensors which exploit the presence of an evanescent wave field. In general, evanescent wave excitation is weaker in comparison with direct excitation. However, in planar geometries, enhanced evanescent wave excitation at the critical angle of incidence is possible through the phenomenon of tunneling as discussed below.

Classical and quantum treatments of electromagnetic fields [7], near a plane dielectric interface, show that the probability of photo-ionization or photo-excitation of an atom exhibits a pronounced peak at the critical angle of incidence of a plane wave propagating in the dense medium. The probability of absorption or emission of a photon is proportional to the photometric intensity of the electromagnetic field. In particular, consider a plane wave propagating in the dense medium with refractive index n_1 , at angle of incidence θ_1 . The intensity of the transmitted field at a distance δy from the interface is given by

$$I(\theta_1, \delta y) = \begin{cases} I_0 4 \left[1 + \sqrt{1 - n^2 \sin^2 \theta_1} / n \cos \theta_1 \right]^{-2}, & \theta < \theta_{1c} \\ I_0 4 [n^2 \cos^2 \theta_1 / (n^2 - 1)] \exp \left[-4\pi \left(\frac{\delta y}{\lambda} \right) \sqrt{n^2 \sin^2 \theta_1 - 1} \right], & \theta > \theta_{1c} \end{cases}, \tag{9}$$

where I_0 is the intensity of the incident wave, $n = n_1/n_2$ and $\theta_{1c} = \sin^{-1}(1/n)$ is the critical angle of incidence.

Figure 4 shows a plot of (9) for $n_1 = 1.46$ and $n_2 = 1.33$ and for several values of the normalized layer thickness, $\delta y/\lambda$. For these parameter values, the enhanced

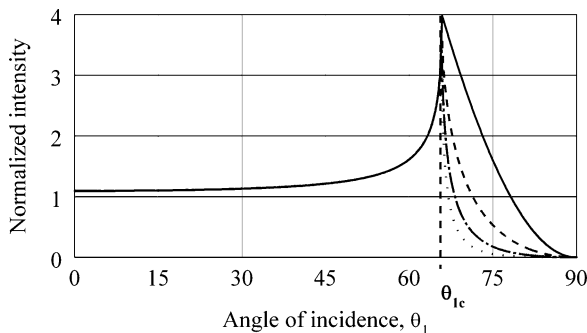


Fig. 4 Intensity of the evanescent wave at a distance δy , from a plane interface between a dense medium of refractive index n_1 and rare medium of refractive index n_2 . Plots of (9) for $n_1 = 1.46$ and $n_2 = 1.33$. $\frac{\delta y}{\lambda} = 0, 0.25, 0.50, 0.75$ - solid, short dash, dash dot, and long dash lines, respectively. (Reprinted from Dhadwal et al. [3], with permission of Elsevier)

probability of absorption occurs near the critical angle of $\theta_{1c} = 66.6^\circ$. The strength of the evanescent field falls off rapidly beyond the critical angle. However, from Fig. 4, it can be ascertained that the total power within the thin coating layer is a sum of the continuum of modes beyond the critical angle. It should be noted that, under uniform excitation of all guided modes, the pronounced contribution to the total evanescent field from a few modes near the cut-off condition is negligible and the total power in the cladding is adequately described by (7). However, sensors based on planar geometries, such as microarray platforms, exploit the tunneling phenomenon by confining illumination to the critical angle. In this configuration, these systems are also providing orthogonal paths for excitation and detection.

2.2 Leaky Optical Waveguides

Consider the situation when the core region of the capillary is filled with a fluid that has a refractive index which is smaller than that of the wall ($n_1 < n_2$). Snell’s law now stipulates that all rays entering the core region will be radiated into the wall, that is, there is no critical-angle condition for total internal reflection at core/cladding interface. As depicted in Fig. 5, rays that enter the liquid core at an angle θ_0 will exit the capillary structure at an angle θ_3 , or be reflected at point C or be partially reflected at point B.

Figure 6 shows a plot of the exit angle as a function of the entrance angle for various values of $n_0, n_1,$ and n_3 . As expected, the exit angle follows the entrance angle for the special case $n_0 = n_1 = n_3 = 1.33$, i.e., a capillary immersed in a homogeneous liquid. Otherwise, in a more typical situation $n_0 = 1.33, n_1 = 1.33, n_3 = 1.0$, the entrance ray remains inside the optical structure as illustrated by the optical path ABCE in Fig. 5, corresponding to $\theta_0 < 45^\circ$.

Decreasing widths of ray lines in Fig. 5 indicate partial reflections at the liquid/glass interface. The partially reflected plane waves combine to form *leaky modes* in the liquid core region. These modes exhibit a high attenuation coefficient along the optical axis of the capillary. For *leaky waveguides*, most of the energy launched into the liquid core is radiated into the cladding as the waves propagate along the core.

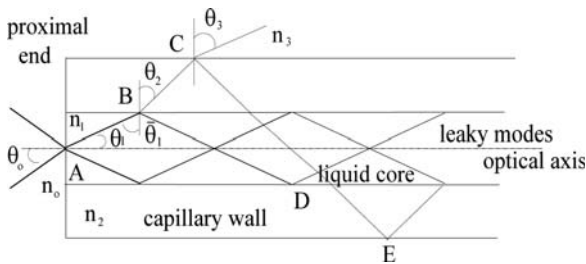


Fig. 5 Leaky modes of a liquid filled capillary with $n_1 < n_2$

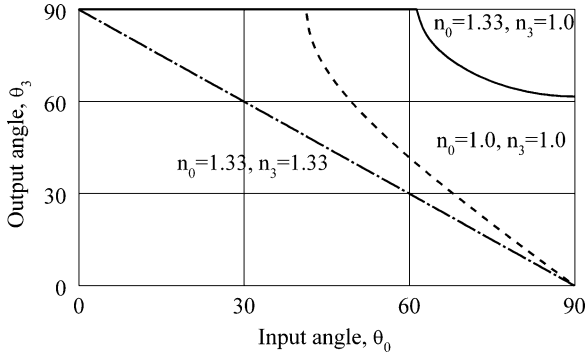


Fig. 6 Entrance and exit angle relationship for a liquid filled capillary with $n_1 = 1.33$, $n_2 = 1.46$

While this longitudinal loss is detrimental for communications or applications involving transport of energy over long distances, this property is potentially very beneficial for sensors utilizing capillaries. Most of the leaky modes will directly excite molecules immobilized on the inner surface of the capillary. The effective attenuation for each of the leaky modes is found to be inversely proportional to the diameter of the capillary and exhibits unacceptable values for all modes with the exception of a few lower order modes, corresponding to almost normal incidence at the proximal end of the capillary, i.e., $\theta_0 \leq 5^\circ$.

The power attenuation coefficient (2α) for lower order leaky modes is given by [4]; thus,

$$2\alpha = 2 \left(\frac{q\pi}{2r_1} \right)^2 \frac{1}{\beta_q 2r_1} 2 \left[\left(\frac{W}{2r_1} \right)^2 + \left(\frac{q\pi}{2r_1} \right)^2 \right]^{-\frac{1}{2}},$$

$$W = k_0 2r_1 [n_3^2 - n_1^2]^{-\frac{1}{2}}, \quad \beta_q = \left[k_0^2 n_1^2 - \left(\frac{q\pi}{2r_1} \right)^2 \right]^{\frac{1}{2}}, \quad (10)$$

where q is the mode integer and β_q is the propagation coefficient. Figure 7 shows a plot of the attenuation coefficient as a function of the width $2r_1$ of the planar waveguide for a few of the lower order modes. Thus, the power in the cladding, due to the radiation modes, can be expressed as

$$\frac{P_{\text{clad}}}{P_{\text{tot}}} = 1 - \exp(-2\alpha z). \quad (11)$$

The fractional power in the cladding increases with mode number and capillary length. Thus, for sensor application, excitation of higher-order leaky modes leads to direct illumination of the immobilized fluorophores on the surface.

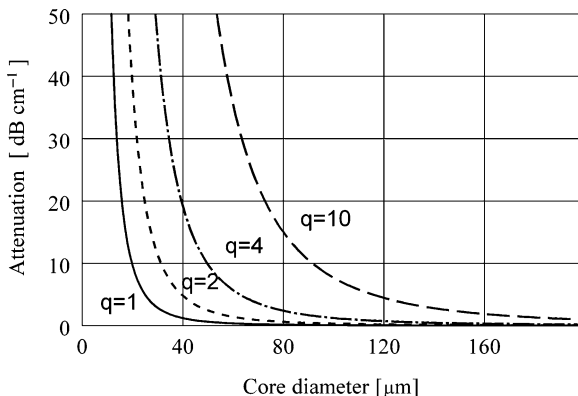


Fig. 7 Power attenuation coefficient for a liquid filled capillary for various lower order modes q . Calculations are based on $n_1 = 1.33$ and $n_2 = 1.46$

2.3 Methods of Excitation

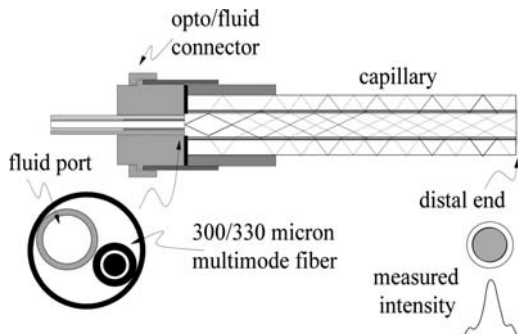
The products of hybridization are detected through the use of fluorescent labeling. These molecular complexes can either be homogeneously distributed in the liquid core or be bound to the interior surface of the capillary through covalent bonding. In both cases, labeled molecules can be excited either by direct illumination with the leaky modes of the liquid filled core, or by the evanescent waves arising from the guided modes of the capillary wall. Direct excitation is less wasteful of incident photon flux and is the method of choice in conventional fluorometers. Evanescent wave excitation becomes a necessity when direct excitation is either not feasible or results in undesirable sensor performance. Both methods of illumination are possible for the CWBP.

2.3.1 Direct Excitation

As illustrated in Fig. 8, leaky modes of the liquid core region illuminate dye molecules located both in the bulk solution and immobilized on the core/cladding surface. The leaky modes are easily launched through the use of a multimode fiber placed in direct contact with the fluid core. In the context of a portable instrument which requires quick assembly and replacement of the capillary, the multimode fiber is mounted into the same housing which transports the fluid to the capillary core. Figure 8 shows a photograph of one such opto/fluid union designated as T1. It is fabricated by modifying a popular fiber optic connector, SMA905 (<http://www.amphenol-fiberoptics.com>). Light from a suitable excitation source can be efficiently launched directly into the proximal surface of a multimode fiber.

The opto/fluid connector comprises a 300/330 μm step index multimode fiber with a NA of 0.39 and an adjacent fluid port. The measured near-field intensity

Fig. 8 Excitation geometry for direct illumination of surface bound molecules. Image on the *left* shows the modified fiber optic connector with a fluid port and adjacent optical fiber. Measured near-field intensity distribution of the distal end confirms propagations of leaky modes

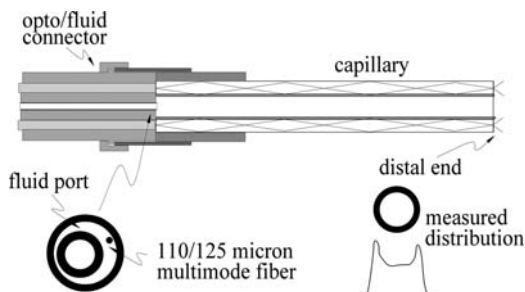


distribution at the distal of a 65-mm-long capillary confirms the propagation of the leaky modes across the liquid core and wall regions. A word of caution, direct excitation of the liquid core as discussed above can damage the multimode fiber through repeated exposure to corrosive liquids, including water. Additionally, disruption of excitation due to spontaneous generation and migration of microbubbles or particulate scatterers can result in inconsistent data. Techniques for efficient coupling of light from optical sources to fibers can be found in most texts on fiber optics and will not be discussed here.

2.3.2 Evanescent Wave Excitation

As discussed in Sect. 2.1, all guided modes are accompanied by an evanescent wave which extends into the less dense cladding region. Fluorescent molecules within this region can readily absorb photons from the evanescent field. The capillary wall forms an asymmetric cylindrical waveguide, with a liquid cladding on the inner surface and air on the outer surface. Thus, the evanescent waves corresponding to the capillary wall guided modes can be used to illuminate fluorescent molecules close to the cladding/ liquid interface. Figure 9 shows one such arrangement using a multimode optical fiber for launching the capillary wall modes. In this case, both the NA and the diameter of the launching fiber should be matched to the capillary wall NA and thickness. However, it should be noted that optical modes inside the capillary wall are quite different from those that might be excited in the core of a conventional optical fiber with an equivalent diameter and NA. The capillary wall forms an optical guiding cylindrical ring, which will support modes that resemble the higher order modes of an equivalent optical fiber. Such modes are characterized by a helical path, corresponding to skew rays. Figure 9 shows a sketch of the modified connector and the measured intensity emanating from the distal end of the capillary. The latter clearly shows the guiding nature of the capillary wall, in contrast to the leaky modes in Fig. 8. In this example, the guided modes of the

Fig. 9 Excitation geometry for evanescent wave illumination of surface bound molecules. Sketch on the *left* show the smaller fiber at the periphery of the connector. Measured near-field intensity distribution shows the guided capillary modes



capillary wall were excited with a step index multimode fiber with a 110/125 μm and a NA of 0.29.

The evanescent field strength may be enhanced by using multiple fibers arranged in a ring pattern covering the entire proximal surface of the capillary wall. However, the actual benefit of this arrangement has to be weighed against the added complexity and difficulty of launching light from a single source into a multiplicity of fibers. However, multiple fiber excitation of the capillary can be exploited to electrically switch between different excitation sources, thereby adding multitarget detection capability to the CWBP.

2.4 Photon Emission from Fluorescent Molecules

Fluorophore molecules absorb photons from the excitation field and radiate lower energy photons in random directions and over a broad spectral band which is defined by the emission spectrum of the fluorophore molecule. The probability of photon absorption within a distance z , calculated from Beer–Lambert law, is given by

$$p(z) = 1 - \exp(-\varepsilon cz), \quad (12)$$

where ε is the molar extinction ($\text{m}^2 \text{mol}^{-1}$) and c (mol L^{-1}) is the concentration. In the limit of low concentration, that is, $\varepsilon cz \ll 1$, the absorption probability can be approximated by

$$p(z) = \varepsilon cz. \quad (13)$$

Fluorescent emission will be proportional to the absorption probability and molecular parameters characterizing the fluorophore complex. Each absorbed photon can reemit energy within the emission spectrum of the dye. The fluorescent

photon flux Φ_{em} emanating from the sensing volume can be expressed in terms of a molecular efficiency η_{mol} as

$$\Phi_{em} = \Phi_{AF} + \eta_{mol}\Phi_{ex} c, \quad (14)$$

where Φ_{AF} is the in-band fluorescence from the buffer, Φ_{ex} is the excitation photon flux. The excitation field will be a function of the method of excitation and can be related to the source photon flux Φ_0 by an excitation efficiency η_{ex} . Thus, in the absence of autofluorescence, the total flux emanating from the sensing volume is

$$\Phi_{tot} = \eta_{ex}\eta_{mol}\Phi_0 c + \eta_{ex}\eta_{bk}\Phi_0, \quad (15)$$

where the second term represents the photon flux at the excitation wavelength, arising from the nonabsorbed photons, scattered photons from various optical interfaces and particulates in the solution. Low-detection-limit fluorescent systems must consider the contributions of Rayleigh scattering from the solution, which adds to the background photon flux at the excitation wavelength [8]. Typically, in the presence of the second term, fluorescence detection is not possible. Thus, intensive optical filtering is used to reduce the background term through the use of holographic notch filters in combination with band pass filters to extract the photons arising from the fluorescence signature of the molecular system. If $H_{SOF}(\lambda)$ defines the transfer function of optical filtering employed, then the photon flux reaching a single counting photo-detector can be expressed by

$$\begin{aligned} \Phi_{det} &= H_{SOF}(\lambda)\eta_{em}\Phi_{tot} \\ &= \eta_{em}\eta_{ex}\eta_{mol}\Phi_0 c, \end{aligned} \quad (16)$$

where η_{em} is the optical collection efficiency of all photons emanating from the sensing volume that are available for detection. For an ideal experiment, it is possible to isolate the molecular parameters η_{mol} , associated with the fluorophore molecules from those describing experimental factors $\eta_{ex}\eta_{em}$ [9]. If a single photon detector is illuminated by the photon flux described by (16), then the average number of photons m_{det} , in time interval T is given by

$$m_{det} = \int_t^{t+T} \Phi_{det} dt = \bar{\Phi}T, \quad (17)$$

where the absolute fluorescent intensity

$$\bar{\Phi} = [\Phi_0\eta_{det}\eta_{ex}\eta_{em}\eta_{mol}] c \quad (18)$$

is the average photon–electron count rate per second, and η_{det} is the quantum efficiency of the photo-detector. Equation (18) represents a concentration calibration curve with a slope, which is a function of both the experimental factors and molecular factors.

Sensitivity of the instrument, which refers to the system response to small changes in concentration, is determined by the signal to noise ratio (SNR) of the measurement, as well as, the concentration slope. The SNR of each measurement may be considerably smaller than variation between measurements made on different occasions. Measurements of concentration from absolute fluorescent intensity ($\bar{\Phi}$) are possible provided that the calibration of the instrument remains unchanged. Reliable fluorescent intensity measurements across different instruments or from repeated measurements with the same instrument are possible only if the above factors can either be eradicated from consideration or be controlled with an experiment independent calibration coefficient. One effective solution proposed the development of a set of standard reference materials (SRMs) for use with identical instruments [9]. Thus, for a particular instrument, the concentration of a test solution can be expressed as a ratio of the fluorescent counts for the test and SRM. Subsequently, it was recommended that the concentration of the test solution could be expressed in molecular equivalent soluble fluorophore (MESF) units. This protocol was developed with respect to the use of flow cytometers, which can be operated close to the ideal experimental conditions. Despite this, measurements of fluorescent intensity in terms of MESF units still have problems, as most fluorescence-based instruments cannot be guaranteed to operate under the same conditions from day to day.

The CWBP is a nonideal field instrument, with a sensing volume surrounding by several optical interfaces, leading to a time varying geometrical factor expressed by the product of $\eta_{\text{det}}\eta_{\text{em}}\eta_{\text{ex}}\eta_{\text{col}}$. The efficiency of the latter will be discussed in Sect. 2.5.1. The microenvironment of the sensing volume in the stop-and-flow measurement of the CWBP can change during the measurement or in between measurements. The photon flux entering and leaving the sensing volume encounters three optical interfaces: (1) the fluid/coating; (2) the coating/capillary wall; and (3) the capillary wall/air. The excitation efficiency is determined by the combined illumination arising from the evanescent wave field and the higher order, weakly guided modes in the interior region of the capillary. The former is strongly dependent on the properties of the three layer optical waveguide. Essentially, the strength and penetration depth of the evanescent wave field is a function of the modal distribution inside the wall of the capillary. The evanescent wave field can be influenced by small perturbations in the waveguide parameters. For example, the appearance of microbubbles at the coating/fluid interface can have a strong effect on the excitation intensity. The source of the microbubbles is not easily identified and due to its random nature is difficult to control reliably. Thus, the combined experimental factor in (18) is subject to erratic behavior for CWBP systems, presenting a serious problem for obtaining consistent quantitative measurements of the concentration of fluorophores based on absolute fluorescent intensity.

As described by (15), the total flux emanating from the sensing volume contains a very strong component at the excitation wavelength. As sketched in Fig. 10, the fluctuations due to the unpredictable variation of experimental factors can be minimized by a dynamic normalization of the fluorescent data with the simultaneous measurement of the excitation power [2]. The photon flux emanating from the sensing volume is split into two optical paths by means of a fiber optic splitter with 1:100 splitting ratio. A small fraction of the emitted photons are transported through fiber F2 and a neutral density filter before being converted to photoelectron pulses by a photomultiplier PMT1. Majority of the emitted photons are guided by fiber F3 to the spectral optical filtering unit SOF. The photon stream is collimated and passed through a holographic notch filter and a band-pass filter. Optical fiber, F4, transports the spectrally filtered photons to PMT2. The average number of photons detected, by the two photomultipliers, in a time interval T are given by

$$m_{ex}(t) = H_{nd}(\lambda)\bar{\Phi}_{tot}T = \Gamma_{nd}\Phi_0\eta_{det}\eta_{ex}\eta_{em}T, \tag{19}$$

$$m_{em}(t) = H_{hnp}(\lambda)H_{bp}(\lambda)\bar{\Phi}_{tot}T = \Phi_0\Gamma_{bp}\eta_{det}\eta_{ex}\eta_{em}\eta_{mol}Tc, \tag{20}$$

where m_{ex} and m_{em} are instantaneous counts in time interval T , corresponding to the excitation and emission spectral bands, respectively, and the optical filter responses are given by,

$$H_{nd}(\lambda) = \Gamma_{nd}, \text{ for all } \lambda, \tag{21}$$

$$H_{hnp}(\lambda) = \left\{ 1 - \Gamma_{hnp}\text{rect}\left[\frac{\lambda - \lambda_{ex}}{\sigma_{ex}}\right] \right\}, \tag{22}$$

$$H_{bp}(\lambda) = \Gamma_{bp}\text{rect}\left[\frac{\lambda - \lambda_{em}}{\sigma_{em}}\right], \tag{23}$$

where Γ s represent the pass-band gain of the filter, and the $\text{rect}(\cdot)$ function, which describes the response of a brick wall filter, is given by

Fig. 10 Dual photomultiplier scheme for fluorescent detection. EP – emitted photon stream from the sensing volume, PS – fiber-optic power splitter, ND – neutral density filter, PMTx – photomultiplier, F1, F2, F3 – 1 mm multimode fibers, F2 – 110/125 MMF, SOF – spectral optical filter unit, BP – band pass filter, HNP – holographic notch plus filter

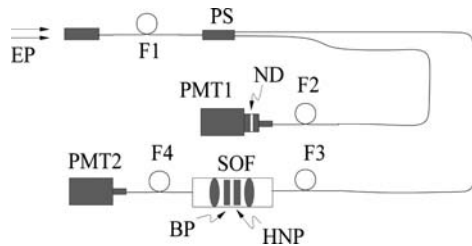
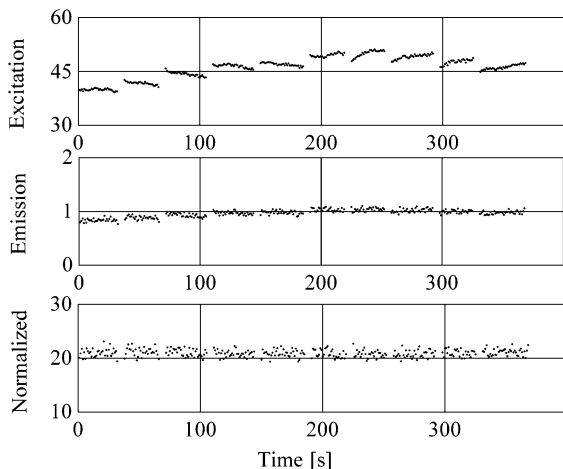


Fig. 11 Sensor output showing three windows: *top* – excitation counts $m_{ex}(t)$, *middle* – emission counts $m_{em}(t)$ and *bottom* – normalized counts $N_S(t) = m_{ex}(t)/m_{em}(t)$. (Reprinted from Dhadwal et al. [2], with permission of Elsevier)



$$\text{rect}\left[\frac{x - x_0}{2\sigma_x}\right] = \begin{cases} 1, & x_0 - \sigma_x < x < x_0 + \sigma_x \\ 0, & \text{otherwise} \end{cases} \quad (24)$$

The filter is centered at x_0 and has a full width of $2\sigma_x$. The instantaneous photon counts averaged over a time interval of T seconds can be normalized to obtain

$$N_S(t) = \frac{m_{em}(t)}{m_{ex}(t)} = \frac{\Gamma_{nd}}{\Gamma_{bp}} \frac{\Phi_0 \eta_{det} \eta_{ex} \eta_{em} \eta_{mol} T c}{\Phi_0 \eta_{det} \eta_{ex} \eta_{em} T} = \frac{\Gamma_{nd}}{\Gamma_{bp}} \eta_{mol} c. \quad (25)$$

Equation (25) shows that the dual PMT detection scheme eliminates the experimental dependence from the measurements and can be used in combination with standard reference materials to provide instrument and laboratory independent measurements. The ratio $\frac{\Gamma_{nd}}{\Gamma_{bp}}$ can be adjusted so that the SNR of the normalized counts is proportional to the emission SNR.

Figure 11 shows the result of the instantaneous normalization for a solution of Alexa-532 fluorophore dye complex (<http://www.ingenta.com>) at a concentration of 367 pg mL^{-1} . The top panel shows the counts corresponding to the excitation band and the middle panel is the fluorescent emission data. The lower panel is the normalized data. The figures show ten cycles of stop-and-flow measurement, between each cycle the fluid was purged from the capillary.

2.5 Optimal Capillary for the Prototype CWBP

As discussed in Sect. 2.3, capillary selection may be undertaken by independent consideration of the excitation and emission geometries. Larger ID capillaries are preferred for direct excitation of leaky modes. Capillaries with thinner walls, i.e.,

low V -values, give rise to stronger evanescent waves. From the perspective of surface probe density, capillaries with larger ID should be the natural choice. Larger IDs also improve handling and coupling issues. However, for rare samples, capillaries with smaller IDs would be preferable. All these constraints can be quantified to select a suitable capillary for optimal excitation.

However, optimal detection of fluorescence requires careful consideration of both the optical geometry and selective optical filtering of the raw photon flux emanating from the sensing volume. The optical receiver can be separated into a front end which maximizes collection of all emitted photons from the sensing volume and a back end which incorporates selective optical filtering to minimize the out of band emission. These two parts can be independently optimized.

This section is devoted to the efficient collection of emitted photons from an effective volume formed by the excitation light source and the field of view of the optical receiver. The source of fluorescence can be homogeneously distributed throughout the liquid core or it can be confined to a thin layer at the liquid cladding interface of the leaky waveguide. An ideal collector needs to capture all photons emitted from the entire cylindrical sensing volume; however, from a practical perspective, this is not a feasible option. Instead, the optical receiver design must be optimized for a geometry that is prudent for a portable instrument. The optical fiber transports photons from the sensing volume, through selective filtering units, to remotely located photodetector(s). Photons emitted from the sensing volume can either radiate through the wall of the capillary into the external medium or be trapped in both the liquid core and the capillary wall and be collected at either end of the capillary. The efficiency of transporting emitted photons through the guided modes of the capillary wall or the leaky modes of the liquid core have been previously investigated [7, 10].

For a planar geometry, the emission process, the inverse of absorption, is also characterized by evanescent photons which show pronounced coupling into the dense medium at the critical angle. Using both classical and quantum descriptions of the electromagnetic fields, they showed that the angular distribution of light emerging in the dense medium follows a similar trend to that discussed in Sect. 2.1, (Fig. 4). An alternative methodology uses wave optics to calculate the collection efficiency of light launched into the fiber core of an optical fiber from incoherent fluorescence sources located in a thin layer surrounding the core [10]. This situation is analogous to the liquid filled core region, with emitted photons from the coating layer tunneling into the capillary wall. For homogeneously distributed fluorescent sources in a step index fiber, the collection efficiency increases roughly proportional to the number of guided modes, which is proportional to the second power of the normalized frequency V . The term “collection efficiency” measures the ratio of the light collected by the guided modes of the fiber core relative to the total amount radiated by the sources in the absence of the core region. For values of V smaller than 30, the collection efficiency is between 1% and 2%, approaching a saturation value of about 60% for $V = 300$. It should be noted that all the light in the core of the collecting fiber is not necessarily delivered to the detector. They concluded that positively guiding fibers ($n_1 > n_2$) gather more light than any other arrangement if

the fibers are sufficiently low loss and long enough. However, for leaky waveguides ($n_1 < n_2$) the coupling efficiency is inversely proportional to V , with a maximum value which is very strongly length dependent. Fluorescent photons that are not trapped in the core of either positively guiding or leaky fibers are radiated into the cladding region and out into the external medium. The CWBP is optimized for the collection of the radiated photons. As the capillary dimensions are considerably larger than the wavelength of the excitation source, efficiency of particular collection geometries can be investigated by means of ray tracing.

Optimal design of the CWBP requires defining the appropriate dimensions of the capillary to provide maximum collection of the fluorescence radiated by molecules immobilized in a thin coating layer ($\delta y/\lambda < 1$). Rigorous calculations are rather cumbersome for tube-like waveguides and particularly difficult for arbitrary geometries. The aim here is to maximize number of photons radiated into the medium surrounding the outer capillary surface. Commercial ray tracing software with the necessary sophistication can be used. However, such commercial packages tend to be beyond the budget of most researchers. It is possible to reduce the complexity of the ray tracing by restricting the analysis to a two dimension problem. Some researchers have developed particular ray tracing solutions for capillaries [11–13].

2.5.1 Optimizing Collection of Radiated Photons

The problem of ray tracing is reduced to exploring designs that maximize the fraction of fluorescence radiated from the capillary surface into the upper hemisphere. Through the use of Snell's law at each interface, rays can be traced from sources located in the coating layer. Various optical configurations can be analyzed in this way. For example, the efficiency of single fiber versus fiber array receivers was investigated. Since a typical capillary used in a CWBP has inner and outer diameters greater than a few hundred microns, the use of geometrical optics to trace rays emanating from the fluorescent source is acceptable. A capillary, with a wall thickness of 150 μm , a refractive index of 1.5, and immersed in water has a V -value of 195. In a planar geometry, this structure would support over twenty thousand electro-magnetic modes. The author developed ray tracing software that allows fluorescent point sources to be located at the coating/fluid interface in the interior region of the capillary waveguide as depicted in Fig. 12. A cone of rays representing hemispherical radiation can be launched from point sources located along the surface of the coating layer. The optical path of each ray is traced through the capillary until it either exits the outer surface or it suffers total internal reflection (dashed line) at the outer surface/air interface. Collection efficiency η_{col} , defined by the ratio of the number of radiated rays to the total number of radiated and nonradiated, is computed as a function inner radius r_1 , and the ratio of outer to inner radii $R_d (=r_3/r_1)$. Capillary length does not affect the design optimization because transmission for silica is nearly loss-less. Additionally, it was found that η_{col} is very weakly dependent on the coating layer thickness. Thus, the design optimization seeks to maximize $\eta_{\text{col}}(R_d, r_1)$.

Fig. 12 Ray tracing model of a capillary. RFE- radiated photons, GFE – fluorescent photons trapped in the capillary wall. (Reprinted from Dhadwal et al. [3], with permission of Elsevier)

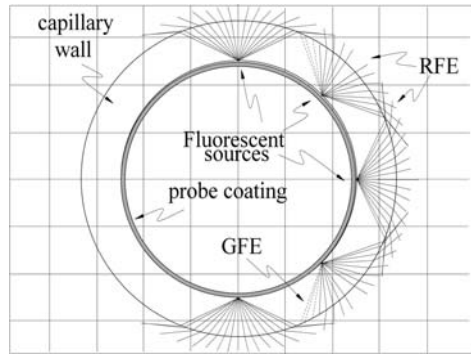
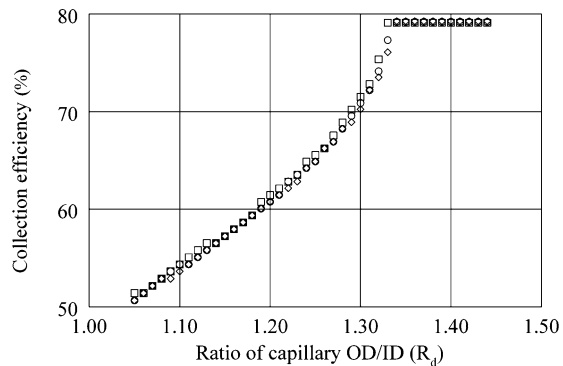


Fig. 13 Collection efficiency $\eta(R_d, d_1)$ computed using 20,000 rays for each point. Squares – $2r_1 = 0.5$ mm, circles – $2r_1 = 0.8$ mm, and diamonds – $2r_1 = 1.1$ mm. All points lie on the same curve. (Reprinted from Dhadwal et al. [3], with permission of Elsevier)



The efficiency calculations were performed by tracing over 20,000 rays from the coating surface layer with a thickness of 0.1λ . Figure 13 shows a plot $\eta_{col}(R_d, r_1)$ for $r_1 = 0.5$ mm, 0.8 mm and 1.1 mm. For these calculations, refractive indices $n_0 = 1.0$, $n_1 = 1.33$, $n_2 = 1.34$, $n_3 = 1.5$, and $n_4 = 1.0$ were used. It was concluded that the maximum collection efficiency is independent of r_1 and has a maximum value of $\sim 80\%$ for values of R_d exceeding 1.34. Thus, the transmission of photons emanating from the outer surface of the capillary is determined only by the ratio of outer to inner diameter. Saturation occurs because the outer surface begins to resemble a planar surface, which increases the number of trapped modes in the capillary wall, thereby reducing the transmission. A capillary with $r_1 = 1.0$ mm and $r_3 = 1.3$ mm was selected for use in the development of the prototype CWBP discussed below. The inner diameter was selected based on the diameter of available fiber optic connectors and to facilitate easy handling.

2.5.2 Fiber Optic Receiver Efficiency

In the previous section, optimal capillary dimensions were selected based on the maximum transmission of emitted photons. These photons have a broad spectral

range which includes the excitation source and the spectral emission characteristics of the fluorophore. There are two aspects to the design of the back end optical receiver: (1) maximize the transport of emitted photons from the capillary surface to a remotely located photo-detector and (2) optimal spectral filtering prior to photo-detection. The latter usually requires collimating optics, with low NA, while the former requires high NA fiber optics. Receiver optimization is defined as the ratio of the number of rays reaching the photo-detector to the number of rays emanating from the capillary surface. Ray tracing software, as described earlier, can be used to generate a spectrum of plane waves (rays) radiated from the capillary surface. Arbitrarily-shaped receiver apertures can be placed above the capillary surface and the efficiency calculated for a particular receiver configuration.

Figure 14 shows the receiver efficiency for a 1 mm slit aperture having a $NA = 0.48$, and placed just above the capillary surface. As expected, the coupling efficiency increases with decreasing values of r_1 , because most of the fluorescent sources fall within the field of view of the receiver aperture. However, r_1 cannot be arbitrarily small as it would compromise the strength of the capillary, and decrease the efficiency of coupling from a source to the capillary wall. Additionally, smaller values of r_1 reduce the surface area of the capillary thereby decreasing the number of immobilized probe molecules. However, a smaller radius may be preferable for improving the hybridization efficiency.

Figure 15 compares the receiver efficiency for three types of two dimensional apertures. The first (triangles) is a single multimode fiber with a core diameter of 1 mm and a $NA = 0.48$; the second is a smaller fiber (squares) with a core diameter of 0.3 mm and a $NA = 0.39$; the third is a linear array (circles) of 17 fibers each with a core diameter of 110 μm and a $NA = 0.29$. In all three cases, there is an optimal location of the receiver aperture. For the linear array, the receiver efficiency is proportional to the number of fibers in the array. Another arrangement might surround the entire capillary outer surface with receiving optical fibers. However, in practice, the total number of fibers that can be used will be determined by the near collimated input beam requirements of the optical filtering components, such as holographic notch and band pass filters.

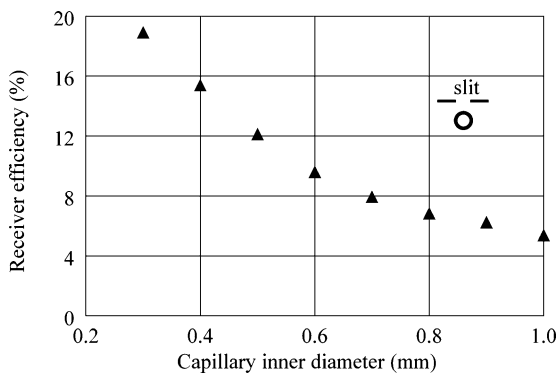
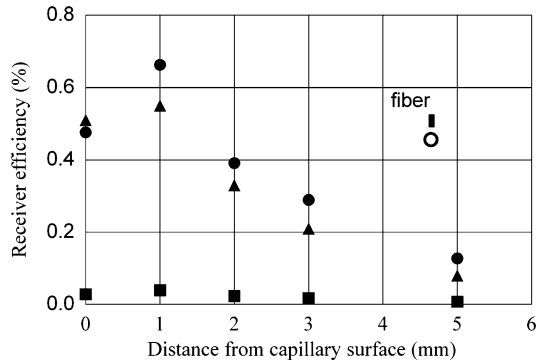


Fig. 14 Receiver efficiency for a capillary with $R_d = 1.34$ and $(r_2 - r_1) = 0.1$ mm. A slit with a width of 1 mm and a $NA = 0.48$ is positioned just above the outer surface of the capillary. (Reprinted from Dhadwal et al. [3], with permission of Elsevier)

Fig. 15 Receiver efficiency as function of the spacing between the fiber RF and the outer surface of the capillary. *Squares* – a single 0.3 mm fiber, *triangles* – a single 1 mm fiber, and *circles* – a linear array of 17 110/125 μm fibers. (Reprinted from Dhadwal et al. [3], with permission of Elsevier)



3 Practical Implementation of a CWBP

A portable CWBP was fabricated and laboratory tested with synthetic target hybridization. Before describing the details of the particular instrument, let us briefly review some aspects of SNR characterization of optical/electronic systems. A successful experiment must consider all possible sources of noise which could compromise overall system performance.

The minimum detectable signal corresponds to a $\text{SNR} = 1$; however, practical sensor systems define a detection limit at the 3-sigma value. It is imperative to minimize all sources of noise, including excitation source noise, which expresses the root-mean-square fluctuations of the source intensity. Source noise can be significant for solid state laser sources, which are typically used at excitation wavelengths of 532 nm. Noise in optical receivers can be separated into shot (photon) noise and circuit noise (thermal in nature). Shot noise originates from the random arrival of photons and is proportional to the photon rate, while circuit noise is due to the random movement of charge carriers in all electronic components. Some photodetectors have internal gain which is accompanied by gain noise. Like amplifiers, the photodetectors with gain are characterized by an excess noise figure. Ideal amplifiers, i.e., noiseless, have a noise figure of unity. Among photodetectors with gain, PMTs can have gains of the order of 10^6 with a noise figure of two. Despite the high quantum efficiency and small size, avalanche photodiodes (apd) have not displaced PMTs in single photon counting applications. The shrinking size, built in dc-to-dc multipliers and low dark counts still make the PMT a good choice for most sensor applications. Optical receivers can be operated either in the analog mode (multiphoton) or single photon detection mode. Single photon counting receivers also have a wide dynamic range and low dark counts. Uncooled PMTs, typically, have dark counts (<25 cps), corresponding to an optical power level of 10^{-18} W. Digital receiver have superior noise performance compared with analog systems. The digital receiver circuit does not require amplifiers, filters and analog-to-digital converters.

3.1 Detection Limit

Typically, the detection limit is expressed in terms of the lowest concentration giving rise to a signal that is three standard deviations above the buffer signal. However, since our optical detector is digital, it is possible to use the ideas from digital communications to express the detection of the target species as being equivalent to a digital signal level *one*, while the absence of target, i.e., the background is a *zero*. The output of the detector is a sequence of counts averaged over time interval T . Thus, target detection is positive if the instantaneous count value is above some predetermined threshold value. The limit of detection can be expressed in terms of a target-detection-error-rate (TDER), which measures the ratio of false-positives E_e , to the total number of measurements E_t . Thus,

$$\text{TDER} = \frac{E_e}{E_t}. \quad (26)$$

For example, a $\text{TDER} = 10^{-3}$ implies that a false-positive was issued once in one thousand measurements, that is, a false detection probability of 0.1%. TDER defines the probability of a false-positive based on the instantaneous normalized count value, N_S . Figure 16 shows, upper panel, a plot of the normalized counts for a 3.6 pg mL^{-1} sample of fluorophore Alexa532 complex (triangles) and the buffer (circles). The lower panel is a frequency distribution of the two. The probability of making a false detection P_e , represented by the shaded area in Fig. 16, is given by [3]

$$P_e = \frac{1}{2} \left[1 - \text{erf} \left(\frac{\sqrt{\text{SNR}}}{\sqrt{2}} \right) \right] \equiv \text{TDER}, \quad (27)$$

where $\text{erf}(\cdot)$ is the error function. The SNR is given by

$$\sqrt{\text{SNR}} = \frac{N_T - N_B}{\sigma_B} = \frac{N_S - N_T}{\sigma_S}, \quad (28)$$

where σ_S and σ_B are the standard deviations of the signal and background counts, respectively. If the threshold is set at the mid-point of the target and background counts, then the SNR can be expressed as

$$\sqrt{\text{SNR}} = \frac{1}{2} (1 - \kappa) \frac{N_S}{\sigma_S}, \quad (29)$$

where $\kappa = N_B/N_S$, is defined as the extinction ratio having a range of values from zero to unity, zero being the ideal value which is equivalent to a background count of zero. The frequency distribution data in Fig. 16 is fit with a Gaussian function to obtain the values: $N_S = 3.11$, $\sigma_S = 0.09$, $N_B = 2.71$, and $\sigma_B = 0.10$. These values

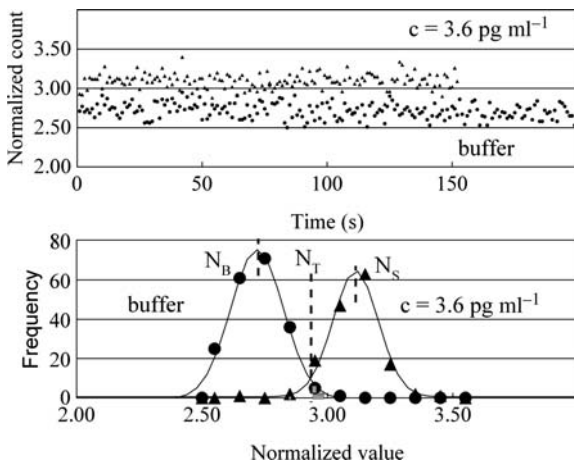


Fig. 16 Upper panel – normalized counts for a fluorophore sample with a concentration of 3.6 pg ml^{-1} (triangles) and the buffer (circles). Bottom panel – frequency distributions for sample and buffer data. Based on the Gaussian fit (solid lines) to the data a TDER of 1.3×10^{-2} is calculated

give a TDER of 1.3×10^{-2} for this data set, that is, the probability of a false-positive based on a single 1 s measurement is 1.3%.

In the photon noise limit, the photon arrival rate at the detector is described by a Poisson process, which has a variance $\sigma_S^2 = N_S$. If the average count rate is $\bar{\Phi}$, then $\left(\frac{N_S}{\sigma_S}\right)$ in (27) can be replaced by $\sqrt{T}\bar{\Phi}$. In other words, the probability of false detection decreases with the square root of the measurement interval T . Figure 17 shows frequency distributions obtained from a 1 pg ml^{-1} sample. The dash-dot lines are Gaussian fits to data recorded at a time interval $T = 1 \text{ s}$, giving a TDER of 0.156. The solid lines are Gaussian fits to the data averaged over $T = 8 \text{ s}$, giving a TDER of 0.015.

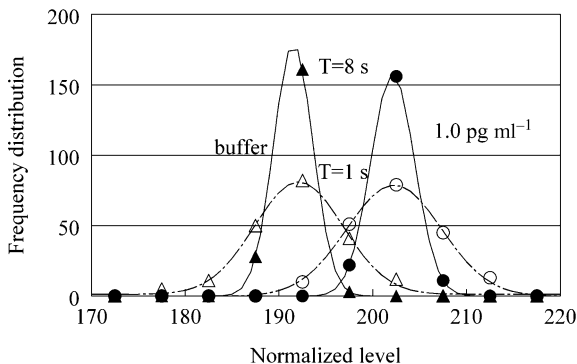
The detection limit can be expressed in several units, depending upon the particular application. For biosensor applications, it may be more appropriate to express the detection limit as the number of target molecules detected or as the minimum number of bacterial cells needed for a positive response from the biosensor. During the testing stages, a solution of fluorophore molecules is used for obtaining a concentration series.

The measured detection limit, specified in terms of pg ml^{-1} , can be converted to number of fluorophore molecules using the transformation

$$M_{\text{TM}} = \frac{\text{detection limit} [\text{gmL}^{-1}] \cdot V_{\text{sens}} [\text{mL}]}{W_{\text{M}} [\text{g mol}^{-1}]} A_{\text{v}} [\text{molecules mol}^{-1}], \quad (30)$$

where W_{M} is the molecular weight of the dye complex, V_{sens} is the effective volume of the sensing region, and A_{v} is Avogadro's number. The detection limit of 1 pg ml^{-1}

Fig. 17 Frequency distribution of data for a sample concentration of 1 pg ml^{-1} . Target detection based on a single one second measurement gives TDER of 15.6%. Averaging over eight seconds reduces the TDER to 1.2% (solid lines)



corresponds to a maximum of 40,000 molecules in the sensing volume of $400 \mu\text{l}$. The fluorophore molecules have a molecular weight of $6,100 \text{ g mol}^{-1}$.

The above detection limit calculation is based on homogeneously distributed fluorophore molecules in the sensing volume. However, in practice, the probe molecules will be bound to the capillary surface, resulting in considerable decrease in the detection limit, assuming a one-to-one mapping into target molecules. The number of surface bound probes M_{PM} is given by

$$M_{\text{PM}} = \gamma \frac{r_1 L}{r_p^2}, \quad (31)$$

where r_p is the radius of an equivalent globular molecule, and γ is the surface utilization of the probe. For example, with values of $L = 1 \text{ mm}$, $r_1 = 0.5 \text{ mm}$, and $r_p = 2.5 \text{ nm}$, the above volume detection limit of forty thousand molecules corresponds to surface utilization of $5 \times 10^{-4}\%$. A probe density of $2.5 \times 10^{12} \text{ molecules cm}^{-2}$ on the interior surface of a capillary has been reported [14]. Thus, utilization of surface bound probes can result in substantial reduction in the detection limit. In practice, the limit will be determined by the quality and quantity of immobilized probes on the interior region of the capillary. Surface utilization of 64% has been reported for oligonucleotides immobilized on glass substrates [15]. The output signal for surface immobilized probes is a function of the probe density, the hybridization efficiency, and the target concentration. The normalized counts from the output of the hybridized sensor can be expressed by the relation

$$\frac{d}{dt}(N_S(t)) = \eta_H \eta_L M_{\text{PM}} M_{\text{TM}}, \quad (32)$$

where M_{TM} is the number of target molecules, and η_H and η_L are the hybridization and labeling efficiencies, respectively.

During the testing phase, labeling of synthetic target molecules is convenient as the output signal will be proportional to target concentration. Detection of synthetic

target will cause the signal $N_S(t)$ to follow a response similar to that of a charging capacitor. The hybridization kinetics are quite complex, but as a first-order approximation, the signal $N_S(t)$ can be described by the function,

$$N_S(t) = N_\infty[1 - \exp(-t/\tau_H)], \quad (33)$$

where N_∞ is given by (29) and the saturation time τ_H will be a function of hybridization kinetics. For detection of natural targets, labeling of surface bound probe molecules may be preferred, giving rise to a maximum signal in the absence of target molecules, or utilize competitive hybridization.

3.2 The Capillary Waveguide Biosensor Platform

Based on the above analysis, the portable CWBP was developed for a capillary of length of 65 mm and an outer diameter of 1.3 mm. While the length of the sensing volume is less than 2 mm, a longer length provided experimental flexibility and easy handling. Figure 18 shows a schematic representation of the capillary housing (CH), which is the central part of the system. Each end of a capillary is mounted in a 15-mm-long stainless steel cylindrical holder (SH). Each end of the mounted capillary is polished to optical flatness ($\lambda/2$), the capillary surface has sufficient optical flatness for efficient excitation of the capillary modes. The outer diameter is compatible with SMA 905 connectors C1 and C2. SMA 905 bulkhead adapters AD are screwed into the copper thermal housing TH mounted inside the outer block CH. The capillary slides easily into the copper housing. Fluid sealing is provided by

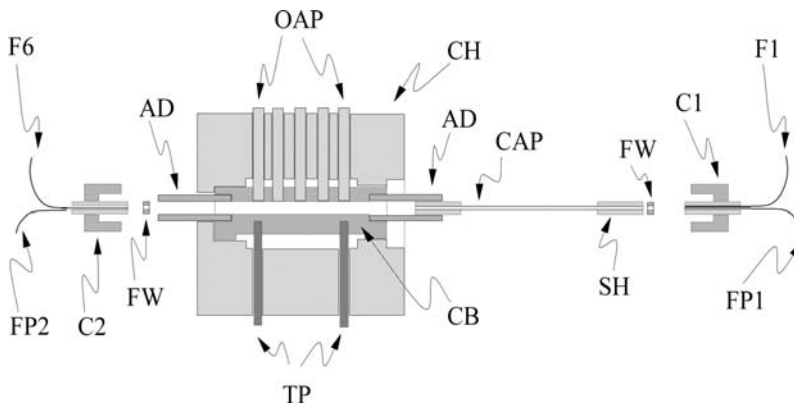


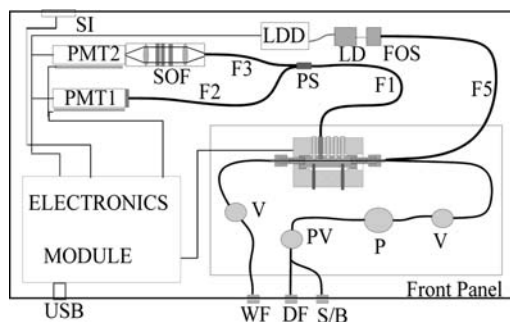
Fig. 18 Detailed schematic of the capillary housing CH. C1, C2 – opto/fluid connectors, AD – SMA bulk head adaptor, CAP – capillary, SH – stainless steel housing, FW – flat washer, FP1 – fluid port, F1, F6 – multimode fibers, CB – copper block, OAP – optical access ports, TP – temperature probes. (Reprinted from Dhadwal et al. [2], with permission of Elsevier)

two flat nylon or Teflon washers FW placed at either end of the capillary. The SMA connectors hold the capillary inside the copper housing while providing the necessary fluid seal and allowing optical access from both ends. Fluid is introduced into the capillary through tubing FP1 and drained through tubing FP2. As discussed in Sect. 2.3, connectors C1 can be swapped easily and we investigated the performance of three different types. Several optical ports OAP provide access to emission along the length of the capillary. The exit connector can also be used for collected photon emission from the liquid core as well as the capillary wall. Temperature of the copper block is monitored and controlled by thermistors TP.

Figure 19 is a diagram of the complete system, which occupies a volume of $38 \times 18 \times 7.5 \text{ cm}^3$. The entire system is controlled through a graphical user interface (GUI) which can run on a Windows XP platform and is written in Visual C++. The GUI is used for the entire control of the instrument, including data logging, real-time displays and postmeasurement playback feature to process archived data files. The sensor is controlled through a USB2.0 serial data interface. During normal operation, three windows display the instantaneous count values of the excitation, the emission, and the normalized counts. A fourth window displays the fluid temperature inside the capillary. The user is provided with full control of the experiment and full access to directory structure.

Fluid flow is controlled using solenoid isolation valves V (#075T2NC12), diaphragm micropump P (#120SPI12), and a 3-way pinch valve PV (#075P3MP12). These devices were purchased from Bio-Chem (<http://www.Bio-Chem.com>). The system can either be run in a manual mode with full control or in batch mode for user-free operation. The latter is based on a 24 vial holder carousel, with rotational and up-down stepper motors.

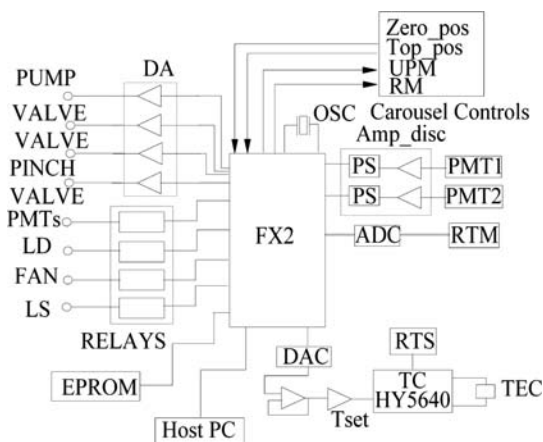
Fig. 19 Schematic of the CWBP. WF – waste port for the fluid, DF – fluid port for denature solution, S/B – port for sample and buffer, can be connected to a carousel dip probe, PV – 3-way pinch valve, V – isolation valves, P – micropump, F5 – illuminating optical fiber, F1 – emission pick-up fiber, PS – fiber optic splitter, F2, F3 – relay fibers, LDD – laser diode driver, LD – laser diode, FOS – fiber optic switch, USB – USB2.0 connector for PC, SI – carousel interface connector. (Reprinted from Dhadwal et al. [2], with permission of Elsevier)



The prototype CWBP is based on the Alexa-532 dye complex which has a high extinction coefficient and a large Stokes shift. A 15 mW diode-pumped solid state laser LD which has a peak emission wavelength of 532 nm with a FWHM spectral width of 5 nm (<http://www.photoptech.com> model#GDL7020) is used in the CWBP. Laser output is coupled into the proximal end of a fiber optic switch FOS, while the distal end connects to the launching fiber F5. In order to avoid photo-damage of the fluorophore molecules, illumination is activated during measurement by means of the fiber optic switch. Direct ON/OFF modulation of the laser should be avoided due to short-term power instabilities. A 1 mm pick-up fiber, F1, with a numerical aperture of 0.48 (<http://www.thorlabs.com> #URT1000), collects photon emission from the capillary surface. A special power splitter, PS, couples most of the photons (>99%) into a second 1 mm fiber, F3, which transports the photons, through the spectral optical filtering unit SOF to a photomultiplier PMT1 (<http://www.hamamatsu.com> #H9305-04). The SOF unit includes collimating optics, a holographic notch filter centered at the excitation wavelength (<http://www.Kaiser.com> #HNPF) and a band-pass emission filter centered at 560 nm with 30 nm width (<http://www.omegafilters.com>). Overall, the out-of-band rejection is better than 10^{-5} . The second port of the power splitter is a 110/125 micron optical fiber F2, which guides the photons through a neutral density filter ND, and a band pass filter BP centered at the excitation wavelength. A second PMT2, which provides the instantaneous photon counts corresponding to the background photon flux from the sample and the various optical interfaces.

Figure 20 shows a block schematic representation of the electronics module of the CWBP. The entire control and data acquisition is designed around the Cypress

Fig. 20 Schematic of the electronics module controlling the CWBP. DA – darlington amplifiers, DAC – digital to analog converter, ADC – analog to digital converter, Amp-disc – amplifier discriminator for the photomultiplier (PMT), PS – pulse stretcher, OSC – oscillator, Zero_pos – zero position sensor, Top_pos – dip probe position sensor, RM – carousel rotary stepper motor, UPM – linear actuator for the dip probe of the carousel, RT – resistance thermistor, TEC – thermoelectric heat exchanger, Tset – set temperature. (Reprinted from Dhadwal et al. [2], with permission of Elsevier)



FX2 (C67C68013), which integrates the USB 2.0 transceiver, serial interface engine (SIE), enhanced 8051 microcontroller, and a programmable peripheral interface into a single chip. This is a very cost-effective solution that shortens development time and provides a small foot print for use in a mobile platform. Although not important in this application, the FX2 can be operated at the maximum USB 2.0 data rate of 45 Mbytes/s. The 8051 microcontroller runs software that can be downloaded to an internal RAM via the USB or from an EPROM (Atmel #24C164). Additionally, the 8051 microcontroller has three high speed counter/timers, which provide data acquisition and control of various components as discussed below.

Four high-current relays (NEC #PS170A) are used to power up the PMTs, the laser diode, an optional fan for the temperature controller, and the laser shutter. The 8051 generates the timing pulses for operating the self priming micropump, two isolation valves, and a 3-way pinch valve. External Darlington amplifiers, DA (Texas Instruments # ULN2003A), provide the current necessary to drive the pump and the valves. Batch operation requires the use of a carousel and a dip probe. The position and height of the dip probe are controlled by a motor RM, (Pik Power # SST42D1020) and the linear actuator, UPM, (Herbach & Rademan #TM96MTR2873) both are powered directly from the FX2, via the 8051. Two optoelectronic interrupt switches provide the zero angle reference and the top of the fluid limit.

Temperature control of the fluid inside the capillary is attained through the use of a TEC (Melcor #CP1) heat exchanger using an analog controller from Hytek Devices (HY5640), which drives the current in a bipolar direction through the series of PN junctions until the set temperature is obtained. A sensing NTC thermistor, RTS, (Betatherm #10K3A1IA) provides the requisite feedback. The operating temperature, in the range of 20–70 °C, is set by the user from the GUI application. An 8-bit digital-to-analog (Maxim 7545) converter inside the FX2 creates an analog voltage corresponding to the thermistor lookup table. A combination of an amplifier and transistor provide an active emulation of the set resistor, Tset, required by the Hytek controller, which uses proportional/integral control to attain temperature stability of 0.1 °C. However, due to the 8-bit digital-to-analog converter, the actual temperature stability is about 1 °C. A second thermistor, RTM, provides an actual measurement of the fluid temperature. The thermistor resistance is converted to a voltage drop, which is converted to 8-bit digital data by the analog-to-digital converter (Maxim 153). The GUI interprets the 8-bit word through another look-up table for continuous update of the fluid temperature display.

4 Results and Discussion

Several factors, such as precision, accuracy, and detection limit, contribute toward the overall utility of any instrument. From a practical perspective, quantitative knowledge of these parameters defines the bounds within which the instrument should be operated.

4.1 Precision and Accuracy

In a typical run, a capillary is mounted into the CWB and loaded with the sample under test. Total volume, including connecting tubing, is ~ 2 ml. The actual sensing volume is ~ 400 μl . A single measurement is taken over a time interval of 30–60 s, with data recorded every second. Any single measurement can be repeated by reloading the sample. Thus, each run includes a series of measurement cycles. A new run is initiated with the remounting of the capillary. The measurement sequence is as follows: purge air to empty capillary; load 2 mL sample into the capillary; wait 60–120 s for fluid to reach set temperature; open the shutter for 30 s to acquire data.

Figure 21 shows the measurements for one run of the uncoated capillary, which was reloaded with the hybridization buffer before each cycle. The three panels represent, the background scattered counts (excitation), the fluorescent counts (emission), and the normalized counts, respectively. The cycle to cycle value of normalized fluorescent intensity shows a reduced variation compared with the raw fluorescent signal. However, on occasions, the background scattered counts will increase sharply, while the raw fluorescent counts do not follow, resulting in erroneous normalization. The source of the sharp changes in the background scattered is conjectured to arise from the spontaneously generated microbubbles migrating inside field of view of the one mm collection fiber. However, this event is infrequent and easily detected.

Figure 22 shows a summary of the data taken with a hybridization buffer. In order to assess the overall benefit of the dual detector technique, five different runs were performed. The following conclusions can be drawn from the data. First, the average signal-to-noise ratio of each 30 s measurement is 27.1 and 27.7 for the raw and normalized fluorescent data, respectively. This is an indication of the system stability during the 30-s-interval and is expected to be the same for both

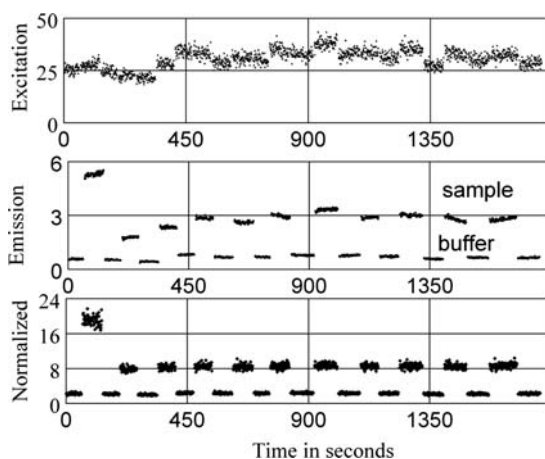


Fig. 21 A typical measurement cycle: $c = 3 \text{ ng mL}^{-1}$ of Alexa-532 complex. The collection is with a 1 mm multimode fiber having a $\text{NA} = 0.48$. The photon count axis have been arbitrarily scaled

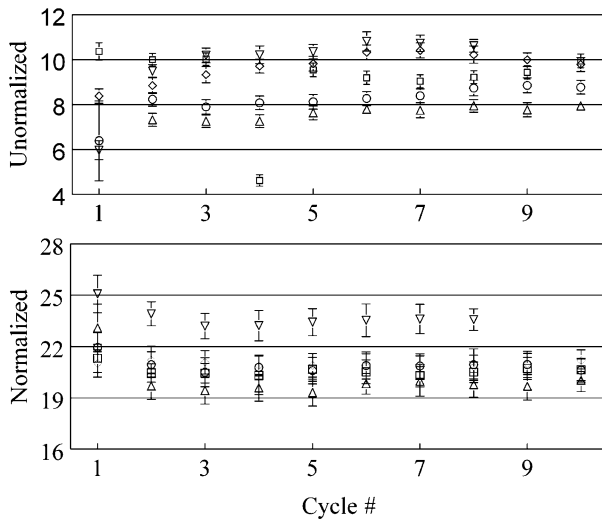


Fig. 22 Summary the fluorescent intensity data for the hybridization buffer. Five separate runs are indicated by different symbols. Each data point is the average of 30 points per cycle. (Reprinted from Dhadwal et al. [2], with permission of Elsevier)

measurements. Second, the relative deviation in the average value of the counts between cycles in one run is 12.6% and 6.7% for the raw and normalized fluorescent signals, respectively. Finally, the relative deviation between the cycles taken over the five runs is 17.9% and 6.3% for the raw and normalized estimates, respectively. These figures clearly confirm that instantaneous normalization, as discussed in Sect. 2.4, gives a significant improvement in the measurement precision of the fluorescent intensity data acquired with the dual detector approach.

Accuracy of measurements is typically assessed by repeated measurements on a set of standard materials. In this case, repeated measurements on a series of samples covering a range of concentrations will suffice. The concentration series was repeated three times, for each of the opto/fluid connectors T1, T2, and T3. The T1 connector excites leaky modes of the liquid core, while T3 excites guided modes of the capillary wall and T2 result in both direct and evanescent wave illumination. T1, T2, and T3 connectors use multimode fibers 300/330, 300/330, and 110/125. The fiber is positioned in the center of the connector for T1 and at the periphery for T2 and T3. Figure 23 shows a concentration series summarizing these results. The error bars represent the variation in the normalized value over three separate runs and two cycles per run. Error bars smaller than the size of the symbol are not visible. The data have been further normalized by subtracting the average value of the normalized buffer signal for the corresponding run. The graphs show a linear dependence between target concentration and normalized fluorescent intensity. Thus, it is possible to accurately extract molecular concentration from the normalized fluorescence data taken at different times.

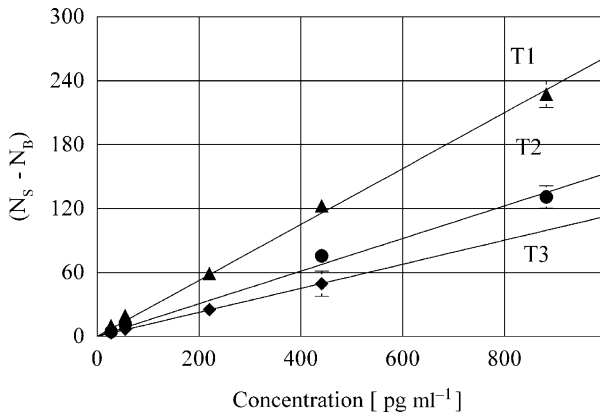


Fig. 23 Concentration calibration for the three opto/fluid connectors T1, T2 and T3. Each data point is averaged over three runs with two cycles per run. T1 – direct excitation, T2 – combination of direct and evanescent wave, and T3 – evanescent wave excitation only. (Reprinted from Dhadwal et al. [2], with permission of Elsevier)

However, the three different methods of excitation do not lead to a unique estimate of concentration, primarily due to the differences in the optical geometries associated with the excitation path. It is possible to use a standard reference material that can be used to scale normalized data taken under different experimental conditions. Figure 24 shows the data of Fig. 23, which have been scaled using the 441 pg ml^{-1} , is independent of the method of excitation. A linear fit to the data gives a concentration accuracy of 5.6% for the sensor. The T1 illuminator requires a lower source intensity for obtaining the same SNR value at the detector. However, these graphs do not show that the T1 opto/fluid connector is prone to corrosive damage resulting from extended exposure to the fluid stream and to signal variability due to migration of microbubbles in the field of view. The significance of bubbles in capillary systems has been discussed [16]. In the current design of the CWBP, the T3 illuminator is preferred for extended use and reliable estimates of concentration from data taken at different times.

The other aspect of sensitivity is the ability of the sensor to detect small changes superimposed on a larger average value. Figure 25 shows the system response for a 10% drop in concentration at 367 pg ml^{-1} has good repeatability. Results from two cycles are superimposed and give a TDER of 2×10^{-2} and 9.9×10^{-4} .

4.2 Hybridization

Hybridization, which anneals two complementary single-stranded DNA sequences into a double strand, is detected by attaching a fluorophore molecule to either of the sDNA probe or its complimentary sequence cDNA target. In the absence of any catalyst, the process completes itself under the influence of the random Brownian

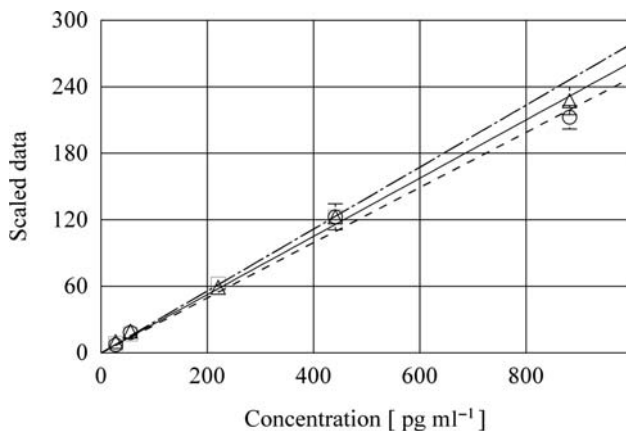


Fig. 24 Data in Fig. 23 scaled using the 441 pg ml^{-1} . Instrument has a unique concentration slope. T1 – solid line; T2 – dash line; T3 – dash-dot line

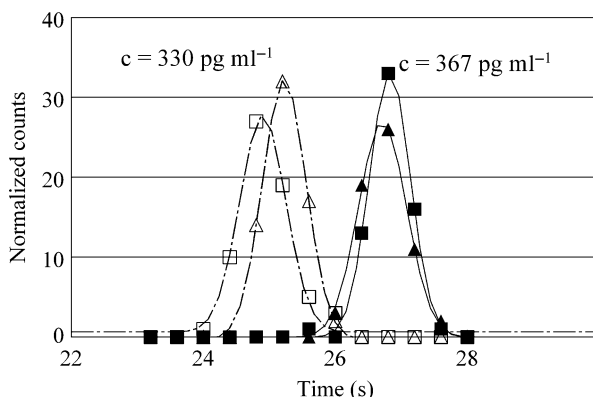


Fig. 25 Sensitivity measurement. Frequency distributions of the normalized data from two measurement cycles at concentrations of 330 pg ml^{-1} and 367 pg ml^{-1} . The two concentrations are detectable based on any single one second measurement, with TDER values of 2×10^{-2} and 9.9×10^{-4}

motion executed by the sDNA molecules. Hybridization rates are strongly dependent on experimental parameters, such as pH, temperature, and relative concentrations of target and probe. Times can vary from minutes to hours. For the purposes of testing, a synthetic target labeled with the Alexa532 fluorophore was used.

4.2.1 Synthetic Target Detection

Synthesized probe DNA was immobilized on the interior surface of silica capillary tubes using the method of Kumar [17]. The silanized probe, obtained by reacting (3-mercaptopropyl) trimethoxysilane with a 5'-thiol-labeled oligonucleotide probe

(<http://www.olisetc.com>) in acetate buffer, was covalently attached to a NaOH-activated capillary surface. Kumar's method leads to a streamlined procedure for rapidly preparing coated capillary tubes. The EUB338 sequence, which targets 16S ribosomal RNA of the phylogenetic domain bacteria, was used for the probe. Capillary preparation requires a few days to complete, but the capillaries can be prepared in batches and stored for months at -80°C .

A capillary coated with an ssDNA probe sequence is exposed to a solution containing a synthetic target with a complementary cDNA sequence, labeled with fluorescent dye molecules. Hybridization time and temperature was adjusted to explore the dynamics of detection. At the end of the hybridization cycle, the target solution is replaced by hybridization buffer and the fluorescence intensity corresponds to the number of target molecules that bound to the immobilized probe. Hybridization and denaturation measurements were performed at 40°C using probe-coated capillaries. Typically, the capillary was loaded with the hybridization buffer solution and allowed to equilibrate for 2 min before acquiring data, to ensure settling of microflows in the capillary. Fluorescence readings were recorded at 1 s intervals for 1 min. A solution of fluorophore-labeled target molecules in a hybridization buffer was then loaded into the capillary. A 10-min hybridization time was typically used, in which target molecules bound to probe molecules immobilized on the interior capillary cell wall. The capillary was flushed with 5 mL buffer to remove unhybridized fluorescent probe, and reloaded with fresh buffer solution for fluorescence measurements. Following measurement, the hybridized target molecules were stripped from the probe molecules by filling the capillary with a denaturing solution (1:1 volume ratio of formamide and hybridization buffer) at 40°C for 2 min. The capillary was then flushed, refilled with hybridization buffer, and the background fluorescence signal recorded.

Figure 26 shows a summary of the rate of hybridization for several target concentrations. As expected, the sensor signal reaches a target concentration dependent saturation level. The CWB response at concentration c can be modeled by (31) as discussed in Sect. 3.1. The solid lines in Fig. 26 show the results of a nonlinear least squares curve fitting to the data using (31). From the fit parameters, N_{∞} and τ_H can be extracted and these are plotted in Fig. 27 as a function of concentration. The standard deviation of the fit parameters is indicated by the error bars, which are visible only if the error is larger than the symbol size. The top panel in Figure 26 shows the expected Beer–Lambert relationship, that is, a linear dependence below a concentration of $1,000 \text{ pg mL}^{-1}$, as indicated by the solid line. The lower panel shows that the relationship between the equilibrium time constant and the target concentration does not follow a simple linear law. However, this is to be expected if one can argue that the equilibrium time is a function of both the available probe and the target concentration. Thus, the equilibrium time will be faster when either of the concentrations is more dominant and will exhibit a slower response when the ratio of the two concentrations is close to unity. This type of hybridization behavior has been observed by other researchers using different types of biosensors [18]. The underlying kinetics of hybridization, particularly nucleic acid probes immobilized on a solid surface, are subject of ongoing experimental

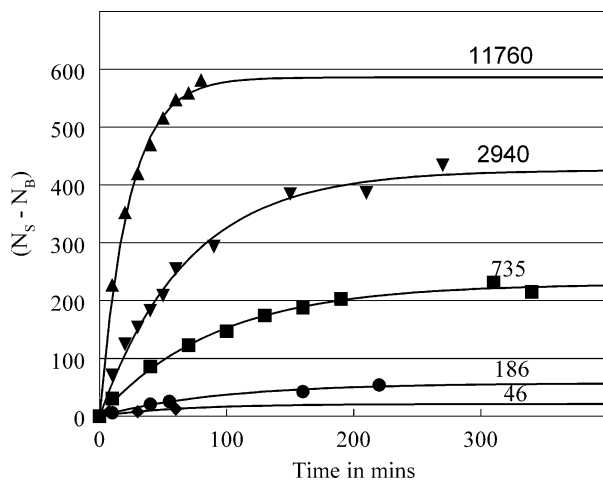


Fig. 26 Summary of hybridization kinetics using different concentrations of synthetic target. Annotations of concentration are in pg ml^{-1} . *Solid lines* are nonlinear least fits using (31). (Reprinted from Dhadwal et al. [2], with permission of Elsevier)

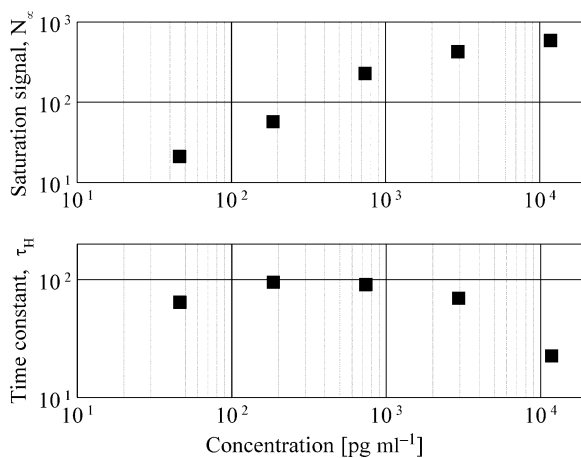


Fig. 27 CWB saturation signal and time constant for synthetic target. *Error bars* smaller than the symbol size are not visible. (Reprinted from Dhadwal et al. [2], with permission of Elsevier)

and theoretical research [19]. We are currently developing protocols for microbial process studies in natural samples.

5 Concluding Remarks

The CWBP uses several novel techniques for instrument independent measurements with a high degree of repeatability $\sim 6\%$. It provides for a reusable nucleic

acid based sensor that can be rearmed for detection through a denaturing step. Furthermore, upon degradation of the sensor due to multiple cycles, it may be possible to replenish the inner surface with new probe molecules without removing the capillary. Successful implementation of this *in vivo* procedure will make long term deployment a reality. Low detection limits (10^{-13} M) have been demonstrated for fluorochrome molecules which are homogeneously distributed throughout the fluid. Target detection through the use of surface bound probes is expected to reduce the detection limit by several orders of magnitude; however, early experiments using synthetic targets have not yet yielded any significant improvement. Planned reduction of the instrument foot print will make it possible to incorporate the CWBP into ocean monitoring instruments, such as, the environment sample processor (http://www.mbari.org/microbial/esp/esp_technology.htm), developed at the Monterey Bay Aquarium Research Institute.

References

1. Dantzler MM (2004) Methods development and analysis of environmental samples using a nucleic acid hybridization based fiber optic sensors. MS thesis, Stony Brook University
2. Dhadwal HS, Mukherjee B, Kemp P et al (2007) A dual detector capillary waveguide biosensor for detection and quantification of hybridized target. *Anal Chim Acta* 598:147–154
3. Dhadwal HS, Kemp P, Aller J et al (2004) Capillary waveguide nucleic acid based biosensor. *Anal Chim Acta* 501:205–217
4. Marcuse D (1974) Theory of dielectric optical waveguides. Academic, New York
5. Saleh BEA, Teich MC (1992) Fundamentals of photonics. Wiley, New York
6. Gloge D (1971) Weakly guiding fibers. *Appl Opt* 10:2252–2258
7. Carniglia CK, Mandel L, Drexage KH (1988) Absorption and emission of evanescent photons. *J Opt Soc Am* 6:479–486
8. Mathies RA, Peck K, Stryer L (1990) Optimization of high-sensitivity fluorescence detection. *Anal Chem* 62:1786–1791
9. Gaigalas AK, Li L, Henderson O et al (2001) The development of fluorescence intensity standards. *J Res Natl Inst Stand* 106:381–389
10. Marcuse D (1988) Launching light into fiber cores from sources located in the cladding. *J Lightwave Technol* 6:1273–1279
11. Keller BK, DeGrandpre MD, Palmer CP (2007) Waveguiding properties of fiber-optic capillaries for chemical sensing applications. *Sensors Actuators B Chem* 125:360–371
12. Vincze L, Janssens K, Adams F (1995) Detailed ray-tracing code for capillary optics. *X-Ray Spectrom* 24:27–37
13. Benoit V, Yappert MC (1996) Effect of capillary properties on sensitivity enhancement in capillary – fiber optical sensors. *Anal Chem* 68:183–188
14. Breimer MA, Gelfand Y, Sadik OA (2003) Integrated capillary fluorescence DNA biosensor. *Biosen Bioelectron* 18:1135–1147
15. Sojka B, Piuino PAE, Wust CC (1999) Evaluating the quality of oligonucleotide that are immobilized on glass supports for biosensor development. *Anal Chim Acta* 395:273–284
16. Wang G, Lowry M, Zhong Z et al (2005) Direct observation of frits and dynamic air bubble formation in capillary electrochromatography using confocal fluorescence microscopy. *J. Chromatogr A* 1062:275–283

17. Kumar A, Larsson O, Parodi D, et al (2000) Silanized nucleic acids: a general platform for DNA immobilization. *Nucleic Acids Res* 28:E71i–E71vi
18. Ahn S, Kulis DM, Erdner DL et al (2006) Fiber-optic microarray for simultaneous detection of multiple harmful algal bloom species. *Appl Environ Microbiol* 72:5742–5749
19. Das S, Chakraborty S (2007) Transverse electrodes for improved DNA hybridization in micro-channels. *AIChE J* 53:1086–1099

Label-Free Optical Ring Resonator Bio/Chemical Sensors

Hongying Zhu, Jonathan D. Suter, and Xudong Fan

Abstract Optical micro-ring resonator sensors are an emerging category of label-free optical sensors for bio/chemical sensing that have recently been under intensive investigation. Researchers of this technology have been motivated by a tremendous breadth of different applications, including medical diagnosis, environmental monitoring, homeland security, and food quality control, which require sensitive analytical tools. Ring resonator sensors use total internal reflection to support circulating optical resonances called whispering gallery modes (WGMs). The WGMs have an evanescent field of several hundred nanometers into the surrounding medium, and can therefore detect the refractive index change induced when the analyte binds to the resonator surface. Despite the small physical size of a resonator, the circulating nature of the WGM creates extremely long effective lengths, greatly increasing light-matter interaction and improving its sensing performance. Moreover, only small sample volume is needed for detection because the sensors can be fabricated in sizes well below 100 μm . The small footprint allows integration of those ring resonator sensors onto lab-on-a-chip types of devices for multiplexed detection.

This chapter gives an introduction to the ring resonator sensing principles. Different ring resonator configurations are illustrated as well, including microspheres, microfabricated planar ring resonators, and capillary-based opto-fluidic ring resonators. Their sensing performances are evaluated and compared quantitatively. Finally, the future development for ring resonator sensors is discussed.

Keywords Ring resonator · Microsphere ring resonator · Planar ring resonator · Opto-fluidic ring resonator · Whispering gallery modes · Applied optics ·

X. Fan (✉)

Department of Biomedical Engineering, University of Michigan, 1101 Beal Ave., Ann Arbor, MI, USA

e-mail: xsfan@umich.edu

Biophotonics · Optical biosensor · Optical chemical sensor · Label free · Refractive index · Sensing principles · Protein · DNA · Virus · Bacterium

Contents

1	Introduction	261
2	Optical Ring Resonator Sensor Principles	262
3	Ring Resonator Configurations	265
3.1	Microsphere Ring Resonator	265
3.2	Planar Ring Resonator	265
3.3	Opto-Fluidic Ring Resonator	266
3.4	Ring Resonator Performance Comparison	267
4	Optical Ring-Resonant Bio/Chemical Sensing Applications	267
4.1	Ring Resonator Chemical Sensor	267
4.2	Ring Resonator Biosensor	269
5	Concluding Remarks	275
	References	275

Abbreviations

BRIS	Bulk refractive index sensitivity
BSA	Bovine serum albumin
DNA	Deoxyribonucleic acid
OFRR	Opto-fluidic ring resonator
RI	Refractive index
RIU	Refractive index units
RNA	Ribonucleic acid
WGM	Whispering gallery mode

Symbols

L_{eff}	Effective light–matter interaction length
m	Integer for angular momentum
n_{buffer}	Buffer solution refractive index
n_{eff}	Effective refractive index
n_{OFRR}	OFRR refractive index
n_{sphere}	Microsphere refractive index
Q	Quality factor ring resonator radius
S	Bulk refractive index sensitivity (BRIS)
α_{ex}	Excess polarizability
$\delta\lambda$	WGM resonant wavelength shift
ε_0	Vacuum permittivity
λ	WGM resonant wavelength
σ	Biomolecule surface density

1 Introduction

Optical bio/chemical sensors, which provide detection and quantification of bio/chemical analyte, have emerged as a field of great interest because of the tremendous needs in medical diagnosis, pharmaceuticals, homeland security, food quality control, and environmental testing. Similar to other types of bio/chemical sensors, such as those based on acoustic [1] or electrochemical methods [2], an optical bio/chemical sensor uses an optical transducer that can convert a biorecognition event into a quantitatively measurable signal [3]. There are two basic detection methods in optical bio/chemical sensors: fluorescence-based detection and label-free detection. In fluorescence-based detection, a biorecognition element carrying a fluorescent tag is usually utilized to identify the presence of the target molecules. The abundance of the target molecules is directly related to the intensity of the fluorescent signal. While fluorescence-based detection is highly sensitive, enabling a detection limit down to a single molecule [4], and is the driving force for the single-molecule studies in molecular and cell biology, it suffers some drawbacks. Fluorescent detection techniques require additional labeling steps beyond the isolation of the target analyte, which implies additional time, complexity, and reagent costs. Furthermore, quantitative fluorescence detection requires relatively expensive photonics equipment. Moreover, fluorescent tags may alter host molecules' natural properties and disrupt the accurate measurement of their kinetic constants. In contrast, in label-free detection, target molecules are detected in their natural forms without any modifications, thus enabling easier and cheaper bio/chemical detection. As a result, label-free detection with comparable sensitivities to fluorescent measurement is highly desirable in the development of state-of-the-art bio/chemical sensors.

Most label-free optical bio/chemical sensors belong to the category of evanescent-wave sensors [5], in which the evanescent field exponentially decays into the surrounding medium for tens to few hundred of nanometers away from the solid sensor surface. These sensors usually utilize the RI change induced by the molecular interaction with the evanescent field as the sensing mechanism. RI change is related to the sample concentration rather than the total sample mass. Therefore, in principle, an RI-based sensor can perform sensitive detection with small sample volumes.

For optical label-free biosensors, light–matter interaction plays a significant role in determining their respective sensitivities and, hence, detection limits. However, with current waveguide-based or optical fiber-based sensors [6–9], the light–matter interaction is mainly limited by the sensor's physical size. To achieve adequate sensitivity, a long sensor physical length is required, which significantly increases the overall sensor footprint and sample consumption, and reduces the sensor multiplexed capability [10].

The optical ring resonator, as a class of evanescent label-free sensors, has been extensively explored in recent years [5] and has shown advantages over other evanescent label-free sensors. The resonant nature of light in a ring resonator

greatly enhances the interaction length between the light and the molecules adsorbed on the ring resonator surface, despite the resonator's small physical size. Thus, ring resonators can provide sensitive label-free detection with an RI detection limit on the order of 10^{-7} RIU [11, 12] and mass detection limit of 1 pg/mm^2 [13–15], comparable to or even better than other types of label-free optical sensors. Moreover, small footprint of the ring resonators allows for integration of them onto a small chip for multiplexed detection.

In this chapter, we introduce the fundamentals of ring resonator sensors and provide an overview of this novel technology. Various ring resonator configurations are discussed and their sensing performances are compared. The applications of ring resonators in detection of chemical and biological molecules are also described.

2 Optical Ring Resonator Sensor Principles

Optical ring resonators have a variety of configurations, including planar ring resonators [12, 16–30], microtoroids [31–33], microspheres [11, 13, 15, 34–48] microknots or loops [49–52], and capillary-based opto-fluidic ring resonators (OFRRs) [10, 14, 53–61], all shown in Fig. 1. In an optical ring resonator, light propagates along the curved surface of the ring resonator via total internal reflection, forming a circulating light mode, which may be called either a WGM or a circulating waveguide mode. For simplicity, the term “WGM” is used to describe both WGMs and circulating waveguide modes in general. The ring resonator sensor is different from the waveguide sensor, where transmitted light only gets one pass

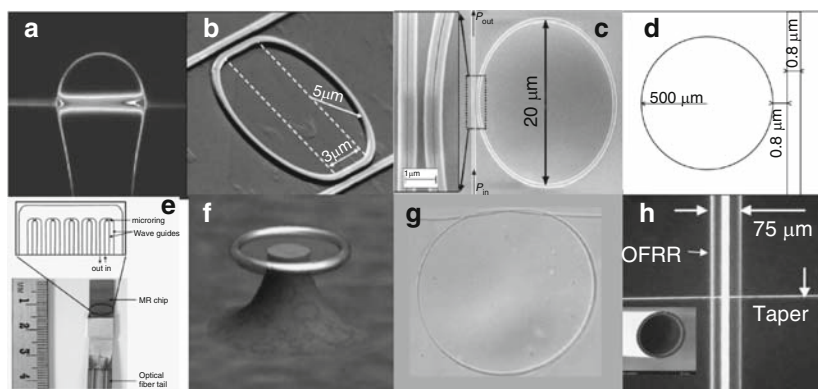


Fig. 1 Various ring resonator sensor configurations. (a) Microsphere. (b) Silicon-on-insulator planar ring resonator. (c) Slot waveguide ring resonator. (d) Planar disc ring resonator. (e) Glass planar ring array. (f) Microtoroid. (g) Microknot. (h) Opto-fluidic ring resonator (OFRR) and the inset is the SEM image of the OFRR cross-section. Reprinted with permissions from refs [13, 28, 30, 32, 50, 53, 70, 86]

through the sensing area. In a ring resonator, the effective light–matter interaction length is no longer limited by the sensor’s physical size, but is rather determined by the ring resonator’s quality factor (Q -factor) [62, 63], which is a parameter related to the number of round trips of the light supported by the ring resonator. The effective interaction length is described as:

$$L_{\text{eff}} = \frac{Q\lambda}{2\pi n}, \quad (1)$$

where λ is the resonant wavelength and n is the RI of the ring resonator. Typical Q -factors for ring resonators range from 10^4 to 10^9 [11, 13, 24, 32, 34, 63, 64], which can result in an effective interaction length from a couple of centimeters to hundreds of centimeters. Therefore, ring resonators can deliver similar sensitivity to waveguide sensors with much smaller sensor dimensions (tens to hundreds of micrometers in diameter) and less sample consumption.

In a ring resonator sensor, the WGM resonant wavelength, λ , must satisfy the following resonant condition [62]:

$$\lambda = \frac{2\pi r n_{\text{eff}}}{m}, \quad (2)$$

where r is the ring outer radius, n_{eff} is the effective RI experienced by the WGM, and m is an integer that describes the WGM angular momentum. The WGM in the ring resonator can be excited through free-space coupling [48, 65] or by using a prism [66, 67], fiber prism [38, 45], tapered optical fiber [13, 31, 32, 34, 53], or planar waveguide [10, 20, 30, 54, 68], as shown in Fig. 2. When the input wavelength matches the WGM resonant condition as in (2), the light evanescently couples into the ring resonator through one of the methods mentioned above and causes the transmission power to drop, leaving a spectral dip on detector # 1, as

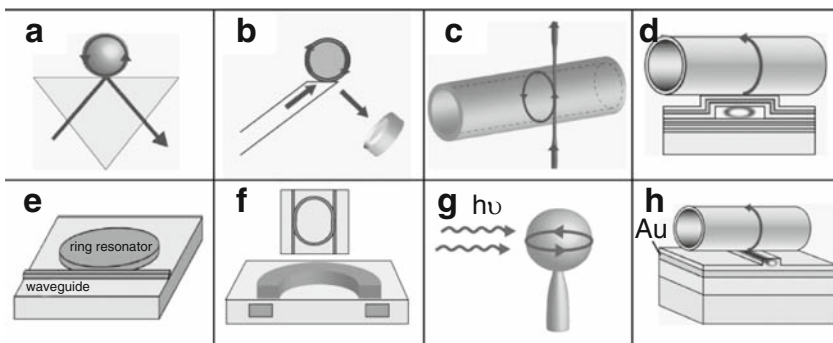


Fig. 2 (a) Prism coupling. (b) Fiber prism coupling. (c) Tapered optical fiber coupling. (d) Anti-resonant reflecting optical waveguide (ARROW) coupling. (e) Planar waveguide side coupling. (f) Planar waveguide vertical coupling. (g) Free space coupling. (h) Gold-cladded waveguide coupling is reprinted with permission from [16]

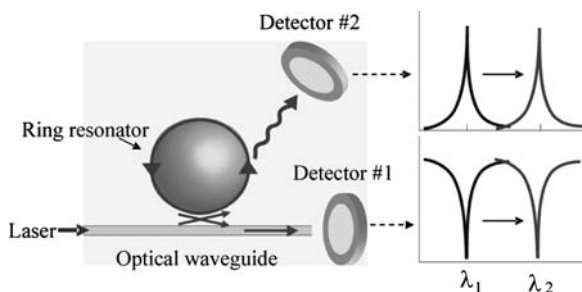


Fig. 3 An optical ring resonant with WGM circulating along the curved surface and its evanescent field interacts with the analytes near the sensing surface. WGM spectral position can be either detected in the form of transmission using detector #1 or scattering using detector #1. WGMs undergo spectral shifts from λ_1 to λ_2 when the analytes bind to the sensing surface

shown in Fig. 3. Meanwhile, the resonant light coupled into the ring resonator is scattered off the ring resonator surface and can be detected as a spectral peak with detector #2 placed above the ring resonator. Both dip and peak can be used to indicate the WGM spectral position.

Ring resonator sensors perform label-free bio/chemical sensing by detecting RI changes on or close to the ring resonator surface. When molecules bind to the ring resonator surface, the effective RI on the ring resonator surface changes, resulting in a shift in the WGM spectral position, as illustrated in Fig. 3. By monitoring the WGM spectral shift versus time, it is possible to obtain the real-time quantitative and kinetic information for the molecular interaction on the ring resonator surface. Alternatively, the WGM spectral position shift can also be detected as the change in light transmission intensity at a fixed laser wavelength [12].

The surface density of the molecules on the ring resonator surface is directly related to the WGM spectral shift. In microsphere ring resonators, this relation is obtained by employing the first-order perturbation theory [35, 36]:

$$\frac{\delta\lambda}{\lambda} = \frac{\alpha_{\text{ex}}\sigma}{\varepsilon_0(n_{\text{sphere}}^2 - n_{\text{buffer}}^2)r}, \quad (3)$$

where λ and $\delta\lambda$ are the WGM resonant wavelength and the wavelength shift, respectively. ε_0 is the vacuum permittivity, r is the sphere radius, and n_{sphere} and n_{buffer} are the RI for the sphere and buffer solutions. α_{ex} is excess polarizability for molecules in water and σ is the molecule surface density. Recently, another simple relationship has been established between bulk RI sensitivity (BRIS), S , and molecule surface density, σ , for OFRRs shown in (4) [14]:

$$\frac{\delta\lambda}{\lambda} = \sigma \alpha_{\text{ex}} \frac{2\pi\sqrt{n_{\text{OFRR}}^2 - n_{\text{buffer}}^2}}{\varepsilon_0\lambda^2} \frac{n_{\text{OFRR}}}{n_{\text{buffer}}^2} S, \quad (4)$$

where n_{OFRR} and n_{buffer} are the RI for the OFRR wall and buffer solution in the capillary core, respectively. Using either (3) or (4), it is possible to predict the ring resonator sensing performance or quantitatively analyze biomolecule surface density from a measured WGM spectral shift.

3 Ring Resonator Configurations

3.1 *Microsphere Ring Resonator*

Dielectric microspheres are three-dimensional ring resonators (Fig. 1a). They are fabricated simply by melting the stripped end of an optical fiber with the heat generated by an acetylene/hydrogen–oxygen torch [34] or a CO₂ laser [11]. Typically, the size of the microsphere is between a few tens to a few hundreds of microns in diameter. Fused silica microspheres have very high Q -factors ranging from 10^6 to 10^9 due to their geometry and extremely low surface roughness [63]. Such high Q -factors enable the characteristic low detection limit. Theoretical analysis predicts that microsphere ring resonator is able to achieve a detection limit of 10^{-8} to 10^{-9} RIU [35, 36], and it is estimated that a single molecule may be able to cause a detectable perturbation in such a high Q -resonant cavity [35]. The microsphere has been applied for detection of a wide range of target molecules, including mercury ions [37], proteins [34, 35, 38, 45], DNA [13, 48], viruses [15], and bacterial cells [69].

3.2 *Planar Ring Resonator*

Planar ring resonators are typically very small waveguides that are fabricated using various microfabrication techniques onto a solid substrate like silicon or silicon nitride. The waveguides are built to guide light in a circular path that may have a radius anywhere between 10 μm and several millimeters [20]. A bus waveguide is typically used to couple optical power into the resonator, which can be manufactured simultaneously on the same chip. Due to the advanced nature of microfabrication technologies today, planar ring resonators are now easy to manufacture to exact specifications. These resonators therefore have some practical advantages over other types. Moreover, due to their small foot-print, they can be fabricated onto a small chip, as shown in Fig. 1e.

Planar ring resonators themselves are available in several distinct geometries. Ring shapes, discs, and slot waveguides have all been actively researched and are illustrated in Fig. 1. While planar ring resonators can easily be fabricated as solid discs (Fig. 1d), the ring configuration (Fig. 1b) reduces the overall mode volume. It is difficult to manufacture planar ring resonators with surfaces that rival the optical

quality of a microsphere or capillary, and therefore the Q -factors tend to be significantly lower, around 10^4 in water [21, 22].

The slot waveguide [25, 29, 70] (Fig. 1c) is a unique configuration that increases the exposure of guided light to the surrounding environment. When the width of the slot is kept small, below the decay length of the evanescent field, close to half of the total guided optical power may be confined to the slot region [70].

A variation to the planar-waveguide-based ring resonator is the microtoroid, which has been developed and characterized extensively recently. Microtoroids have shown promise for sensitive detection of bio/chemical molecules because they are able to achieve very high Q -factors, above 10^8 while maintaining very small mode volume [31–33]. The WGMs are usually excited using a well positioned fiber taper. As illustrated in Fig. 1f, the microtoroids are elevated above their solid substrate by a silica post. The toroids are manufactured using photolithography and RIE techniques, resulting in discs on top of a pillar structure. The edges are then illuminated with a powerful CO_2 laser in order to allow the material to reflow. Experiments have demonstrated fabrication of many microtoroids onto a chip [71, 72]. Further design improvements have made it possible to create arrays of microtoroids which are easily detachable from their stems so that they can be individually positioned within complicated photonic devices [73].

3.3 *Opto-Fluidic Ring Resonator*

In the previous sections, we have already introduced microsphere and various planar ring resonators. Planar ring resonators can be mass-produced using standard fabrication technologies and are compatible with optoelectronic integration. However, their low Q -factors and need for separate microfluidics fabrication hinder their practical applications. In contrast, microsphere ring resonators have extremely high Q -factors which may reach 10^9 [63] and can be fabricated easily. However, it is difficult to mass produce microspheres with reproducible specifications. Additionally, they lack robustness and fluid integration capability. To overcome those problems, the opto-fluidics ring resonator (OFRR), a novel type of ring resonator platform, is designed [53]. The architecture of the OFRR is illustrated in Fig. 1h. It employs a piece of fused silica capillary with a few tens to a few hundreds of micrometers in outer diameter. The circular cross section of the capillary forms ring resonators that support the WGMs. The capillary wall is sufficiently thin ($<4 \mu\text{m}$) so that WGMs with high Q -factors are exposed to the core and interact with sample flowing through the capillary. The OFRR architecture combines the dual functionalities of the capillary as a sensor and as a fluidic channel in a way that is unparalleled among ring resonators. Therefore, it preserves the merits of other ring resonators, including high Q -factors, excellent sensitivity, and small sample consumption volume, while exhibiting the excellent fluid-handling capability

inherent to capillaries [74]. The OFRR can be fabricated cost-effectively using a capillary pulling station [58] or a fiber draw tower [56], and can be used in conjunction with any kind of coupling device as shown in Fig. 2.

3.4 Ring Resonator Performance Comparison

There are two primary parameters used to characterize ring resonator sensing performance: sensitivity and detection limit. Sensitivity is a measure of the magnitude of WGM shift in response to a given RI change. The detection limit presents the smallest RI change that can be accurately measured by the ring resonator sensor, which is dependent on sensor's spectral resolution [75]. So far, the experimentally demonstrated values for RI limits of detection are still a few orders of magnitude higher than the theoretical maximum of 10^{-9} RIU mentioned before [36]. Planar ring resonators have high RI sensitivity ranging from 70 to 400 nm/RIU [24, 26, 27]. However, those ring resonators suffer from low Q -factors (around 10^4) due to the surface roughness. Low Q -factors lead to detection limits on the order of 10^{-5} RIU [24, 26, 27]. Although microsphere ring resonators have a lower sensitivity (20–50 nm/RIU) [11], they have a better detection limit (10^{-6} – 10^{-7} RIU), resulting from significantly improved spectral resolution due to their high Q -factors ($>10^6$) [11, 13, 34]. Capillary-based OFRR sensors can be produced with a bulk RI sensitivity of approximately 40 nm/RIU or higher [76], Q -factors larger than 10^6 , and a detection limit on the order of 10^{-7} RIU [64]. This compares quite closely with the performance of microspheres [11, 13, 34, 35].

4 Optical Ring-Resonant Bio/Chemical Sensing Applications

Optical ring resonator sensors can be used to detect the RI of the ring resonator surrounding medium or the presence of the bio/chemical molecules on the ring resonator surface. This section will focus on presenting examples of applications of optical ring resonator bio/chemical sensors for detection of chemical contaminants and a wide range of biomolecules.

4.1 Ring Resonator Chemical Sensor

The detection of chemical contaminants is very important to environmental protection and homeland security. Since the relevant chemicals tend to be very small molecules (molecular weight $<1,000$ Da), ultrasensitive analytical tools are needed to detect them at low concentrations, down to ng/mL or even pg/mL. Optical ring

resonators with excellent sensitivity have great potential for chemical sensing and have been used for the detection of heavy-metal ions [37], chemical vapors [20, 77–80], and pesticides [59] using direct assay method with low detection limits.

4.1.1 Heavy-Metal Detection

Although ring resonator sensors are generally very sensitive, and until now, only the microsphere ring resonator has been used for heavy metal ions detection. In this study, a fused silica microsphere with a diameter of 125 μm and Q -factor of 2.5×10^5 is employed for mercuric ion (Hg (II)) detection [37]. The microsphere surface is first functionalized with thiol groups, which have a high affinity for mercuric ions. A water sample containing Hg (II) is introduced into the sensor's fluid cell. The WGM undergoes a spectral shift when the Hg (II) binds to the thiol groups. The experimental results show that the microsphere ring resonator is capable of detecting Hg (II) 50 ppb (w/w) within a few minutes. This capability offers researchers a sensitive technique to potentially detect other heavy metals at useful concentrations to provide information for environmental monitoring.

4.1.2 Chemical Vapor Detection

Chemical vapor sensor is an important tool in applications, such as environmental monitoring, breath diagnosis, and food freshness analysis. Optical ring resonators are capable of detecting chemical vapors by measuring the RI change that occurs when gas molecules are absorbed into polymers coated on the sensor surface. RI changes may result from polymer swelling/shrinkage or from doping effects when the vapor molecules are embedded in the polymer matrix.

Recently, several studies have been carried out to explore the potential of ring resonator sensors for chemical vapor detection [20, 77–80]. In one of those studies, an OFRR sensor is used for ethanol and hexane detection. Figure 4a, b shows the response of the OFRR whose interior surface is coated with the moderately polar polymer methyl phenol polysiloxane or with the highly polar polymer polyethylene glycol (PEG) 400 to various concentrations of ethanol and hexane vapor. The insets of Fig. 4 show the real-time WGM response to those chemical vapors. The target vapors cause the WGM spectral to experience a red-shift, which reaches equilibrium within 10 s. After the detection, the gas flow through the OFRR is switched to H_2 and the WGM shifted back to its initial spectral baseline, indicating complete removal of vapor molecules from the polymer layer. Based on those results, it is clear that the OFRR can perform very rapid and efficient chemical vapor detection with a detection limit of 200 ppm. The detection limits for chemical vapor detection using ring resonators are summarized in Table 1. Experimental details can be found in the included references.

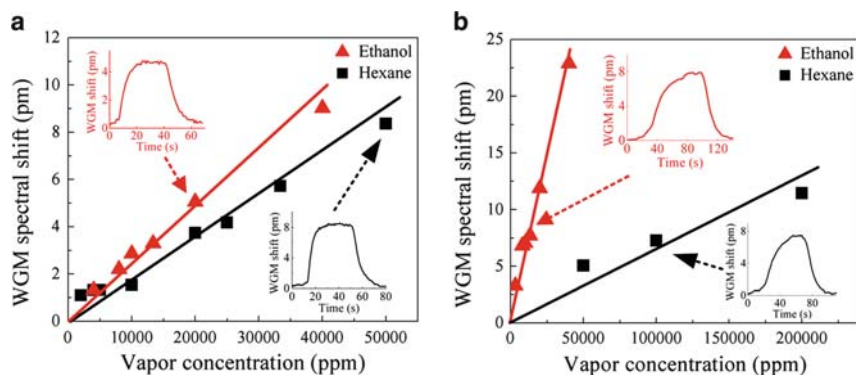


Fig. 4 OFRR response to various concentrations of ethanol (triangles) and hexane (squares) vapors. The OFRR is coated with a 200-nm-thick OV-17 (a) and PEG-400 (b). Insets are the sensorgrams taken by monitoring the WGM shift in real time. Reprinted with permission from ref. [80]

Table 1 Chemical vapor detection performance

Analyte	Sensing platform	Detection limit	Reference
Isopropanol	Planar ring resonator	50 ppm	[20]
Alcohols	Planar ring resonator	31 ppm	[77]
Ammonia	Planar ring resonator	4‰	[78]
Ethanol	OFRR	200 ppm	[80]

4.1.3 Pesticide Detection

Detection of organosporous (OP) pesticides, which contribute significantly to overall cancer mortality, has been performed with the OFRR very recently [59]. In this work, parathion-methyl is chosen as the model system for demonstration of pesticide detection. Direct assay format is used, in which an AChE enzyme acting as the receptor is immobilized on the OFRR sensing surface. A detection limit of 3.8×10^{-11} M is achieved with an analysis time of about 0.5 min, which is sufficient to detect these pesticides on the level of their admissible concentrations in environmental as well as food matrices. The sensor surface is regenerated using 10 mM HEPES–NaOH pH 7.4 without loss of enzyme activity and reused for several analyses, with good reproducibility (RS = 3.5%, $n = 5$). The ring resonator sensor offers good opportunities for direct, rapid, highly sensitive, and inexpensive detection of harmful contaminants in the field.

4.2 Ring Resonator Biosensor

Ring resonant sensors with different configurations have been demonstrated for label-free detection of a broad range of biomolecules. Discussed in this section are

the results from proteins [12, 14, 21, 24, 27, 30, 33–35, 37, 47, 54, 60, 68], DNA [13, 48, 76], viruses [15, 61], and bacterial cells [30, 69].

4.2.1 Biomolecule Receptors and Their Immobilization

For the purpose of specific sensing, a layer of molecular receptors that are capable of binding target molecules with high affinity have to be immobilized on the sensing surface first. Several different types of receptors have been used in ring resonator sensors, including antibodies [15, 61], aptamers [45], nucleic acids [13, 48, 76], and peptide displayed bacteriophages [60]. Antibodies are the most widely used receptors in biosensor applications. They have high specificity, high affinity, and are commercially available. However, antibodies need to be produced through immune responses in animals. Therefore, it is difficult to get the homogeneous qualities without batch-to-batch variation. Furthermore, antibodies are easily denatured, making it hard to regenerate the receptor layer and also limit its application in real environmental sensors [81]. On a practical note, antibodies are also very expensive and may not be affordable in some applications.

Aptamers and peptide-displayed bacteriophages are two good alternatives to antibodies as receptors. Aptamers are artificial synthetic short-stranded DNA or RNA molecules that can fold into well-defined three dimensional structures capable of binding the target molecules [81]. Peptide-bearing bacteriophages are affinity-selected from large phage libraries displaying billions of random peptides and can bind a wide range of target biomolecules [82]. Both aptamers and bacteriophages have distinct advantages over antibodies. They can be produced cheaply, and can be selected *in vitro* to bind any target molecules. Moreover, they have high affinity and specificity to the target molecules. They are also very robust and can withstand harsh environmental condition. As a result, they have drawn increasing attention from biosensor researchers in recent years.

The methods for receptor immobilization on the sensing surface are also very important to sensing performance. Proper immobilization methods are required to maintain the stability and activity of the surface bound receptors. Direct physical adsorption and covalent binding are the two most commonly used methods. Direct physical adsorption is very easy to perform. However, the receptors adsorb on the sensing surface with random orientations and have the potential to lose biological activities. In contrast, covalent binding can provide robust attachment of receptors to the sensing surface with relatively high surface density and controllable receptor orientation. The sensing surface first needs to be activated using silane, followed by covalent linkage of the receptors using either homobiofunctional or heterobiofunctional cross-linkers. To better control the receptors immobilization orientation, especially antibody orientation, commonly antibody-binding proteins, such as protein A and protein G that target the antibody Fc region can be first covalently immobilized on the sensing surface [83]. After immobilization of the receptors, the sensing surface needs to be further treated with a blocking agent, such as bovine serum albumin (BSA), to prevent or minimize nonspecific adsorption. This is

especially important for detecting the target molecules in a complex matrix. Detecting biomarkers in a serum sample would be a good example for this.

4.2.2 Protein Detection

Biotin and (strept)avidin exhibit famously high binding affinity ($K_d = 10^{-15}$ M) [84] and have been chosen as the model system to perform protein detection on chip-based planar ring resonator made with different materials [12, 27, 68]. Fused silica microspheres also have been used to detect streptavidin [34]. Meanwhile, trypsin detection for protease studies [37] and thrombin detection using aptamer as receptor [45] are also carried out with a microsphere ring resonator. Furthermore, as the microsphere ring resonator supports both TE and TM modes, they can be used to study the biomolecular orientation on the microsphere surface [47]. Protein detection is also accomplished with the capillary-based OFRR. The detection limit for BSA is approximately 3 pM [14], corresponding to a surface density of 0.5 $\mu\text{g}/\text{mm}^2$ and a total mass of a few femto-grams, comparable to the commercialized SPR sensor. Recently, the OFRR has demonstrated detection of streptavidin using peptide-displayed bacteriophages as a receptor with a detection limit of 100 pM and the sensing surface is successfully regenerated by using a cocktail regeneration buffer [60, 85] without losing receptor functionality.

A typical sensorgram for protein detection using a ring resonator is shown in Fig. 5. The sensing surface is first immobilized with receptor peptide-displayed

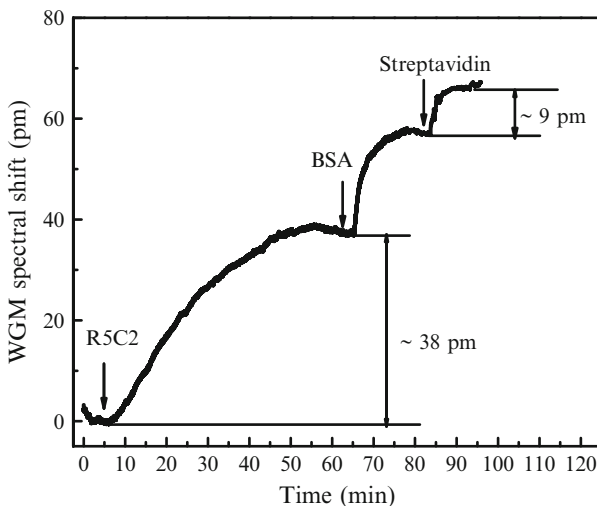


Fig. 5 Sensorgram for streptavidin detection using the OFRR. The interior surface of the OFRR is first immobilized with probe bacteriophage R5C2, and then the unoccupied sites are blocked with BSA. Finally, the sensing surface is exposed to streptavidin. Reprinted with permission from ref. [60]

Table 2 Proteins detected by ring resonator sensor platforms

Analyte	Sensing platform	Detection limit	Reference
Avidin	Si _x N _y /SiO ₂ planar ring resonator	0.1 nM	[68]
Avidin	Silicon-on-insulator planar ring resonator	10 ng/ml	[27]
Streptavidin	Polymer ring resonator	250 pg/mm ²	[21]
Trypsin	Microsphere ring resonator	10 ⁻⁴ unit/ml	[38]
Thrombin	Microsphere ring resonator	1 NIH unit/ml	[45]
BSA	OFRR	3 pM	[14]
Streptavidin	OFRR	100 pM	[60]

bacteriophages and then blocked with BSA at a concentration of 1 mg/mL to reduce the nonspecific adsorption. Upon injection of the streptavidin, it bound to the bacteriophages, causing the WGM spectral position to shift 9 pM. Table 2 lists proteins that have been detected with different ring resonator sensor configurations and the corresponding detection limit.

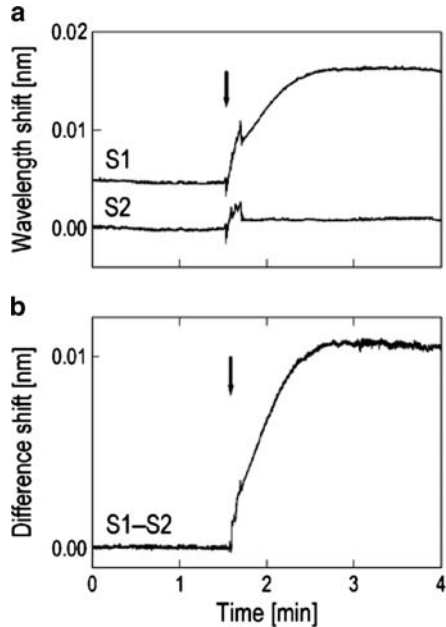
4.2.3 DNA Detection

DNA is almost universally detected using a hybridization assay where the DNA probes that are complementary to the target DNA are immobilized chemically onto the sensor surface. DNA detection with microspheres has been investigated in recent years by Vollmer et al., [13]. By developing a sophisticated model to estimate surface coverage, they measured 3.6×10^{13} hybridized 27-base nucleotides on a single sphere with a diameter of 200 μm . The estimated detection limit for this sensor is 6 pg/mm². The authors are also able to demonstrate DNA detection with two microspheres coupled to a single optical fiber for multiplexed detection. Data from this work are shown in Fig. 6. Figure 6a includes hybridization curves for 1 μM 11-base target and from 1-base mismatched target strands. Figure 6b demonstrates signal noise reduction from subtraction of the mismatched curve from the complementary one. Such excellent single base mismatch detection capability is important in biological research and disease diagnosis.

Another microsphere-based DNA detection strategy involves the use of 7.5 μm diameter silica microspheres with rhodamine fluorophores and probe DNA strands immobilized onto the surface [48]. Light emitted from the fluorophore coupled into WGMs in the microspheres at resonant wavelengths and is evanescently collected into an optical fiber and directed to a photodetector. Although this technique utilizes dye molecules, the target DNA is still unlabeled, so it still may be referred to as a “label-free” biosensor. These very small spheres are only able to achieve Q -factors close to 500 and their RI sensitivities are not characterized. The available data plots signal response for different target strand lengths, but do not attempt to predict limits of detection.

Cylindrical OFRRs have also been used for DNA detection [76]. A recent study demonstrated the ability to detect as little as 10 pM bulk concentration of 25-base

Fig. 6 DNA detection. 1 μM 11-mer target hybridized onto microsphere resonator. Complementary and single base mismatched target are differentiated (a) and the signal difference is used to remove noise from sample introduction (b). Reprinted with permission from ref. [13]



target oligonucleotides. The probe oligonucleotide is 25 bases in length and is attached to the silanized interior surface of the capillary via a covalent cross-linker called dimethyl adipimidate (DMP). The limit of detection for this system is estimated at 4 pg/mm^2 surface loading, corresponding to roughly 2.7×10^{10} oligonucleotides/ cm^2 .

Using planar waveguides made out of Hydrex glass, one study demonstrated detection of 500 nM bulk concentration of 24-base target oligonucleotides [30]. The surface of the resonator in this case is treated with an epoxysilane compound that reacted with amine-modified probe nucleotides. However, this particular study includes no characterization of limits of detection.

4.2.4 Bacteria and Virus Detection

Bacterial detection has been demonstrated using planar waveguides in a few limited examples. In one case, *E. coli* is detected using a resonator coated with monoclonal antibodies [30]. The study begin by detecting 10^9 CFU/mL and then lower the concentration in subsequent experiments until it reached 10^5 CFU/mL, which is determined to be the limit of detection. Data from this work are shown in Fig. 7. These data show how a reference channel may be used to subtract bulk RI effects.

With microspheres, *E. coli* adsorption is detected and modeled by Ren et al. [69]. Spheres are treated with poly-L-lysine, creating an ionic attraction for bacterial cells. Using a silica microsphere with a Q -factor of 4.3×10^5 , they estimated that the limit of detection for this bacterium is around 1.2×10^2 CFU/ mm^2 . Assuming a

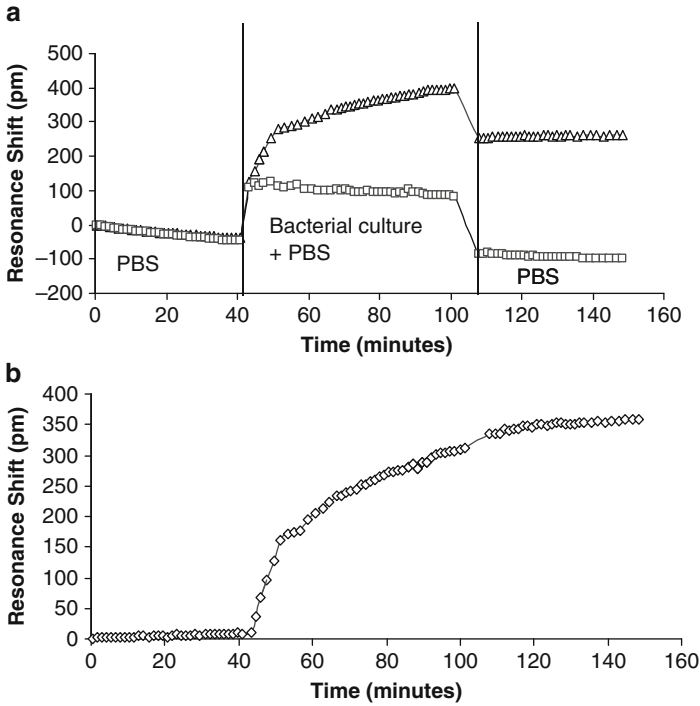


Fig. 7 (A) *E. coli* bacterial detection using planar ring resonators (a), with control channel (b). (B) Subtraction of control signal yields cleaner binding curve. Reprinted with permission from ref. [30]

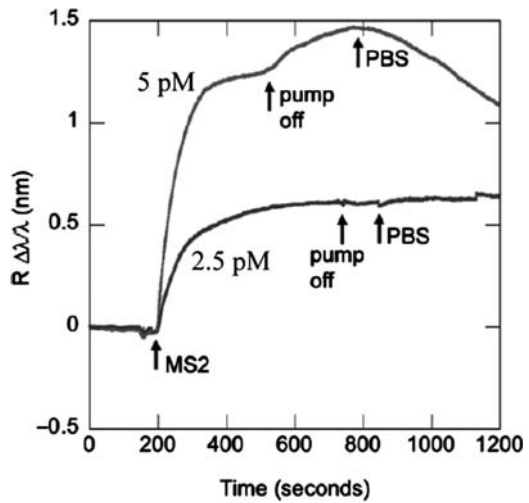


Fig. 8 MS2 viral detection with microsphere at bulk concentrations of 5 pM (top curve) and 2.5 pM (bottom curve). Reprinted with permission from ref. [69]

sphere surface area of 0.36 mm^2 , this quantity corresponds to the detection of 44 total bacterial cells. Although this method is very nonspecific, it is useful for characterizing the sensor's performance. Specific detection of viral particles (MS-2) of a few pM with microspheres has also been demonstrated, using covalently immobilized antibodies [15]. The data for these two concentration levels are shown in Fig. 8.

Limits of detection, using the OFRR for viral particle detection, of 2.3×10^3 pfu/mL have been demonstrated with the M13 virus using antibodies bound to the inside of the capillary with protein A [61]. The circular nature of the capillary enables efficient capture and rapid detection of viruses. The results show that most M13 virus capture occurs within 5 min. Meanwhile, given the small volume of fluid inside the $\sim 100 \text{ }\mu\text{m}$ OD capillary, this may correspond to a signal from only a few virus particles in total.

5 Concluding Remarks

In this chapter, we have given an overview of the optical ring resonator sensors and their applications for bio/chemical sensing. Optical ring resonator sensors possess many excellent characteristics that put them in the forefront of label-free bio/chemical sensor technologies, including excellent detection limit, real-time detection, small size, small sample consumption, and relatively low fabrication cost. However, ring resonator sensor platforms are not mature yet. The future research will be focused to improve the ring resonator optical structures and their microfluidics design, enabling integration of those ring resonator sensors onto a small chip as a portable device without sacrificing their sensing performance. Meanwhile, surface chemistries for biomolecule immobilization can be refined and novel biorecognition elements can be used to enhance the sensing performance. Biocompatible materials that can reduce nonspecific bindings should be employed to detect target molecules in complex medium. Moreover, multianalyte sensing with sensor array is another future trend for ring resonator sensors. Various imprint technologies will be of value to pattern biorecognition elements onto the array. Sensor reusability also needs to be explored to reduce the detection cost.

References

1. Olsen EV, Sorokulova IB, Petrenko VA et al (2006) Affinity-selected filamentous bacteriophage as a probe for acoustic wave biodetectors of *Salmonella typhimurium*. Biosens Bioelectron 21:1434–1442
2. Jena BK, Raj CR (2006) Electrochemical biosensor based on integrated assembly of dehydrogenase enzymes and gold nanoparticles. Anal Chem 78:6332–6339
3. McDonagh C, Burke CS, MacCraith BD (2008) Optical chemical sensors. Chem Rev 108:400–422
4. Moerner WE (2007) Single-molecule chemistry and biology special feature: new directions in single-molecule imaging and analysis. Proc Natl Acad Sci USA 104:12596–12602

5. Fan X, White IM, Shopova SI et al (2008) Sensitive optical biosensors for unlabeled targets: a review. *Anal Chim Acta* 620:8–26
6. Heideman RG, Lambeck PV (1999) Remote opto-chemical sensing with extreme sensitivity: design, fabrication and performance of a pigtailed integrated optical phase-modulated Mach–Zehnder interferometer system. *Sensors Actuators B Chem* 61:100–127
7. Ymeti A, Kanger JS, Greve J et al (2003) Realization of a multichannel integrated Young interferometer chemical sensor. *Appl Opt* 42:5649–5660
8. Tazawa H, Kanie T, Katayama M (2007) Fiber-optic coupler based refractive index sensor and its applications to biosensing. *Appl Phys Lett* 91:113901
9. Ymeti A, Greve J, Lambeck PV et al (2007) Fast, ultrasensitive virus detection using a Young interferometer sensor. *Nano Lett* 7:394–397
10. White IM, Suter JD, Oveys H et al (2007) Universal coupling between metal-clad waveguides and optical ring resonators. *Opt Express* 15:646–651
11. Hanumegowda NM, Stica CJ, Patel BC et al (2005) Refractometric sensors based on microsphere resonators. *Appl Phys Lett* 87:201107
12. Chao C-Y, Guo LJ (2006) Design and optimization of microring resonators in biochemical sensing applications. *J Lightwave Technol* 24:1395–1402
13. Vollmer F, Arnold S, Braun D et al (2003) Multiplexed DNA quantification by spectroscopic shift of two microsphere cavities. *Biophys J* 85:1974–1979
14. Zhu H, White IM, Suter JD et al (2007) Analysis of biomolecule detection with optofluidic ring resonator sensors. *Opt Express* 15:9139–9146
15. Arnold S, Ramjit R, Keng D et al (2008) Microparticle photophysics illuminates viral biosensing. *Faraday Discuss* 137:65–83
16. Blair S, Chen Y (2001) Resonant-enhanced evanescent-wave fluorescence biosensing with cylindrical optical cavities. *Appl Opt* 40:570–582
17. Chao C-Y, Guo LJ (2003) Biochemical sensors based on polymer microrings with sharp asymmetrical resonance. *Appl Phys Lett* 83:1527–1529
18. Krioukov E, Greve J, Otto C (2003) Performance of integrated optical microcavities for refractive index and fluorescence sensing. *Sensors Actuators B Chem* 90:58–67
19. Guo J, Vawter GA, Shaw JM et al (2004) Characterization of $\text{Si}_3\text{N}_4/\text{SiO}_2$ planar lightwave circuits and ring resonators. *Proc SPIE* 5350:13–22
20. Ksendzov A, Homer ML, Manfreda AM (2004) Integrated optics ring-resonator chemical sensor with polymer transduction layer. *Electron Lett* 40:63–65
21. Chao C-Y, Fung W, Guo LJ (2006) Polymer microring resonators for biochemical sensing applications. *IEEE J Sel Top Quantum Electron* 12:134–142
22. Martinez L, Lipson M (2006) High confinement suspended micro-ring resonators in silicon-on-insulator. *Opt Express* 14:6259–6263
23. Xu DX, Janz S, Cheben P (2006) Design of polarization-insensitive ring resonators in silicon-on-insulator using MMI couplers and cladding stress engineering. *IEEE Photon Technol Lett* 18:343–345
24. Yalcin A, Popat KC, Aldridge JC et al (2006) Optical sensing of biomolecules using microring resonators. *IEEE J Sel Top Quantum Electron* 12:148–155
25. Barrios CA, Gylfason KB, Sánchez B et al (2007) Slot-waveguide biochemical sensor. *Opt Lett* 32:3080–3082
26. Dai D, He S (2007) Highly-sensitive sensor with large measurement range realized with two cascaded-microring resonators. *Opt Commun* 279:89–93
27. De Vos KM, Bartolozzi I, Bienstman P et al (2007) Optical biosensor based on silicon-on-insulator microring cavities for specific protein binding detection. *Proc SPIE* 6447:64470K
28. Schweinsberg A, Hoché S, Lepeshkin NN et al (2007) An environmental sensor based on an integrated optical whispering gallery mode disk resonator. *Sensors Actuators B Chem* 123:727–732
29. Barrios CA, Bañuls MJ, González-Pedro V et al (2008) Label-free optical biosensing with slot-waveguides. *Opt Lett* 33:708–710

30. Ramachandran A, Wang S, Clarke J et al (2008) A universal biosensing platform based on optical micro-ring resonators. *Biosens Bioelectron* 23:939–944
31. Armani DK, Kippenberg TJ, Spillane SM et al (2003) Ultra-high-Q toroid microcavity on a chip. *Nature* 421:925–928
32. Armani AM, Vahala KJ (2006) Heavy water detection using ultra-high-Q microcavities. *Opt Lett* 31:1896–1898
33. Armani AM, Kulkarni RP, Fraser SE et al (2007) Label-free, single-molecule detection with optical microcavities. *Science* 317:783–787
34. Vollmer F, Braun D, Libchaber A et al (2002) Protein detection by optical shift of a resonant microcavity. *Appl Phys Lett* 80:4057–4059
35. Arnold S, Khoshshima M, Teraoka I (2003) Shift of whispering-gallery modes in microspheres by protein adsorption. *Opt Lett* 28:272–274
36. Teraoka I, Arnold S, Vollmer F (2003) Perturbation approach to resonance shifts of whispering-gallery modes in a dielectric microsphere as a probe of a surrounding medium. *J Opt Soc Am B* 20:1937–1946
37. Hanumegowda NM, White IM, Fan X (2005) Aqueous mercuric ion detection with microsphere optical ring resonator sensors. *Sensors Actuators B Chem* 120:207–212
38. Hanumegowda NM, White IM, Oveys H et al (2005) Label-free protease sensors based on optical microsphere resonators. *Sens Lett* 3:315–319
39. Noto M, Khoshshima M, Keng D et al (2005) Molecular weight dependence of a whispering gallery mode biosensor. *Appl Phys Lett* 87:223901
40. Noto M, Vollmer F, Keng D et al (2005) Nanolayer characterization through wavelength multiplexing of a microsphere resonator. *Opt Lett* 30:510–512
41. White IM, Hanumegowda NM, Fan X (2005) Subfemtomole detection of small molecules with microsphere sensors. *Opt Lett* 30:3189–3191
42. Gaathon O, Culic-Viskota J, Mihnev M et al (2006) Enhancing sensitivity of a whispering gallery mode biosensor by subwavelength confinement. *Appl Phys Lett* 89:223901
43. Teraoka I, Arnold S (2006) Theory of resonance shifts in TE and TM whispering gallery modes by nonradial perturbations for sensing applications. *J Opt Soc Am B* 23:1381–1389
44. Teraoka I, Arnold S (2006) Enhancing the sensitivity of a whispering-gallery mode microsphere sensor by a high-refractive-index surface layer. *J Opt Soc Am B* 23:1434–1441
45. Zhu H, Suter JD, White IM et al (2006) Aptamer based microsphere biosensor for thrombin detection. *Sensors* 6:785–795
46. Keng D, McAnanama SR, Teraoka I et al (2007) Resonance fluctuations of a whispering gallery mode biosensor by particles undergoing Brownian motion. *Appl Phys Lett* 91:103902
47. Noto M, Keng D, Teraoka I et al (2007) Detection of protein orientation on the silica microsphere surface using transverse electric/transverse magnetic whispering gallery modes. *Biophys J* 92:4466–4472
48. Nuhiji E, Mulvaney P (2007) Detection of unlabeled oligonucleotide targets using whispering gallery modes in single, fluorescent microspheres. *Small* 3:1408–1414
49. Jiang X, Chen Y, Vienne G et al (2007) All-fiber add-drop filters based on microfiber knot resonators. *Opt Lett* 32:1710–1712
50. Vienne G, Li Y, Tong L (2007) Effect of host polymer on microfiber resonator. *IEEE Photon Technol Lett* 19:1386–1388
51. Xu F, Brambilla G (2007) Manufacture of 3-D microfiber coil resonators. *IEEE Photon Technol Lett* 19:1481–1483
52. Xu F, Brambilla G (2008) Demonstration of a refractometric sensor based on optical microfiber coil resonator. *Appl Phys Lett* 92:101126
53. White IM, Oveys H, Fan X (2006) Liquid-core optical ring-resonator sensors. *Opt Lett* 31:1319–1321
54. White IM, Oveys H, Fan X et al (2006) Integrated multiplexed biosensors based on liquid core optical ring resonators and antiresonant reflecting optical waveguides. *Appl Phys Lett* 89:191106

55. Ling T, Guo LJ (2007) A unique resonance mode observed in a prism-coupled micro-tube resonator sensor with superior index sensitivity. *Opt Express* 15:17424–17432
56. Sumetsky M, Windeler RS, Dulashko Y et al (2007) Optical liquid ring resonator sensor. *Opt Express* 15:14376–14381
57. Zamora V, Díez A, Andrés MV et al (2007) Refractometric sensor based on whispering-gallery modes of thin capillarie. *Opt Express* 15:12011–12016
58. Zhu H, White IM, Suter JD et al (2007) Integrated refractive index optical ring resonator detector for capillary electrophoresis. *Anal Chem* 79:930–937
59. Yang G, White IM, Fan X (2008) An opto-fluidic ring resonator biosensor for the detection of organophosphorus pesticides. *Sensors Actuators B Phys* 133:105–112
60. Zhu H, White IM, Suter JD et al (2008) Phage-based label-free biomolecule detection in an opto-fluidic ring resonator. *Biosens Bioelectron* 24:461–466
61. Zhu H, White IM, Suter JD et al (2008) Opto-fluidic micro-ring resonator for sensitive label-free viral detection. *Analyst* 133:356–360
62. Chang RK, Campillo AJ (eds) (1996) *Optical processes in microcavities*. World Scientific, Singapore
63. Gorodetsky ML, Savchenkov AA, Ilchenko VS (1996) Ultimate Q of optical microsphere resonators. *Opt Lett* 21:453–455
64. Fan X, White IM, Zhu H et al (2007) Overview of novel integrated optical ring resonator bio/chemical sensors. *Proc SPIE* 6452:6520M
65. Tzeng HM, Wall KF, Long MB (1984) Laser emission from individual droplets at wavelengths corresponding to morphology-dependent resonances. *Opt Lett* 9:499–501
66. Gorodetsky ML, Ilchenko VS (1999) Optical microsphere resonators: optimal coupling to high-Q whispering-gallery modes. *J Opt Soc Am B* 16:147–154
67. Mazzei A, Götzinger S, Menezes LDS et al (2005) Optimization of prism coupling to high-Q modes in a microsphere resonator using a near-field probe. *Opt Commun* 250:428–433
68. Ksendzov A, Lin Y (2005) Integrated optics ring-resonator sensors for protein detection. *Opt Lett* 30:3344–3346
69. Ren H-C, Vollmer F, Arnold S et al (2007) High-Q microsphere biosensor – analysis for adsorption of rodlike bacteria. *Opt Express* 15:17410–17423
70. Xu Q, Almeida VR, Panepucci RR et al (2004) Experimental demonstration of guiding and confining light in nanometer-size low-refractive-index material. *Opt Lett* 29:1626–1628
71. Kippenberg TJ, Spillane SM, Vahala KJ (2004) Demonstration of ultra-high-Q small mode volume toroid microcavities on a chip. *Appl Phys Lett* 85:6113–6115
72. Armani AM, Vahala KJ (2007) Soft lithographic fabrication of microresonators, *Digest of the IEEE LEOS Summer Topical Meetings* 133–134
73. Hossein-Zadeh M, Vahala KJ (2007) Free ultra-high-Q microtoroid: a tool for designing photonic devices. *Opt Express* 15:166–175
74. Landers JP (1996) *Handbook of capillary electrophoresis*. CRC Press, Boca Raton, FL
75. White IM, Fan X (2008) On the performance quantification of resonant refractive index sensors. *Opt Express* 16:1020–1028
76. Suter JD, White IM, Zhu H et al (2008) Label-free quantitative DNA detection using the liquid core optical ring resonator. *Biosens Bioelectron* 23:1003–1009
77. Pang F, Han X, Chu F et al (2007) Sensitivity to alcohols of a planar waveguide ring resonator fabricated by a sol-gel method. *Sensors Actuators B Chem* 120:610–614
78. Passaro VMN, Dell’Olio F, De Leonardis F (2007) Ammonia optical sensing by microring resonators. *Sensors* 7:2741–2749
79. Shopova SI, White IM, Sun Y et al (2008) On-column micro gas chromatography detection with capillary-based optical ring resonators. *Anal Chem* 80:2232–2238
80. Sun Y, Shopova SI, Frye-Mason G et al (2008) Rapid chemical-vapor sensing using opto-fluidic ring resonators. *Opt Lett* 33:788–790
81. Tombelli S, Minunni M, Mascini M (2005) Analytical applications of aptamers. *Biosens Bioelectron* 20:2424–2434

82. Petrenko VA, Vodyanoy VJ (2003) Phage display for detection of biological threat agents. *J Microbiol Methods* 53:253–262
83. Jung Y, Jeong JY, Chung BH (2008) Recent advances in immobilization methods of antibodies on solid supports. *Analyst* 133:697–701
84. Weber PC, Ohlendorf DH, Wendoloski JJ et al (1989) Structural origins of high-affinity biotin binding to streptavidin. *Science* 243:85–88
85. Andersson K, Hamalainen M, Malmqvist M (1999) Identification and optimization of regeneration conditions for affinity-based biosensor assays. A multivariate cocktail approach. *Anal Chem* 71:2475–2481
86. De Vos K, Bartolozzi I, Schacht E et al (2007) Silicon-on-insulator microring resonator for sensitive and label-free biosensing. *Opt Express* 15:7610–7615
87. White IM, Zhu H, Suter JD et al (2007) Refractometric sensors for lab-on-a-chip based on optical ring resonators. *IEEE Sens J* 7:28–35

Part IV
Terahertz Biosensing

Terahertz-Biosensing Technology: Progress, Limitations, and Future Outlook

Abdellah Menikh

Abstract After more than three decades of niche applications in the space sciences area, the field of terahertz (THz) technology is entering a new era of biomedical sensing and imaging. The past few years have seen an unprecedented expansion of terahertz ray technology in medical science, spanning applications as diverse as tumor recognition, dental cavities detection, and ligand–analyte sensing interaction. High cost, large sample volume, low sensitivity, lack of massive parallelism, and water absorption are still major challenges facing THz label-free sensing and imaging. The primary goal of current research in this field is to improve the THz sensor dynamic ranges, achieve faster data acquisition, and reduce water vapor absorption. In this chapter, THz biosensing capabilities, progress, and limitations are highlighted and discussed.

Keywords Far Infrared · THz · Biosensor · Optics · Imaging · Diagnostics · Spectroscopy · Biomolecules · ZnTe source · Detector · ATR-FTIR · Raman · Wave guide · Fluorescence · SPR · Refractive index · Biorecognition · Laser · DNA · Array

Contents

1	Introduction	284
2	THz-Generation Principles	286
3	THz Biosensor Applications	287
4	THz Bioimaging	291
5	Comparison of THz Waves and Existing Optical Biosensors	292
6	Concluding Remarks	294
	References	294

A. Menikh

Department of Instrument Systems, Siemens Medical Solutions Diagnostics, 62-Flanders-Bartley Road, Flanders, NJ 7876, USA

e-mail: abdellah.menikh@siemens.com

Abbreviations

ATR-FTIR	Attenuated total reflection Fourier transform infrared
AFM	Atomic force microscopy
QWP	Quarter wave plate
SPR	Surface plasma resonance
WHO	World Health Organization

1 Introduction

Within the last decade, collaborative efforts in biology, physics, and chemistry have resulted in enormous advances in biosensor technology. Improved techniques in microfabrication and integrated optics have driven biosensor technology to smaller, faster, and more powerful detection devices. In any biosensing scheme, the final goal is to simplify sample preparation steps, provide high sensitivity and selectivity, portability, reliability, and low cost. To respond to these demands, a plethora of optical sensing methods have been developed and perfected, including electrochemical, optical, and piezoelectric devices. Optical biosensors have been given special priority due to low cost and great impact they have had on biomolecular detection since their introduction more than two decades ago.

Fluorescence and surface plasmon resonance (SPR) based detection are among the most sensitive, reliable, and cost-effective methods. Though the fluorescence methodology remains the cornerstone of most biological research protocols, the technique is still suffering from a number of limiting factors, such as efficiency, interference, cross-reactivity, and variability from one molecule to another. In addition, attaching fluorophores may influence the way the ligand binds to other analytes and causes background signals [1].

Label-free detection methodologies have emerged as a potential remedy to overcome some of these flaws. In this regard, SPR commercialized by Biacore, Neuchtel, and Applied Biosystems has shown tremendous success in the marketplace as a direct detection scheme for unlabelled molecules. The quest for reliable, portable, low cost, and sensitive devices in applications such as food safety, molecular diagnostics, chemical and biological warfare, genomic, proteomic, and drug discovery has driven Texas Instruments to develop and commercialize a miniature cost-effective SPR device called “Spreeeta,” which includes the entire required component in a total volume of 7 cm³ and weighs 7 g. This newly developed SPR biosensor is able to measure all necessary properties, such as refractive index changes and association–dissociation constants of avidin–biotin, DNA–DNA, and antigen–antibody binding [2]. However, the sensitivity of the state-of-the-art SPR sensors cannot be reached by “Spreeeta” because the sensor performance is restricted by a low signal-to-noise ratio (SNR), due to the compact design of its electronic components. Undoubtedly, integrating SPR biosensor

to hundreds of thousands of channels, each capable of performing a specific measurement, will open up new avenues for parallel processing of several label-free biorecognition elements simultaneously, thus, giving a new dimension to portability with a wide time response range for slow and fast kinetics, with maximum versatility and flexibility.

In spite of the progress that had been registered during the past decade in optical detection methodologies, the number of biosensor operating in the far infrared region of the electromagnetic spectrum is almost inexistent or scarce. The only methods that have been used extensively to monitor the ligand–analyte binding in the aforementioned spectral region are ATR-FTIR and Raman spectroscopy [3]. Nevertheless, the anomalies associated with the cryogenic detector in FTIR and with Raleigh lines in Raman spectroscopy have hampered these techniques from being widely used.

Recently a new detection modality based on terahertz waves has been proposed as a new alternative for detecting minute amount of biological materials. THz technology took a major leap forward half dozen years ago when Hyun–Shik Kang of the Chonbuk National University in Korea was on sabbatical year at Rensselaer Polytechnic Institute. Professor Kang developed a unique form of ZnTe crystal which is now the basis for THz generation and detection in more than 100 laboratories around the world. Over the past few years, research and development in material science provided new and higher power sources, leading to a remarkable progress in developing small and relatively cheap devices [4].

Terahertz (THz) spectroscopy systems utilize far-infrared radiation to extract molecular spectral information in an otherwise inaccessible region of the electromagnetic spectrum where various rotational, vibrational, and translational modes of molecules are located, 0.1–10 THz (Fig. 1). As the wavenumber range is narrowed, THz-radiation can yield more specific information about a particular chemical component within the system. Unlike most spectroscopic techniques, THz instrument measures the wave temporal electric field, which can be Fourier transformed to yield THz pulse amplitude and phase. This added capability allows precise

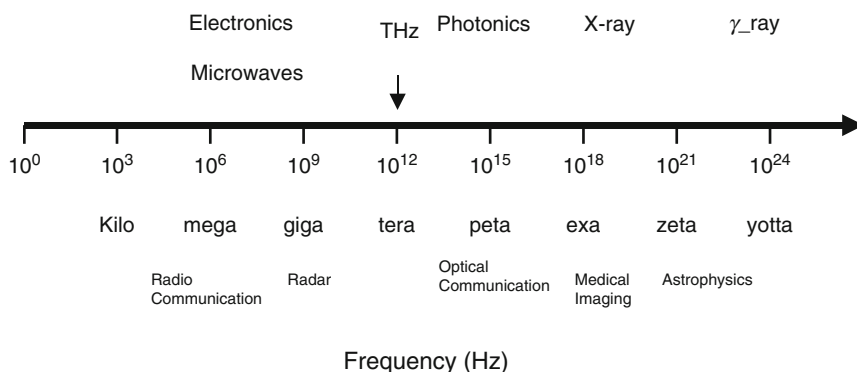


Fig. 1 Electromagnetic spectrum showing the THz-ray band spectral range

measurement of both refractive index and absorption coefficient, a property that makes THz sensing extremely attractive research field in a variety of disciplines.

THz sensing and imaging technology is relatively new with numerous applications from sectors as diverse as semiconductor, medical, manufacturing, space, and defense industries. In this chapter, a broad survey of terahertz-biodetection technology from its infancy to more recent biomedical use is presented. The focus is directed mainly on terahertz radiations that can be specifically applied to label-free ligand–analyte interaction. The uniqueness, limitations, and potential capabilities of THz biosensor are discussed.

2 THz-Generation Principles

With the improvement of compact solid state femtosecond (fs) lasers, emitters, and detector sources, THz time domain system has recently emerged as an extremely useful and powerful probe of charge transport in both solid state and biological materials. The heart of the double modulated THz system is a mode locked femtosecond laser which generates short pulses of 150 fs width, 86 MHz repetition rate, and 1.5 W average powers. A beam splitter separates the laser rays into excitation and reference pulses. The excitation pulse illuminates an unbiased Gallium arsenide (GaAs) emitter wafer to generate a THz beam which is collimated and focused onto $\langle 110 \rangle$ Zinc telluride (ZnTe) crystal with paraboloidal mirrors (Fig. 2). A pellicle located after the second paraboloid mirror allows the reference beam to travel collinearly with the THz wave through the electrooptic crystal $\langle 110 \rangle$ ZnTe detector. When both THz and reference beams propagate through the ZnTe, the structure of the crystal changes slightly, which cause small alteration in the probe beam polarization. A QWP polarizes the THz wave elliptically and

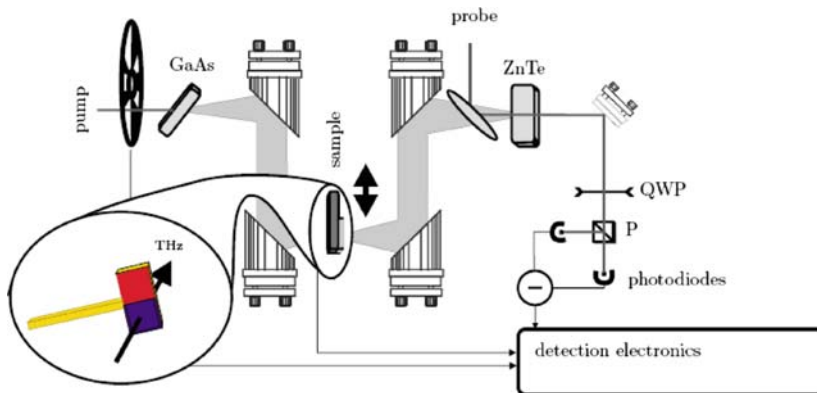


Fig. 2 Optical set up of a typical THz system without beam stop

the Wallaston prism (P) separates it into its horizontal (s) and perpendicular (p) components. A pair of photodiodes measures the difference in current intensities between s and p. The time domain spectrum of the THz pulse is measured by scanning the time delay between the THz wave and the reference beam. Typical THz time-domain spectroscopy systems have a frequency bandwidth loosely between 0.1 and 10 THz, a spectral resolution of 50 GHz, an acquisition time under 1 min, and a dynamic range of 1×10^5 in electric field. THz rays penetrate most dry objects and nonpolar solvents. However, metals and polar liquids are completely opaque.

Perhaps the most important elements in THz systems are sources and detectors. Sources are vaguely classified into two categories: pulsed broadband and continuous narrowband. The most common approaches for generating broadband THz pulses are photoconductive antenna and optical rectification, while voltage controlled oscillators or dielectric resonators are the two widely used sources for generating low power narrowband continuous THz waves [5].

The low power of THz sources coupled with relatively high thermal background has necessitated highly sensitive detection systems. In this respect, broadband detection based on thermal absorption is commonly used to detect low THz signal. The drawback of these detectors, however, is the fact that they require cooling units, to reduce thermal background. For pulsed THz detection, in THz time domain systems, coherent detectors are required.

3 THz Biosensor Applications

For decades, scientists have sought to develop new, rapid, and sensitive detection modality using biological elements, such as antibodies, enzymes, lectins, nucleic acids, and cells. Specific interactions between the target analyte and the biorecognition element produce a physico-chemical change which is measured and detected by electronic device. Recent advances in immunochemistry and molecular biology have expanded the range of the biomolecular recognition element, while the advent of laser, fiber optics, and micromachining technology have accelerated the development of small, inexpensive optical transducers [6, 7, 8]. An interesting recent development in this regard has been described by the Epstein group [9], which made use of fiber-optic biosensor microsphere arrays capable of reaching a detection limit of zeptomole (10^{-21} mol~600 DNA molecules), with the advantage of high throughput, sensitivity, and flexibility.

Although recent development in optical biosensors has reached unprecedented progress in terms of high sensitivity, smaller sample, and massive parallelism, there is a continual need for development of new biosensors that operate in the far-infrared region for the reasons outlined above. Motivated by the fact that the same fundamental design principles lay at the heart of the new developments, translating those principles into the realm of newer technologies is a real challenge.

Attempts to apply THz ray to biological and chemical materials met with success when the THz differential time domain technique was used to monitor the binding between avidin and biotin in a membrane lipid-like environment. The conjugation procedure of avidin to glass slides and the subsequent biotin–avidin interactions have been highlighted in a previous article [10]. In brief, the glass slide has been derivatized using thiol- terminal silane followed by succinimide cross-linker. Half of the avidin coated glass slide was exposed to a solution containing biotin molecules; the other half of the slide was used as a reference. Alternating THz-ray between the sample and the reference gives signal directly proportional to the difference in film thickness between avidin and avidin–biotin complexes. A small, yet, measurable signal exists when similar experiments have been conducted without biotin molecules. The remaining signal is, presumably, due to avidin surface inhomogeneity and/or to instrument noise.

The THz difference time domain is able to detect thin layers of submicron thickness with less than $0.1 \mu\text{g cm}^{-2}$ of biotin, which is comparable to other surface analytical techniques, such as ellipsometry and integrated optics [11]. It is possible that higher sensitivity can be achieved by changing the reflective index and/or the thickness on the biotin half side. Towards this objective and in order to improve the signal to noise ratio of THz system, an approach was used based on immobilizing a hydrophobic substrate, octadecanol, on a hydrophilic quartz substrate using a process that is widely referred to as molecular self assembly (Fig. 3). Subsequent immersion of the quartz chip in biotin solution increased the sample thickness to 5 nm cm^{-2} , as measured by AFM. Conjugating agarose beads to avidin and applying the conjugate to half of the quartz surface modified biotin, the THz

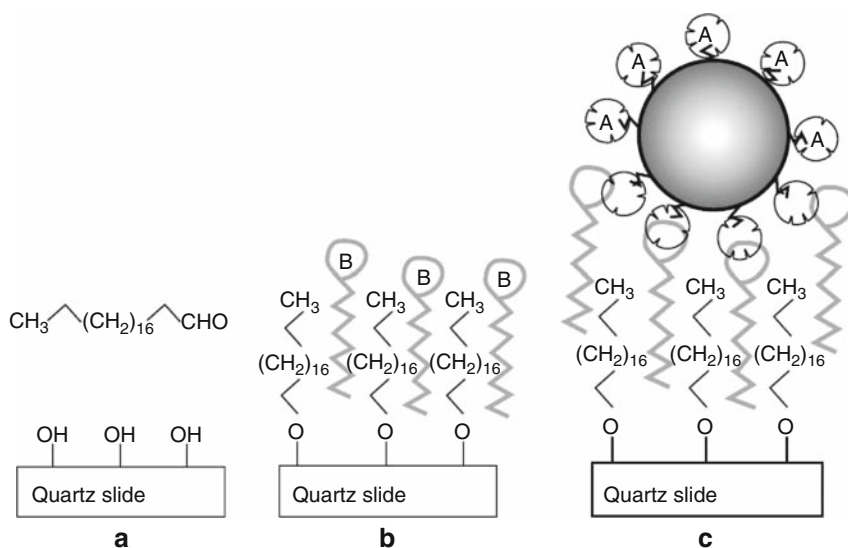


Fig. 3 Octadecanol self-assembly on quartz crystal surface (a), followed by biotin monolayer (b). Avidin conjugated agarose beads–biotin complex, on a quartz surface modified octadecanol (c)

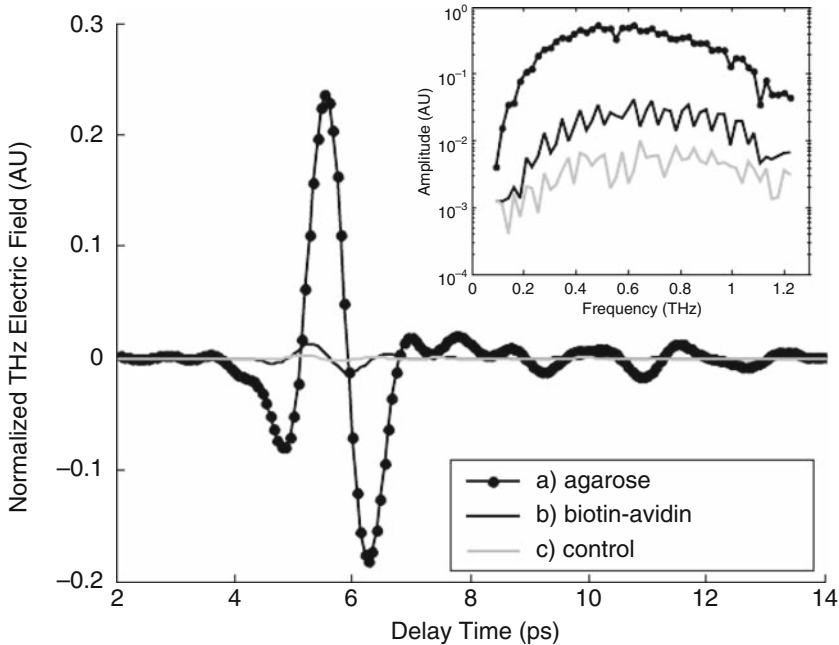


Fig. 4 Time domain THz pulses obtained by measuring the difference signal between biotin and biotin–avidin conjugated agarose (a), biotin and biotin–avidin complexes without beads (b), reference sample (c)

difference time domain signal between biotin and biotin –avidin complex increased considerably (Fig. 4). The technique is able to detect less than 10.3 ng cm^{-2} avidin, almost eightfold higher than its counterpart, without agarose beads. It is believed that the signal enhancement is most likely due to either refractive index or thickness changes. By applying the electromagnetic theory to two different dielectric surfaces (Fig. 5) [12], we obtain

$$E_{\text{ref}}(\omega) = t_{13}E_0(\omega) \exp \frac{i\omega d}{c}, \tag{1}$$

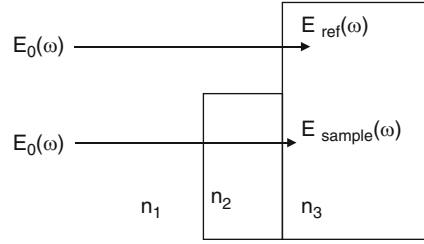
where $E_0(\omega)$ is the incident electric field, t_{13} is the transmission coefficient, c is the speed of light in vacuum, and d is the sample thickness.

The propagating wave in the sample is given by [13]

$$E_{\text{sample}}(\omega) = \frac{t_{12}t_{23} \exp[i\delta(\omega) - \alpha(\omega)d]}{1 - r_{21}r_{23} \exp[2i\delta(\omega) - 2\alpha(\omega)d]} E_0(\omega), \tag{2}$$

where $\alpha(\omega)$ is the absorption coefficient, r_{21} and r_{23} are the reflection coefficients at the air–sample, and sample–substrate interfaces, respectively; $\delta(\omega)$ is the phase changes and is given by the well-known relation $\delta(\omega) = n_2(\omega) \frac{\omega d}{c}$.

Fig. 5 Schematic representation showing the refractive indices n_1 , n_2 and n_3 for air, sample and substrate. $E_0(\omega)$, $E_{\text{ref}}(\omega)$, and $E_{\text{sample}}(\omega)$ are the electric field components in air, reference and sample, respectively; d is the sample thickness



For thin films, the phase changes $\delta(\omega) \ll 1$, and (2) can be written approximately as

$$\frac{E_{\text{diff}}(\omega)}{E_{\text{ref}}(\omega)} \approx i \frac{\omega d}{c} \left[n_2 - 1 + \frac{(n_2 - n_1)(n_2 - n_3)}{n_1 + n_3} \right] - \alpha(\omega)d \times \left[1 + \frac{(n_2 - n_1)(n_2 - n_3)}{n_1 + n_3} \right], \quad (3)$$

where $E_{\text{diff}}(\omega) = E_{\text{sample}}(\omega) - E_{\text{ref}}(\omega)$, and n_1 , n_2 and n_3 are the refractive indices of the air, the sample, and the reference, respectively. For less absorbing materials, $\alpha(\omega) \ll 1$, (3) can be simplified further to

$$\frac{E_{\text{diff}}(\omega)}{E_{\text{ref}}(\omega)} \approx i \frac{\omega d}{c} \left[\frac{n_1 n_3 + n_2^2}{n_1 + n_2} - 1 \right], \quad (4)$$

with $n_1 = 1$ (air),

If the refractive index of the deposited material is higher than that of the substrate.

$n_2 \gg n_3$,

$$\frac{E_{\text{diff}}(\omega)}{E_{\text{ref}}(\omega)} \approx i \frac{\omega d}{c} \left[\frac{n_2^2}{1 + n_2} - 1 \right]. \quad (5)$$

Indeed (5) shows that the difference signal depends on the material refractive index and its thickness. This finding opens up new possibilities for future applications of THz sensing, including DNA–DNA hybridization, mutation, and antigen–antibody detection.

In an effort to improve further the signal to noise ratio and therefore THz sensitivity, Nagel's team [14] used a planar-integrated wave guide based on micro-strip line resonators to spot particular sequences of DNA at femtomolar detection level. A significant advantage of this system is its enhanced sensitivity, rapidity, accuracy, and scalability to a high throughput array. Most importantly, and in contrast to conventional THz design, the integrated THz wave guide is less sensitive to water vapor absorption. This methodology seems to be one of the most

promising concepts for detecting label-free molecules at femtomolar level sensitivity with possibility of parallel integration. The main drawbacks of this design, however, are the complexity of the fabrication and the meticulous adjustment of the optical components. To circumvent these problems, Kraemer and colleagues [15] have integrated an optoelectronic micro-THz source into a glass microchip in a size of 1 mm^2 without need of optical adjustment. The system allows distinction between illicit drug powders with a nanograms sensitivity, a value comparable to the current forensic toxicology identification techniques [16]. The newly developed THz system can be easily multiplexed to an array; its unique capability to detect macromolecules in their native state could be a major mile stone for future THz lab on chip.

It was common opinion that water is a major hurdle for THz technology [17]. Until recently, almost all successful experiments set up have been conducted using either dry or low water content samples. Several tentative attempts, however, have been made to examine DNA vibrational modes in liquid over the spectral region $10\text{--}25 \text{ cm}^{-1}$. The results demonstrate that there is little interference between the spectral features of the probed sample and the water background, except for the band located at 18.6 cm^{-1} , where the water absorption is clearly predominant [18]. The extreme sensitivity of THz-rays to water can be turned into an advantage in distinguishing between healthy and cancerous tissue [4], because cancerous tissue tends to have higher water content than healthy tissue.

4 THz Bioimaging

Breast cancer is the second leading cause of death in women today. According to the World Health Organization (WHO), an estimated 1.2 million people worldwide were diagnosed with breast cancer in 2004. For years, X-ray mammography has been considered as one of the most advanced technology for early breast cancer diagnosis. Undoubtedly, early detection of small tumors greatly improves women chance for successful treatment. The drawbacks, however, is the fact that X-ray mammography process consists of squeezing the patient breast, and injecting relatively high level radiation dose which may cause patients discomfort, skin damage, and pain. More importantly, X-ray mammography has proven to be ineffective for women with dense breasts; therefore, an alternative noninvasive imaging tool may be of value.

Recently, THz-ray imaging has emerged as a powerful promising detection tool, able to pinpoint specific regions of a diseased tissue and to create two- and three-dimensional images. THz-rays penetrate relatively deeper into many tissues without the damage associated with ionizing radiation, such as in X-ray [16], thereby allowing effective detection of epithelial cancer cells safely and less invasively. It has been demonstrated that THz-ray could potentially detect differences between normal breast tissue, tumor, and even early-stage in-situ cancers in excised tissue samples [19]. Preliminary data, from Terra View Inc, have showed that terahertz

imaging is capable of detecting skin cancers and tumors that form invisibly beneath the skin. In another ambitious research effort, excised breast tissue were imaged and compared with the corresponding histology section, the data showed that the size and shape of tumor regions in terahertz images correlate well to that of histology. This progress of THz imaging has paved the way toward a number of perspective benefits, including improved medical imaging, and instant fingerprinting of chemical and biological materials in solid state.

Application of THz rays in early detection of dental cavities has also shown enormous potential. Traditionally, dental demineralization in tooth enamel was monitored either by X-ray or fluorescence based technology. However, these techniques are less sensitive and often detect the diseased teeth after the cavities had begun. In contrast, THz technology is capable of distinguishing between the enamel and dentin layers in teeth [20]. Initial experiment on enamel slabs in vitro suggest that the signal may provide information about the depth of the lesion demineralization and early detection of dental caries. The only drawback that may complicate the use of THz in dentistry is the presence of saliva; therefore, care should be exercised when interpreting THz images.

Newly developed imaging systems based on THz time-domain spectroscopy and THz tomography have been shown to be able to perform measurements on, and obtain images of, samples which are opaque in the visible and near-infrared regions of the electromagnetic spectrum. Importantly, THz-time domain produces radiation that is both coherent and broadband, leading to far more information than a conventional image. Since THz-difference time domain is limited by sample thickness and its absorption, care should be exercised in interpreting THz data, because it is extremely difficult in distinguishing changes caused by the sample from those caused by long-term fluctuations in the driving laser source or experiment. Yet, still more work is needed to fully explore the potential of THz imaging for medical diagnosis.

5 Comparison of THz Waves and Existing Optical Biosensors

Numerous optical biosensing approaches and possibilities have been proposed in the past few years, and some of them have reached the commercial development. THz-ray has emerged as a technique of choice and has become increasingly important for biological applications. Progress relating to generation and detection of THz radiation with relatively compact devices at room temperature has been achieved. In the past few years, generation and detection of THz-ray was not possible without bulky and expensive equipment, such as lasers, thermal sources, and liquid helium cooled bolometer detectors.

While there is a relatively wide application of THz-ray in biomedical sensing and imaging, the potential usefulness of THz should not be overstated. The technique is still in its infancy, and may not compete efficiently with existing technologies. The problem of water absorption, which may in certain circumstances be

turned to an advantage, is still a major handicap in detecting the target molecule and hampers THz from being used as a diagnostic tool. A serious disadvantage of THz based affinity detection arises from the difficulty of detecting low molecular weight. This is due to very small changes in thickness of the half layer immobilized on the surface sensor associated with the binding reaction. The difficulty lays not so much in obtaining data but in extracting useful information. Changes in the THz pulses that are caused by the sample can be difficult to distinguish from those caused by long-term fluctuations in the driving laser source. The difference signal between the reference and target samples may not be detectable from instrument background noise, in such a case, special care should be exercised in interpreting the acquired data. The detection limit of THz biosensor can be significantly improved if adequate strategies are devised. For instance, the sensitivity can be dramatically enhanced by coupling the target molecule to a secondary affinity reaction that involves either high molecular weight or THz absorbed beads [10]. A more elegant strategy for amplifying the terahertz difference signal would be based on labeling the target probes with colloidal nanoparticles. In such a system, the most simple amplification approach consists of using terahertz time domain difference on reflection or on transmission modes. In contrast to THz-ray, SPR sensor permits the detection of molecular binding as small as 200 Da without using any type of molecular enhancer. In addition, the association and dissociation constants of ligand–analyte binding can also be determined.

In spite of the large amount of effort that has been devoted to THz sources and detectors, the cost is still far beyond any optical sensing methodology. Future success of biological THz technology applications will strongly depend on the development of compact, low-cost, reliable, sensitive, and flexible systems. However, it is not only the high cost that has prevented THz detection technology from taking off. There are two other main factors that have contributed to this phenomenon. The first is the fact that until now THz development has kept a very low research and development profile, though recently certain academic groups have taken the initiative and begun to investigate possible application of THz in medical science. It is evident that such research efforts in THz would lead to an advancement of the technology and an uptake on a global scale. Second, skepticism still remains about THz growth as an alternative tool to existing biosensing and bioimaging methods.

When compared to other integrated biosensor techniques, the THz-ray sensitivity is in the same order of magnitude as other optical methods (Table 1), but the reliability is still lacking. The comparison is somewhat vague because the sensitivity of biosensors depends largely on two main factors: The capacity of the ligand to bind analyte and the optical detection limit of the device. The first depends on both the affinity of interaction and the number of binding sites accessible to the analyte. The second depends mainly on the signal to noise ratio and the device thermal drift.

The possibility of observing a ligand–analyte interaction directly without the use of labels is one of the key advantages of terahertz technology. Its ability to detect single base mutation in a single copy of gene and pin point its structural changes will undoubtedly impact our knowledge about the way macromolecules interact.

Table 1 Comparison of sensitivities for different biosensors [21]

Sensing method	Detection limit (pg/mm ²)
SPR	1–5
Waveguide-SPR	2
Resonant mirror	5
Grating coupler	1–10
Mach-Zehnder interferometer	0.1
Differential mode interferometer	1
Young interferometer	0.7
Reflectometric interference spectroscopy	1–5

This will opens up a new avenue for detecting molecules that preserve their structural integrity in dry environment.

6 Concluding Remarks

Much work remains to be done for developing a robust THz system. The future device needs to provide adequate power, while in the same time being compact and cost effective. THz sensing and imaging have witnessed a major leap during the past decade. Industry participants are already planning for the growth of new markets that capitalize on the new unique capabilities of THz technology. However, with all the legitimate promise of terahertz systems, the field has been clouded by the hype. The backlash is still ongoing between two schools of thought. One, lead by Xi-C Zhang, claiming that although there are a number of challenges to be overcome there is no doubt that THz technology will play a major role in many disciplines including medical and forensic sciences. The other experts working on the development of THz system have adopted more skeptical attitude and unfairly dismiss viable applications that are likely to create significant markets. Certain applications have been widely promoted that are not practical or, in some cases, even feasible.

References

1. D'Orazio P (2003) Biosensors in clinical chemistry. *Clin Chim Acta* 334:41–69
2. Chinowsky TM, Quin JG, Bartholomew DU (2003) Performance of the “Spreeta 2000” integrated surface plasmon resonance affinity sensor. *Sensors Actuators B Chem* 91:266–274
3. Menikh A, McColl R, Mannela CA, Zhang X-C (2002) Terahertz biosensing technology: frontiers and progress. *Chem Phys Chem* 3:655–658
4. Rainsford T, Mickan SP, Abbott D (2005) T-ray sensing applications: review of global developments. *SPIE* 5649:826–838
5. Ferguson B, Zhang Xi-C (2002) Materials for terahertz science and technology. *Nat Mater* 1:26–33

6. Taylor JR, Fang MM, Nie S (2000) Probing specific sequences on single DNA molecules with bioconjugated fluorescent nanoparticles. *Anal Chem* 72:1979–1986
7. Ebenstein Y, Mokari T, Banin U (2004) Quantum-dot-functionalized probes for fluorescence energy transfer based microscopy. *J Phys Chem B* 108:93–99
8. Ueberfeld J, Walt DR (2004) Reversible ratiometric probe for quantitative DNA measurements. *Anal Chem* 76:947–952
9. Epstein JR, Lee M, Walt DR (2002) High density fiber-optic genosensor microsphere array capable of zeptomole detection limites. *Anal Chem* 74:1836–1840
10. Menikh A, Mickan SP, Liu H, MacColl R, Zhang Xi-C (2004) Label-free amplified bioaffinity detection using terahertz wave technology. *Biosens Bioelectron* 120:658–662
11. Lechuga LM (2005) Optical biosensors. In: Gorton L (ed) *Biosensors and modern bio-specific analytical techniques*, *Comprehensive analytical chemistry*. Elsevier, Amsterdam, pp 209–250
12. Jiang Z, Li M, Zhang X-C (2000) Dielectric constant measurement for thin films differential time-domain spectroscopy. *Appl Phys Lett* 76:3221–3223
13. Born M, Wolf E (1980) *Principals of optics*, 6th edn. Cambridge University Press, London
14. Nagel M, Haring Boliver P, Brucherseifer M, Kurz H, Bosserhoff A, Buttner R (2002) Integrated planar terahertz resonators for femtomolar sensitivity label free detection of DNA hybridization. *Appl Opt* 41:2074–2078
15. Lu JY, Chen LJ, Kao TF, Chang HH, Chen HW, Chen YC, Wu RB (2006) Terahertz microchip for illicit drug detection. *IEEE Photon Technol Lett* 18:2254–2256
16. Kraemer T, Theis GA, Weber AA, Maurer HH (2000) Studies on the metabolism and toxicological detection of the amphetamine-like anorectic fenproporex in human urine by gas chromatography – mass spectrometry and fluorescence polarization immunoassay. *J Chromatogr B* 738:107–118
17. Nagel M, Forst M, Kurz H (2006) THz biosensing devices: fundamental and technology. *J Phys Condens Matter* 18:S601–S618
18. Globus T, Woolard D, Crowe TW, Khromova T, Gelmont B, Hesler J (2006) Terahertz Fourier transform, characterization of biological materials in a liquid phase. *Appl Phys* 39:3405–3413
19. Knobloch P, Schmalstieg K, Koch M, Rehberg E, Vauti F, Donhuijsen K (2001) THz imaging of histo-pathological sample. *Proc SPIE* 4434:239–245
20. Hall A, Girkin JM (2004) A review of potential new diagnostic modalities for caries lesions. *J Dent Res* 83:C89–C94
21. Lechuga LM, Prieto F, Sepulveda B (2003) Optical sensors. In: Narayanaswamy R, Wolfbeis OS (eds) *Industrial environment and diagnostic applications*. Springer, Heidelberg, pp 227–248

Index

A

Absorption 115, 195, 209
Absorption-based sensors, detection strategies 47
Affinity coatings 171
AIR 5
Alcohol sensing 162
Alkyne–azide cycloadditions, copper-catalyzed 13
Antibodies 8
Antibody microarrays 27, 30, 31
Antifreeze, LPG 164
Antigen–antibody binding 6
Antireflection coating (ARC) 85
Applied optics 257
Aromatic organic compounds 166
ARROW waveguide 195, 208
Aryldiazirine cross linker 8
ATR-FTIR 281

B

Bacillus subtilis 9
Bacteria 258
Bacterial lipid A 9
Bacteriophage MS2 virus 8
Biomolecules 281
Biophotonics 258
Biorecognition 281
Biosensors 73, 195, 219, 281
Blood, whole, detection 19
Borophosphosilicate glass (BPSG) 213
Bovine serum albumin (BSA) 7, 77

Bragg filters/mirrors 6, 206
 reflector 7
 waveguide 206

C

Calcium chloride (CaCl_2), LPG 164
Capillary waveguides 202, 219
 biosensors 244
Carbodiimide 8
Carbohydrate microarrays 27, 30
Cellular microarray 27
Chemical sensors 127, 195
Chloride ion detection, LPG 166
Cladding etching 131
Click reactions 13
Coherent anti-Stokes Raman scattering (CARS) 92
Confinement 195
Core-based optical fiber sensors 123
Corrosion monitoring 166
CWBP, implementation 240
 optimal capillary 235

D

Detection, label-dependent 35
 label-independent 37
Detection channel 12
Detectors 281
Diagnostics 281
Dielectrics 195
Diffraction grating structures, resonances 81

- Diffusion, monitoring 16
- Dimethyl–methyl phosphonate (DMMP) 130
 - vapors 136
- Dinitrophenyl 170
- DNA 4, 213, 258
 - PSi microcavity sensor 8
- DNA hybridization 6
- DNA microarrays 27, 30, 281
- DNA monolayer thickness sensing 170
- DNA polymerase molecules 211
- DNA quantification 77
- DNA target detection 163
- Drug delivery 16
- Dynamic mass redistribution 27

- E
- E. coli* 8, 10
- Endoscopes 177
- Enzymatic reactions, porous silicon 15
- (EO)6-Si chip 18
- Ethanol 162
 - detection, sol–gel coating 170
- Ethylene glycol 165
- Evanescent field 195
 - sensors 122, 124
- Evanescent waves 78
- Extrinsic sensors 114, 123

- F
- Fabry–Pérot interferometer 6
- Far infrared 281
- FBG-based sensors 161
- Fiber bending, sensor performance 55
- Fiber Bragg gratings 154
- Fiber etching 131
- Fiber modification 131
- Fiber-optic capillary 204
- Fiber-optic sensors 45, 151, 195
- Fibers, numerical aperture 113
- Fibrinogen 77
- Fluorescence 119, 195, 210, 281
 - energy transfer 120
 - surface-enhanced 95
- Fluorescence correlation spectroscopy (FCS) 210
- Fluorescence effect 96

- Fluorescence lifetime imaging microscopy (FLIM) 211
- Fluorescent molecules, photon emission 231
- Fluorophores 97, 120
- Förster resonance energy transfer (FRET) 210
- Fresnel waveguides 204
- FT-IR 177
 - fiber probe 184

- G
- G protein-coupled receptor microarray 27
- β -Galactosidase 171
- Gelatinase activity 15
- Glutamine sensor 16
- Grating waveguide structures (GWS) 77
- Guided-mode resonance (GMR) 77, 82
 - sensor/tunable filter 85

- H
- HCl vapors 134
- Heptane, LPG 166
- HIV proteins 171
- Hollow core 195
- Hollow fibers 219
- Hollow-core photonic bandgap fibers 49
- Hollow-core photonic crystal fiber (HC-PCF) 207
- Hollow-fiber Raman probe 187
- Hollow-optical fibers 177, 179
- Humidity sensor, porous sol–gel fiber 125
- Hybridization 219, 250
- Hydrazine vapor 135
- Hydrocarbon groups, hydrosilylation 6
- Hydrofluoric acid, etching 131
- Hydrogel-embedded sensor 9
- Hydrogen detection/concentration 162, 172
- Hydrogen peroxide 135
- Hydrosilylation, hydrocarbon groups 6

- I
- IgG 12
- Imaging 281
- Infrared spectroscopy 177
- Intermodal interference-based sensors 172
- Intrinsic sensors 123

Ionic self-assembled multilayers (ISAM)
168
Isopropyl alcohol (IPA) 162

L

Label free 258
Label-dependent detection 35
Label-independent detection 37
Lab-on-a chip sensor 170
Lactobacillus acidophilus 9
Lambda virus DNA 8
Lasers 281
Light-emitting diodes (LED) 142
Lipid A 9
Lipid crystals 87, 88
Liquid-core optical ring resonators
(LCORRs) 213
Liquid-core waveguides (LC-WG) 195,
197, 199
Liquid-liquid-core waveguides 201
Localized surface plasmon resonance
(LSPR) 76, 89
Long-period gratings (LPG) 151, 154, 164
cascaded 172
interferometers 151
Michelson interferometer 173
Loss 195

M

Membrane protein microarrays 30, 31
p-Mercaptobenzoic acid (pMBA) 95
Metal-clad waveguides 203
Metallic nano apertures 97
Metallic nanostructures 73
Metalloproteinase-2 (MMP-2) 15
Methanol 162
Microarrays 27, 30
cellular 32
DNA 30
fabrication 32
membrane proteins 31
resonant waveguide grating biosensor 33
technologies 29
Microcavity 6
Microsphere ring resonator 257, 263
Modal power distribution (MPD) 110
Monoclonal antibodies 171

MS2 bacteriophage 8
Multiplexing techniques 160

N

Nano apertures 75, 97
Nano-enhancement 89
Nanophotonics 73
Nanoporous cladding waveguides 200
Naphthalene-disulfonic acid (NDSA) 130
NH₃ vapors 134
Nonresonant sensing 50
Nucleic acid detection 219
Nylon, unclad fibers 119

O

Optical biosensors 27, 258
Optical chemical sensor 258
Optical mode 195
Optical ring resonator 260
Optical waveguides 223
leaky 227
Optics 281
Opto-fluidic ring resonator 257
Organic conducting polymers (OCPs) 118
Orthogonal subspace signal processing
algorithm (OSPA) 16

P

PBG sensors, 2D 20
Peptide synthesis, monitoring 13
PSi microcavity, on-chip optical
monitoring 13
Petroleum hydrocarbon detection, LPG
164
pH sensing 161
Photoluminescence 5, 97
Photon emission, fluorescent molecules 231
Photonic bandgap 45
Photonic crystal fibers (PCF) 99
Photonic crystal-waveguides, 2D 207
Photonic crystals 195
biosensing 99
Planar ring resonator 257
Plasmon-assisted sensing, PCFs 56
PMMA, unclad fibers 119
Polarization 214

- Poly(alamine hydrochloride) (PAH) 168
Poly{ 1-[4-(3-carboxy-4-hydroxy-phenylazo) benzenesulphonamido]-1, 2-ethanediy, sodium salt} (PCBS) 168
Polyacetylenes 118
Polyaniline 118
 electrical conductivity 127, 128
Polyethylene glycol (PEG) 18
Polyindoles 118
Poly-L-lysine (PLL) 171
Polythiophene 118
Polypyrrole 118
 electrical conductivity 127, 128
Polystyrene, unclad fibers 119
Porous silicon (PSi) 6
 double-layer, self-referenced 12
 enzymatic reactions 14
 filtration capacity 19
 microcavities 8
 single-layer interferometers 6
 surface derivatization 17
Propylene glycol solutions 162
Protein A – IgG binding 12
Protein microarrays 27, 31
Proteins 258
PSi, glutamine sensor 16
 peptide synthesis 13
 waveguide sensor 17
- Q
Quantitation of protease (pepsin) 15
- R
Raman effect 120
 resonant (RRE) 92
Raman probes 177
Raman spectroscopy 177, 281
Reference channel 12
Reflective interferometric Fourier-transform spectroscopy (RIFTS) sensor 12
Refractive index 195, 213, 258, 281
Resolution 195
Resonant Raman effect (RRE) 92
Resonant sensing 52
Resonant waveguide grating biosensor 27
 microarrays 33
RIFS 5
- Rigorous coupled wave approximation (RCWA) 84
Ring resonator 257
 biosensor 267
 chemical sensors 265
 configurations 263
 optical 260
 opto-fluidic 264
 performance 265
 planar 263
Rugate filters 7
RWG imager/biosensor 34
- S
Salts, LPG 164
Scattering 195, 211
Sensing principles 258
Sensitivity 195
Sensor efficiency, PSi 18
Signal-to-noise ratio (SNR) 240
Silicon, macroporous 5, 8
 mesoporous 5, 8
 nanoporous 5
 porous (PSi) 6
Silicon microcavity, hydrogel-embedded 11
SIM, chemical sensors 144
Single-layer 6
Slot waveguides 201
Small-molecule analytes 15
Smart bandages, wound healing 9
Smart dust 7
Sodium chloride (NaCl), LPG 164
Sol-gel fiber, CoCl₂ doped 123
Spatial (2D) intensity modulation (SIM) 110
Spatial division multiplexing (SDM) 161
Spatial intensity modulation 138
SPR sensors, photonic bandgap Bragg fibers 62
 photonic bandgap honeycomb fibers 65
 planar photonic bandgap waveguides 59
Stopband 7
Streptavidin 20
Sucrose solutions 163
 biosensing 170
Sugar solutions 162
Sugars, LPG 164
Surface electromagnetic waves (SEWs) 99

- Surface enhanced effects 73, 89
- Surface enhanced fluorescence (SEF) 76
- Surface enhanced Raman scattering (SERS) 76, 92, 121
- Surface passivation 6
- Surface plasmon cross emission (SPCE) 96
- Surface plasmon resonance (SPR) 27, 75, 121, 281
 - sensors 17, 197
- Surface plasmon sensitivity (LSPR technique) 89
- Surface plasmons 73
- Surface-enhanced fluorescence 95
- Surface-enhanced resonance Raman spectroscopy (SERRS) 94

- T
- Target-detection-error-rate (TDER) 241
- Thrombin 77
- Thue–Morse filter/mirror/sequence 6, 7
- THz 281
- THz bioimaging 289
- THz biosensors, applications 285
- THz generation 284
- THz waves 290
- Tilted fiber Bragg gratings (TFBG) 151
- Time division multiplexing (TDM) 161
- TNBS–BSA 16

- TNT, displacement assay 16
- Total internal reflection 195
- Transducers 115
- Transduction 115
- Trichlorododecyl-silane-treated mirror 18
- Trichloroethylene (TCE) 210
- TWTCP 8

- V
- Viruses 258

- W
- Waveguides 17, 195, 281
 - interference-based 205
 - non-TIR-based 202
 - total internal reflection 199
- Wavelength division multiplexing (WDM) 161
- Whispering gallery modes (WGMs) 76, 257

- X
- Xylene, LPG 166

- Z
- Zero-mode waveguides (ZMWG) 205
- ZnTe source 281

Erratum to:

Fiber-Optic Chemical and Biosensors

Mahmoud El-Sherif
Photonics Laboratories, Inc
1117 Hillcrest Rd
Narberth PA 19072
USA
melsherif@photonicslabs.com

M. Zourob and A. Lakhtakia (eds.), *Optical Guided-wave Chemical and Biosensors II*,
Springer Series on Chemical Sensors and Biosensors 8,
DOI 10.1007/978-3-642-02827-4_5, © Springer-Verlag Berlin Heidelberg 2010

DOI 10.1007/978-3-642-02827-4_12

The following acknowledgment to the chapter by Mahmoud El-Sherif “Fiber-Optic Chemical and Biosensors” (pp. 109–149) has been deleted accidentally in proof:

Acknowledgements Special thanks to the members of the research team who worked with me for the past 20 years at the Fiber Optics and Manufacturing Engineering Center, Drexel University and at Photonics Laboratories, Inc., Philadelphia, Pennsylvania, on the development of various types of chemical and biosensors. I am most grateful to late Alan MacDiarmid, the recipient of the 2000 Nobel Prize in Chemistry, for the technical collaboration on conductive polymer’ application to fiber-optic chemical sensors, and to late Jayakumar Radhakrishnan, Jianming Yuan, Lalit Bansal, Stephen Mastro, Saif Khalil, and Bulent Kose for their technical contributions to fiber-optic sensors while they were working on their PhD theses, under my supervision, at Drexel University. Special thanks goes to both Lalit Bansal and Vasileios Nasis for their help on the preparation of the literature review of this chapter. Also, the author acknowledge that most of the R&D presented in this chapter were conducted at Drexel University and Photonics Laboratories, Inc., and were mainly supported by the U.S. Department of Defense (Army, Navy, and Air forces) and NASA Lewis Research Center, through several funded programs, such as the MURI-ARO (Army Research Office) Grant #DAAH 01-96-1-0018, funded for 6 years.

The original online version for this chapter can be found at http://dx.doi.org/10.1007/978-3-642-02827_5
